CONTENTS

Technical Papers

Conference Announcements

Editors-in-Chief

S.L. Chan, *The Hong Kong Polytechnic University, Hong Kong*

W.F. Chen, *University of Hawaii at Manoa, USA*

R. Zandonini, *Trento University, Italy*

ADVANCED STEEL CONSTRUCTION

VOL.5, NO.3 (2009)

Advanced Steel Construction
an international journal

Cover: Skylight at MGM, Macau, China
     designed by second-order P-Δ-δ analysis without assumption of effective length

General Information
Advanced Steel Construction, an international journal

Aims and scope
The International Journal of Advanced Steel Construction provides a platform for the publication and rapid dissemination of original and up-to-date research and technological developments in steel construction, design and analysis. Scope of research papers published in this journal includes but is not limited to theoretical and experimental research on elements, assemblages, systems, material, design philosophy and codification, standards, fabrication, projects of innovative nature and computer techniques. The journal is specifically tailored to channel the exchange of technological know-how between researchers and practitioners. Contributions from all aspects related to the recent developments of advanced steel construction are welcome.

Instructions to authors
Submission of the manuscript. Authors may submit double-spaced manuscripts preferably in MS Word by emailing to one of the chief editors as follows for arrangement of review. Alternatively papers can be submitted on a diskette to one of the chief editors.

All manuscripts submitted to the journal are recommended to accompany with a list of four potential reviewers suggested by the author(s). This list should include the complete name, address, telephone and fax numbers, email address, and at least five keywords that identify the expertise of each reviewer. This scheme will improve the process of review.

Style of manuscript
General. Author(s) should provide full postal and email addresses and fax number for correspondence. The manuscript including abstract, keywords, references, figures and tables should be in English with pages numbered and typed with double line spacing on single side of A4 or letter-sized paper. The front page of the article should contain:
   a)   a short title (reflecting the content of the paper);
   b)   all the name(s) and postal and email addresses of author(s) specifying the author to whom correspondence and proofs should be sent;
   c)   an abstract of 100-200 words; and
   d)   5 to 8 keywords.

The paper must contain an introduction and a conclusion. The length of paper should not exceed 25 journal pages (approximately 15,000 words equivalents).

Tables and figures. Tables and figures including photographs should be typed, numbered consecutively in Arabic numerals and with short titles. They should be referred in the text as Figure 1, Table 2, etc. Originally drawn figures and photographs should be provided in a form suitable for photographic reproduction and reduction in the journal.

Mathematical expressions and units. The Systeme Internationale (SI) should be followed whenever possible. The numbers identifying the displayed mathematical expression should be referred to in the text as Eq. (1), Eq. (2).

References. References to published literature should be referred in the text, in the order of citation with Arabic numerals, by the last name(s) of the author(s) (e.g. Zandonini and Zanon [3]) or if more than three authors (e.g. Zandonini et al. [4]). References should be in English with occasional allowance of 1-2 exceptional references in local languages and reflect the current state-of-technology. Journal titles should be abbreviated in the style of the Word List of Scientific Periodicals. References should be cited in the following style [1, 2, 3].

Journal: [1]   Chen, W.F. and Kishi, N., "Semi-rigid Steel Beam-to-column Connections, Data Base and Modelling", Journal of Structural Engineering, ASCE, 1989, Vol. 115, No. 1, pp. 105-119.
Book: [2]   Chan, S.L. and Chui, P.P.T., "Non-linear Static and Cyclic Analysis of Semi-rigid Steel Frames", Elsevier Science, 2000.
Proceedings: [3]   Zandonini, R. and Zanon, P., "Experimental Analysis of Steel Beams with Semi-rigid Joints", Proceedings of International Conference on Advances in Steel Structures, Hong Kong, 1996, Vol. 1, pp. 356-364.

Proofs. Proof will be sent to the corresponding author to correct any typesetting errors. Alternations to the original manuscript at this stage will not be accepted. Proofs should be returned within 48 hours of receipt by Express Mail, Fax or Email.

Copyright. Submission of an article to "Advanced Steel Construction" implies that it presents the original and unpublished work, and not under consideration for publication nor published elsewhere. On acceptance of a manuscript submitted, the copyright thereof is transferred to the publisher by the Transfer of Copyright Agreement and upon the acceptance of publication for the papers, the corresponding author must sign the form for Transfer of Copyright.

Permission. Quoting from this journal is granted provided that the customary acknowledgement is given to the source.

Page charge and Reprints. There will be no page charges if the length of paper is within the limit of 25 journal pages. A total of 30 free offprints will be supplied free of charge to the corresponding author. Purchasing orders for additional offprints can be made on order forms which will be sent to the authors. These instructions can be obtained at the Hong Kong Institute of Steel Construction, Journal website: http://www.hkisc.org

The International Journal of Advanced Steel Construction is published quarterly by non-profit making learnt society, The Hong Kong Institute of Steel Construction, c/o Department of Civil & Structural Engineering, The Hong Kong Polytechnic University, Hung Hom, Kowloon, Hong Kong.

EDITORS-IN-CHIEF

**Asian Pacific, African
and organizing Editor**
S.L. Chan
*The Hong Kong Polyt. Univ.,
Hong Kong*
Email: ceslchan@polyu.edu.hk

American Editor
W.F. Chen
Univ. of Hawaii at Manoa, USA
Email: waifah@hawaii.edu

European Editor
R. Zandonini
Trento Univ., Italy
Email: riccardo.zandonini@ing.unitn.it

Advanced Steel Construction
an international journal

VOLUME 5   NUMBER 3   SEPTEMBER 2009

Technical Papers

Conference Announcements

PRACTICAL FINITE ELEMENT PROCEDURE
FOR ACHIEVING MESH OBJECTIVITY IN
LOCAL BUCKLING ANALYSIS OF STEEL STRUCTURES
BY BEAM ELEMENTS

Eiki Yamaguchi

Professor, Department of Civil Engineering,
Kyushu Institute of Technology, Tobata, Kitakyushu, Japan
E-mail: yamaguch@civil.kyutech.ac.jp

ABSTRACT: Since the nonlinear finite element analysis of a steel structure by shell/solid elements is expensive, effort has been made to conduct the local buckling analysis of a steel structure by beam elements. To this end, the structural deterioration due to local buckling of a steel member is implemented in constitutive relationship. The approach inevitably leads to the constitutive relationship of softening type, which however does not readily yield mesh objective result. The present study proposes a finite element procedure to overcome the problem: in a local-buckling zone, average state variables instead of local state variables are used. The effectiveness of the proposed procedure is verified by solving example problems. Moreover, the applicability of a simple trilinear type of constitutive relationship associated with the proposed beam-element analysis is investigated in comparison with shell-element analysis by ABAQUS.

Keywords: Steel structure; local buckling; beam element; mesh objective; softening-type constitutive relationship

1.   INTRODUCTION

Structural steel has been used exclusively as a thin-walled member in its civil and building application. One of its major failure modes is a local buckling, which may deteriorate the member strength considerably. Therefore, the phenomenon has been studied for many years.

Nevertheless, a number of steel structures underwent local buckling in the 1995 Hyogo-ken Nambu Earthquake also known as Kobe Earthquake, which was the very first time steel structures in service were damaged so badly in Japan, surprising many Japanese researchers who had confidence in the safety of steel structures. Quite a few experimental researches were then conducted in Japan [1]. Analytical approach was also taken and the local buckling has been simulated successfully not only by experiment but also by 3-dimensional finite element analysis using shell/solid elements [2-3].

Along this line, effort has been made also to analyze local-buckling behavior by beam elements for the reduction of computational cost. To this end, the structural deterioration due to local buckling is implemented in constitutive relationship, which is inevitably of a softening type [4-6]. In fact, the reduction of computational cost has been a challenging subject in various engineering fields. For buckling analysis, for example, the work of Little is noted [7].

The softening type of constitutive relationship has been used for the cracking analysis of concrete. A problem associated with this approach is dependence on finite element mesh: numerical result by the simple application of a softening-type constitutive relationship would not converge as the mesh becomes finer. In other words, mesh objective result is not obtained. To solve this problem, nonlinear fracture mechanics has been explored and, to be specific, it has been solved by controlling the slope of a softening branch of a constitutive relationship [8-10]. However, the issue of mesh objectivity has not been thoroughly understood in conjunction with the local buckling of steel structures.
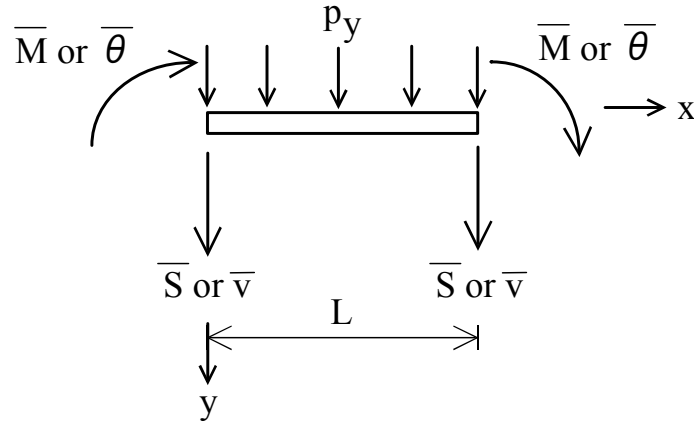
Figure 1. Bending Problem of Beam

In the present study, the mesh objectivity is first looked into, which shows that just like in the concrete cracking analysis, result does not converge with the refinement of mesh in the analysis of a steel structure by beam elements coupled with the simple application of the softening-type constitutive relationship. The objective of the present study is then to propose a finite element procedure to yield mesh objective result. The effectiveness of the proposed procedure is demonstrated by solving example problems. Nonlinear analysis of a two-dimensional beam is conducted to this end.

2.   CONVENTIONAL FORMULATION FOR NONLINEAR BEAMS

The conventional finite element procedure for the bending behavior of a two-dimensional beam is briefly described in this section for the sake of self-sufficiency. Nonlinearity is in constitutive relationship.

Assuming that displacement is small, the Bernoulli-Euler beam theory for the beam shown in Figure 1 leads to the following governing equations:

Equilibrium equations:
$$M'' - p_y = 0 \qquad (1)$$

Curvature-displacement relationship:
$$\kappa = v'' \qquad (2)$$

Moment-curvature relationship:
$$\dot{M} = C\,\dot{\kappa} \qquad (3)$$

Boundary conditions: $\bar{S} = -S$ or $\bar{v} = v$, $\bar{M} = -M$ or $\bar{\theta} = v'$ at $x = 0$ \qquad (4)

$\qquad\qquad\qquad \bar{S} = S$ or $\bar{v} = v$, $\bar{M} = M$ or $\bar{\theta} = v'$ at $x = L$ \qquad (5)

where M, p_y, κ, v, S and θ are bending moment, distributed load in the y-direction, curvature, displacement in the y-direction, shear force and rotational angle, respectively. A quantity with the top bar such as $\bar{S}$ is the prescribed one. The top dot such as that in $\dot{M}$ and the prime such as that in M' represent the rate and the derivative with respect to x, respectively. C is bending rigidity and is equal to EI (the product of the Young Modulus and the moment of inertia) at the initial stage of deformation. As deformation increases, C may vary, initiating nonlinear behavior.

Practical Finite Element Procedure for Achieving Mesh Objectivity in
Local Buckling Analysis of Steel Structures by Beam Elements

226
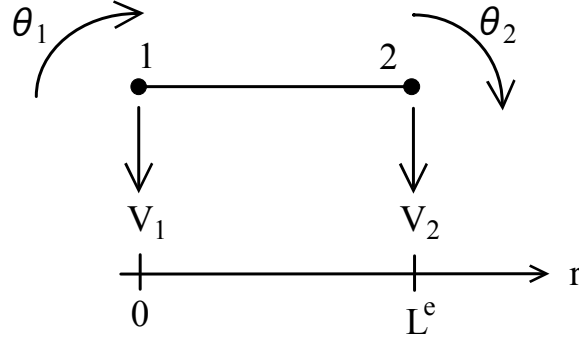
Figure 2. Standard 2-node Four-d.o.f. Beam Element

The application of the weighted residual method to these equations yields

$$H = \int_0^L Mw'' \, dx - \int_0^L p_y w \, dx - \left[\bar{S}w + \bar{M}w' \right]_{x=0,L} = 0 \tag{6}$$

where w is the weight function. Using a standard 2-node four-d.o.f. beam element shown in Figure 2 [11] and the Galerkin method, the displacement and the weight are discretized as

$$v = \mathbf{N}\mathbf{U}^e = \begin{bmatrix} N_{V1} & N_{\theta 1} & N_{V2} & N_{\theta 2} \end{bmatrix} \begin{bmatrix} V_1 & \theta_1 & V_2 & \theta_2 \end{bmatrix}^T \tag{7}$$

$$w = \mathbf{N}\mathbf{W}^e = \begin{bmatrix} N_{V1} & N_{\theta 1} & N_{V2} & N_{\theta 2} \end{bmatrix} \begin{bmatrix} W_{V1} & W_{\theta 1} & W_{V2} & W_{\theta 2} \end{bmatrix}^T \tag{8}$$

where

$$N_{V1} = 1 - \frac{3r^2}{L^{e2}} + \frac{2r^3}{L^{e3}}, \quad N_{\theta 1} = r - \frac{2r^2}{L^e} + \frac{r^3}{L^{e2}}, \quad N_{V2} = \frac{3r^2}{L^{e2}} - \frac{2r^3}{L^{e3}}, \quad N_{\theta 2} = -\frac{r^2}{L^e} + \frac{r^3}{L^{e2}} \tag{9}$$

L^e is the length of a beam element and r is the local coordinate attached to each element, taking 0 at Node 1 and L^e at Node 2.

The discretization by this beam element gives the following expression for each element:

$$H^e = \mathbf{W}^{eT} \left(\mathbf{F_{IN}}^e - \mathbf{F_{EX}}^e \right) \tag{10}$$

where

$$\mathbf{F_{IN}}^e = \int_{L^e} \mathbf{B}M \, dr \tag{11}$$

$$\mathbf{F_{EX}}^e = \int_{L^e} \mathbf{N}p_y \, dr + \left[\bar{S} + \bar{M} \right]_{r=0,L^e} \tag{12}$$

$$\mathbf{B} = \frac{d^2\mathbf{N}}{dr^2} = \left[-\frac{6}{L^{e2}} + \frac{12r}{L^{e3}} \quad -\frac{4}{L^e} + \frac{6r}{L^{e2}} \quad \frac{6}{L^{e2}} - \frac{12r}{L^{e3}} \quad -\frac{2}{L^e} + \frac{6r}{L^{e2}} \right] \tag{13}$$

The assemblage of all the element contributions and the arbitrariness of the weight function yield the following discretized governing equations:

$$\mathbf{F}_{IN} - \mathbf{F}_{EX} = \mathbf{0} \tag{14}$$

Because of the nonlinearity of Eq. 3, Eq. 14 is a set of nonlinear equations. To obtain the solution, Eq. 14 is linearized as

$$\mathbf{K}(\mathbf{U}^{(m)})\,\Delta\mathbf{U}^{(m)} = \mathbf{F}_{EX} - \mathbf{F}_{IN}(\mathbf{U}^{(m)}) \tag{15}$$

The coefficient matrix $\mathbf{K}$, also known as the stiffness matrix, has the following expression at an element level:

$$\mathbf{K}^e = \int_{L^e} \mathbf{B}^T C \mathbf{B}\, dr = \frac{C}{L^{e3}}\begin{bmatrix} 12 & 6L^e & -12 & 6L^e \\ & 4L^{e2} & -6L^e & 2L^{e2} \\ & & 12 & -6L^e \\ sym. & & & 4L^{e2} \end{bmatrix} \tag{16}$$

Eq. 15 is solved for $\Delta\mathbf{U}^{(m)}$ and $\mathbf{U}$ is updated. The procedure is repeated until convergence is obtained. The superscript m in the parenthesis shows the number of iteration.

In reality, shear deformation contributes to deflection. The Timoshenko beam theory can be used to include the effect of shear deformation. In this theory, the deflection is expressed as the sum of those due to bending and shear deformation:

$$V_1 = V_1^b + V_1^s \tag{17}$$

$$V_2 = V_2^b + \left(V_1^s - \frac{SL^e}{GkA}\right) \tag{18}$$

where the superscripts b and s stand for the contributions due to bending and shear deformation, respectively, G is the shear modulus, A is a cross-sectional area and k is the correction factor that accounts for the difference from actual shear stress distribution over a cross section. The value of k depends on the cross section of a beam, and for a thin-walled member the ratio of the cross-sectional area of a web over the whole cross-sectional area A can be assigned to k [12]. The coefficient matrix $\mathbf{K}^e$ for the Timoshenko beam theory is then given by

$$\mathbf{K}^e = \frac{C}{L^{e3}(1+\phi)}\begin{bmatrix} 12 & 6L^e & -12 & 6L^e \\ & (4+\phi)L^{e2} & -6L^e & (2-\phi)L^{e2} \\ & & 12 & -6L^e \\ sym. & & & (4+\phi)L^{e2} \end{bmatrix} \tag{19}$$

where
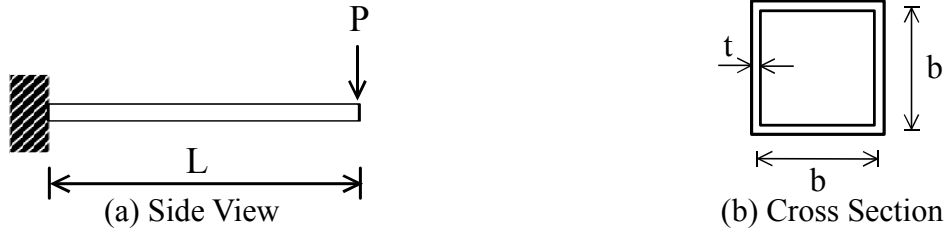
Figure 3. Cantilever Beam
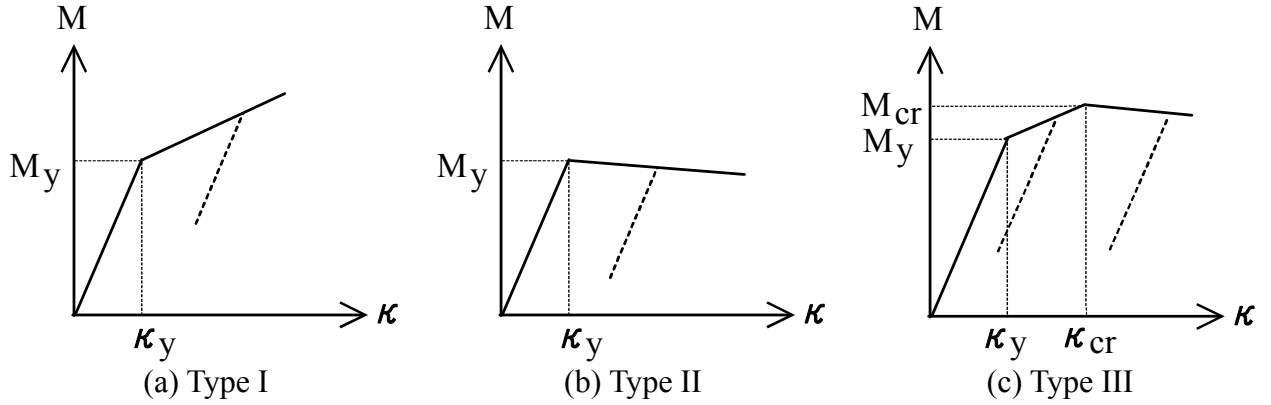
Figure 4. Bending Moment M – curvature κ Relationships

$$\phi = \frac{12C}{GkAL^{e2}} \tag{20}$$

3.   NUMERICAL ANALYSIS I: MESH DEPENDENCE

The two-dimensional behavior of a steel cantilever beam subjected to a concentrated load at the free end (Figure 3) is employed as a numerical example herein. The beam length L is 10 m and the cross section is a square box consisting of four thin plates, whose width b is 2000 mm and thickness t is 40 mm. The Young Modulus E is 206 kN/mm^2 and the yield stress σ_y is 235 N/mm^2. The main objective of this section is to shed light on the difficulty in dealing with the constitutive model of a softening type. To this end, it is sufficient to consider only the bending behavior of the beam: no shear deformation is taken into account in this section.

For nonlinear behavior, three simple constitutive relationships between the bending moment M and the curvature κ shown in Figure 4 are assumed. Type I represents a typical elasto-plastic behavior. No descending branch (softening branch) exists. Type II has no hardening branch but has the softening branch, which embodies the deterioration due to local buckling without undergoing plastic deformation. Type III includes both hardening and softening branches: the elastic behavior is followed by the elasto-plastic behavior, which then leads to the deterioration due to local buckling. The slopes of the hardening and softening branches are assumed to be $EI/10$ and $-EI/100$, respectively. For Type III, κ_{cr} is assumed to be twice as large as κ_y, i.e. $\kappa_{cr} = 2\kappa_y$. In the hardening and softening branches, unloading behavior may take place. The slope of the unloading $M-\kappa$ relationship is the same as that of the elastic behavior, which is illustrated by dotted lines in Figure 4.

(a) Type I

(b) Type II

(c) Type III
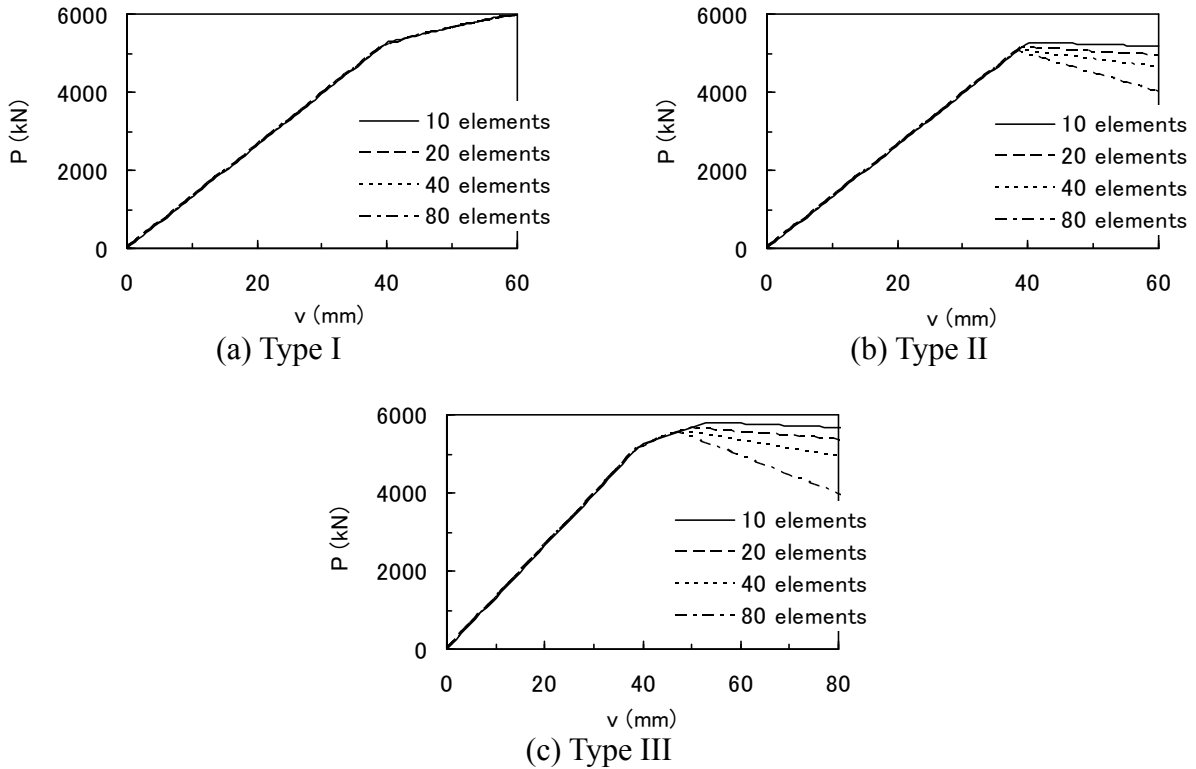
Figure 5. Load *P* – Displacement *v* Curves of Cantilever Beam

Using the beam elements described earlier, four finite element meshes are constructed to see the influence of the mesh on numerical result. The four meshes use 10, 20, 40 and 80 elements, respectively. All the elements in each mesh are equal in length.

The numerical results of Type I are presented in the form of the load *P* – displacement *v* relationship at the loading point in Figure 5(a). Even though dependence on the mesh is not significant, closer observation reveals the tendency of the convergence: as the element length becomes smaller, the result tends to converge. The 20-, 40- and 80-element meshes yield practically the same response. For instance, at *v*=60 mm, *P* is equal to 5993 kN in the case of the 10-element mesh while it is just about 5970 kN in the other three cases. Mesh objective result is thus obtained with Type I.

Figure 5(b) shows the results of Type II. The dependence on the mesh is recognized more clearly, as the results by the four meshes are very different from each other. Unlike the previous result of Type I, no tendency of the convergence is observed in this type of constitutive model, which indicates that the result herein is not mesh objective.

The *P* – *v* relationship due to Type III is presented in Figure 5(c). This figure clearly indicates the dependence on the mesh. As the mesh becomes finer, the dependence reduces in the hardening portion of the *P* – *v* relationship while such tendency is not observed in the softening portion. The problem associated with the softening type of constitutive relationship is made apparent again by Type III.

Figure 6. Fixed-fixed Beam
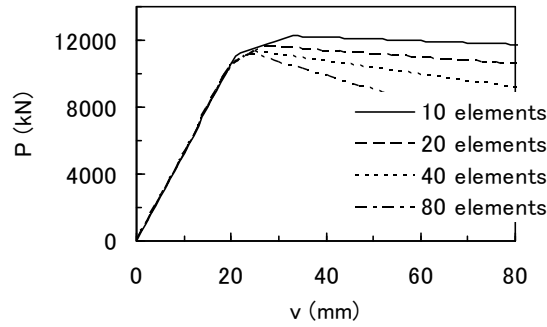
Figure 7. Load P – Displacement v Curves of Fixed-fixed Beam (Type III)

Additionally, a statically indeterminate structure of a steel fixed-fixed beam with a concentrated load at the mid-span (Figure 6(a)) is also analyzed with Type III. The total length of the beam $2L$ is 20 m and the cross section is the same as that of the cantilever (Figure 3(b)). Since it is sufficient to consider only a half of the beam due to symmetry, the analysis of the beam shown in Figure 6(b) is conducted. The numerical results in the form of the $P - v$ relationship at the loading point are plotted in Figure 7. This figure shows that mesh objective result is not obtained in the statically indeterminate structure as well.

4.   PROPOSED FORMULATION FOR SOFTENING BEHAVIOR

The following observations are generally made in the local buckling phenomenon of a steel thin-walled member:

1. Region subjected to local buckling is limited. (The region is hereafter called the local-buckling zone or LBZ for short.)
2. Strain distribution in LBZ depends on buckling mode and is very complicated in general, so that strain in LBZ varies from point to point wildly.

It is noteworthy that the study on LBZ has been conducted, providing the following empirical formula for evaluating the length of LBZ of a box-section member [13]:

$$L_{LBZ} = Min(0.7b, a) \tag{21}$$

where L_{LBZ} is the length of LBZ, a is the distance between two adjacent diaphragms and b is the width of a flange. *Min* indicates that the smaller of the two values in the parenthesis shall be taken.

Making use of the above observations, the constitutive relationship between $\dot{M}$ and $\dot{\kappa}$ in LBZ is assumed to be controlled by the average quantity in LBZ in the present study. To be specific, the constitutive relationship of Eq. 3 is replaced by

$$\dot{M} = C(\kappa)\,\dot{\kappa} \qquad \text{for} \ \ \kappa_{av} \leq \kappa_{cr} \tag{22a}$$

$$\dot{M} = C(\kappa_{av})\,\dot{\kappa} \ \ \text{for} \ \ \kappa_{av} > \kappa_{cr} \tag{22b}$$

where κ_{av} is the average curvature in LBZ. Specifically, κ_{av} is defined by

$$\kappa_{av} = \frac{1}{L_{LBZ}} \int_{L_{LBZ}} \kappa\,dx = \frac{1}{L_{LBZ}} \sum_{e} \int_{L_{LBZ}^e} \kappa\,dr \tag{23}$$

where L_{LBZ}^e is the length of the element located in LBZ. The proposed approach may be viewed as a kind of nonlocal formulation with L_{LBZ} being the characteristic length [14, 15].

For the beam element employed in this study, the curvature varies as follows:

$$\kappa = \frac{d^2 v}{dr^2} = \mathbf{B}\mathbf{U}^{eT} \tag{24}$$

As Eq. 13 indicates, $\mathbf{B}$ is a set of linear functions with respect to r. Therefore, κ varies in a linear fashion within a beam element. Eq. 23 can then be rewritten as

$$\kappa_{av} = \frac{1}{L_{LBZ}} \sum_{e} L_{LBZ}^e\, \kappa\!\left(\frac{L_{LBZ}^e}{2}\right) \tag{25}$$

where $\kappa\!\left(L_{LBZ}^e / 2\right)$ is the value of κ evaluated at the middle of the element. If the lengths of the elements in LBZ are equal to each other, the above equation can be further simplified as

$$\kappa_{av} = \frac{1}{N} \sum_{e} \kappa\!\left(\frac{L_{LBZ}^e}{2}\right) \tag{26}$$

where N is the number of elements located in LBZ.

It is also noted that Eq. 22b leads to

$$\dot{M}_{av} = \frac{1}{L_{LBZ}} \int_{L_{LBZ}} \dot{M}\,dr = \frac{1}{L_{LBZ}} \int_{L_{LBZ}} C(\kappa_{av})\,\dot{\kappa}\,dr = \frac{C(\kappa_{av})}{L_{LBZ}} \int_{L_{LBZ}} \dot{\kappa}\,dr = C(\kappa_{av})\,\dot{\kappa}_{av} \tag{27}$$

where $\dot{M}_{av}$ is the average bending moment in LBZ. Since deformation in LBZ is complicated, experiments provide information only for this class of constitutive relationship in practice, i.e. the relationship only in terms of average state variables [5, 6]. In other words, $C(\kappa_{av})$ can be determined experimentally.

It is noted that the finite element procedure described earlier can be used with this constitutive relationship of Eq. 22.

5.   NUMERICAL ANALYSIS II: EFFECTIVENESS OF PROPOSED APPROACH

The two problems of the cantilever beam (Figure 3) and a half of the fixed-fixed beam (Figure 6(b)) are solved by the proposed approach. Since the cross section at the fixed end does not deform and a diaphragm is placed at the cross section under the concentrated load, LBZ can develop near the fixed end in both beams and also near the loading point in the case of the fixed-fixed beam. Following Eq. 21, it is decided that the length of each LBZ is 1400mm.

The proposed constitutive relationship of Eq. 22 is applied to these LBZs. The values of the parameters in the constitutive relationship are assumed to be the same as those employed in the previous analysis, i.e. Numerical analysis I. However, the physical meaning of the critical value κ_{cr} for the judgment on the initiation of local buckling has become different: it is now in terms of the average curvature κ_{av} while it is local curvature κ in the previous analysis. Outside LBZ no local buckling takes place so that no structural deterioration occurs. The constitutive relationship outside LBZ is therefore assumed to be given by Type I (Figure 4(a)) and the parameters take the same values as those employed previously.

Four finite element meshes are employed in this analysis. In the coarsest mesh, seven elements are used for the whole beam: LBZ is modeled by one element and the remaining zone is modeled by the rest of the elements. The element mesh is refined by halving the element length, so the four meshes consist of 7, 14, 28 and 56 elements, respectively, and LBZs in the four meshes are modeled by 1, 2, 4 and 8 elements, respectively. The elements in LBZ are equal in length and the elements in the remaining zone are equal in length as well, but the element lengths in LBZ and the remaining zone are slightly different from each other.

The results are shown in Figures 8 and 9. Both figures indicate that the variations due to the difference in mesh are much smaller than the counterparts in the previous analysis with Type III (Figures 5(c) and 7). Not only have the variations been reduced but the convergence is observed as the mesh becomes smaller, which can be realized more clearly in Figures 8(b) and 9(b). The convergence appears to be relatively slow in the fixed-fixed beam, yet the 28- and 56-element meshes have yielded indistinguishable responses. The effectiveness of the proposed approach is thus verified.

(a) Overall Range   (b) Close-up of Peak Region
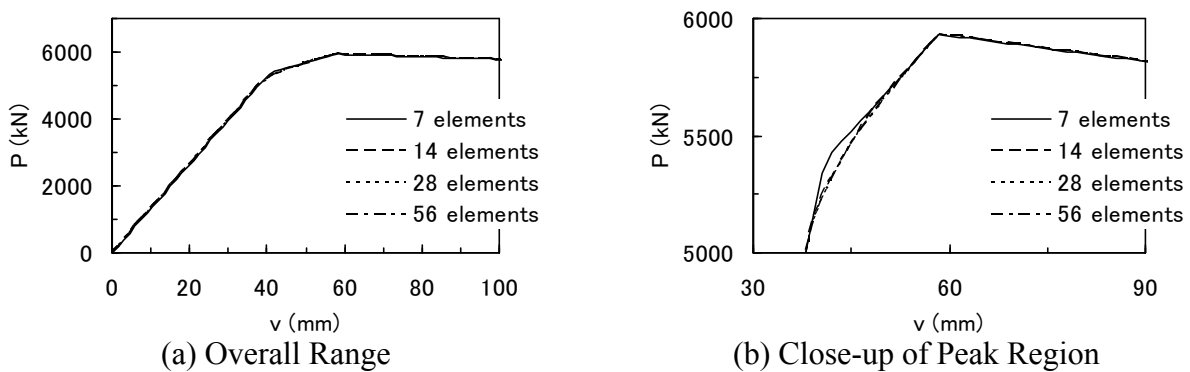
Figure 8. Load P – Displacement v Curves of Cantilever Beam by Proposed Approach

(a) Overall Range   (b) Close-up of Peak Region
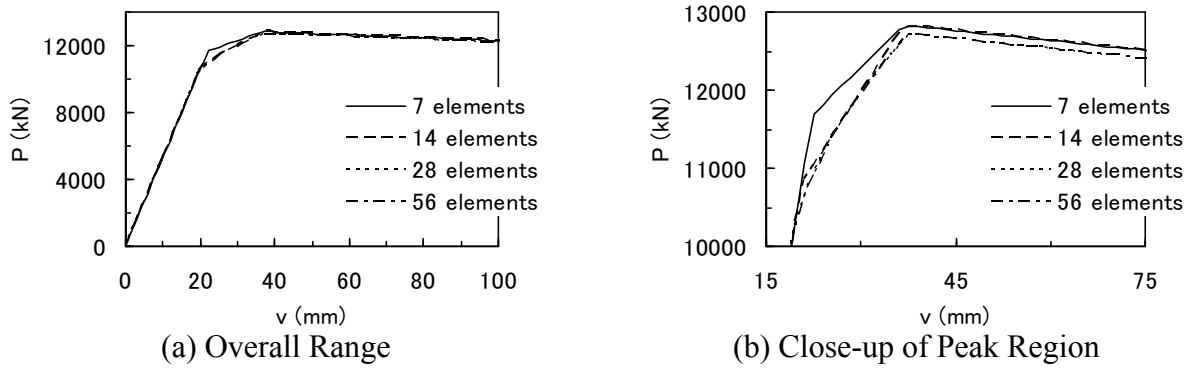
Figure 9. Load P – Displacement v Curves of Fixed-fixed Beam by Proposed Approach

6.   NUMERICAL ANALYSIS III: APPLICABILITY OF TRILINEAR TYPE OF CONSTITUTIVE RELATIONSHIP IN TERMS OF BENDING MOMENT M AND CURVATURE κ

The finite element procedure for achieving mesh objectivity is proposed and its effectiveness is confirmed in the above. Since the objective of the present study is to propose the mesh-objective finite element procedure, the constitutive relationship used is one of the simplest softening-type models. Yet it may be interesting to examine the applicability of this simple trilinear type of constitutive relationship from practical point of view. Therefore, the comparative study between the proposed beam-element analysis with the trilinear type of constitutive relationship and the shell-element analysis by ABAQUS [16] is carried out herein.

The ABAQUS analysis takes advantage of symmetry, and each beam is modeled by 4040 four-node shell elements. The material in the ABAQUS analysis is assumed to be a von Mises type of elasto-plastic material and its uniaxial behavior is bilinear with the second slope being equal to E/100. The Poisson ratio is 0.3, and the Young Modulus E and the yield stress σ_y take the same values as those in the previous beam-element analysis.

(a) Load P – Displacement v Curves   (b) Deformed Configuration (ABAQUS)
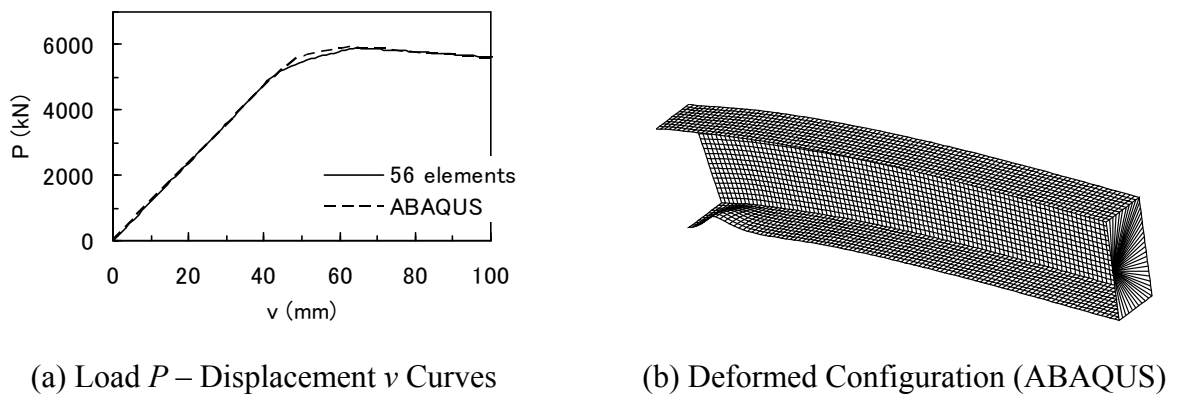
Figure 10. Analysis of Cantilever Beam under Concentrated Load

Since in the ABAQUS analysis, shear deformation contributes to deflection, the Timoshenko beam theory needs to be incorporated into the proposed beam-element analysis. This can be done simply by employing Eq. 19 instead of Eq. 16. Furthermore, care must be taken in the determination of the values of the bending rigidities C and the critical curvature κ_{cr}, since they are not pure material properties but include the structural characteristics, particularly cross-sectional properties. To this

end, the cantilever problem with the concentrated load (Figure 3) is solved first by ABAQUS. Referring to this ABAQUS result, the bending rigidities and the critical curvature are evaluated by trial and error, and $C = EI/11.20$ for the hardening behavior, $C = -EI/46.82$ for the softening behavior and $\kappa_{cr} = 2.07\kappa_y$ are obtained. These values are to be used not only for the cantilever problem with the concentrated load, but also for all the other problems.

The same four meshes as those described in the previous section are used again in this comparative study. As is in the previous examples (Figures 8 and 9), the numerical result converges also herein with the refinement of the mesh: the responses obtained by the 28-element mesh and the 56-element mesh are practically the same. Because of the convergence, only the numerical result by the 56-element mesh is presented in Figure 10(a) together with that due to ABAQUS. The difference in the maximum load between the two results is 0.10 %. The post-peak deformed configuration obtained by the ABAQUS analysis is given in Figure 10(b). For the clear presentation, the deformation is magnified by the factor of 30 in this figure. The local buckling is clearly observed in the compression flange near the fixed end. Compared to this ABAQUS result, the LBZ length of 1400mm employed in the proposed beam-element analysis appears justifiable.

Replacing the concentrated load with uniformly distributed load, the cantilever beam (Figure 11(a)) is analyzed again. All the values of the parameters in the constitutive relationship of the proposed approach including the values of C and κ_{cr} remain the same as those in the cantilever-beam problem with the concentrated load. The numerical result obtained is presented in Figure 11(b) together with that due to ABAQUS. Because of the convergence, only the numerical result by the 56-element mesh is given. The two results are in good agreement with each other: the difference in the maximum load is 3.56 %. The deformed configuration in the ABAQUS analysis is presented in Figure 11(c). The deformation is magnified by the factor of 30. The local buckling is clearly observed in the compression flange near the fixed end, and the LBZ length of 1400 mm appears good also in this problem.

(a) Cantilever Beam under Distributed Load

(b) Load P – displacement v Curves

(c) Deformed Configuration (ABAQUS)
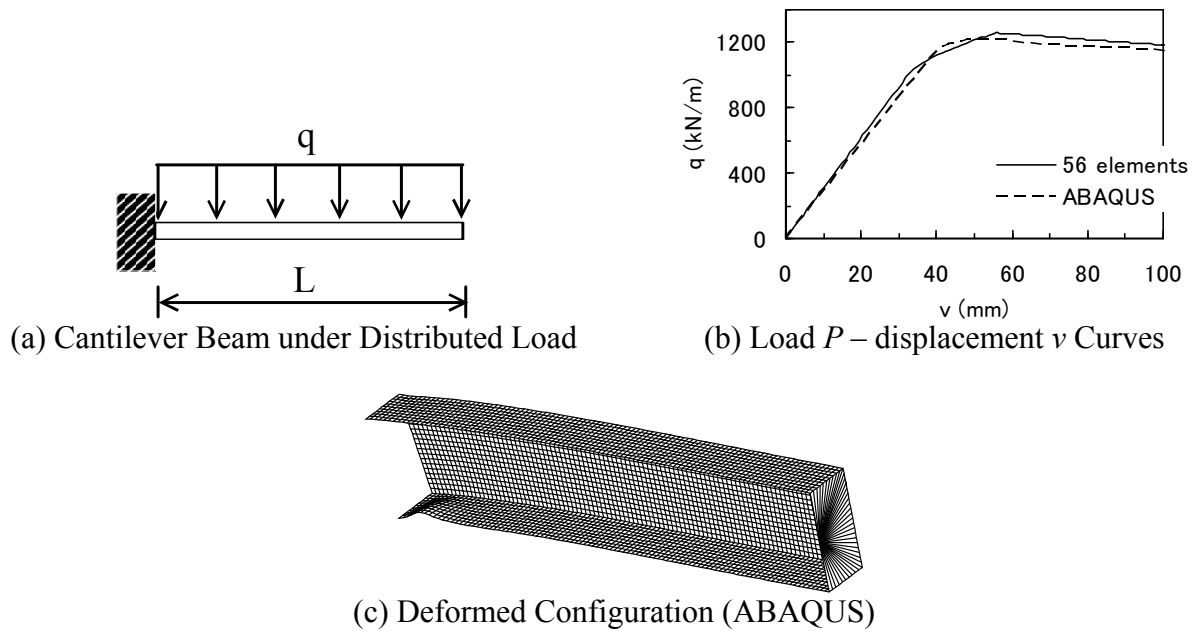
Figure 11. Analysis of Cantilever Beam under Distributed Load
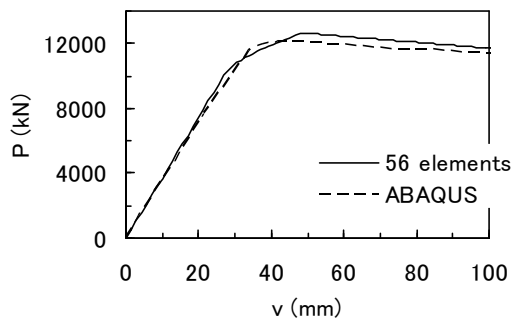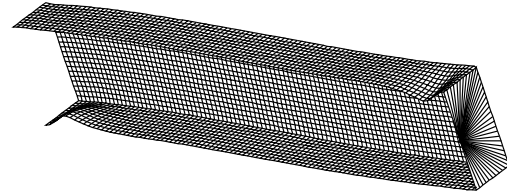
(a) Load P – Displacement v Curves   (b) Deformed Configuration (ABAQUS)

Figure 12. Analysis of Fixed-fixed Beam

A half of the fixed-fixed beam (Figure 5(b)) is then analyzed. All the values of the parameters in the constitutive relationship are kept the same as those in the preceding two examples. The numerical result is presented in Figure 12(a) together with that due to ABAQUS. Because of the convergence, only the numerical result by the 56-element mesh is given. The proposed approach agrees well with the ABAQUS result: the difference in the maximum load is 4.20 %. Figure 12(b) shows that local buckling occurs in the compression flanges near the fixed end and the middle section of the beam where the concentrated load is applied, which matches the result of the proposed beam-element analysis: LBZs in these two regions undergo the softening behavior. The occurrence of the local buckling in the multiple locations is attributed to the fact that the beam is statically indeterminate. The length of 1400 mm appears good for both LBZs in the analysis of the fixed-fixed beam.

Based on the results obtained in this section, it may be stated that the trilinear type of constitutive relationship is promising in the practical analysis of a steel beam undergoing local buckling in spite of its extreme simplicity.

7.   CONCLUDING REMARKS

Local buckling of a steel structure can be simulated well by shell-element analysis. Nevertheless, such an analysis requires much computational cost and is yet to be practical. Hence, effort has been made to implement the structural deterioration due to local buckling in the constitutive relationship so that a beam element can be used for the local buckling analysis of steel structures. However, such a constitutive relationship has a softening branch inevitably, and as demonstrated in this study, simple application of the softening-type constitutive relationship does not lead to mesh objective result.

Against this background, the present study has proposed a finite element procedure that uses the average state variables in the local-buckling zone to control the structural deterioration due to local buckling. The effectiveness of the proposed finite element procedure has been confirmed by solving example problems: the mesh objectivity is shown to be achieved. It is noted that the application of the underlying concept of the proposed procedure is not restricted to the constitutive relationship employed in the present study: it can be applied straightforwardly to any constitutive relationships.

One of the simplest constitutive relationships that include the influence of the structural deterioration due to local buckling is the one employed in the present numerical examples. At the end, the present study has explored the applicability of this simple trilinear constitutive relationship in comparison with the shell-element analysis by ABAQUS. The results have indicated that this type of constitutive relationship is promising in the practical analysis of a steel beam undergoing local buckling in spite of its extreme simplicity. Yet much remains to be done as to how the bending rigidities and the critical curvature for a given steel member are determined, which is in fact a subject of an on-going project in the author's research group.

REFERENCES

[1]   Public Works Research Institute et al., "Seismic Design for Highway Bridge Piers", Technical Report of Joint Research, PWRI, Ministry of Construction, Japan, 1997.

[2]   Goto, Y., Wang, Q. and Obata, M., "FEM Analysis for Hysteretic Behavior of Thin-walled Column", Journal of Structural Engineering, ASCE, 1998, Vol. 124, pp. 1290-1301.

[3]   Yamaguchi, E., Nagamatsu, T. and Kubo, Y., "Influence of Finite Element Mesh on Buckling Analysis of Steel Pipe-sectioned Bridge Piers", Fifth World Congress on Computational Mechanics (WCCM V), Paper No. 80566, 2002.

[4]   Yamaguchi, E., Abe, K. and Kubo, Y, "Analysis of Steel Bridge Piers Undergoing Local Buckling by Beam Elements", Proceedings of 5th International Colloquium on Stability and Ductility of Steel Structures, 1997, pp. 267-272.

[5]   Sakimoto, T., Watanabe, H. and Nakashima, K., "Hysteretic Models of Steel Box Members with Local Buckling Damage", Journal of Structural Mechanics and Earthquake Engineering, JSCE, 2000, No.647/I-51, pp. 343-355.

[6]   Watanabe, H. and Sakimoto, T., "Seismic Response Analysis of Concrete-filled Steel Box Piers Considered on Local Buckling", Journal of Structural Mechanics and Earthquake Engineering, JSCE, 2000, No. 647/I-51, pp. 357-368.

[7]   Little, G.H., "Rapid Analysis of Plate Collapse by Live Energy Minimisation", International Journal of Mechanical Science, 1974, Vol. 19, No. 12, pp. 725-744.

[8]   Hillerborg, A., Modeer, M. and Peterson, P.E., "Analysis of Crack Formation and Crack Growth in Concrete by Means of Fracture Mechanics and Finite Elements", Cement and Concrete Research, 1976, Vol. 6, pp. 773-782.

[9]   Bazant, Z.P. and Oh, B.H., "Crack Band Theory for Fracture of Concrete", Materials and Structures, RILEM, 1983, Vol. 16, pp. 155-177.

[10]   Yamaguchi, E. and Chen, W.F., "Cracking Model for Finite Element Analysis of Concrete Materials", Journal of Engineering Mechanics, ASCE, 1990, Vol. 116, pp. 1242-1260.

[11]   Cook, R.D., Malkus, D.S. and Plesha, M.E., "Concepts and Applications of Finite Element Analysis", 3rd Edition, New York , NY, John Wiley & Sons, 1989.

[12]   Nishino, F. and Hasegawa, A., "Elastic Analysis of Structures", Gihoudo, 1983.

[13]   Usami, T. (editor), "Guidelines for Seismic and Damage Control Design of Steel Bridge", Tokyo, Japan, Gihodo, 2006.

[14]   Bazant, Z.P., "Nonlocal Damage Theory Based on Micromechanics of Crack Interactions", Journal of Engineering Mechanics, ASCE, 1994, Vol. 120, pp. 593-617.

[15]   Khaloo, A.R. and Tariverdilo, S., "Localization Analysis of Reinforced Concrete Members with Softening Behavior", Journal of Structural Engineering, 2002, Vol. 128, pp.1148-1157.

[16]   ABAQUS/Standard User's Manual, Ver.5.7, HKS, 1997.

EXPERIMENTS AND SIMULATIONS OF POST WELD TREATMENT WITH HIGH FREQUENCY NEEDLE PEENING FOR WELDED JOINTS

P. Schaumann and C. Keindorf [*]

Institute for Steel Construction, Leibniz University Hannover
Appelstr. 9A, 30167 Hannover, Germany
*(Corresponding author: E-mail: keindorf@stahl.uni-hannover.de)

ABSTRACT: This paper deals with fatigue tests on welded joints carried out in order to estimate the influence of a post weld treatment method called Ultrasonic Impact Treatment. With this method the fatigue resistance could be increased significantly. Furthermore, tubular joints of tripods were analysed with numerical simulations to judge these welded joints with the hot-spot-concept. The stress concentration factor for the treated weld toe geometry was determined numerically and compared to experimental results. In the next step numerical simulations were carried out for seam butt welds using an arc welding process followed by a process of UIT. The objective of these numerical investigations was to analyse the influence of residual stresses on the fatigue life for welded steel plates with and without post weld treatment. The fatigue life until crack initiation was calculated applying the notch strain approach. Both, experimental and numerical investigations attested a significant increase in fatigue resistance due to the post weld treatment by UIT compared to the as-welded condition.

Keywords: Welded joints, post weld treatment, needle peening, fatigue, uit, offshore, wind energy

1. INTRODUCTION

For the planned German offshore wind farm Kriegers Flak in the Baltic Sea a fatigue design study was carried out including experimental and numerical investigations for welded joints of a tripod. A tripod is one kind of a supporting structure for wind energy converters as shown in Figure 1. The calculations took into account on Baltic Sea conditions with 25 m water depth and for a 2 MW turbine. The welded joints were designed for a fatigue life of 20 years with numerical simulation based on the hot-spot-concept.

Furthermore, experiments were carried out to determine the fatigue resistance for such welded joints. Because of the large dimensions of tripods fatigue tests can not be performed in full scale. Hence, a small representative sector of the joint was tested.

12 specimen (Y-joints) were tested with $t_c = 90$ mm thickness for the chord and $t_b = 40$ mm for the brace welded in an angle of $\theta = 60°$. The plate thicknesses are comparable with those of tripods. The objective of these tests was to quantify the fatigue resistance for welded joints with thick plates. Additionally, the influence of post weld treatment by Ultrasonic Impact Treatment (UIT) should be investigated. This method introduces compressive stresses and plastic deformations the weld toe, reducing residual stresses and stress concentrations. Because of these effects the fatigue strength increases significantly compared to as welded conditions.

Furthermore, different types of tubular joints for offshore structures were investigated with numerical simulations to estimate the fatigue limit state for both conditions, as welded and treated by UIT. The stress concentration factors (SCF) for the treated weld toe geometry were determined numerically using sub-model analysis and compared to experimental results. Finally a comparison between welded and cast iron joints was carried out in a fatigue design study under consideration of UIT-effects.
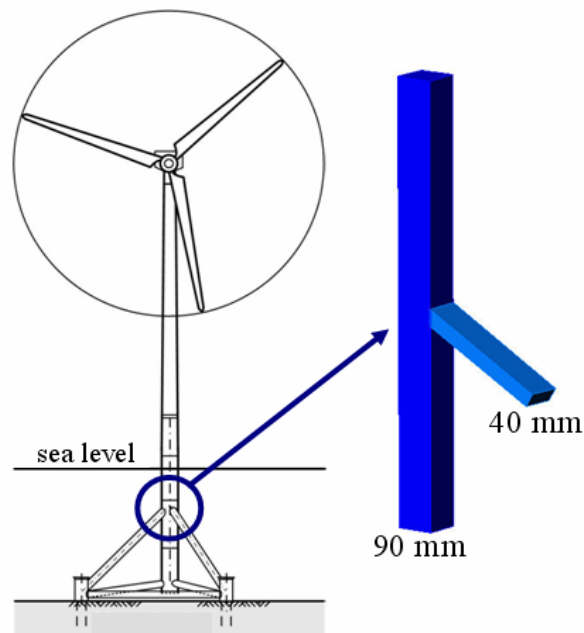
Figure 1. Offshore Wind Energy Converter with Tripod as Support
Structure and Y-joint for Experiments (Schaumann et al. [11])

2.   EXPERIMENTS WITH Y-JOINTS AND UIT

2.1   Test Specimen

The test specimens are Y-joints with $t_c = 90$ mm thickness for the chord and $t_b = 40$ mm for the brace. Chord and brace were welded in an angle of 60° with fillet welds. The Y-joints were fabricated of a steel S 355 J2. Chemical and mechanical properties of this steel are presented in Tables 1 and 2.

Table 1. Chemical Composition of Material S355 J2 in [%]

C	Si	Mn	P	S	N	Cr	Ni
0.16	0.34	1.43	0.014	0.004	0.006	0.07	0.06

Table 2. Mechanical Properties of Material S355 J2

Yield strength $R_{e,H}$	Ultimate strength R_m	Elongation at failure A_5	Impact Ductility KV
[MPa]	[MPa]	[%]	[J, -40°C]
386	537	23.5	106

The specimen geometry with detailed dimensions of these welded joints is shown in Figure 2.
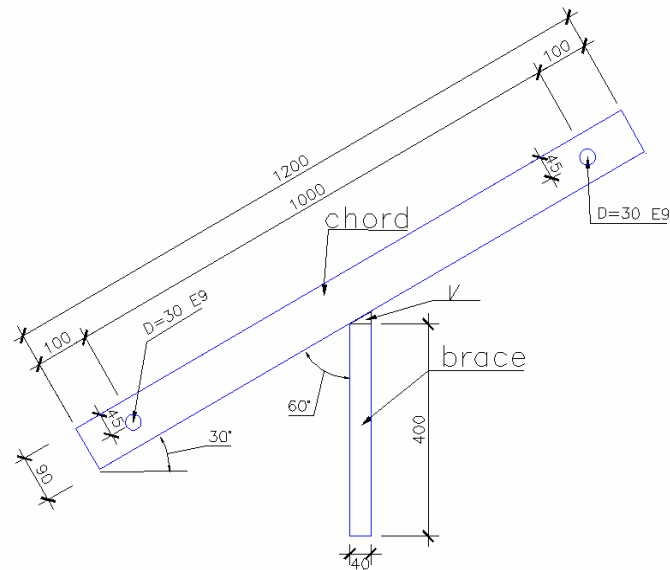
Figure 2. Test Specimen

2.2 Experimental Setup for Fatigue Testing

Fatigue testing was performed using a 600 kN servo-hydraulic test frame. The experiments were carried out up to 2 million cycles with test frequencies between $f_P = 3 - 5$ Hz depending on the value of the force amplitude. The test setup consisted of four columns with base plates and two horizontal bracing members. The Y-joint was supported by bolted connections at both ends of the chord. The position of the brace was vertical to fix the end of the brace in the testing machine.

The dynamic force loaded at the end of the brace induced a stress range $\Delta\sigma$. During the tests the dynamic force was measured with a load cell. The deformations were recorded online by inductive displacement transducers. In addition some of the test specimen strain gauges were applied to evaluate the local stress state near the weld toe and weld root.
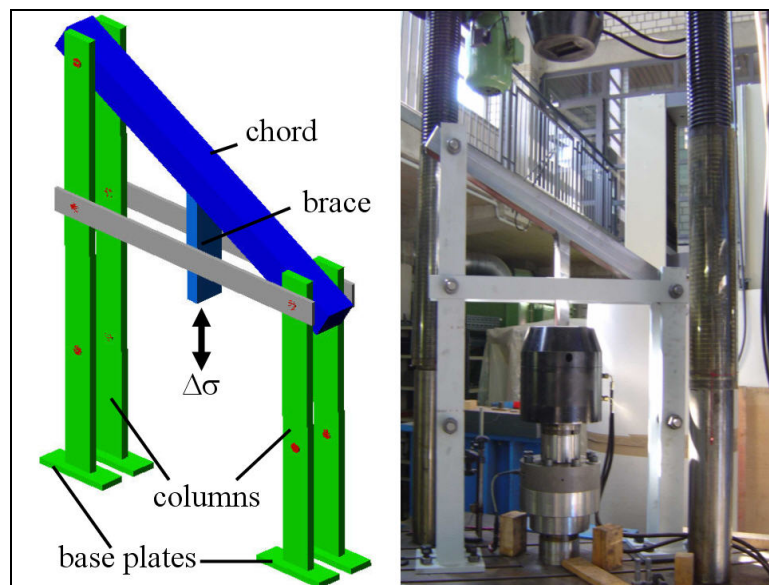
Figure 3. Test Setup for Y-joints

2.3   Ultrasonic Impact Treatment (UIT) after welding

Due to the plate thickness effect the fatigue resistance has to be reduced according to offshore-guideline (Germanischer Lloyd [1]). For example the reduced fatigue resistance at the chord is given by:

$$\sigma_{c,red} = \left(\frac{t_{ref}}{t_c} \right)^{0.25} \cdot \sigma_c = 0.73 \cdot \sigma_c \tag{1}$$

where t_{ref} = 25 mm as reference plate thickness and σ_c = fatigue resistance at 2 million cycles.

The reduction in fatigue resistance due to thickness effect (e.g. for the chord thickness 27 %) has to be considered in design studies, which is mostly limiting for the dimensions of tubular joints for offshore structures.

But the fatigue resistance of welded joints can be enhanced by post weld treatment. One method for this is Ultrasonic Impact Treatment (UIT). It is a proprietary technology developed originally in the Soviet Union for use on naval ships to reduce welding stresses (Statnikov et al. [2]). The equipment comprises a handheld tool and an electronic control box (Figure 4). The tool is easy to handle during application. It operates at the head movement with a mechanic frequency of 200 Hz overlain by an ultrasonic frequency of 27000 Hz. The noise is negligible compared to other peening devices. Several kinds of heads and pins are available and can be chosen on the basis of the surface condition of the weld details to be treated. The method involves post-weld deformation treatment of weld toe by impacts from single or multiple indenting needles excited at ultrasonic frequency, generating mechanic impulses on the work surface (Statnikov et al. [3]).

The objective of the treatment is to introduce beneficial compressive residual stresses at the weld toe zones and to reduce stress concentration by improving the weld toe profile. Furthermore the area being treated is plastically deformed which has the effect of work hardening.
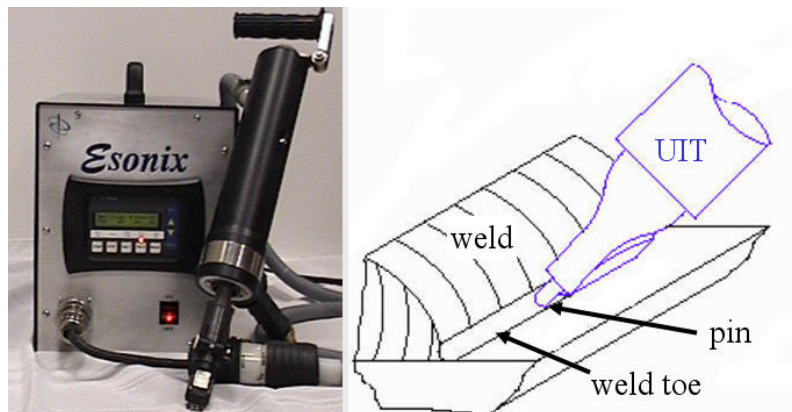
Figure 4. Ultrasonic Impact Treatment (UIT), Applied Ultrasonics [4]

Compared to other impact treatment methods such as air hammer peening or shot peening, UIT is claimed to be more efficient involving a complex effect of strain hardening, reduction in weld strain, relaxation in residual stresses reduction in stress concentration and thereby achieving a deeper cold worked metal layer (Statnikov et al. [3]).

2.4   Test Program

The test program comprises two test series on Y-joints with and without post weld treatment by UIT (Table 3). The first test series without post weld treatment (Y_1 - Y_6) was carried out to get a reference S-N-curve for Y-joints for the as-welded condition. The dynamic loads were recorded as nominal stress ranges $\Delta\sigma_n$ which were varied for the test specimens. The ratio between minimum and maximum stresses was R = σ_{min} / σ_{max} = 0.08 – 0.16 depending on the servo-hydraulic system of the testing machine.

The second test series (Y_7 - Y_12) have been performed with the same procedure like the first test series but with additional post weld treatment by UIT. The treatment was carried out according to the manufacturer's procedure document [4]. The indenter consisted of three 3 mm diameter pins, fitted in a single holder. The treatment was carried out in short multiple passes.

Table 3. Test Program

Test series	Test No.	weld toe [-]	$\Delta\sigma_n$ [MPa]	R [-]	N [$\cdot 10^6$]
1	Y_1	as welded	28.8	0.13	0.12
	Y_2	as welded	25.6	0.08	0.15
	Y_3	as welded	15.0	0.15	1.10
	Y_4	as welded	19.8	0.13	0.24
	Y_5	as welded	10.2	0.16	3.39
	Y_6	as welded	16.4	0.13	0.45
2	Y_7	UIT	27.1	0.15	0.82
	Y_8	UIT	22.7	0.12	3.75
	Y_9	UIT	34.5	0.12	0.16
	Y_10	UIT	26.1	0.11	0.75
	Y_11	UIT	32.0	0.10	0.18
	Y_12	UIT	28.5	0.10	0.51

3.   FATIGUE TEST RESULTS

3.1   Failure Modes

During the tests fatigue cracks occurred at two positions either at the toe or at the root of the weld. For test specimens without additional fillet welds at the root the crack was always detected at the root because of higher notch effects. But for tests with additional fillet welds at the root the position of cracks changed to the toe.

It could be noticed that welding with additional fillet welds at the root has a great influence on the place where the fatigue crack began. For a good performance of post weld treatment by UIT, it is therefore desirable to match the fatigue crack growth life from root defects to the fatigue life of the treated toe. In this way larger size fillet weld reduced stress concentration adjacent to the weld root contributing to increased fatigue life. An example for a fatigue crack is shown in Figure 5.
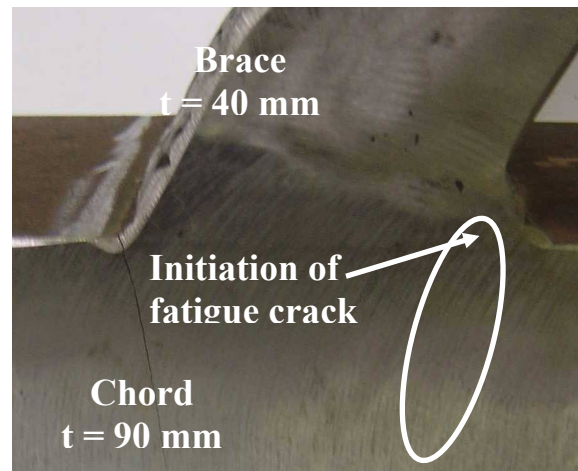
Figure 5. Test Specimen Y_2 with Fatigue Crack at the Weld Toe

After the fatigue tests several weld details and crack surfaces were cut out from the Y-joints and were examined for origins of fatigue cracks. Figure 6 presents the weld toe of test specimen Y_5 for as welded conditions. In the near of weld toe three zones can be identified: 1. weld metal, 2. heat affected zone and 3. base material. The notch radius of the weld toe is $r_{as\ welded} = 0.4$ mm.
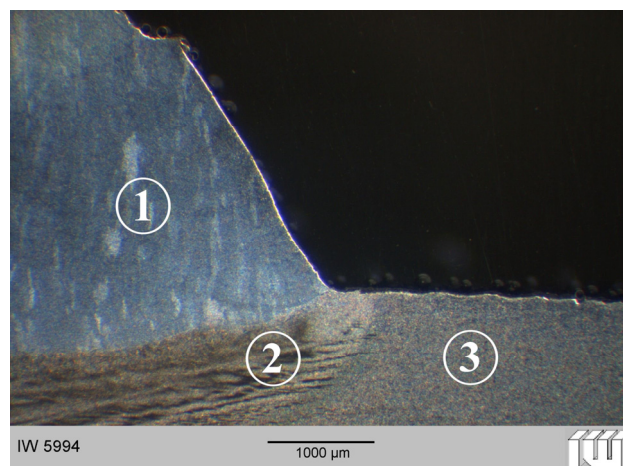
Figure 6. Weld Toe of Y_5 (as Welded)
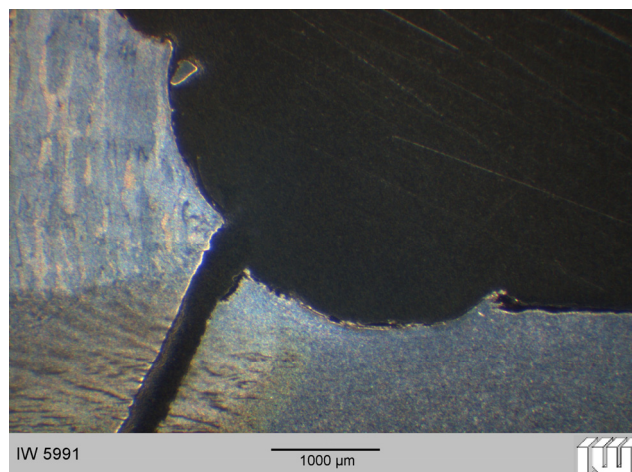
Figure 7. UIT-treated Weld Toe of Y_9 with Fatigue Crack

Figure 7 shows a photomicrograph of a typically treated weld toe at 50x magnification. Due to the post weld treatment by UIT the surface of the weld toe was highly plastically deformed and the notch was rounded. The weld toe of test specimen Y_9 is shown in Figure 7 after post weld treatment and fatigue testing. Analog to the test specimen Y_5 in Figure 6 the three zones are visible. The notch radius of the treated weld toe increased to $r_{uit} = 1.8$ mm. Furthermore the fatigue crack can be observed starting from surface between the weld metal and the heat affected zone. Fatigue Cracks in welded joints are often detected at this position because the heat affected zone has a high level of hardness.

3.2   S-N Curves

All test results are summarized in two S-N-curves (Figure 8). The S-N curve of the joints with UIT shows a significant increase in fatigue resistance compared to as welded joints. The as welded joints can be classified in FAT 90. This result corresponds with recommendations for tubular joints according to the offshore-guideline (Germanischer Lloyd [1]) based on the hot-spot-concept.
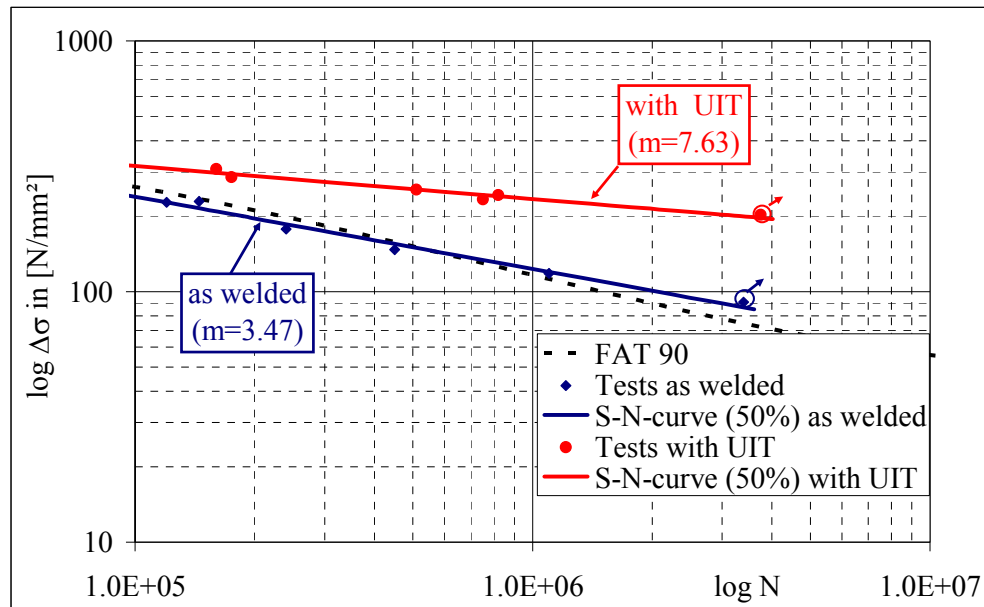
Figure 8. S-N-Curves of Both Test Series (as Welded and UIT-Treated)

With $\Delta\sigma_c = 204.5$ N/mm² for 2 million cycles the fatigue strength after post weld treatment by UIT was more than doubled compared to as-welded ($\Delta\sigma_c = 95.5$ N/mm²). The slope of the first test series with as-welded joints is $m = 3.47$. This value can be compared to recommendations of design guidelines for fatigue limit state ($m = 3$ for $N < 5 \cdot 10^6$). However, for the second test series with UIT the slope with $m = 7.63$ is significantly higher. With the experimental results the validity of the thickness effect could be confirmed also for plate thicknesses of 90 mm. The parameters of both S-N-curves are shown in Table 4.

Table 4. Parameters of S-N-Curves

Test series	$\Delta\sigma_c$	Slope m	N_R for $\Delta\sigma_c = 100$
	[MPa]	[-]	[x10^6 cycles]
as welded	95.5	3.47	1.7
UIT	204.5	7.63	475.1

4.   NUMERICAL SIMULATIONS OF Y-JOINT

At first a 3D-model of the whole test specimen was analyzed using commercially available finite element code ANSYS (Figure 9). This model contained all boundary conditions, but excluded the actual weld notch effects. The weld profile was modeled as a notch having 60° flank angle with a theoretically zero toe radius. With this model the stress concentrations at the weld could be observed using the hot spot concept.
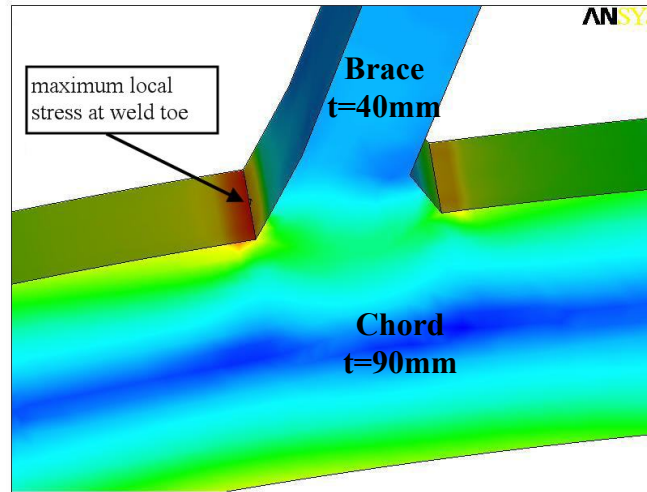
Figure 9. Stress Concentrations at Toe and Root of the Weld

The stress concentration factors (SCF) were determined for the toe and root of the weld with the following equation:

$$SCF = \frac{\sigma_S}{\sigma_N} \tag{2}$$

where σ_S = local stress at the hot spot and σ_N = nominal stress at the end of the brace.

To determine the hot spot stress two extrapolation points are necessary. The first point is located at the chord surface in a distance of $0.4 \cdot t_C$ from the hot spot the second in a distance of $1.0 \cdot t_C$. The calculation is comparable to the calculation for strain concentration factors in case the stresses remain in the linear elastic range. The experimental SCFs at the chord were measured with strain gauges in the near of toe and root of the weld. The SCFs derived with numerical simulations are compared to experimental results. The comparison is presented in Table 5. The experimental and numerical SCFs for weld toe and also for weld root show a very good agreement.

Table 5. Comparison of Strains and SCFs at the Chord

hot spot	method	ε_S (0.4 t_C)	ε_S (1.0 t_C)	SCF
		[μm/m]	[μm/m]	[-]
weld toe	FEM	725	632	6.61
	Experiment	707	614	6.46
weld root	FEM	598	509	5.53
	Experiment	609	524	5.59

Figure 10 shows a curve of the stress path perpendicular to the weld at the chord. The curve was estimated with the FE-model. The stress increases nonlinear in the near of the weld toe. Furthermore the diagram includes all SCF values measured with strain gauges at the chord for the same load level. The test results agree very well with the numerical stress curve. So it can be noticed that the stress concentration due to the local geometry of the Y-joint is comprised correctly in the 3D-model.
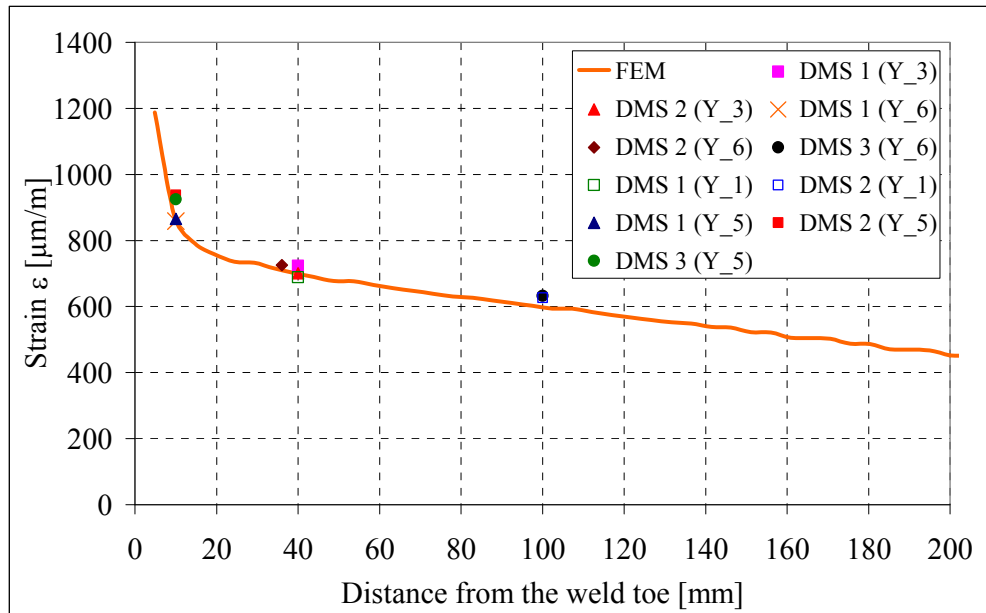
Figure 10. Numerical Stress Curve Perpendicular to the Weld

5.   COMPARISON BETWEEN WELDED AND CAST JOINTS

5.1   Geometry of Offshore Structure (Tripod)

Welded and cast joints for Tripods are analyzed for the Baltic Sea conditions of the planned wind farm Kriegers Flak. The water depth is assumed to 25 m for a 2 MW turbine. The diameter of the central tube (chord) is $D_C = 4.0$ m and for the braces $D_B = 2.0$ m which are connected to the chord in an angle of 45°. The objective of the design study is optimize the thicknesses t_C and t_B for fatigue resistance.
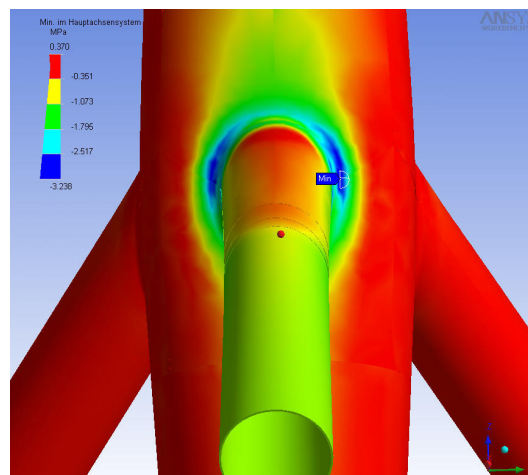
Figure 11. Geometry of Tripod and Stress Concentration

The loads of wind and wave calculated with the deterministic concept are summarized in a rainflow count and load classes. The joints are designed for fatigue limit state with hot-spot-concept. With techniques of sub-modelling the hot-spot-stresses of the joints are calculated to estimate finally the linear cumulative fatigue damage by Palmgren-Miner. The stress concentration factors for cast joints can be optimized by variable fillet radiuses. Thus the cumulative fatigue damage for cast joints is decreased and the thicknesses of chord and brace can be reduced significantly compared to welded joints. Weight saving between 20% and 40% are possible for different types of joints for tripods. The consideration of wave spreading allows further reduction for plate thicknesses, but this is possible for both variants. During the fatigue tests a nonlinear loss of stiffness for the joint could be monitored with strain gauges. This has to be taken into account for the dynamic behaviour of support structures.

5.2   Comparison of Fatigue Strength

The experimental results are taken into account in a reanalysis for tubular joints of tripods. In this way the fatigue resistance of welded joints can significantly be increased by post weld treatment with UIT. The estimated value in Table 4 for the treated condition by UIT is higher than fatigue class (FAT) for the unnotched base material thus the maximum fatigue resistance is assumed to $\Delta\sigma_c$ = 160 MPa. The parameter of the fatigue classes for both condition are presented in Table 6:

Table 6. Parameters of S-N-Curves

Fatigue classes (FAT)	FAT $\Delta\sigma_c$ [MPa]	slope m_1 [-]	slope m_2 [-]	Damage D [-]
as welded	100	3	5	27.2
UIT	160	7	7	1.4

Two effects of UIT cause a better fatigue performance in the treated condition. At first the higher value for $\Delta\sigma_c$ and second the lower slope of the S-N curve. The lower cumulative fatigue damage for the same life time estimated in Table 6 allows weight savings which are comparable with savings by cast iron joints. The optimized thicknesses for different type of joints are compared in Table 7. For welded joints of future offshore wind farms the fatigue design would be more competitive if the effects of post weld treatment by UIT will be considered.

Table 7. Comparison of Plate Thicknesses

type of joint	upper tripod-joint		lower tripod-joint	
	t_C [mm]	t_B [mm]	t_C [mm]	t_B [mm]
welded without UIT	200	100	120	50
welded with UIT	90	60	80	50
cast iron	90	60	80	50

But for detailed numerical analyses of UIT-effects a sub-model is necessary. In this way a second level of numerical study have to carry out with simulations for a single weld seam including the welding process and afterwards the needle peening process.

6.   NUMERICAL SIMULATIONS OF WELDING AND UIT-PROCESS

6.1   Geometry of Sub-Model

A sub-model for a steel plate with a single butt weld was generated to analyze the influence of UIT-effects. The symmetric half model consists of three zones the weld, the heat affected zone and the base material of the steel plate (Figure 12).
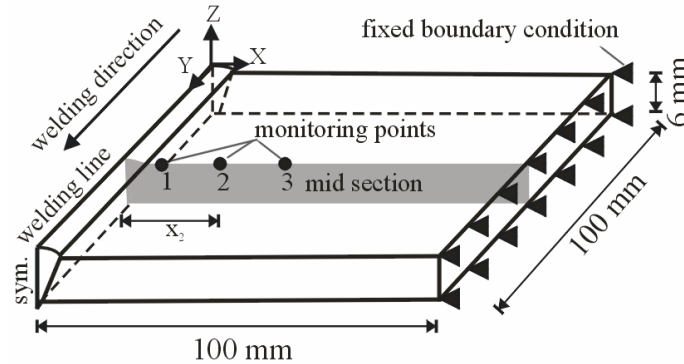
Figure 12. Geometry of a Steel-Plate with a Single Butt Weld

The dimensions of the steel plate fabricated from S355 J2 are 100 x 100 x 6 mm. The material properties depending on temperature published in (Wichers [5]) are implemented for the steel plate. The notch at the weld toe has a variable radius to consider the actual weld geometry for as welded and treated conditions. The smallest dimension of an element at the notch was 0.2 mm in direction of thickness. The sub-models were driven by displacement boundary conditions.

With this FE-model two main effects are investigated. First the transient field of residual stresses due to welding and post weld treatment and second the change in geometry of weld profile. Both effects have a significant influence for the fatigue life of the welded joints. To simulate the post weld treatment a pin of the UIT handheld tool with a diameter of 3 mm is also shown in Figure 13.
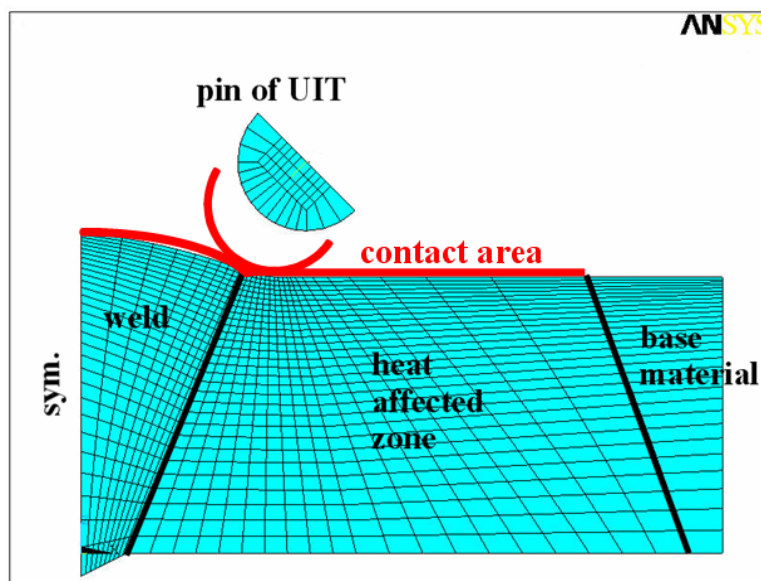
Figure 13. FE-Model with Butt Weld and UIT-Pin

6.2   Thermal Analysis of Welding Process

The simulation of the welding process consists of two analyses. At first the transient field of temperature is calculated during arc welding process. After the transient thermal analysis the structural analysis is following to estimate the residual stresses.

For the transient thermal analysis a half symmetric steel plate having a length of 100 mm (welding direction), width of 100 mm and thickness of 6 mm is modeled with 3D-thermal elements (Solid70). These elements have eight nodes with a single degree of freedom, temperature, at each node. The butt weld is generated as single pass welding process with a welding speed of $v_{weld} = 5$ mm/s. The electric input is $U = 23.5$ V and $I = 165$ A, and the arc efficiency is assumed to be $\eta = 90\%$. Parametric meshing is used in order to easily track the results along a certain predefined path in any direction. For thermal symmetry the heat flux passing across the surface of symmetry shown in Figure 12 is assumed to be zero, and, for structural symmetry, the translation in the x-direction of the same surface is also zero.

It is important to note that the automatically estimated time increment in the analysis drops to a very small value due to the vast difference in the temperatures. This effect can be dramatic for small element size of the weld pool at the fusion surface the parting surface. But the meshing in the weld pool must be fine enough to account for the high temperature gradient calculation.

The transient temperature profile during the welding process was analyzed using Goldak's formulation of the double-ellipsoidal heat source (Goldak [6]). The total heat input Q is evaluated according to electric arc welding with

$$Q = \eta \cdot U \cdot I \tag{3}$$

where η = arc efficiency, U = weld voltage and I = current intensity.

The heat flux q is applied in the model to calculate the thermal load at a certain time and location within the volume of elements according to Eq. 4.

$$q_{vol}(x, y, z) = q_{max} \cdot e^{-3\left(\frac{x^2}{a^2} + \frac{y^2}{b^2} + \frac{z^2}{c^2}\right)} \tag{4}$$

where q_{vol} = heat flux in a volume, q_{max} = maximum heat flux in the center; x, y, z = distance from the center point of heat source and a, b, c = distance with 5% of q_{max} for limiting the heat source. The form of the heat source for electrical arc welding using Goldak's formulation is shown in Figure 14 for example in a single block.

The heat source begins at edge of plate in $y_0 = 0$ mm at time $t_0 = 0$ s taken for the center point of the heat to reach the first node. The motion of the heat load zone along the welding line is considered by

$$y_{source} = y_0 + t \cdot v_{weld} \tag{5}$$

where y_{source} = y-coordinate of center, y_0 = edge of plate, t = welding time; v_{weld} = welding speed (5 mm/s).
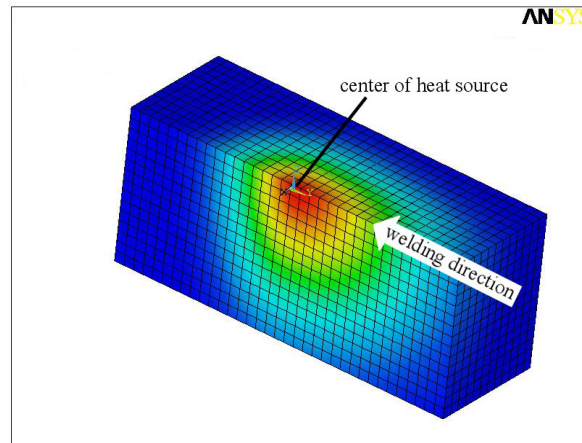
Figure 14. Moving Heat Source for Electrical Arc Welding

In this way, as the time increases, y_{source} increases along the welding line as shown in Figure 13. The thermal boundary conditions include the radiation and convection to the environment from all sides of the welded plate except the symmetry surface.

The results of the transient thermal analysis are presented in Figure 15 for the monitoring point 2 indicated in Figure 12 along the mid transverse line on the top surface. The monitoring point 2 has a distance of 3 mm perpendicular to the weld toe, where the temperature sensor was positioned in the experiment.
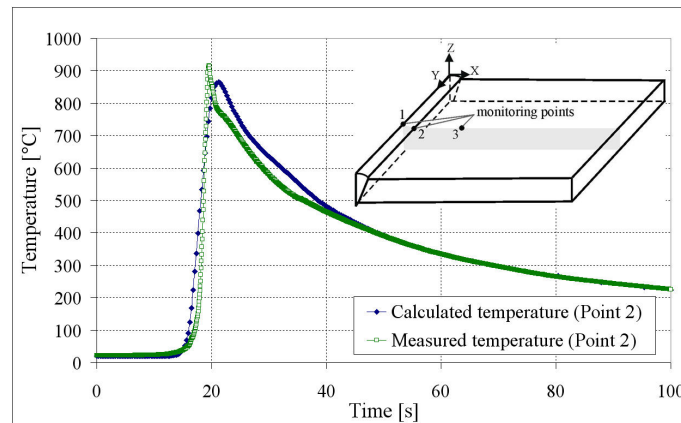
Figure 15. Temperature History

The maximum temperature $T_{2,max,measured} = 914°C$ was measured at $t = 20$ s shortly after the center of the heat source reaches the mid section. The curve is compared with a result of a numerical simulation for this welding process. The maximum calculated temperature is estimated to $T_{2,max,calculated} = 865°C$ at nearly 20 s. The experimental and numerical results agree very well. It can be seen that the temperature curves rise highly for this monitoring point when the heat source is passing. After $t = 40$ s both curves are coincident during the cooling time. The cooling process is terminated at nearly $t = 2000$ s.

6.3   Structural Analysis of Welding Process

After thermal analysis the element type in ANSYS is changed from Solid70 to Solid45. For structural boundary conditions the surface at $x = 100$ mm shown in Figure 11 is constrained in x, y and z-direction. In addition the translation in x-direction at the surface of symmetry ($x = 0$) is also zero.

The metal deposition of the filler material is considered using the element birth technique. This technique is based on deactivating and reactivating the elements of the weld pool as the welding progresses. The meshing of the base plate and the butt weld has a clear parting surface between them.

The nodal temperatures over time determined in thermal analysis are the load for the following structural analysis of welding process. The simulation is carried out up to t = 2000 s to estimate the residual stresses during the cooling period. The final residual stress distribution transverse to the welding line (sx) is shown in Figure 16. The maximum transverse stress is located at the weld toe with values in tension near the yield stress. Because of this high residual stress state the weld toe is often the area where the fatigue crack is initiated.
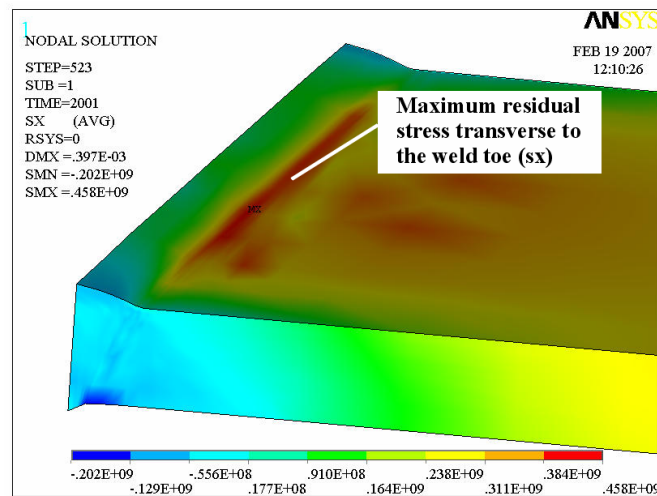
Figure 16. Residual Stresses Transverse to the Weld Toe (sx)

6.4   Simulation of Post Weld Treatment by UIT

The post weld treatment by UIT is considered using a contact algorithm with element types CONTA173 and TARGE 170. For the simulation only the top of the UIT-pin shown in Figure 13 was modeled. The pin is positioned in the mid section with an initial gap to the base plate. After restarting the transient structural analysis the pin moves in an angle of 60° to the weld toe and deformed this surface. The residual stress state in x-direction after post weld treatment is shown in Figure 17.
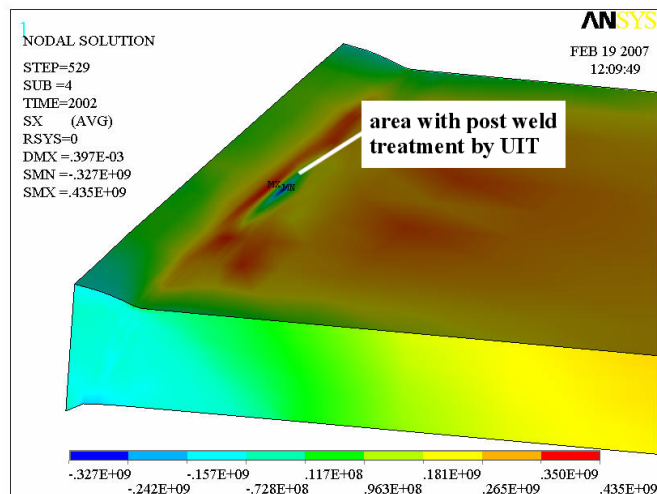
Figure 17. Residual Stresses Transverse to the Weld Toe (sx)
after Post Weld Treatment by UIT in Mid Section

The transverse stress in the treated area changed from tensile residual stresses (σ_{R,T,as_welded} = +458 MPa) to compressive residual stresses near the yield stress ($\sigma_{R,T,uit}$ = -327 MPa). Due to introduced compressive stresses which is one effect of UIT the fatigue strength increases significantly compared to as welded. Furthermore the weld geometry is rounded by the pin and the toe notch radius increases.

The residual stress distribution transverse to the weld toe is compared in Figure 18 for the as welded and treated conditions in mid section.
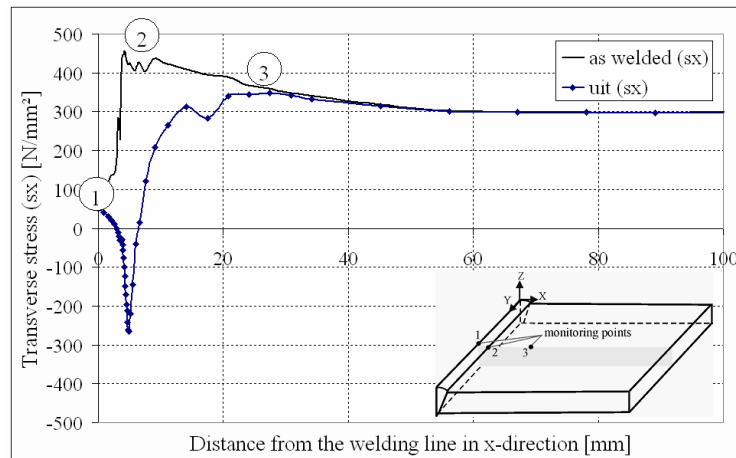
Figure 18. Comparison of Residual Stresses Transverse to the Weld Toe (sx)

The transverse stress distribution for the as welded condition rises up from the welding line (monitoring point 1) to the maximum value at the toe (monitoring point 2) and decreased slowly to a stress level of 300 MPa in the base plate (monitoring point 3). In contrast to the as welded situation the stress distribution after post weld treatment has a negative peak located at the weld toe. The compressive stress reaches a minimum value of -280 MPa. In the near of the peak the residual stress are also reduced. But with more distance to the welding line the curve reaches the stress level like in the as welded condition.

The local treatment at the toe in mid section reduced also the residual stresses along the weld toe line. This effect is noticed for the longitudinal stresses presented in Figure 19.
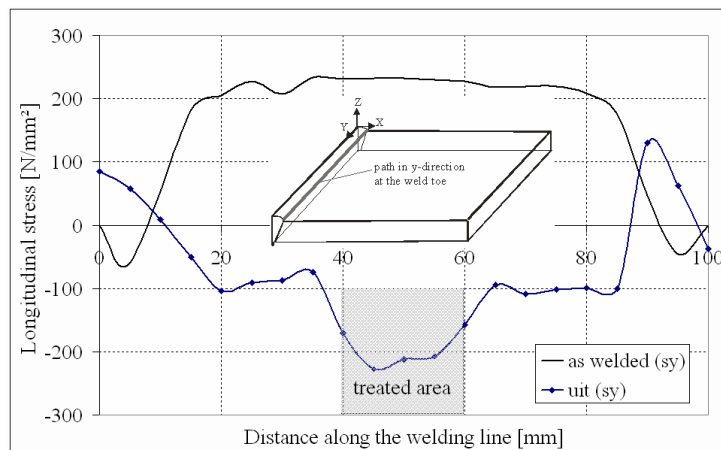
Figure 19. Comparison of Residual Stress Distribution Along the Weld Toe Line
(Longitudinal Stresses sy)

The longitudinal stress distribution in as welded condition increased from the edges of the plate to a stress plateau nearly 220 MPa in the mid section. This stress behavior is typical for arc welding of two coplanar plates with a butt weld processed as single pass. After cooling period was finished the weld toe was treated by UIT. Thereby the pin of UIT was positioned in the toe area from y = 40 – 60 mm. The longitudinal residual stresses are reduced significantly with a minimum value of -220 MPa in the treated area. The maximum penetration reached a value of 0.1 mm.

Furthermore the stress distribution in thickness direction (z) is analyzed for both conditions. The comparison is presented in Figure 20 for the transverse stress curves.
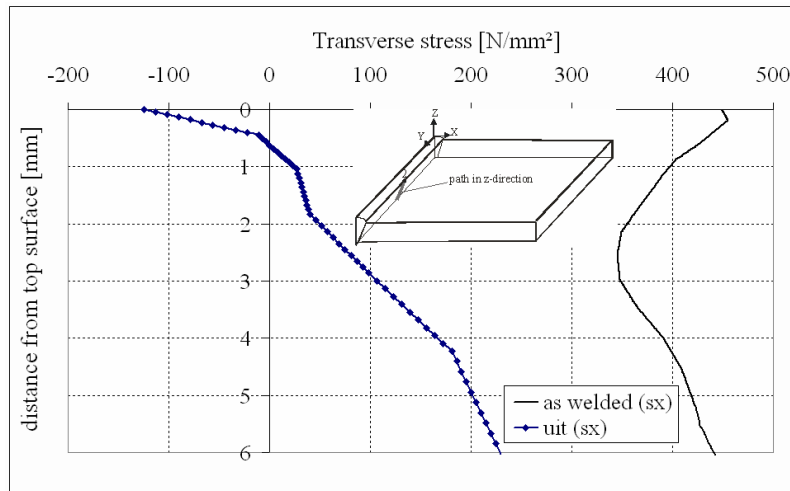
Figure 20. Residual Stresses Transverse to the Weld Toe (sx) in Thickness Direction (z)

The transverse stresses in as welded condition are completely in tension. The maximum value is located at the top surface with 458 MPa. During post weld treatment the residual stresses were reduced significantly in thickness direction. At the top surface the maximum tensile stress changed to minimum compressive stress and the compressive stress state is visible up to a depth of 0.5 mm.

Finally it can be noticed that the post weld treatment by UIT has e great influence on the local stress state at the weld toe which is often the position for crack initiation. Due to introduction of compressive residual stress and plastic deformations at the top surface micro cracks can be closed. The numerical results are suitable to estimate the fatigue strength under consideration of the changed residual stress state at the weld toe.

7.   ESTIMATION OF FATIGUE STRENGTH

7.1   Theory of Notch Strain Approach

The notch strain approach is used for assessing the fatigue strength of the welded joint up to technical crack initiation. The idea behind this approach is that the mechanical behaviour of the material at the notch root in respect of local damage is similar to the behaviour of a miniaturized, axially loaded, unnotched specimen in respect of global damage. The comparison specimen is imagined to be positioned at the notch root. It should have the same microstructure, the same surface condition inclusive of residual stresses and, if possible, the same volume as the highly stressed material at the notch root (Radaj et al. [7]).

7.2 Basic Formulae According to Version of Seeger

The following equations are basic formulae for the stain notch approach according to the version of Seeger.

7.2.1 Cyclic stress-strain curve

At first the cyclic stress-strain curves according to Ramberg and Osgood have to be described by:

$$\varepsilon_a = \varepsilon_{a,el} + \varepsilon_{a,pl} = \frac{\sigma_a}{E} + \left(\frac{\sigma_a}{K'}\right)^{1/n'} \tag{6}$$

Where ε_a = total strain amplitude; $\varepsilon_{a,el}$ = elastic strain amplitude; $\varepsilon_{a,pl}$ = plastic strain amplitude; σ_a = stress amplitude; E = elastic modulus; K' = cyclic strain-hardening coefficient and n' = cyclic strain-hardening exponent.

7.2.2 Strain S-N curve

The strain S-N curve according to Manson and Coffin inclusive of the mean stress effect to Morrow describing technical crack initiation is given by:

$$\varepsilon_a = \varepsilon_{a,el} + \varepsilon_{a,pl} = \frac{\sigma'_f - \sigma_m}{E}(2N)^b + \varepsilon'_f(2N)^c \quad (N \leq N_E) \tag{7}$$

where σ_f' = fatigue strength coefficient; ε_f' = fatigue ductility coefficient; b = fatigue strength exponent; c = fatigue ductility exponent; σ_m = mean stress; N = number of cycles up to crack initiation and N_E = number of cycles at the technical endurance limit.

7.2.3 Cyclic material parameters

The cyclic material parameters in Eqs. 6 and 7 are presented by (Bäumel and Seeger [8]) for non welded base metals according to the uniform material law, shown in Table 8:

Table 8. Cyclic Material Parameters after Bäumel & Seeger [8]

Material parameters	basic formulae for steel, unalloyed and low-alloy	S 355 J2
σ_u	R_m	510
σ_f'	$1.50 \cdot \sigma_u$	765
b	-0.087	-0.087
ε_f'	$0.59\,\psi$	0.59
c	-0.58	-0.58
σ_E^b	$0.45 \cdot \sigma_u$	229.5
ε_E^b	$0.45 \cdot \sigma_u/E + 1.95 \cdot 10^{-4} \cdot \psi$	$1.287 \cdot 10^{-3}$
N_E	$5 \cdot 10^5$	$5 \cdot 10^5$
K'	$1.65 \cdot \sigma_u$	841.5
n'	0.15	0.15
ψ	$\psi = 1.0$ for $\sigma_u/E \leq 3 \cdot 10^{-3}$	1.0
	$\psi = (1.375 - 1.25\sigma_u/E) \leq 0$ for $\sigma_u/E > 3 \cdot 10^{-3}$	

7.2.4 *Hysteresis loop*

The curve branches of the stress-strain hysteresis loop, rising or dropping from the cusp point, are described according to Masing by:

$$\varepsilon = \varepsilon_a + \frac{\sigma - \sigma_a}{E} + 2 \left(\frac{\sigma - \sigma_a}{2K'} \right)^{1/n'} \tag{8}$$

where σ and ε = stress and strain on the hysteresis curve branch; σ_a = stress amplitude; E = elastic modulus; K' = cyclic strain-hardening coefficient and n' = cyclic strain-hardening exponent.

7.2.5 *Elastic-plastic state at the notch*

The stresses and strains at the notch root in the elastic-plastic state, according to Neuber [9] as macrostructural support formulae is given by:

$$\sigma_k \varepsilon_k = \left(\frac{\sigma_n \cdot K_t}{E} \right)^2 \tag{9}$$

where σ_k and ε_k = maximum notch stress and strain in the elastic plastic state; σ_n = nominal stress; E = elastic modulus; K_t = elastic stress concentration factor.

The elastic stress concentration factor K_t for the weld toe geometry was determined numerically for as welded and also for treated condition. The notch radius for as welded is considered according to (Radaj et al. [7]) with r = 1 mm and for the treated toe with r = 1.5 mm. In test series with Y-joints a notch radius of r_{uit} = 1.8 mm was measured, but for idealized the radius for UIT is assumed theoretically to the radius of the pin with r_{pin} = 1.5 mm. The detailed notch geometry is presented in Figure 21 with the corresponding smooth comparison specimen at the notch root.
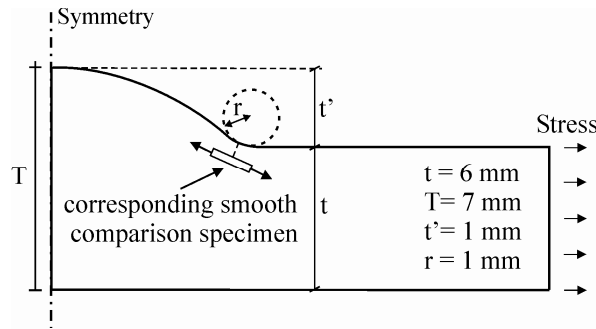
Figure 21. Geometry of the Butt Weld

In addition to the numerical solution the elastic stress concentration factor K_t can be calculated with the following formulae given in FKM Guideline [10]:

$$K_t = 1 + \frac{1}{\sqrt{0.5 \cdot \frac{r}{t} + 5 \cdot \frac{r}{t} \left(1 + 2 \cdot \frac{r}{t} \right)^2}} \tag{10}$$

where K_t = elastic stress concentration factor; r = notch radius and t = thickness of plate.

The comparison of the numerical and analytical results is shown in Table 9. The results have a good agreement for both conditions.

Table 9. Comparison of Elastic Stress Concentration Factor

weld toe	notch radius r	elastic stress concentration factor K_t	
	[mm]	analytical	numerical
as welded	1.0	1.72	1.66
UIT	1.5	1.53	1.57

7.2.6 Influence of residual stresses

Local residual stresses have to be taken into account when determining the stress-strain hysteresis loops by the elastic-plastic analysis. This analysis can be based on a modification of Neuber's macrostructural support formula.

$$\sigma_k \left(\varepsilon_k - \varepsilon_r \right) = \frac{1}{E} \left(\sigma_n \cdot K_t \right)^2 \tag{11}$$

where σ_k and ε_k = maximum notch stress and strain in the elastic plastic state; σ_n = nominal stress; E = elastic modulus; K_t = elastic stress concentration factor and $\varepsilon_r = \sigma_r / E$ initial local residual strain .

7.2.7 Damage parameter

The damage parameter P-N curves comprise the effect of mean stress σ_m on the S-N curve with respect to technical crack initiation. Thus the damage parameter P allows the conversion of a stress-strain hysteresis loop with non-zero mean stress into a damage-equivalent loop with zero mean stress. The damage parameter P_{SWT} most often used has been defined for uniaxial loading by Smith, Watson and Topper given by:

$$P_{SWT} = \sqrt{\left(\sigma_a + \sigma_m \right) \cdot \varepsilon_a \cdot E} \tag{12}$$

where P_{SWT} = damage parameter; σ_a = stress amplitude; σ_m = mean stress; ε_a = strain amplitude; E = elastic modulus.

7.2.8 Damage contribution

For each load cycle j the corresponding number cycles N_j must be estimated. After that the damage contributions of the hysteresis loops are determined linear by Palmgren-Miner rule for each load cycle j. Finally all damage contributions are summing up till the total damage is equal to 1.0.

$$D = \sum_{j=1}^{N_i} D_j = \sum_{j=1}^{N_i} \frac{1}{N_j} \leq 1.0 \tag{13}$$

where D = total damage parameter; D_j = damage contribution by the load cycle j; N_i = crack initiation life with variable-amplitude loading and N_j = crack initiation life with the amplitude of the load cycle j.
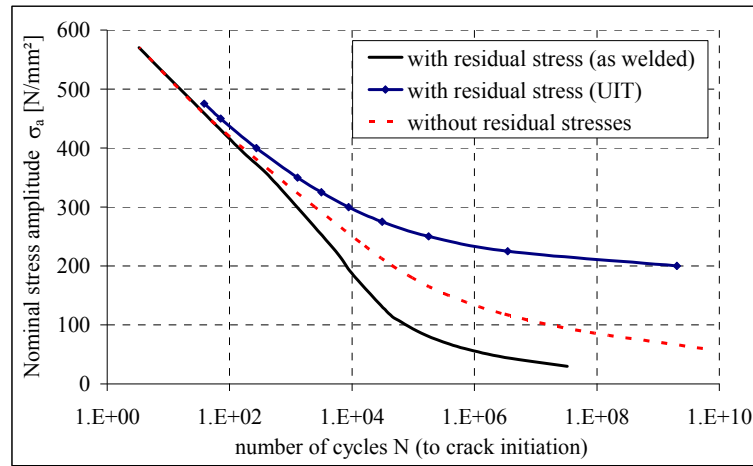
Figure 22. Predicted S-N Curves for Crack Initiation

7.3   Estimation of Fatigue Life

The crack initiation life was calculated on the basis of notch strain approach using the version of Seeger. The S-N curve was determined with the damage parameter P_{SWT} assuming the material properties of the base material. Elastic-plastic behavior, residual stresses and the different elastic stress concentration factors for both conditions were taken into account. The predicted S-N curves for crack initiation of butt weld are presented in Figure 22.

The numbers of cycles N are plotted depending on the nominal stress amplitude σ_a for alternating loading (R = -1). The curve for as welded condition has the lowest fatigue strength because of the tensile residual stresses. In contrast to as welded condition the butt weld with the treated toe has higher fatigue strength. The post weld treatment introducing compressive stresses in the notch root are highly effective in this case. The analysis indicates that the influence of residual stresses at the weld toe is significant for the crack initiation life. The results for both conditions are compared with the S-N curve without considering residual stresses which S-N curve is obviously between these both cases.

Finally, the results are shown graphically as plots using the tool which is implemented in ANSYS®. Thereupon it is extended at the consideration of residual stresses according to Seeger's attempt of residual stresses in thin surface layers and according to Lawrence characterization of residual stresses as mean stress. For the application of this tool, it has to be mentioned critically that the iterations for the elastic-plastic stress-strain behavior at notch and finally the one for getting life cycle is very time-consuming in the calculation. For reducing computing time the accuracy for the iteration of stress-strain path at notch is set to $\Delta\sigma = 0.1$ MPa and for the iteration of life cycle to $\Delta N = 500$. This means in every step of iteration the stress or number of cycle is raised for this delta amount. The amplitude is set to $\sigma_a = 0.5 \cdot \sigma_y = 180.0$ MPa with a stress range R = -1 and $\sigma_m = 0.0$ MPa. Besides, for getting adequate results there is a need for fine meshing especially at crack critical sites a the weld transition. Thus, these plots can only be used for qualitative declarations and considerations at which locations the number of life cycles are critical and cracks may be initiated.
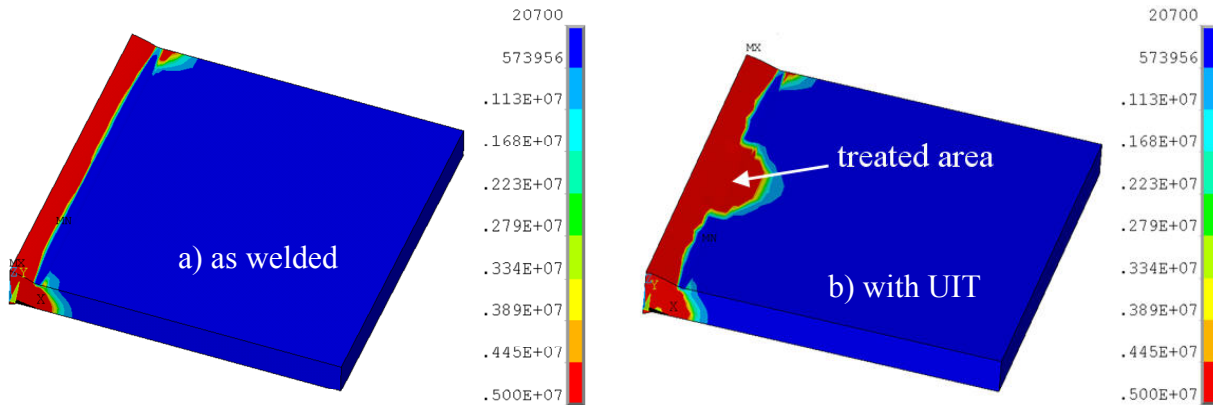
Figure 23. Number of Cycles until Crack Initiation for as Welded (a) and Treated Condition (b)

For the butt-welded plate as expected the critical location for crack initiation is at the weld transition (Figure 23a). Figure 23b shows the weld after treatment with UIT. To evaluate the effect of UIT the region of static pressing of bolt has to be regarded. It has to be mentioned that only the midsection of the weld toe line was treated. Thereby the pin of UIT was positioned in the toe area from y = 40 – 60 mm. In this case the location of crack initiation deflects away from the weld transition. Despite of treatment with UIT, in most cases failure of component occurs still at weld transition or in some cases also at base material.

8.   CONCLUSIONS

Under the aspect of fatigue resistance welded joints present one of the weakest points in steel structures. Induced residual stresses or changing of material properties due to heating are only a few influencing notch effects. For improving fatigue resistance Ultrasonic Impact Treatment (UIT) as method of high frequency needle peening is applied. Fatigue tests on welded joints were carried out to estimate the influence of post weld treatment by UIT. This method introduces compressive stresses and plastic deformations at the weld toe thus residual stresses and stress concentration factors can be reduced. Because of these effects the fatigue strength increased significantly up to $\Delta\sigma_c$ = 204.5 MPa compared to as welded condition with $\Delta\sigma_c$ = 95.5 MPa. This result corresponds with recommendations for tubular joints according to actual offshore-guidelines based on the hot-spot-concept. A second effect is observed for the slope of S-N curve which changed from 3.47 to 7.63 after post weld treatment by UIT.

The experimental results were compared with numerical solutions on a 3D-model of the whole test specimen using commercially available finite element code ANSYS. This model contained all boundary conditions, but excluded the actual weld notch effects. With this model the stress concentration at the weld could be analyzed using the hot spot concept. The stress concentrations factors derived in experiments and numerical simulations have a very good agreement for the weld toe and also for the weld root.

Furthermore different types of tubular joints for offshore structures were investigated with numerical simulations to estimate the fatigue limit state for both conditions, as welded and treated by UIT. The stress concentration factor for the treated weld toe geometry was determined numerically using sub-model analysis. Additionally a comparison between welded and cast iron joints was carried out in a fatigue design study under consideration of experimental results. The lower cumulative fatigue damage for the treated condition allows weight savings which are

comparable with savings by cast iron joints. For welded joints of future offshore wind farms the fatigue design would be more competitive if the effects of post weld treatment by UIT will be considered.

With a sub-model for a seam butt welded joint numerical simulations are carried out using an arc welding process followed by a process of needle peening, like UIT. The objective of numerical investigations was to analyze the influence of residual stresses at the fatigue life for welded joints with and without post weld treatment. The visualization of fatigue life until technical crack shows that the crack is initiated at the weld toe in as-welded condition. After treatment the weld toe in the midsection by UIT the predicted location of crack initiation moves for the treated area from the weld toe to the heat affected zone. Finally the fatigue life until crack initiation was estimated with notch strain approach. The positive effect of post weld treatment by UIT is significant for the fatigue resistance compared to the as-welded condition.

ACKNOWLEDGMENTS

REFERENCES

[1]   Germanischer Lloyd, Rules and Regulations IV, Non-marine Technology, Part 2: Offshore Wind Energy, Hamburg, Germanischer Lloyd Industrial Services, 2004.

[2]   Statnikov, E.S. et al., "Ultrasonic Impact Tool for Strengthening Welds and Reducing Residual Stresses", New Physical Methods of Intensification of Technological Processes, 1977.

[3]   Statnikov, E.S. et al., "Applications of Operational Ultrasonic Impact Treatment (UIT) Technologies in Production of Welded Joints", IIW, Doc. XIII-1668-97, International Institute of Welding, Paris, France, 1997.

[4]   Applied Ultrasonics, "Esonics Ultrasonic Impact Treatment: Technical Procedure Document", Applied Ultrasonics, Birmingham, AL, USA, 2002.

[5]   Wichers, M., "Schweißen unter einachsiger, zyklischer Beanspruchung – experimentelle und numerische Untersuchungen", PhD-thesis, Institute for steel construction, TU Braunschweig, Germany, 2006.

[6]   Goldak, J. et al., "A New Finite Element Model for Welding Heat Sources", Metallurgical Transactions B, 1984, Vol. 15B, pp. 299-305.

[7]   Radaj, D., Sonsino, C.M., Fricke, W., "Fatigue Assessment of Welded Joints by Local Approaches", Second Edition, Woodhead Publishing Limited and CRC Press LLC, 2006.

[8]   Bäumel, A., Seeger, T., "Materials Data for Cyclic Loading", Suppl. 1, Amsterdam, Elsevier Science, 1990.

[9]   Neuber, H., "Über die Berücksichtigung der Spannungskonzentration bei Festigkeitsberechnungen, Konstruktion", 1968, Vol. 20, No. 7, pp. 245-251.

[10]   FKM Guideline, Rechnerischer Festigkeitsnachweis für Maschinenbauteile, Germany, 2002.

[11]   Schaumann, P., Keindorf, C., "Enhancing Fatigue Strength by Ultrasonic Impact Treatment for Welded Joints of Offshore Structures", Third International Conference on Steel and Composite Structures (ICSCS07), Manchester, UK, 2007.

NONLINEAR NATURAL FREQUENCIES
OF A TAPERED CANTILEVER BEAM

M. Abdel-Jaber [1], A.A. Al-Qaisia[2,*] and M.S. Abdel-Jaber [3]

[1] *Department of Civil Engineering, Faculty of Engineering, Applied Science University, Amman, Jordan*
[2] *Department of Mechanical Engineering, Faculty of Engineering and Technology,*
University of Jordan, Amman, Jordan
[3] *Department of Civil Engineering, Faculty of Engineering and Technology,*
University of Jordan, Amman, Jordan
*(Corresponding author: E-mail: alqaisia@ju.edu.jo)

ABSTRACT: The non-linear natural frequencies of the first three modes of a clamped tapered beam are investigated. The mathematical model is derived using the Euler-Lagrange method and the continuous system is discretized using the assumed mode method. The resulted uni-modal nonlinear equation of motion was solved using the harmonic balance (HB) to obtain approximate analytical expressions for the nonlinear natural frequencies. Results were obtained for two types of taper; double taper, i.e. the beam width and thickness are varied linearly along the beam axis and single taper "wedge shaped beams", i.e. the variation is in thickness only. The effects of vibration amplitude and taper ratio on the nonlinear natural frequencies for the first three modes are obtained and presented in non-dimensional form.

Keywords: Nonlinear, free vibration, harmonic balance, tapered beam, cantilever beam

1.   INTRODUCTION

It is known that a lot of engineering structures can be modeled as beam. Some can be modeled as tapered beams, such as piles, fixed-type platforms, tower structures, high buildings and robot arms.

In general, due to various excitation loads "wind and waves", high aspect ratio and flexibility such structures might have large deformations and deflections. The prediction of the dynamic behavior is extremely important during the design process.

The linear vibration theory predicts the natural frequencies to be independent of the amplitude. But in many cases, the deflection in structures may reach large values and consequently, using the linear vibration assumption is not valid. In order to take into consideration the nonlinearities arised due to large deformations, the nonlinear vibration theory must be used to predict with high accuracy the dynamic behavior like; natural frequencies and dynamic responses.

In this paper, the non-linear planar large amplitude free vibration of a tapered cantilever beam is studied for two cases; double tapered beam and single tapered 'wedge shaped beam".

Most of the pertinent literature is directed towards the calculation of linear natural frequencies and mode shapes [1-6] with different end conditions and with attached inertia elements at the free end of the beam. In [7], a simple formulation for the large amplitude free vibrations of tapered beams was presented. The method is based on an iterative numerical scheme to obtain results for tapered beams with rectangular and circular cross sections.

The objective of the present work is to extend the results and analysis obtained in [8] to study the non-linear planar large amplitude free vibrations of a cantilever tapered beam for the cases of a double taper beam and a single taper "wedge shaped beam". The mathematical model is derived

using the Lagrange method and the resulting continuous equation is discretized using the assumed mode method [9, 10]. The inextensibility condition [11] is used to relate the axial shortening due to transverse deflection in the formulation of the kinetic energy of the beam and the nonlinear curvature is used in the potential energy expression.

2. MATHEMATICAL MODEL

2.1 System Description and Assumptions

A schematic drawing of the beam under study is shown in Figure 1. The physical properties, modulus of elasticity E and density ρ, of the beam are constants. While the beam thickness and width are varied linearly along the beam axis. The beam is clamped at one end and free at the other, the cross sectional area and moment of inertia at the large (Clamped end) are A_{b1} and I_{b1}, respectively.

The thickness of the beam is assumed to be small compared to the length of the beam, so that the effects of rotary inertia and shear deformation can be ignored. The beam transverse vibration can be considered to be purely planar and the amplitude of vibration may reach large values.
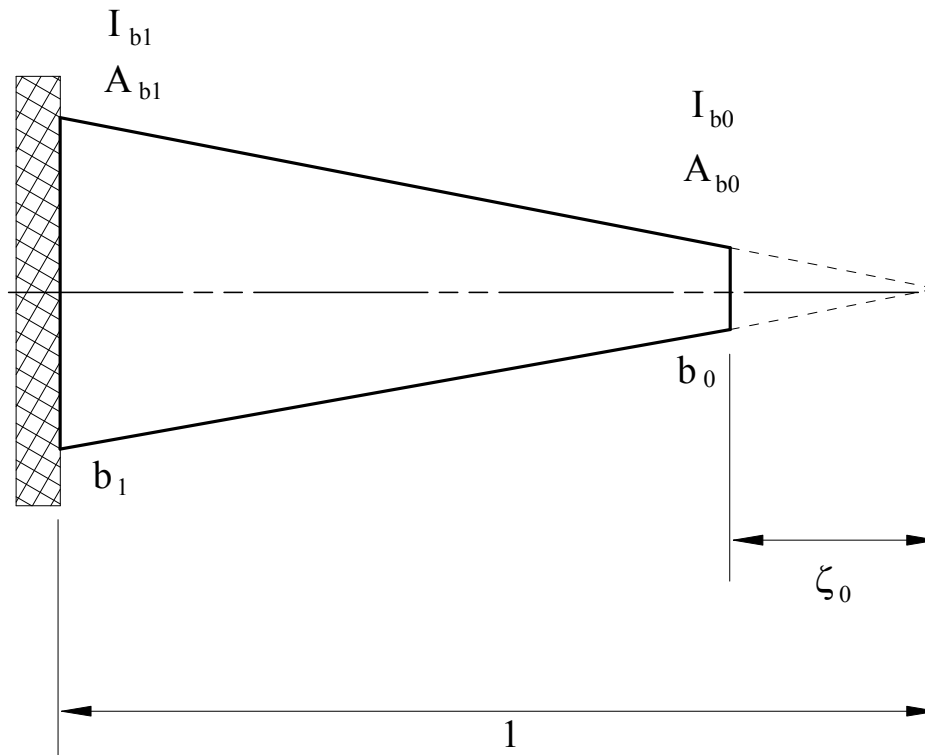
Figure 1. A Schematic Drawing of the Tapered Cantilever Beam

2.2 Derivation of the Equation of Motion

Using the deformed beam, see Figure 2, the potential energy of the beam can be written as

$$V = \frac{El}{2} \int_0^1 I(\zeta) R^2 d\zeta)$$

(1)

where $\zeta = s/l$, $I(\zeta)$ is the variable second moment of area and R is the curvature of the beam neutral axis and can expressed as [8, 10]

$$R = \lambda \phi'$$

(2)

where $\lambda = 1/l$, the prime is the derivative with respect to the dimensionless length, ζ, and   is the change of the slope along the beam (see Figure 2). In order to express the exact curvature in terms of the transverse deflection, v, it is noted that $\cos \phi = \sqrt{1 - \sin^2 \phi}$. This implies that $\sin \phi = dv/ds = \lambda v'$ (as in Figure 2). Differentiating $\sin \phi = \lambda v'$ with respect to ζ, using the above trigonometric identities, expanding the resulted term in a power series and retaining the terms up to the fourth order, the nonlinear curvature R can be written as

$$R^2 = \lambda^4 \left(v''^2 + \lambda^2 v''^2 v'^2 \right)$$

(3)

The kinetic energy T of the beam can be written as

$$T = \frac{1}{2} \rho \, l \int_0^1 A(\zeta) \left[\dot{u}^2 + \dot{v}^2 \right] d\zeta$$

(4)

where u is the axial shortening due to bending deformation as can be seen in Figure 2. The inextensibility condition dictates that a total axial shortening u is given by [11]

$$\lambda u = \zeta - \int_0^\zeta \cos \phi d\zeta = \zeta - \int_0^\zeta \sqrt{1 - (\lambda v')^2} \, d\zeta$$

(5)

Expanding the radical term in a power series, assuming that $(\lambda v')^2 \ll 1$, the axial shortening can be represented as

$$u = \frac{1}{2} \int_0^\zeta \left(\lambda v'^2 + \frac{\lambda^3}{4} v'^4 \right) d\zeta$$

(6)

Differentiating Eq. 6 with respect to time yields

$$\dot{u} = \frac{1}{2} \frac{d}{dt} \int_0^\zeta \left(\lambda v'^2 \right) d\zeta$$

(7)
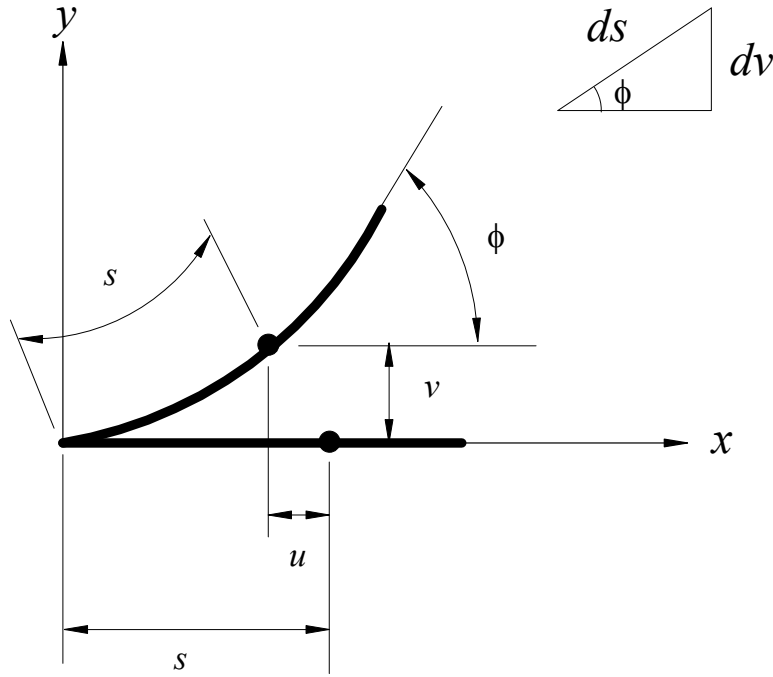
Figure 2. The Deformed Inextensible Beam

The Lagrangian of the beam under consideration can be expressed as

$$L = T - V \tag{8}$$

It is clear that the continuous system in Eq. 8 does not admit a closed form solution. The interest here is in the case where the beam motion is governed by single active mode. The Lagrangian of the system L can be discretized by using the assumed mode method and substituting

$$v(\zeta, t) = \phi_i(\zeta) q(t) \tag{9}$$

where $\phi_i(\zeta)$ is the normalized, self-similar (i.e. independent of the motion amplitude) assumed mode shape of the beam and $q(t)$ is an unknown time modulation of the assumed deflection mode $\phi_i(\zeta)$. In the present work $\phi_i(\zeta)$ for a double tapered beam is (see reference [6]):

$$\phi_i(\zeta) = \zeta^{-1}\left[C_1 J_2(Z) + C_2 Y_2(Z) + C_3 I_2(Z) + C_4 K_2(Z)\right] \tag{10}$$

where $A(\zeta) = A_{b1}\zeta^2$ and $I(\zeta) = I_{b1}\zeta^4$, and   for wedge-type beams (single taper)

$$\phi_i(\zeta) = \zeta^{-1/2}\left[C_1 J_1(Z) + C_2 Y_1(Z) + C_3 I_1(Z) + C_4 K_1(Z)\right] \tag{11}$$

And $A(\zeta) = A_{b1}\zeta$ and $I(\zeta) = I_{b1}\zeta^3$

For both cases $Z = 2\beta\zeta^{1/2}$, $\beta^4 = \dfrac{\rho A_{b1} L_l^4 \omega_l^2}{EI_{b1}}$, ω_l is the linear frequency of vibration, J and Y

are Bessel functions of the first and second kind, respectively, and I and K are modified Bessel functions of the first and second kind, respectively. C_1, C_2, C_3 and C_4, are arbitrary constants to be determined by imposing the following boundary conditions to both ends of the beam; zero bending moment and zero shear force at the free end and zero deflection and zero slope at the clamped end.

$$EI(\zeta)\phi_i''(\zeta_0) = 0$$

$$\frac{\mathrm{d}}{\mathrm{d}\zeta}\left(EI(\zeta)\phi_i''(\zeta_0)\right) = 0$$

$$\phi_i'(1) = 0$$

$$\phi_i(1) = 0 \tag{12}$$

Using Eqs. 7, 9 and 10 or 11 the Lagrangian expression of the tapered beam under consideration can be expressed as, for the *i-th* mode of vibration

$$L = \rho\, l^3 (\beta_1 \dot{q}^2 + \beta_2 q^2 \dot{q}^2 - \beta^2 \beta_3 q^2 - \beta^2 \beta_4 q^4) \tag{13}$$

where

$$\beta_1 = \int_0^1 A_1^* \phi^2 \mathrm{d}\zeta \tag{14}$$

$$\beta_2 = \int_0^1 A_1^* \left\{\int_0^\zeta \phi'^2 \mathrm{d}\chi\right\}^2 \mathrm{d}\zeta \tag{15}$$

$$\beta_3 = \int_0^1 I_1^* \phi''^2 \, d\zeta \tag{16}$$

$$\beta_4 = \int_0^1 I_1^* \phi'^2 \phi''^2 \mathrm{d}\zeta \tag{17}$$

For the double tapered beam; $A_1^* = A_{b1}\zeta^2$ and $I_1^* = I_{b1}\zeta^4$ and for single tapered beam, the wedge beam $A_1^* = A_{b1}\zeta$ and $I_1^* = I_{b1}\zeta^3$.

Applying the Euler-Lagrangian equation to the system Lagrangian

$$\frac{\mathrm{d}}{\mathrm{d}t}\left(\frac{\partial L}{\partial \dot{q}}\right) - \frac{\partial L}{\partial q} = 0 \tag{18}$$

the following non-linear, non-dimensional uni-modal equation of motion is obtained:

$$\beta_1 \ddot{q} + \beta_2 \left(q^2 \ddot{q} + q \dot{q}^2 \right) + \beta^2 \left(\beta_3 q + 2\beta_4 q^3 \right) = 0 \tag{19}$$

Due to the fact that, some of the coefficients β_i, defined by Eqs. 14-17, may have large values, Eq. (19) for convenience is scaled to the form;

$$\ddot{q} + q + \varepsilon_1 \left(q^2 \ddot{q} + q \dot{q}^2 \right) + \varepsilon_2 q^3 = 0 \tag{20}$$

A dot is used to denote a derivative with respect to the non-dimensional time. $t^* = \left(\beta^2 \beta_3 / \beta_1 \right)^{1/2} t$, $\varepsilon_1 = \dfrac{\beta_2}{\beta_1}$ and $\varepsilon_2 = \dfrac{2\beta_4}{\beta_3}$ are dimensionless coefficients.

Eq. 20 describes the non-linear non-dimensional planar flexural free vibration of the inextensible tapered beam. In this equation, the terms $\varepsilon_1 \ddot{q} q^2$ and $\varepsilon_1 q \dot{q}^2$ are inertia non-linearities arised from using the inextensibility condition in the kinetic energy and they are of softening type (i.e., they lead to a decrease in the natural frequency when the vibration amplitude increases). The non-linear term $\varepsilon_2 q^3$ is due to the potential energy stored in bending and arises as a result of using non-linear curvature and it is of hardening static type (i.e., it leads to an increase in the natural frequency when the vibration amplitude increases). The nonlinear natural frequencies of the beam are dominated by the two competing non-linearities mentioned above, and the behaviour of the tapered beam considered in this work is either hardening or softening depending on the ratio $\varepsilon_1 / \varepsilon_2$ [10].

3.   METHOD OF SOLUTION

The calculations of the coefficients β_i in Eqs. 14-17, ε_1 and ε_2 indicate that the non-linear oscillator described in Eq. 20 is strongly nonlinear, and the nonlinear natural frequencies are calculated using the Harmonic Balance method (HB). The initial conditions are taken to be $q(0) = A$ and $\dot{q}(0) = 0$ where A is the amplitude of the motion.

According to the HB method, an approximate single term solution (SHB) [8, 9] takes the form

$$q(t^*) = A \cos(\omega t^*) \tag{21}$$

where ω is the non dimensional nonlinear natural frequency, i.e. the ratio of the nonlinear frequency to the linear one. Substituting Eq. 21 and its derivatives into Eq. 20 and equating coefficients, one obtains

$$\omega^2 = \frac{1 + (3/4)\varepsilon_2 A^2}{1 + (\varepsilon_1 A^2/2)} \tag{22}$$

To improve the accuracy of the assumed solution, more terms can be added and a two term solution is sought (2THB), such that

$$q(t^*) = A_1 \cos(\omega t^*) + A_3 \cos(3\omega t^*) \tag{23}$$

As one can see, the added term is of order three and this is due to the fact that the nonlinear terms

in Eq. 20 " $\varepsilon_1 \ddot{q} q^2$, $\varepsilon_1 q \dot{q}^2$ and $\varepsilon_2 q^3$ "are odd and of order three.

Using the above mentioned initial conditions, yields

$$A = A_1 + A_3 \tag{24}$$

Substituting Eq. (23) and their derivatives into Eq. (20) and equating the coefficient of each of the assumed harmonics, one obtains

$$A_3 = \frac{(\varepsilon_2/4)(A_1^3 + 3A_3^3) - (\varepsilon_1 \omega^2 / 2)(A_1^3 + 9A_3^3)}{(1 + (3\varepsilon_2 A_1^2 / 2) - \omega^2 (9 + 5\varepsilon_1 A_1^2))} \tag{25}$$

$$\omega^2 = \frac{1 + (3\varepsilon_2 / 4)(A_1^2 + A_1 A_3 + 2A_3^2)}{1 + (\varepsilon_1 / 2)(A_1^2 + 3A_1 A_3 + 10A_3^2)} \tag{26}$$

Eqs. 25 and 26 are solved numerically for a given amplitude A, using an iterative technique with an accuracy of 10^{-6}.

4.   RESULTS AND DISCUSSION

The derived non-linear non-dimensional uni-modal equation of motion given in (20) is valid for vibrations with large amplitudes and small rotations, i.e. $(\lambda v')^2 \ll 1$, which is the case in structures with high slender ratio.

The coefficients of the terms β_i given in Eq. 19 are calculated by integrating numerically the coefficients given in Eqs. 14-17. Also, it is worth mentioning that the range of motion amplitudes to be considered in the present work, (i.e., the values of vibration amplitude A), is assumed to be up to 1.0 for the first mode, 0.4 for the second mode and 0.2 for the third mode, to be consistent with the assumption of large amplitude vibration. For example, a vibration amplitude of 1 corresponds to a ratio of tip displacement/length of the beam.

The accuracy of the calculated nonlinear natural frequencies was first examined by comparing the results obtained using: the Harmonic Balance method using single (SHB) and two terms (2THB) given in Eqs. 22 and 26, for the double tapered beam and $\alpha = b_0/b_1 = 0.1$, as shown in Figure 1. Results were obtained and presented in Figures 3-5, for the first three modes. As one, can see the SHB fails to predict the correct nonlinear natural frequency, specially for the second and third mode, and the 2THB method is more accurate. Consequently, all the remaining results were obtained using the method of Harmonic Balance method with two terms (2THB).

In Figures 6-8, results were obtained for the double tapered beam and for different values of the taper ratio $\alpha = b_0/b_1$. Results have shown that the behavior of the first and second modes is changed from hardening to softening when the taper ratio is increased, while the third mode is of a softening type regardless the value of the taper ratio α. This is due to the fact that when the taper ratio α increases the mode shape is modified accordingly, which in turn affects the values of the calculated coefficients β_i given in Eq. 19 and the values of ε_1 and ε_2.

1st Mode, α = 0.1
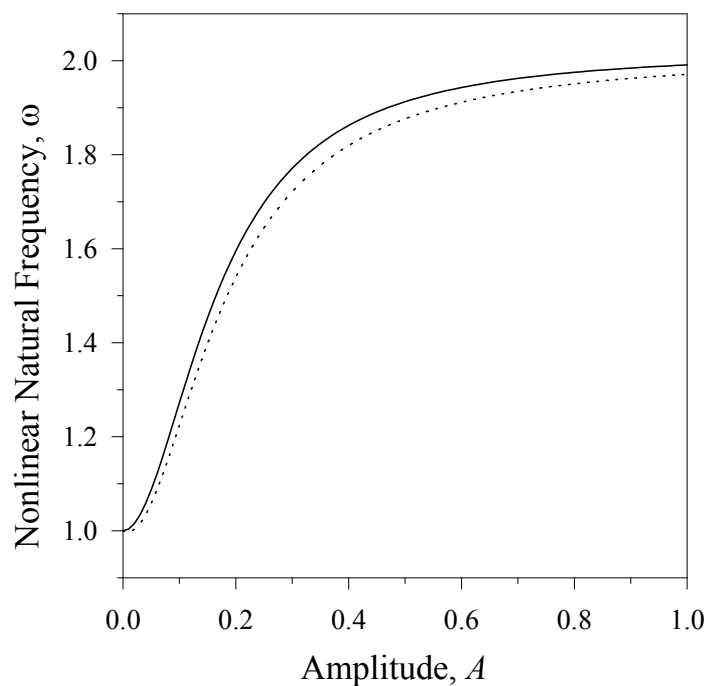
Figure 3. Nonlinear Natural Frequency Versus Amplitude of the First Mode, Double Tapered Beam and for α = 0.1 ———————— SHB, ···················· 2THB

2nd Mode, α = 0.1
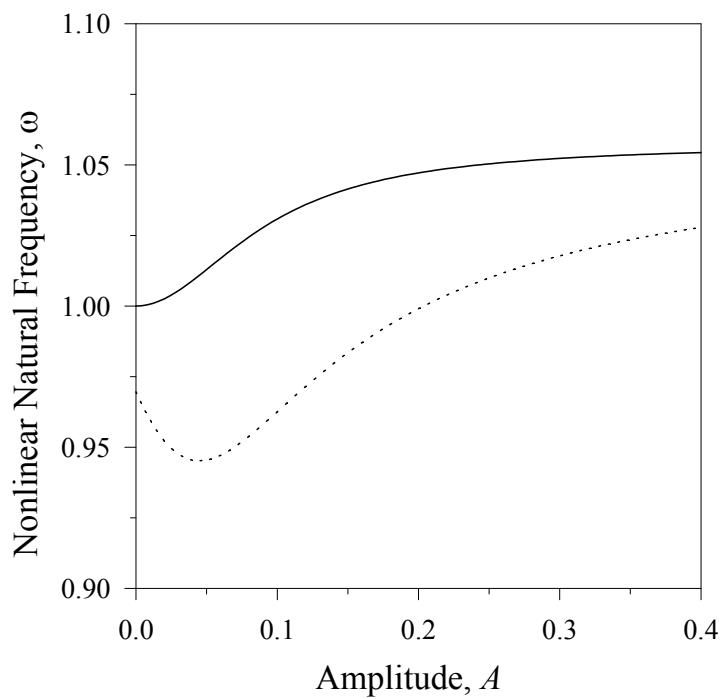
Figure 4. Same as in Figure 3, but for the Second Mode

3rd Mode, α = 0.1
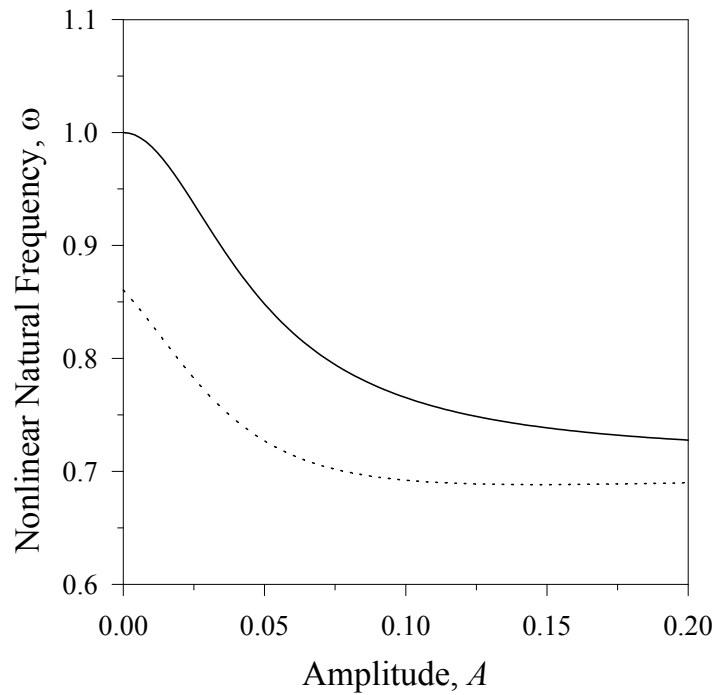
Figure 5. Same as in Figure 3, but for the Third Mode

1st Mode, α = 0.1, 0.2, 0.3, 0.4, 0.5
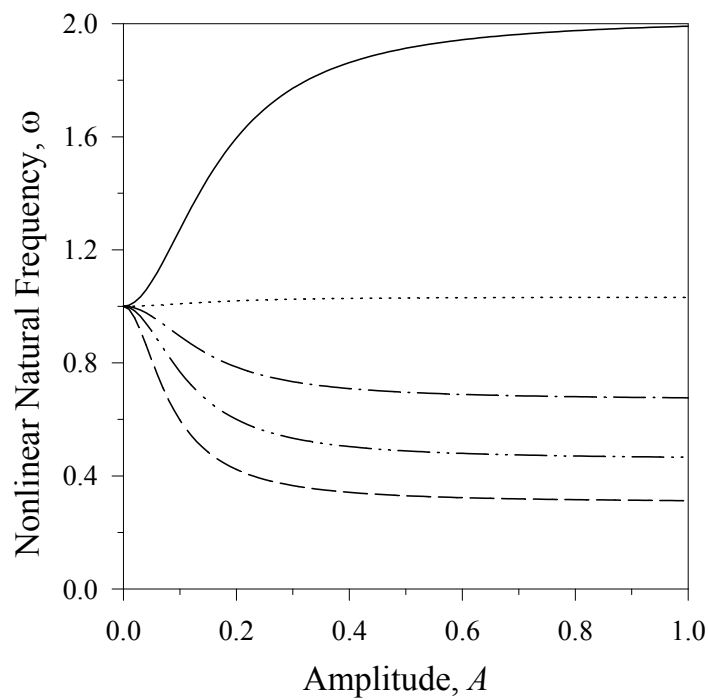
Figure 6. Nonlinear natural frequency versus Amplitude of the first mode, double tapered.
——————— $\alpha = 0.1$, ... $\alpha = 0.2$, — · — · — · — · — $\alpha = 0.3$,
— ·· — ·· — $\alpha = 0.4$, — — — — — — $\alpha = 0.5$

2nd Mode, α = 0.1,0.2,0.3,0.4,0.5
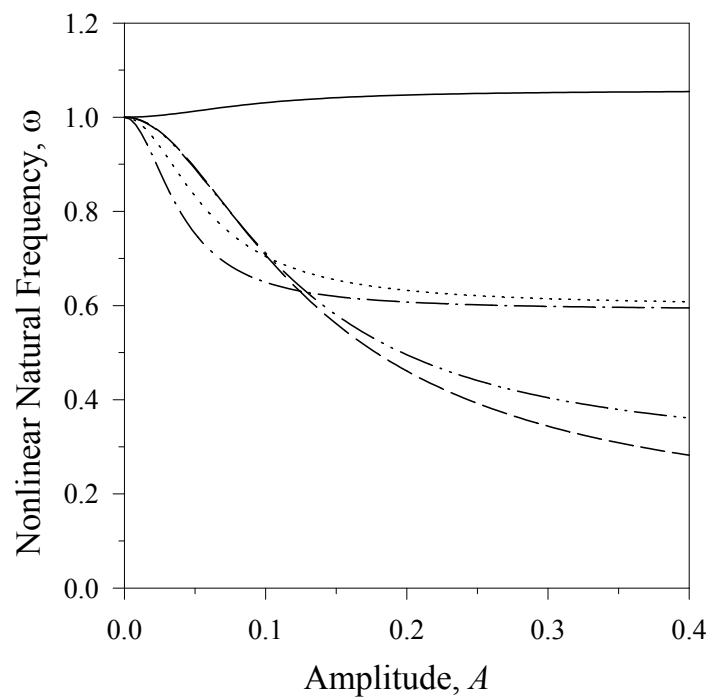
Figure 7. Same as in Figure 6, but for the second mode

3rd Mode, α = 0.1,0.2,0.3,0.4,0.5
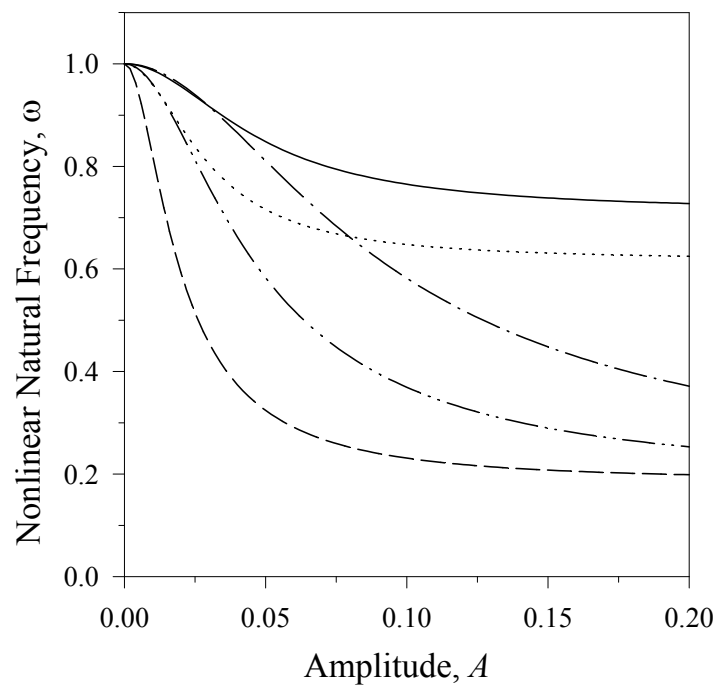
Figure 8. Same as in Figure 6, but for the third mode

The nonlinear equation of motion given in Eq. 20, as mentioned before, is dominated by the non linearities; ($\varepsilon_1 \ddot{q} q^2$ and $\varepsilon_1 q \dot{q}^2$) and $\varepsilon_2 q^3$, inertia and static nonlinearities, respectively and the behavior is of hardening type when the ratio $(\varepsilon_1/\varepsilon_2) \leq 1.6$ and of softening type when $(\varepsilon_1/\varepsilon_2) > 1.6$ [10].

In Figures 9-11 a comparison between the double tapered and wedge type beams for different values of taper ratio $\alpha = b_0/b_1$ is presented also. Results have shown that for a given value of taper ratio α, the nonlinear natural frequency of a double tapered beam is higher than that of a wedge type "single taper beam".

$$1st\ Mode, \alpha = 0.1, 0.3, 0.5$$
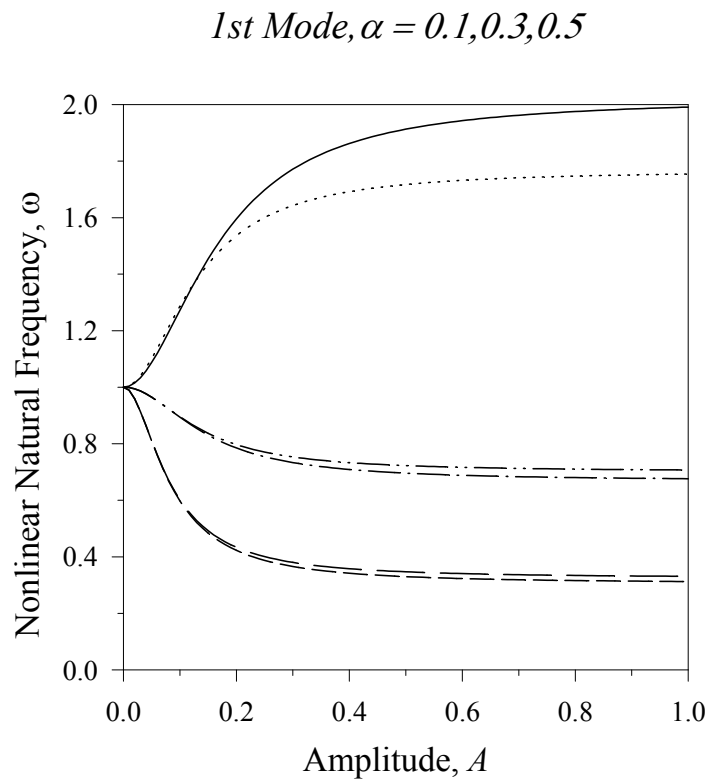
Figure 9. A comparison between the double tapered beam (D) and "wedge" single tapered (S) of the Nonlinear natural frequency versus Amplitude of the first mode.

———————— $\alpha = 0.1$ (D), ···················· $\alpha = 0.1$ (S)

— · — · — · — · $\alpha = 0.3$ (D), — · · — · · — $\alpha = 0.3$ (S)

— — — — $\alpha = 0.5$ (D), – – – – – – $\alpha = 0.5$ (S)

2nd Mode, α = 0.1, 0.3, 0.5
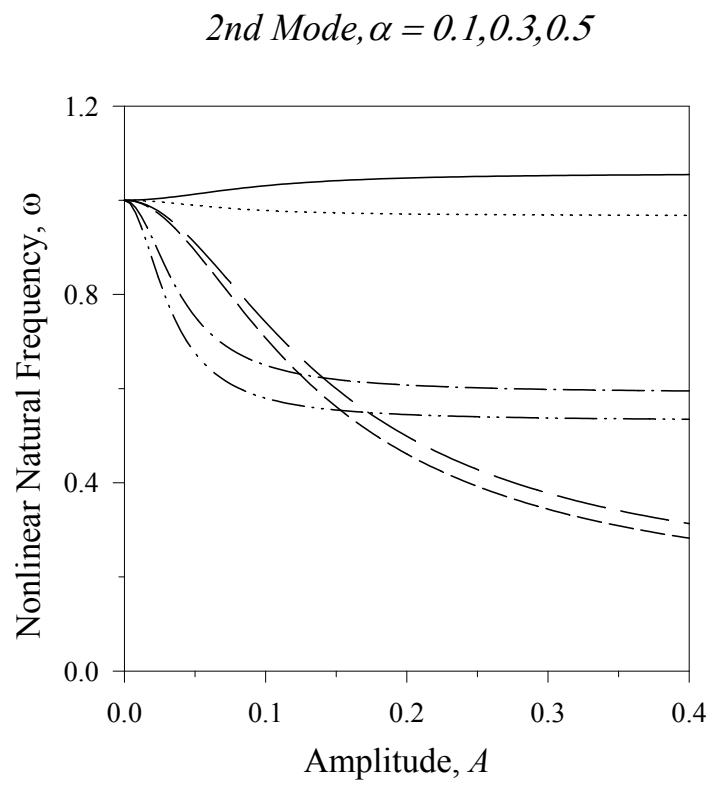
Figure 10. Same as in Figure 9, but for the second mode.

3rd Mode, α = 0.1, 0.3, 0.5
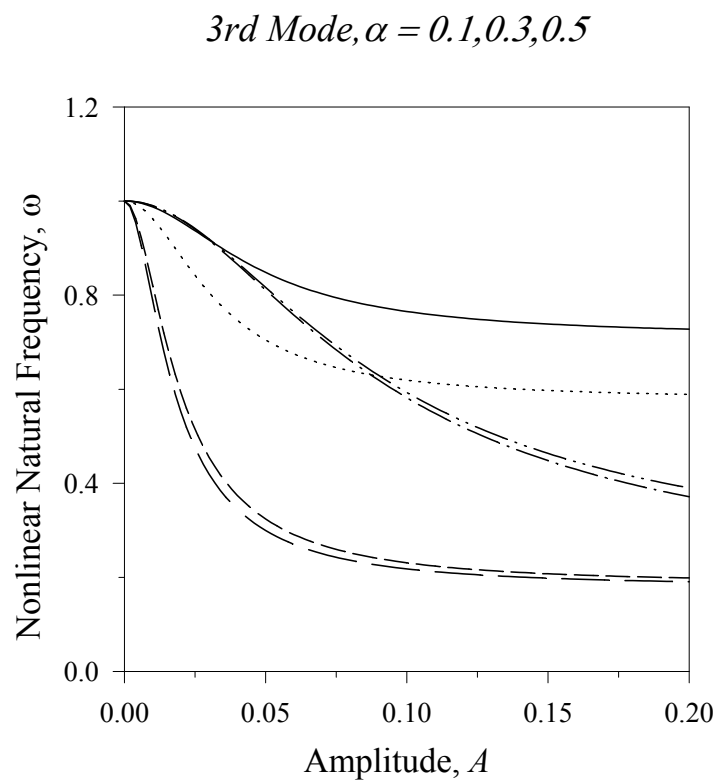
Figure 11. Same as in Figure 9, but for the third mode.

5. CONCLUSIONS

A mathematical model for calculating the nonlinear natural frequencies of a tapered cantilever beam is derived. The axial shortening due to transverse deflection and the nonlinear curvature are used in the formulation of the kinetic and potential energy, respectively. The assumed mode method is used to discretize the continuous Lagrangian of the system and the resulted uni-modal nonlinear differential equation of motion is solved using the Harmonic Balance method (HB) to calculate the nonlinear natural frequencies for the first three modes of vibrations and for different values of the taper ratio $\alpha = b_0/b_1$ for two types of beams; double taper and single taper "wedge shaped".

Results have shown that for the first and second modes the behavior is changed from hardening to softening type when the taper ratio α is increased, while the third mode is of a softening type regardless the value of the taper ratio α. Also, for a given value of a taper ratio, the nonlinear natural frequency of a double tapered beam is higher than that of a single tapered beam.

From the results presented for the effect of taper ratio α on the nonlinear natural frequencies, a qualitative change was noticed, i.e. when the nonlinear natural frequency changes from hardening type to a softening type. This would require a more detailed analysis to study the dynamic response of the beam under a given excitation load which is currently under consideration and beyond the scope of the present work.

REFERENCES

[1] Auciello, N.M. and Nole, G., "Vibrations of a Cantilever Tapered Beam with Varying Section Properties and Carrying a Mass at the Free End", Journal of Sound and Vibration, 1998, Vol. 214, pp. 105-119.

[2] Nagaya, K. and Hai, Y., "Seismic Response of Underwater Members of Variable Cross Section", Journal of Sound and Vibration, 1985, Vol. 119, pp. 119-138.

[3] Laura, P.A. and Gutierrez, R.H., "Vibrations of an Elastically Restrained Cantilever Beam of Varying Cross Sections with Tip Mass of Finite Length", Journal of Sound and Vibration, 1986, Vol. 108, pp. 123-131.

[4] Shong, J.W. and Chen, C.T., "An Exact Solution for the Natural Frequency and Modes Shapes of An Immersed Elastically Wedge Beam Carrying an Eccentric Tip Mass with Mass Moment of Inertia", Journal of Sound and Vibration, 2005, Vol. 286, pp. 549-568.

[5] Chen, D.W. and Wu, J.S., "The Exact Solutions for the Natural Frequency and Modes Shapes of Non-Uniform Beams with Multiple Spring-Mass Systems", Journal of Sound and Vibration, 2002, Vol. 255, pp. 299-322.

[6] Goorman, D.J., "Free Vibrations of Beams and Shafts", John-Wiley & Sons, 1975, pp. 365.

[7] Rao, B.N. and Rao, G.V., "Large Amplitude Vibrations of a Tapered Cantilever Beam", Journal of Sound and Vibration, 1988, Vol. 127, pp. 173-178.

[8]   Al-Qaisa, A.A., Shatnawi, A., Abdel-Jaber, M.S., Abdel-Jaber M. and Sadder, S., "Non-Linear Natural Frequencies of a Tapered Cantilever Beam",. Proceedings of the Sixth International Conference on Steel and Aluminum Structures (ICSAS'07), Oxford, UK, July 24-27, 2007, pp. 266-273.

[9]   Al-Qaisia, A.A., "Effect of Fluid Mass on Non-Linear Natural Frequencies of a Rotating Beam", Proceedings of ASME Pressure Vessels and Piping Conference PVP2003, Cleveland, OHIO, USA, July 20-24, PVP-2003-2178, pp. 243-249.

[10]   Al-Qaisia, A. A. and Hamdan, M. N., "On the Steady State Response of Oscillators with Static and Inertia Non-Linearities", Journal of Sound and Vibration, 1999, Vol. 223, pp. 49-71.

[11]   Al-Qaisia, A.A. and Hamdan, M.N., "Bifurcation and Chaos of an Immersed Cantilever Beam in a Fluid and Carrying an Intermediate Mass", Journal of Sound and Vibration, 2002, Vol. 253, pp. 859-888.

FIRE BEHAVIOUR OF STEEL-CONCRETE COMPOSITE MEMBERS WITH AUSTENITIC STAINLESS STEEL

C. Renaud [1] and B. Zhao [2],*

[1] *Dr, Fire Research and Engineering Section, CTICM,*
Espace technologique l'Orme des Merisiers F-91193 Saint Aubin - France
[2] *Head of the Fire Research section, Research and Engineering Section, CTICM,*
Espace technologique l'Orme des Merisiers F-91193 Saint Aubin - France
*(Corresponding author: E-mail: binzhao@citicm.com)

ABSTRACT: Within the scope of a European research project, a part of the work was focused on both experimental and numerical investigation of the fire performance of steel-concrete composite members with austenetic stainless steel. For the experimental investigation, an important number of fire tests have been carried out with different composite members. Based on these fire tests, corresponding numerical analysis has been made using advanced calculation models to check, on the one hand, the validity of these models, and on the other hand, to perform parametric studies with the purpose of developing simple calculation methods in order to provide a practical rule for daily design of composite members with austenitic stainless steel. It has been shown through the comparison with both numerical results and fire tests that the proposed calculation methods are suitable to predict with a good accuracy the fire resistance of composite columns with hollow stainless steel section and partially protected floor beams with stainless steel part exposed to fire.

Keywords: Fire resistance, stainless steel, composite column with hollow steel section, floor-beams

1.   INTRODUCTION

Although many European research projects have already shown its remarkable fire resistance, the use of high-strength austenitic stainless steel as steel-concrete composite members remains not very common in practice because of the lack of knowledge on the fire behaviour of this type of structural members. Due to its good performance at elevated temperatures, stainless steel could become a practical alternative solution to conventional structural carbon steel reducing for example the cross-section size of steel profiles or the ratio of additional reinforcing bars which often are needed with carbon steel to achieve the required fire resistance. So, in order to investigate the fire behaviour of composite members with austenitic stainless steel, a total of nine fire tests have been carried out, including both rectangular hollow sections filled with concrete and partially protected slim-floor beams with stainless steel part exposed to fire and carbon steel part encased in concrete. All test members were in grade EN 1.4404 stainless steel, one of the grades commonly used in construction. Based on fire tests, corresponding numerical analyses have been made using the advanced finite element model SISMEF capable of simulating the mechanical behaviour and resistance of composite members exposed to fire. This model was proved already to be in good agreement with several fire tests performed on composite members with conventional structural carbon steel [1-4]. This numerical model was used then to perform parametric studies in order to develop simple design rules for composite columns and floor beams. The proposed design methods are consistent with the general flow charts in EN 1994-1-2 used to check the fire resistance of composites members but including some specific characteristics [5].

The present paper is then devoted to present test results, corresponding numerical simulations and the development of design guidance for investigated composite members with stainless steel.

2.   EXPERIMENTAL PROGRAM

Fire tests on seven columns and two beams were conducted in France (Fire station of CTICM in "Maizières-Les-Metz") for the purpose of obtaining experimental evidence about the structural behaviour of stainless steel-concrete composite members subjected to fire.

2.1   Test Specimens

The main characteristics of tested composite columns are summarized in Table 1. All columns were square hollow steel sections with cross-section sizes ranging from 150x8 to 300x8 mm. The column length was 4000 mm. Stainless steel tubes were filled with either reinforced or non-reinforced concrete core. Additional reinforcement, if used, was in four identical longitudinal bars, with a diameter chosen to achieve a ratio of reinforcement $A_s/(A_s+A_c)$ of approximately two percent and an axis distance of reinforcing bars $u_s = 30$ mm. The stainless steel grade was EN 1.4401. Columns were tested under centric or eccentric load. For centrically loaded columns, a small loading eccentricity of 5 mm was applied to both column ends in order to induce an overall flexural buckling mode of failure under the fire condition.

Table 1. Characteristics of Tested Composite Columns with Hollow Steel Section
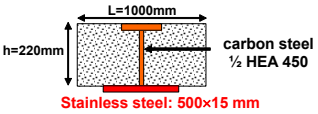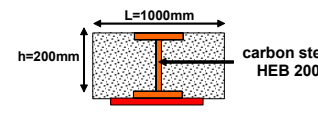
Column	Cross-section	Stainless Steel grade	Rebars		Loading		Length
	b×e (mm)		Diameter	Cover* (mm)	Load (KN)	Ecc.	(mm)
n°1	150×8	EN1.4401	none	-	400	5 mm	4000
n°2	200×8	EN1.4401	none	-	240	0.25×b**	4000
n°3	200×8	EN1.4401	4Φ14	30	630	5 mm	4000
n°4	200×8	EN1.4401	4Φ14	30	240	0.25×b**	4000
n°5	300×8	EN1.4401	none	-	750	0.5×b**	4000
n°6	300×8	EN1.4401	4Φ22	30	1000	0.125× b**	4000
n°7	300×8	EN1.4401	4Φ22	30	800	0.25× b**	4000

* distance between the axis of longitudinal reinforcements and the border of concrete core
** external side of hollow steel section

The main structural characteristics of tested beams are reported in Table 2. Beams were simply supported hybrid I-section (stainless steel lower flange, carbon steel web and top flange) with a span of 5m. Two different I cross-sections have been tested. The first beam is composed of half HEA 450 and 15mm thick × 500 mm stainless steel plate. The second beam is composed of carbon steel HEB 200 and 15mm thick × 360 mm stainless steel plate. The carbon steel part of the beams was partially encased with concrete. The loading was applied in two points so that uniform bending moment was present in mid-span area of beams. The load P applied on beams was 100 kN and 75 kN respectively.

Table 2. Structural Characteristics of Tested Beams

Beam	Cross-section	Stainless steel grade	Load P (KN)	Length (m)
n°1	L=1000mm, h=220mm, carbon steel ½ HEA 450, Stainless steel: 500×15 mm	EN1.4401	-100.0	4.90
n°2	L=1000mm, h=200mm, carbon steel HEB 200, Stainless steel :360×15 mm	EN1.4401	-75.0	4.90

2.3   Test Set-Up

Test set-up of columns and beams is described in Figure 1. Each column was located at the centre of the furnace. The load was applied before fire test and kept constant during the test until the failure. Columns were exposed to heating conditions according to ISO-834 standard fire curve. Columns were tested with both ends hinged. For that, support conditions at the top end and the bottom end of columns were built-up from additional end plates and cutter bearings (see Figure 3). Moreover, to obtain eccentric load, cutter bearings were shifted in comparison to the gravity center of the cross-section. Both ends of the specimens were free to rotate about the axis perpendicular to cutter bearings but restrained to rotate about the other axis. Loading was applied by a hydraulic jack of capacity one hundred tons located outside and above the furnace chamber. The constant load was controlled manually and measured using pressure transducers.

During all the tests, the furnace temperature will be continuously measured with twelve plate thermometers on four sides of the specimen at 100 mm from the surface of the specimen. Thermocouples were also installed on the hollow steel section and the reinforcing bars as well as in the concrete core. Three cross-sections were equipped with thermocouples along the column length in order to measure the temperature field. In fact, only three-quarter of the columns were heated because the top of the column should be outside the furnace to allow its loading. Axial deformations of the test specimen were determined by measuring the displacement of the top of the column (outside the furnace) using transducers. The rotations of the lower supporting end plate along two axes were also measured during the test by two rotation sensors. Failure time measured during all the test corresponds to the condition when each column could not bear the applied load any more.

Beams were located at the upper part of the furnace. The load was applied to the beam at least 15 minutes before the heating period and was maintained until the beam failed. During the tests, the heating of the beams was measured on five sections, uniformly distributed along the heated part of the beams. Temperatures were recorded by means of thermocouples located at several points over the cross-section (stainless steel plate, carbon steel profile and concrete). Furnace temperatures were recorded using 5 plate thermometers located at the level of the five preceding sections. Two linear displacement transducers were positioned above the mid-span of the beam to measure the central deflection of the beam during the test.

Specimens from steel profiles, reinforcing bars and concrete were used to determine the real mechanical properties (yield and ultimate tensile strengths of steel and compressive strength of concrete).
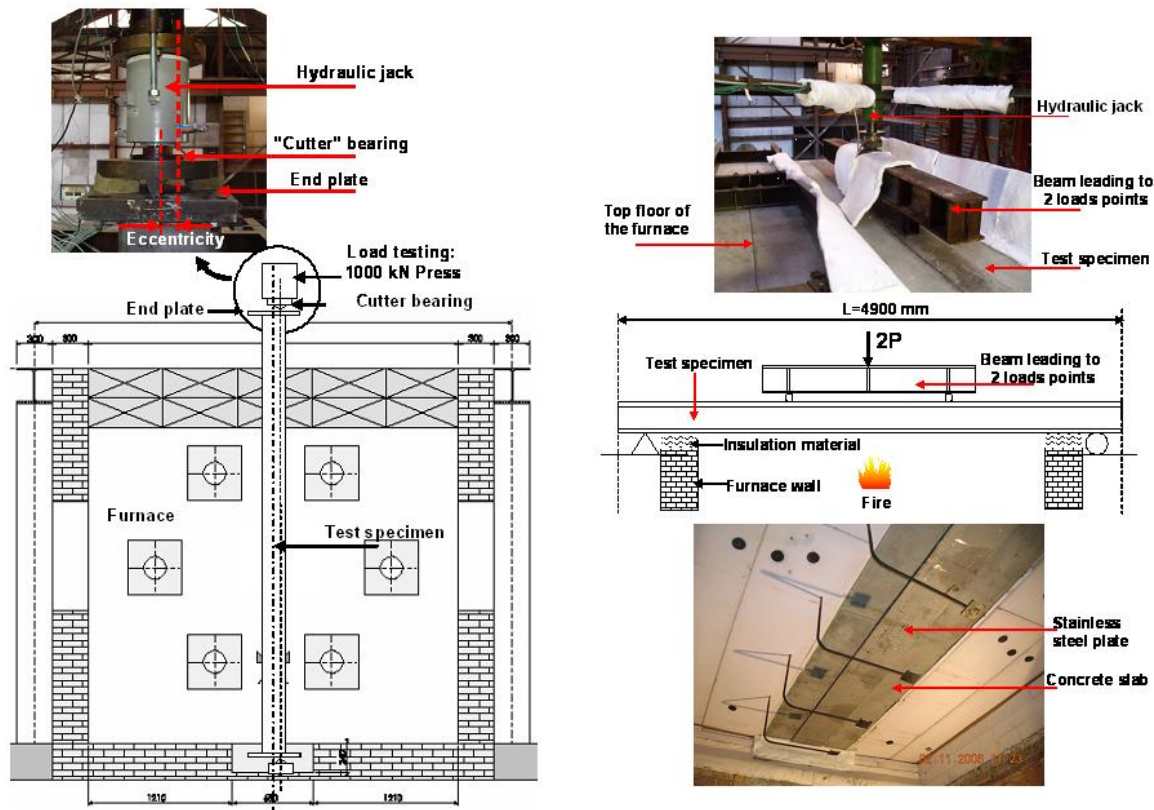
Figure 1. Test Set-Up of Structural Members

2.4   Test Results

Experimental failure times of columns which correspond to the condition when columns could not bear the applied load any more are reported in Table 3. All failure times were higher than expected fire ratings, namely R30 and R60. The main reason is that initial design of columns was made using nominal values of the mechanical properties of materials and assuming a uniform temperature distribution along full column height.

Column failures were caused by simple global flexural buckling or flexural buckling combined with local buckling (see Figure 2). The observation after the test shows that the maximum deflection of the column was located either close to the bottom (lower part of the column) or near the mid-height of the specimen. For specimens with the larger cross-section (300x8mm), maximum deflection was observed on the lower part of the columns (due to the non-uniform heating of columns during fire tests). The thermocouple recordings on the other RHS columns showed that columns can be considered to be uniformly heated. In this case, the maximum deflection was observed near the mid-height of the specimen. It is observed also that the local buckling had occurred in hollow steel section of tested columns with large cross-section sizes (200x8mm and 300x8mm). This local buckling may be explained by the fact that these columns have excessive wall slenderness. No local buckling has been observed in the column with small cross-section sizes (150x8mm).

Figure 2. View of Some Test Specimen after Test

Table 3. Failure Times of Columns

Column	Load ratio*	Failure time (min)	Failure mode
N°1	0.42	42.0	Flexural buckling
N°2	0.22	59.5	Flexural buckling
N°3	0.31	56.0	Flexural & local buckling
N°4	0.20	71.0	Flexural & local buckling
N°5	0.46	38.0	Flexural & local buckling
N°6	0.29	70.5	Flexural & local buckling
N°7	0.29	62.0	Flexural & local buckling

* The load ratio is defined as the ratio between the test load and the buckling resistance of column (according to the load eccentricity) calculated using numerical model.

Elapsed time of the fire tests carried out on beams and their failure times are reported in Table 3. The beams are deemed to have failed when they can no longer support the test load. The failure criteria is considered to be reached as a deflection of L/20 is exceeded (where L is the span of the specimen). The first beam reached the limiting deflection just after 79 minutes. Just before the imposed load was removed (at 90 minutes), the rate of deflection reached a maximum value of 15mm/min. The second beam reached the limiting deflection just after 76 minutes. Just before the imposed load was removed (at 86 minutes), the rate of deflection reached a maximum value of 10mm/min.

Table 4. Failure Time of Tested Beams

Beams	Load ratio*	Fire duration (min)	Failure time (min)
N°1	0.43	90	79
N°2	0.65	86	76

* the load ratio is defined as the ratio between the maximum moment due to applied loads and the moment resistance at room temperature obtained from numerical analysis.

3.   NUMERICAL SIMULATIONS

The mechanical behaviour of tested composite members has been simulated using the FEM model SISMEF. Temperature distributions in members have been obtained separately, either from 2D heat transfer analyses (based on finite difference or finite element method) or from test data. These temperatures have been used as input data for SISMEF.

3.1   Assumptions for Numerical Simulations

In addition to the loading, boundary and heating conditions described in the previous paragraph, the fire behaviour of composite members has been analysed with the following assumptions:

- The thermal and mechanical material properties of concrete and reinforcing steel bars as a function of temperature are in accordance with EN 1994-1-2. Material models for stainless steel are from EN 1993-1-2 [6]. It should be underlined that the creep strains of steel and concrete are implicitly included in the stress-strain relationships at elevated temperatures. Moreover, the effect of residual stresses is neglected.

- Temperature distributions have been assumed to be uniform over the column height, except at the top of the column where a temperature gradient has been taken into account. The reason is that the top of the column was outside the furnace during the test and was not heated directly by the fire. Temperature distribution over the cross-section of column has been computed separately from 2D heat transfer analysis. To calculate the heat flow transmitted to the surface of hollow steel section during the fire exposure, it is necessary to introduce into the model the values of the convection heat transfer coefficient (h_c), the emissivity of fire (ε_f) and the emissivity of steel (ε_m). In practice, whatever the nature of materials, the convection coefficient inside the furnaces is taken equal to h_c=25 W/m²K under ISO fire. In EN 1991-1-2 [7] and EN 1993-1-2, the emissivity of the fire is taken in general as unity. In the present work, the emissivity of the fire is also assumed as unity. The surface emissivity of the column is applied in accordance with EN 1993-1-2, namely ε_m =0.4. The influence of moisture is considered in a simplified way in the calculation of the temperature filed of columns by assuming that all moisture evaporates, without any moisture mass transfer, at the temperature of 100°C or another temperature within a narrow range with the heat of evaporation giving a corresponding change in the enthalpy-temperature curve. Direct heat transfer was assumed between stainless steel hollow section and concrete core (no gap due to differential thermal elongation of materials).

- For beams, temperature distribution has been assumed uniform along their length. The temperature development of the two beam tests was modelled numerically with the computer code ANSYS [8], using the same parameters as those adopted for columns and an emissivity of 0.7 for concrete slab.

- The mechanical interaction between the hollow steel section and the concrete core is neglected, that is slipping has been assumed to occur without significant bond between the steel wall and the concrete core.

- Contribution of the concrete slab on the mechanical fire resistance of beams is neglected.

3.2   Presentation of Some Results

The measured temperature rises on composite members were systemically compared to the predicted temperature rises. As example, Figure 3 shows comparisons for reinforced column n°3 and beam n°1.

a) Composite column n°3	b) Floor-beam n°1
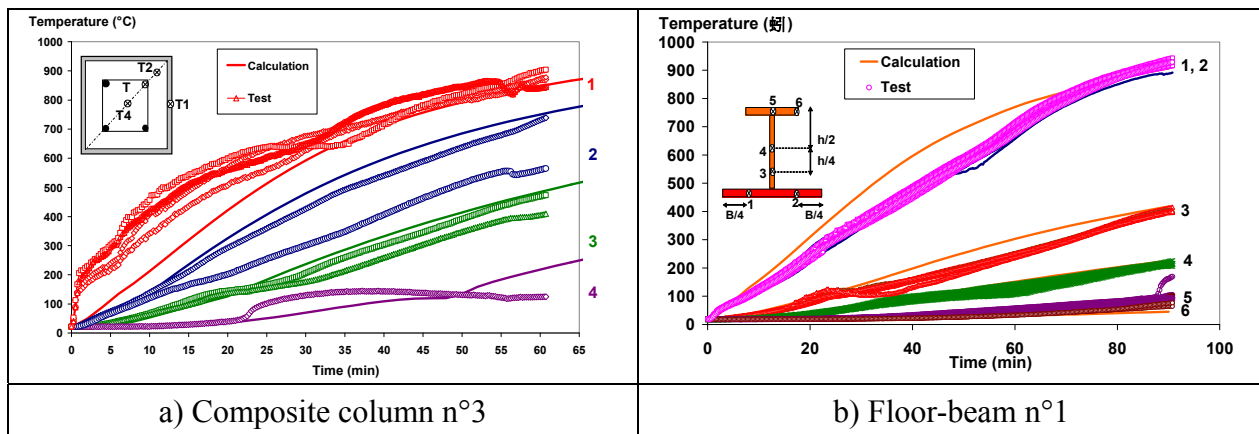
Figure 3. Comparison between Calculated and Predicted Temperatures

The temperature rises predicted for the hollow steel sections are in good agreement with the measured ones. However, Figure 3 shows fairly large discrepancies between the predicted temperatures and the measured temperatures, particularly for the first 20 minutes. In fact, predicted temperatures rise more slowly. The difference is less than 150°C during the early stage of the tests and decreases quickly with the fire duration. The faster rise in temperature of the hollow steel section might be explained by the role of "heat shield" played by the gap which occurs usually between the hollow section and the concrete core of heated composite columns. This gap is due to the differential thermal elongation of materials (steel and concrete) in the radial direction. It interrupts direct heat conduction between the steel wall and the concrete core. The concrete core is mainly heated then by the thermal radiation from the heated hollow steel section.   The temperatures in the longitudinal reinforcing steel bars are evaluated satisfactorily between 0 to 100°C. Once the temperature of 100°C is reached close to the reinforcement, calculated temperatures become more important than those measured (the maximum difference is about 200°C). Globally, the predicted temperature rise rate beyond 100°C is analogous with that observed in test, but somewhat translated towards lower time instants. This translation between the curves is due, on the one hand, to the delaying effect as a result of the gap between the hollow steel section and the concrete core (not taken into account in the thermal analyses) and on the other hand, to the time necessary to the vaporisation of water really enclosed in the concrete. With regard to the point inside the concrete core, the agreement is not so good, but can nevertheless be considered as satisfactory. The difference with calculated curves is of no significant consequence: for low temperatures, the concrete mechanical properties are not affected and for higher temperatures the calculated curve is on the safe side.

As seen during tests, the bottom of the floor-beam heated up faster than the top, due to fire protection given by the concrete slab. Moreover, it can be noted that the temperatures of stainless steel plates obtained from the numerical model are higher than the test data between 10 to 70 minutes. Then, they become quite close to the measured temperatures. The largest temperature difference in this case is about 100°C at 45 minutes. One reason for this difference might be that the surface properties of the stainless steel plate undergo some changes, which could affect the value of emissivity during the fire exposure. Globally, temperatures calculated for the carbon steel profile are quite close to the measured values.

Finally, assuming the thermal parameters recommended in EN 1993-1-2 for stainless steel, the temperature rises predicted for the hollow steel sections are in good agreement with the measured ones. Globally, all calculated temperatures remain overall on the side safe.

The many temperature rises recorded during the test allow introducing temperature fields with enough accuracy in the mechanical simulations. So, calculated as well as experimental temperature fields have been systematically used to check the mechanical analyses conducted with SISMEF. As example, axial displacement calculated at the top of the reinforced column n°7 is shown in Figure 4. These displacements are compared with the test values. Same comparison is also given in for beam n°1.

From this figure, it can be noted that there is a reasonably good agreement between measured and calculated displacements. The numerical model SISMEF predicts the deformation behaviour of the tested composite columns at a satisfactory level of accuracy. During the early stages of the fire exposure, axial displacement of column increases rapidly due to the quick heating of the external unprotected hollow steel section. As the steel column expands more rapidly than the concrete core, it carries all the applied load. With temperature increase high enough, the load becomes critical due to the decrease of steel strength at elevated temperatures. Then the steel (as well as the column) suddenly contracts with eventual local buckling. At this time the concrete core is loaded almost suddenly and then supports progressively more and more the load with temperature rises. The concrete core, due to lower thermal conductivity and higher heat capacity of concrete, loses its strength more slowly than steel. It provides the fire resistance of the column at these later stages of fire exposure. If the concrete core is reinforced, the composite column can remain stable and the axial displacement decrease more slowly. The strength of the concrete also decreases with time and ultimately, when the concrete core can no longer support the load, failure occurs by buckling.

It can be seen that there is also a good correlation between the predicted and the measured displacements of beam, with some differences at the end of test. Displacement increases approximately linearly during the first stage of test and increase very rapidly just before failure occurs by flexural.

| a) Composite column n°7 | b) Floor-beam n°1 |
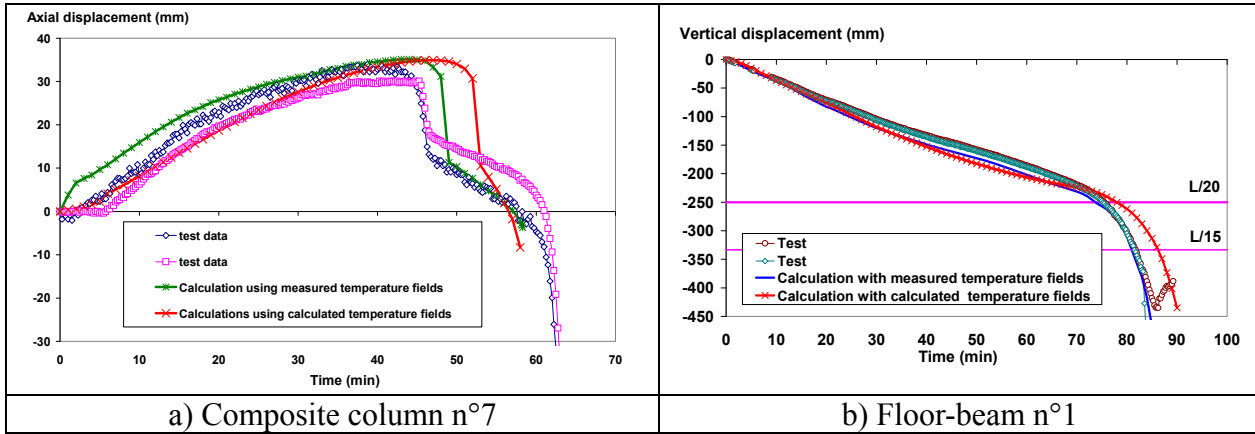
Figure 4. Comparison between Test and Calculation

3.3   Synthesis of Results

All calculated failure times of the composite members are reported in the Figure 5. They are quite close to the experimental failure times. Globally, the comparison between failure times ascertained either numerically or experimentally shows a divergence less than 10%, what is reasonable considering uncertainties inherent to tests data, such as the uniformly heated length of members, the degree of rotational restraint at the ends, unintentional eccentricity of load and the initial out-of straightness.
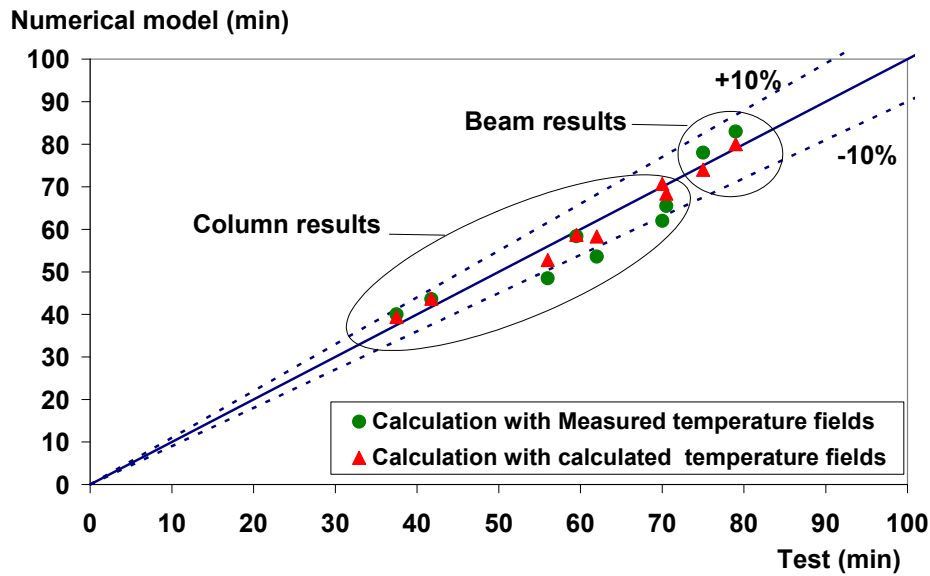
Figure 5. Comparison of Fire Resistances between Numerical Model and Test

4.   DEVELOPEMENT OF DESIGN GUIDANCE

Parametric studies with the purpose of developing simple calculation models providing a practical rule for daily design have been performed with FEM model SISMEF by varying sensitive parameters susceptible of affecting the fire resistance of composite members under standard fire conditions, such as cross section size, load conditions, eccentricity of loading, buckling length, etc.

4.1   Main Features of Proposed Simple Calculation Method for Composite Columns

The simplified design method follows the general flow chart specified in 4.3.5.1.1 of EN 1994-1-2 to check other types of composite columns but includes some specific characteristics which are presented hereafter.

4.1.1   Determination of the axial buckling load in fire situation

For a given temperature distribution within the cross-section, the load bearing capacity of a composite column, $N_{fi,Rd}$, can be determined from an appropriate buckling column curve which relates the load capacity, $N_{fi,Rd}$, to the plastic load, $N_{fi,pl,Rd}$, and the elastic critical load, $N_{fi,cr}$, as follows:

$$N_{fi,Rd} = \chi(\overline{\lambda}_{\theta})N_{fi,pl,Rd} \tag{1}$$

where χ is the reduction factor for flexural buckling depending on the relative slenderness $\overline{\lambda}_{\theta}$.

The reduction factor for flexural buckling is expressed by the following relationships (familiar in steel construction):

$$\chi\left(\overline{\lambda}_{\theta}\right) = \frac{1}{\varphi + \sqrt{\varphi^2 - \overline{\lambda}_{\theta}^2}} \tag{2}$$

with $\varphi = \frac{1}{2}\left(1 + \alpha\ (\overline{\lambda}_{\theta} - \overline{\lambda}_0) + \overline{\lambda}_{\theta}^2\right)$ and α=0.76 and $\overline{\lambda}_0 = 0.2$ (buckling curve "d")

The design value of the plastic resistance to axial compression in the fire situation is given by:

$$N_{fi,pl,Rd} = \sum_{j}(A_{a,j}.f_{ay,\theta_j})/\gamma_{M,fi,a} + \varphi_{c,\theta}\left(\sum_{k}(A_{s,k}f_{sy,\theta_k})/\gamma_{M,fi,s} + \sum_{m}(A_{c,m}f_{c,\theta_m})/\gamma_{M,fi,c}\right) \tag{3}$$

where:

- A_i is the area of the element "i" of the cross-section.
- $f_{ay,\theta,}$ $f_{sy,\theta}$ and $f_{c,\theta}$ are the characteristic strengths at elevated temperature of the steel of hollow section, the steel of reinforcing bars and the concrete respectively. For hollow section, the 0.2 % proof characteristic strength of stainless steel is used.
- $\varphi_{c,\theta}$ is a reduction coefficient taking into account the differential effects of thermal stresses.

     It's the same coefficient as that used for the calculation of the effective flexural stiffness.

The relative slenderness of the column in fire situation is given by:

$$\overline{\lambda}_\theta = \sqrt{N_{fi,pl,R} / N_{fi,cr}} \qquad (4)$$

where $N_{fi,pl,R}$ is the value of $N_{fi,pl,Rd}$ according to (3) when the partial security factors $\gamma_{M,fi,a}$, $\gamma_{M,fi,s}$ and $\gamma_{M,fi,c}$ of the materials are taken as 1.0.

$N_{fi,cr}$ is the Euler elastic critical load effective flexural stiffness in fire situation:

$$N_{fi,cr} = \pi? \, EI)_{fi,eff} / l_\theta{}^2 \qquad (5)$$

where l_θ is the buckling length of the column in fire situation.

The effective flexural stiffness of the cross-section, $(EI)_{fi,eff}$, is calculated as follows:

$$(EI)_{fi,eff} = \varphi_{a,\theta} \sum_j (E_{a,\theta_j} . I_{a,j}) + \varphi_{c,\theta} \left(\sum_m (E_{c,\theta_m} . I_{c,m}) + \sum_k (E_{s,\theta_k} . I_{s,k}) \right) \qquad (6)$$

where:

- $E_{i,\theta}$ is the characteristic modulus of material "i" at the temperature θ. For steel, it's the modulus of elasticity. For concrete, $E_{c,\theta} = 1.5 \times E_{c,sec,\theta}$ where $E_{c,sec,\theta}$ is the characteristic value for the secant modulus of concrete given by $f_{c,\theta}$ divided by $\varepsilon_{cu,\theta}$.
- I_i is the second moment of area of material "i" of the composite cross-section.
- $\varphi_{a,\theta}$ (for steel wall) and $\varphi_{c,\theta}$ (for concrete core including reinforcements) are reduction coefficients due to the differential effects of thermal stresses. Values resulting from numerical calibration appear rather different from those attributed to other types of composite cross-section.

In the present method, reduction coefficient $\varphi_{a,\theta}$ depends on the fire rating only. Coefficient $\varphi_{c,\theta}$ is defined by means of six parameters depending on the cross-section size (external size (b) and thickness (e) of the hollow steel section), the column buckling length , the ratio of reinforcement As/(As+Ac) and the fire rating. The coefficient $\varphi_{c,\theta}$ is ranging from 1 to 0 to take account of the specific behaviour of composite column with stainless steel hollow section. When the coefficient $\varphi_{c,\theta}$ is taken as the unity, the column works as a composite element with significant interaction between steel and concrete. When $\varphi_{c,\theta}$ is taken as zero, the fire resistance of the column is provided by the hollow steel section only. In fact, numerical simulations have shown the non-reinforced columns or columns with low additional ratio of reinforcement behave as simple steel columns when the column slenderness is too important.

More detailed developments on the above topic can be found in [9].

4.1.2 *Determination of the axial buckling under an eccentric load*

For a load eccentricity δ, the design buckling resistance $N_{fi,Rd,\delta}$ is obtained from:

$$N_{fi,Rd,\delta} = \phi\, N_{fi,Rd} \qquad\qquad (7)$$

Where ϕ is a correction factor depending on the relative eccentricity $\bar{\delta} = \delta/b$ and $N_{fi,Rd}$ is the design axial buckling resistance obtained from (1) but using appropriate values of the reduction coefficient $\varphi_{c,\theta}$ (corresponding to the case of eccentric load) to calculate the effective flexural stiffness of the cross-section $(EI)_{fi,eff}$ and the plastic resistance to axial compression $N_{fi,pl,Rd}$.

4.1.3 *Comparison between the proposed design method and the numerical results*

An exhaustive comparison between the proposed simplified design method and the numerical model cannot be carried out here. However, to show the quite acceptable accuracy of the simplified design method, some comparisons are shown in Figure 6. In this figure, the marks of ratio $N_{fi,Rd}$ / $N_{fi,pl,Rd}$ are arranged as a function of the relative slenderness calculated at elevated temperature in accordance with (4), $N_{fi,Rd}$ is the correct buckling load given by the advanced numerical model and $N_{fi,pl,Rd}$ is the value of the plastic resistance according to (3).
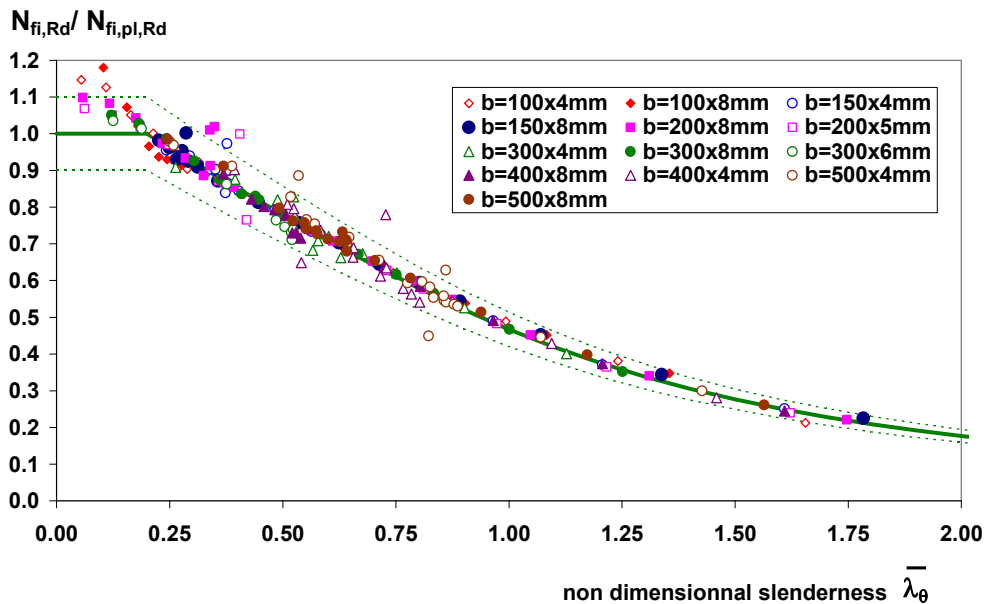
Figure 6. Comparison between Numerical Results and Simplified Method for
Axially Loaded Non-Reinforced Columns and Fire Rating R30

It can be noted that the proposed design method is in general on the safe side when comparing to the numerical results, except in the case of columns with intermediate buckling lengths where some points are slightly on the unsafe side (but less than 15%). Globally, the difference between the simplified method and the numerical model does not exceed 10% on the unsafe side, which is fully acceptable.

4.2 **Floor Beams with Concrete Fire Protection**

The proposed design method is based on the simple plastic moment theory. It allows to assess the fire resistance of a beam by calculating its moment capacity using the temperature distribution at the required fire resistance time and the corresponding reduced material strength.

The following simplifying assumptions have been made:

- The concrete does not contribute to the load bearing capacity at elevated temperatures and thus may be ignored.
- Failure of beams occurs when maximum mechanical strain exceeds 2% on the exposed stainless steel plate.

4.2.1 Main features of proposed simple calculation method

The design moment resistance $M_{fi,t,Rd}$ of floor-beams can be determined from:

$$M_{fi,t,Rd} = \sum_{i=1}^{n} A_i z_i f_{y,\theta,i} / \gamma_{M,fi}$$

(8)

where z_i is the distance from the plastic neutral axis to the centroid of the elemental area A_i.

For the calculation of the design value of the moment resistance, the cross-section of the beam is divided into various components: the stainless steel plate, the lower flange of the carbon steel profile (when used); the web of the steel profile (divided in two parts) and the upper flange of the carbon steel profile. For each of these parts, simple rules have been developed which define temperatures and corresponding reduced characteristic strength in function of the standard fire resistance R30, R60, R90 or R120 (see Figure 7 and Table 5).
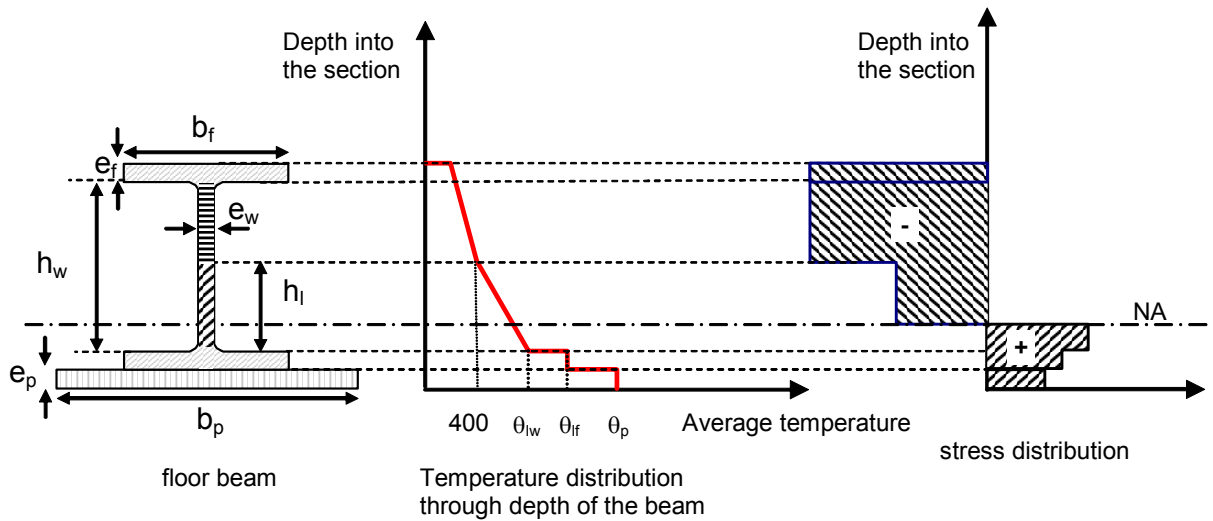
Figure 7. Temperature and Stress Distributions Along the Depth of Floor Beam

The height h_l of the lower part of the web is calculated to:

$$h_l = -\sqrt{\frac{2\alpha t}{\beta}} \ln\left(\frac{380}{\theta_{lw} - 20}\right)$$

(9)

Where:
- t is the time (s)
- $\beta = 12.25$
- $\alpha = \rho_a / \rho_a C_a$ ($\lambda_a = 45$ W/mK, $C_a = 600$ J/KgK, $\rho_a = 7850$ Kg/m^3)
- $\theta_{lw} = \kappa_3 \, \theta_s$ is the mean temperature at the bottom edge of the web, θ_s is the temperature of the stainless steel plate and κ_3 is a reduction factor given Table 6.

Table 5. Values of Parameter θ_o, a and b

Part i of the beam	Area A_i	Temperature θ_i*	Characteristic strength $f_{y,\theta i}$
Stainless steel plate	Full area $A_p = e_p \times b_p$	Uniform temperature distribution For IF-beam: $\theta_p = \theta_o - \kappa_1 \times e_p$ For SF-beam: $\theta_p = \theta_o - \kappa_1 \times (e_p + e_f)$	$k_{2,\theta p} \times f_{sy,20}$
Lower flange	Full area $A_{lf} = e_f \times b_f$	Uniform temperature distribution $\theta_{lf} = \kappa_2 \times \theta_p$	$k_{y,\theta lf} \times f_{ay,20°C}$
Lower part of the web	$A_{wl} = e_w \times h_l$	Changes linearly from θ_{lw} to 20°C	$f_{ay,20°C} \times (1 + k_{y,\theta lw})/2$
Upper part of the web	$A_{ul} = e_w \times (h_w - h_l)$	Lower than 400°C	$f_{ya,20°C}$
Upper flange	Full area $A_{uf} = e_f \times b_f$	Lower than 400°C	$f_{ya,20°C}$

* θ_o, κ_1 and κ_2 are empirical coefficients depending of fire rating only

Table 6. Values of Parameter θ_o, κ_1, κ_2 and κ_3

Fire rating	θ_o		κ_1		κ_2	κ_3	
	IF beam	SF-beam	IF beam	SF-beam		IF beam	SF-beam
30	570	500	7	3	0.75	-	-
60	830	775	6	3	0.85	0.77	0.76
90	920	930	3	3	0.90	0.83	0.81
120	980	1025	2	3	0.95	0.87	0.84

4.2.2   *Comparison between the proposed design method and the numerical results*

A comparison was made between advanced numerical model and simple design model described above for investigating the precision and the validity of the latter. Five beam cross-sections, namely ½ HEA450-500×15, ½ HEB200-500×15, ½ HEB280-500×20; HEB300-360×15 and HEB600-480×20, and three fire ratings, from 60 to 120 minutes, were taken in the comparison. Steel grade of carbon steel profile is S235. Stainless steel grade is EN1.4404 with a 0.2% proof strength $f_{0.2p} = 240$ Mpa and an ultimate strength, $f_u = 2.04 \times f_{0.2p}$.

For each cross-section, design moment resistances given by the simple design model (M_{SM}) have been divided by the corresponding moment resistances (M_{NM}) obtained from FE-analysis (see Figure 8). It is clear that the proposed design method gives good agreement with the numerical model.
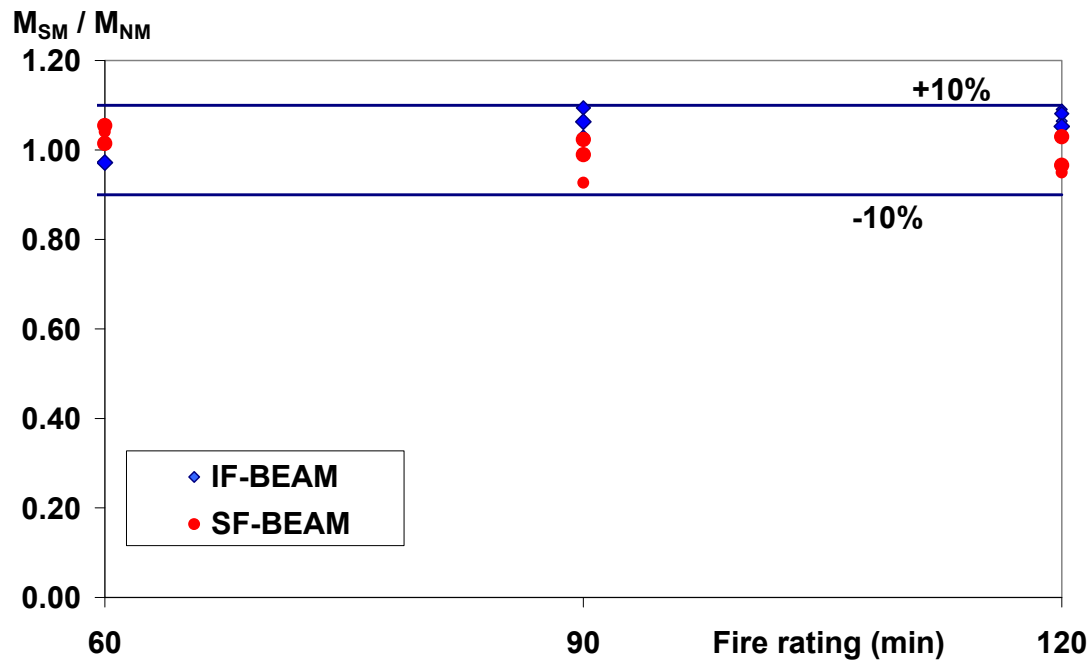
Figure 8. Comparison of the Proposed Design Method with Numerical Model

4.   CONCLUSION

In order to investigate the fire behaviour of steel and concrete composite members with austenitic stainless steel, a series of fire tests are conducted within the scope of a European project. The corresponding experimental results are presented in detail in this paper. In parallel, using the advanced finite element model SISMEF, the fire performances of several composite members with stainless austenitic steel have been evaluated and compared with fire test results. These comparisons have shown that the model is capable of predicting the behaviour of composite columns and partially protected Slim-floor beams (failure time, displacements,…) with a good accuracy.

Then, the fire behaviour of previous composite members has been investigated with a wide range of parametric simulations. Referring to this base of numerical results, simple design methods consistent with the general flow chart used in EN 1994-1-2 to check the other types of composites members but including some specific characteristics have been proposed. It has been shown through the comparison with numerical results that the simple design methods are capable of predicting with a quite good accuracy the fire resistance of composite columns with hollow stainless steel section and partially protected slim-floor beams.

REFERENCES

[1]   Renaud, C., "Modélisation Numérique, Expérimentation et Dimensionnement Pratique des Poteaux Mixtes Avec Profil Creux Exposés à l'incendie", Thèse de Docteur en génie Civil, INSA de Rennes, France, 2003.
[2]   Renaud, C., Aribert, J.M. and Zhao, B., "Advanced Numerical Model for the Fire Resistance of Composite Columns with Hollow Steel Section", Journal of Steel and Composite Structures, 2003, Vol. 3, No. 2, pp. 75-95.

[3]   Zhao, B. and Aribert, J.M., "Finite Element Method for Steel-Concrete Composite Frames Taking Account of Slip and Large Displacements", European Journal of Finite Element, 1996, Vol. 5, No. 2, pp. 221-249.

[4]   Zhao, B., "Modélisation Numérique des Poutres et Portiques Mixtes Acier-béton Avec Glissements et Grands Déplacements", Thèse de docteur en Génie Civil, INSA de RENNES, Franc, 1994.

[5]   prEN 1994-1-2, Eurocode 4, "Design of Composite Steel and Concrete Structures: Structural Fire Design", CEN, 2004.

[6]   EN 1993-1-2, Eurocode 3: "Design of Steel Structures – Part 1.2: General Rules – Structural Fire Design", CEN, 2005.

[7]   EN 1991-1-2 - Eurocode 1 "Actions on Structures" – Part 1-2: General Actions – Action on Structures Exposed to Fire, CEN, 2005.

[8]   ANSYS, "ANSYS User's Manual for Revision 8.0 – Volume IV – Theory", Swanson Analysis SYSTEM, INC., Houston USA, 1992.

[9]   CTICM, Stainless Steel in Fire (SSIF), Research Contract: RFS-CR-04048; WP2: Composite Members in Fire, Final Report SRI – 07/110 - CR/PB, August 2007.

THE BEHAVIOUR OF SINGLE-STOREY INDUSTRIAL STEEL FRAMES IN FIRE

Yuanyuan Song[1,*], Zhaohui Huang[1], Ian W. Burgess[1] and Roger J. Plank[2]

[1] *Department of Civil and Structural Engineering, The University of Sheffield, Sheffield S1 3JD, UK*
[2] *School of Architectural Studies, The University of Sheffield, Sheffield S10 2TN, UK,*
*(Corresponding author: E-mail: yysongshef@googlemail.com)

ABSTRACT: A new dynamic model and a quasi-static solution procedure has been developed and incorporated into the finite element software Vulcan [1-3]. This new numerical model is tested in this paper on benchmark problems which relate to the behaviour of steel portal frames under fire conditions. The capabilities and the accuracy of this numerical model have been validated against other advanced finite element software (ABAQUS [4], ANSYS [5] and SAFIR [6]). A case study on the behaviour of steel portal frames under fire conditions has been carried out using this new tool. The effects of different rotational stiffnesses at the column bases are compared for two different heating profiles. A second failure mechanism, based on large deformation rather than the initial configuration of the steel portal frames, is observed after an initial instability of the roof frame has re-stabilised in an inverted configuration at high temperatures.

Keywords: Dynamic analysis, temporary failure, snap-through, steel portal frames

1.   INTRODUCTION

The pitched-roof portal frame is a typical single-storey steel structure widely used for industrial applications in the United Kingdom and elsewhere. For Ultimate Limit State design at ambient temperature, such frames are usually designed assuming that column base connections act as frictionless hinges [7]. In fire conditions it is imperative that building walls adjacent to the boundary of a site stay close to vertical and are not liable to collapse, so that fire is not allowed to spread to adjacent property [8]. A current UK fire design guide [9] allows the rafters, which are normally unprotected against fire, to collapse. To ensure the lateral stability of boundary walls, column base connections and foundations have to be designed to resist the forces and moments generated by this collapse of the rafters. However, the method makes a number of apparently arbitrary assumptions, and does not attempt to model the true behaviour of the frame during fire. Therefore the method can lead to very uneconomical, and even potentially unsafe, design of portal frames [10].

A fundamental aspect of the collapse of portal frame rafters under fire conditions is that they often lose stability in a "snap-through" mechanism. This is capable of re-stabilising at high deflections, when the roof has inverted but the columns remain close to vertical. By most static analysis methods only the initial loss of stability is identifiable. In the modelling of a small-scale test [11] on a single-storey single-bay portal frame, all the static analysis stopped at the point at which the snap-though occurred. The maximum vertical displacement of the apex in these numerical analyses was about 17% of the roof rise, while the deflection of the apex almost reached eaves level in the actual fire test. It was therefore impossible to identify the final Equilibrium state or the intermediate column movements.

Schematically, the true snap-through behaviour should follow the solid curve in Figure 1 when nonlinearity is considered. However, in load-controlled numerical analysis this behaviour can not be traced beyond the initial limit-point because the Equilibrium loses stability and the solution becomes divergent. Instead of tracing the static Equilibrium deformation curve, the dynamic

motion of the frame can be used to allow the analysis to find the second stable state C, if it exists, as shown by the dashed curve in Figure 1. Damping is used to ensure that the analysis can return to a stable Equilibrium curve, by reducing the amplitude of oscillation about this stable path until it is sufficiently small to justify assuming that the structure has regained stability. The main objective of using a dynamic model in this analysis is to allow global structural behaviour to be tracked after a transient loss of stability, or a partial failure, occurs.
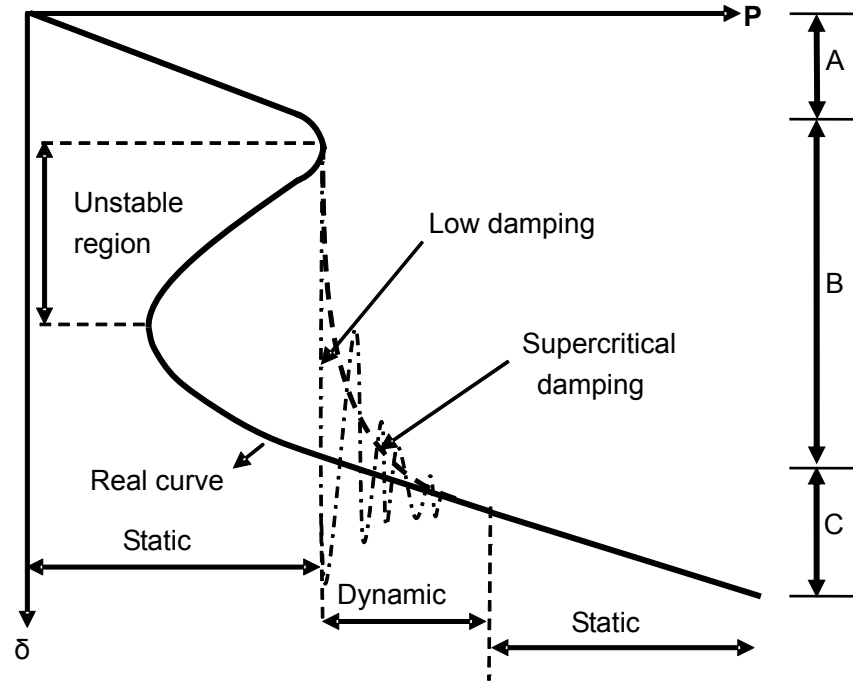
Figure 1. Effect of Damping in Snap-through Process

In this research a simplified dynamic solution procedure [12] has been developed, in which both damping and inertial effects have been added to the static stiffness formulation, and an effective stiffness matrix, which always has positive diagonal values, is generated. The procedure can deal with the instabilities which cause singularity in previous static analyses, and the re-stabilisation after temporary snap-through instability of portal frames at elevated temperatures can be investigated properly. Vibration introduced by the dynamic behaviour can be damped out rapidly by super-critical damping, of which the value can be determined from the lowest natural frequency of the structure (see Figure 1). The exact nature of the dynamic motion during Period B is not very important for this study. The limit point at the end of period A and the behaviour beyond period B are the main considerations in this research, as statically stable regions. It is the ability of the dynamic system to mimic the real structure in moving across the region of temporary instability without encountering numerical singularity that is important.

2.   DYNAMIC MODEL

In the static model, the internal forces balance the external forces to achieve Equilibrium, so the governing Equilibrium Equation is:

$$\mathbf{F}^{Int}(t) = \mathbf{F}^{Ext}(t) \tag{1}$$

where, $\mathbf{F}^{Int}(t)$ is the internal nodal force vector, and $\mathbf{F}^{Ext}(t)$ is the external nodal force vector. This nonlinear Equation is solved iteratively using the Newton-Raphson solution method. The iterations are based on Eqns. (2) and (3):

$$\overline{\mathbf{g}}_{t+\Delta t} = \mathbf{F}^{Int}(t+\Delta t) - \mathbf{F}^{Ext}(t+\Delta t) \qquad (2)$$

$$\overline{\mathbf{g}}_{t+\Delta t,n+1} = \overline{\mathbf{g}}_{t+\Delta t,n} + \frac{\partial \overline{\mathbf{g}}}{\partial \mathbf{U}} \delta \mathbf{U}_{n+1} = 0 \qquad (3)$$

where $\overline{g}_{t+\Delta t,n}$ is the unbalanced force at time-step $t+\Delta t$ and the nth iteration. If a snap-through is encountered in an analysis, some negative or null values will appear on the leading diagonal of the stiffness matrix, which leads to divergence of the analysis. In fact, the snap-through initiates dynamic behaviour which may be bounded by two stable equilibrium states. When the snap-through finishes, the whole structure may return to stable static equilibrium, provided that it is loaded at a slow rate.

In this research the Newmark integration scheme for nonlinear dynamic problems [13, 14] is adopted, due to its significant advantage in numerical computational efficiency. Because the behaviour of portal frames within Stage B (see Figure1) is quasi-static, it is not necessary to carry out a full dynamic solution procedure, which needs more computing time but finds the same results in regions of stable static equilibrium. A quasi-static solution procedure is therefore carried out to find out the steady-state behaviour of the structure. The dynamic model is activated only when singular values are detected on the leading diagonal of the stiffness matrix, and the static model can resumes the analysis when a new steady-state is found in the dynamic modelling.

For dynamic analysis, both inertial and damping terms are added to the left-hand side of Eq. 1:

$$\mathbf{F}^{I}(t) + \mathbf{F}^{D}(t) + \mathbf{F}^{Int}(t) = \mathbf{F}^{Ext}(t) \qquad (4)$$

The dynamic unbalanced force at step $t+\Delta t$ is then given by:

$$\overline{\mathbf{g}}_{t+\Delta t} = \mathbf{F}^{Int}(t+\Delta t) - \mathbf{F}^{Ext}(t+\Delta t) + \mathbf{F}^{I}(t) + \mathbf{F}^{D}(t) \qquad (5)$$

where $\mathbf{F}^{I}(t)$ is the inertial force and $\mathbf{F}^{D}(t)$ is the damping force. When negative values appear on the leading diagonal of the stiffness matrix, the damping and inertial forces are added, to generate an effective stiffness matrix which always has positive diagonal values. This is very helpful to the Newton-Raphson solver which can still solve for the incremental displacements when partial failure of the structure happens.

To restrain the vibration of the structure about equilibrium states in fire a high damping, in excess of the system's critical damping, is required, so numerical damping, which only gives convergence at relatively small values, is not ideal for this model. Because the exact path of the motion is not very important in this case, the mass and damping are assumed to be lumped at the nodes, and the critical damping, relative to the lowest natural frequency and mass, is adopted in the model. The procedure discussed here has been incorporated into Vulcan [1-3] for modelling of steel structures in fire.

3.   VALIDATION

3.1   Pitched Portal Frame

To test the capability of the dynamic model in dealing with geometrically nonlinear problems, a simplified pitched frame (Figure 2) with an increasing point load was tested by the dynamic model in Vulcan and the results compared with the commercial software ABAQUS [4]. Purely elastic material properties were assumed in this case, in order that the geometrical nonlinearity of the roof frame could be presented and the whole snap-through behaviour of the roof frame could be traced.
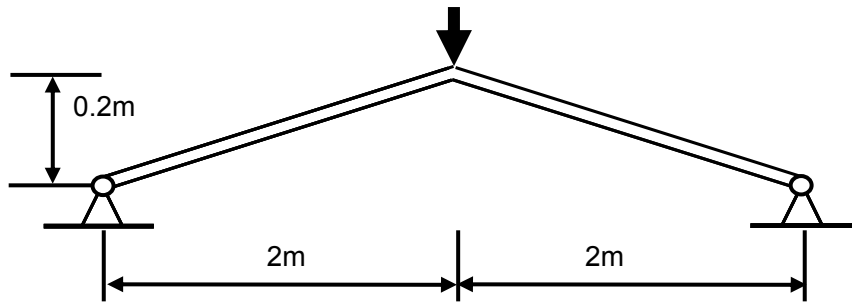
Figure 2. Initial Configuration of the Pitched Roof Frame

For this ideal symmetrical case, a bifurcation is encountered under completely symmetric loading. This causes a problem, even for dynamic analysis, in breaking the inherent symmetry, and the motion must be given the facility to move in an asymmetric fashion by introducing a small imperfection, which in this case is a very small additional load on one rafter. Beyond the limit-point the frame collapses dynamically until it reaches its almost-inverted position.

Because only two Gauss points control integration on each beam element, the accuracy of the result may relies on the element mesh density.   According to the parametric study those results are shown in Figure 3 it is found that, after the deflection jump, the load-deflection curves of models with different element mesh density always tend towards the same stable static curve, on which the stiffness of the frame recovers due to the generation of tension in the members.   Four elements per member are found to be adequate for convergence of the results, and the position of the limit point corresponds very closely to that given by full dynamic results from ABAQUS [4].   It is evident that this new dynamic model is capable of capturing the new stable position after snap-through of the pitched roof frame in a load-controlled analysis.
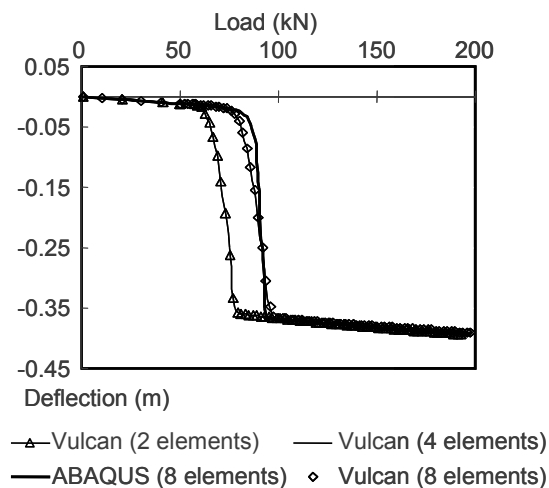
Figure 3. Vertical Displacements of the Apex

3.2   Twin-Bay Single-Storey Steel Portal Frame

A test was carried out on a twin-bay single-storey steel portal frame, as shown in Figure 4, which had been designed by Franssen and Gens [15].   This was modelled using 61 geometrically nonlinear beam-column elements [3].   The two-dimensional analyses of this model were adopted as a benchmark for several finite element programs [16], such as SAFIR [6] Dynamic, ABAQUS [4] Dynamic and ANSYS [5] Dynamic.   Both dynamic and quasi-static analyses were performed to simulate this case; Figures 5 to 11 show the comparisons.   It is evident that very good agreement was achieved between the current model (Vulcan) and the other software.   The right-hand half-frame kept almost its original shape when the left-hand locally heated part had collapsed to column-base level.   The collapsed shape of the frame is shown in Figure 12. This also attests that the current dynamic model can handle partial or local failure conditions in steel structures.

The current dynamic and Quasi-static analyses (Vulcan) give very close results for this case, but it is worth noting that the difference between the curves from these two methods reveals that, although very high damping is used, there is still some dynamic effect which remains in a transient dynamic analysis, and this may influence the results. To eliminate the dynamic effect in the analysis, quasi-static analysis is carried out in the following case studies.
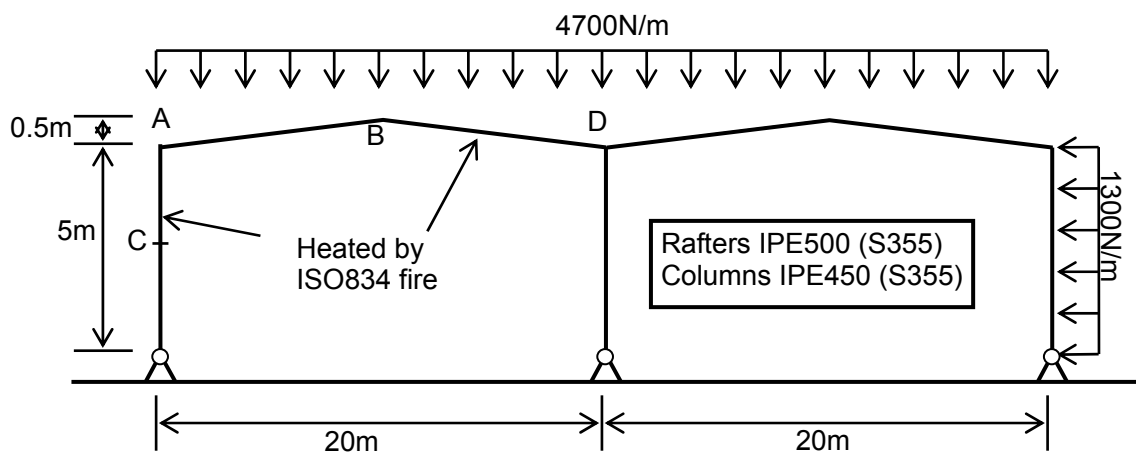
Figure 4. Initial Configuration and Loading Arrangement of Franssen's Model
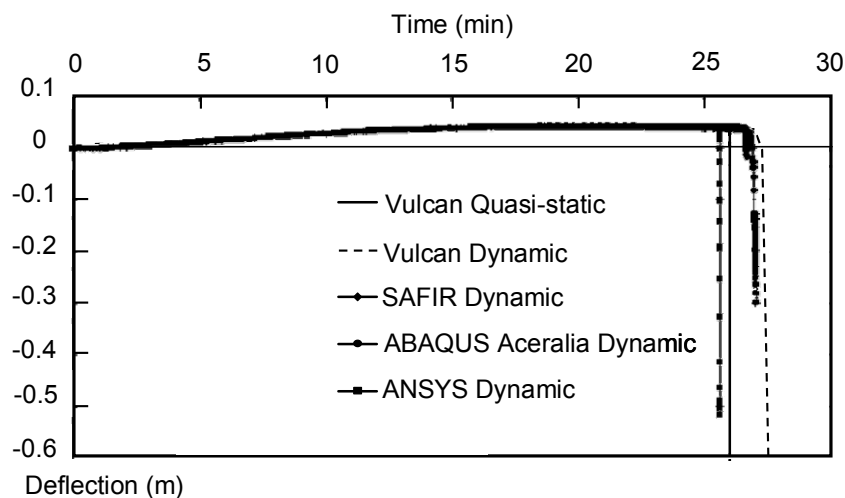
Figure 5. Vertical Displacement at Node A
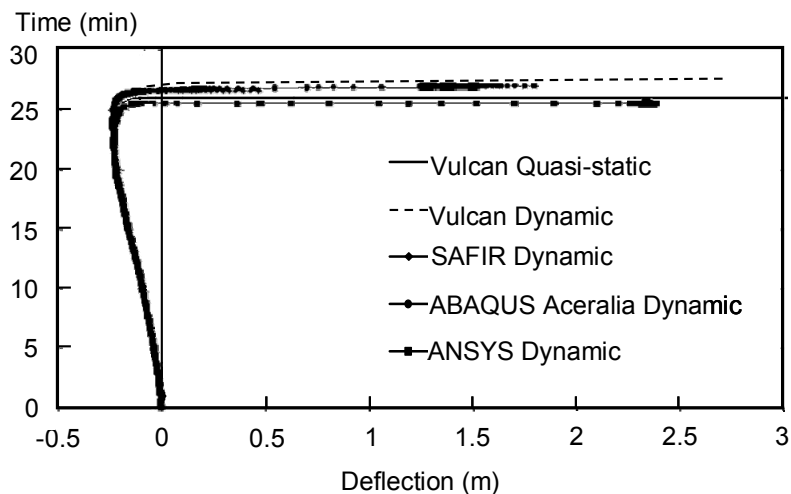
Figure 6. Horizontal Displacement at Node A
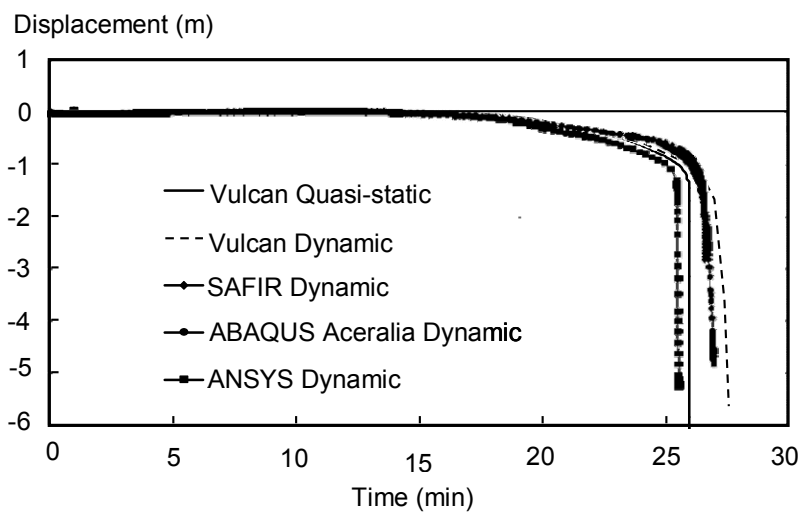
Figure 7. Vertical Displacement at Node B
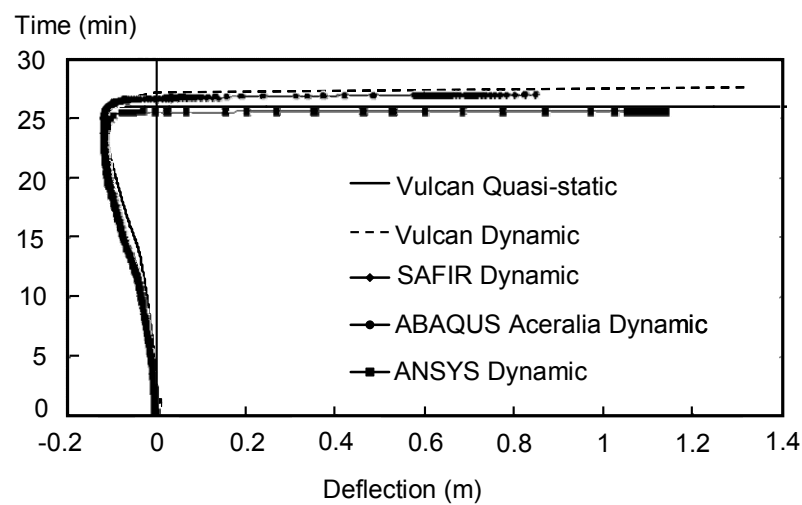
Figure 8. Horizontal Displacement at Node B
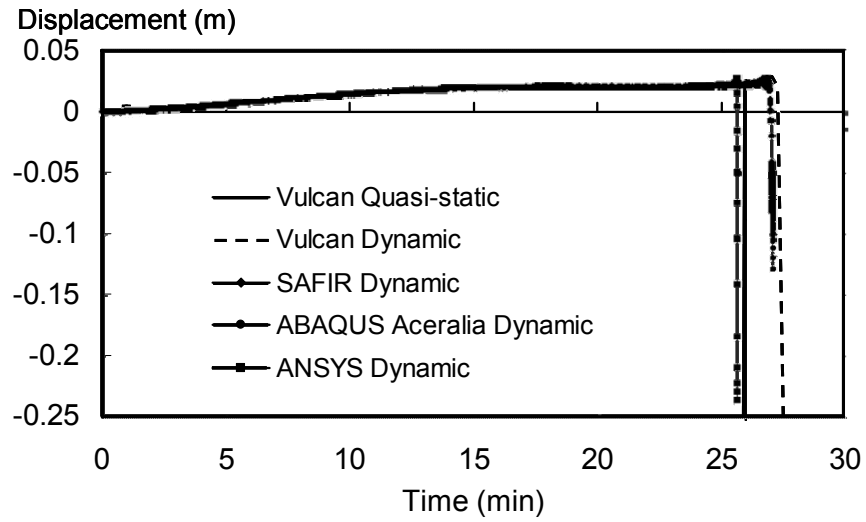
Displacement (m)

Figure 9. Vertical Displacement at Node C
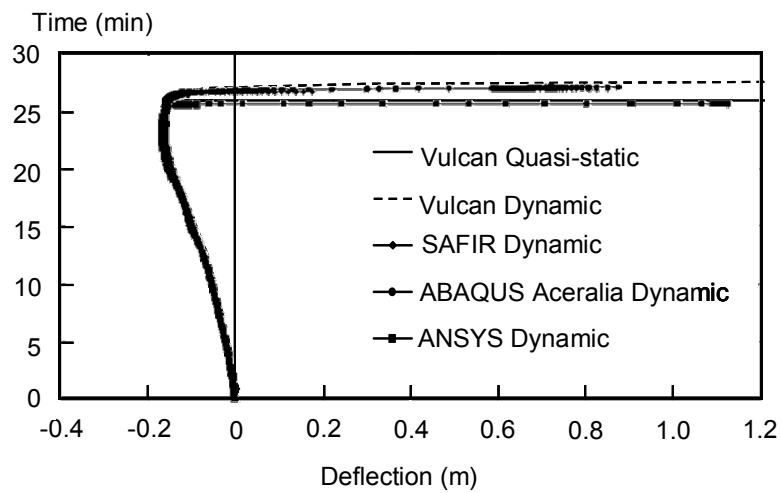
Figure 10. Horizontal Displacement at Node C
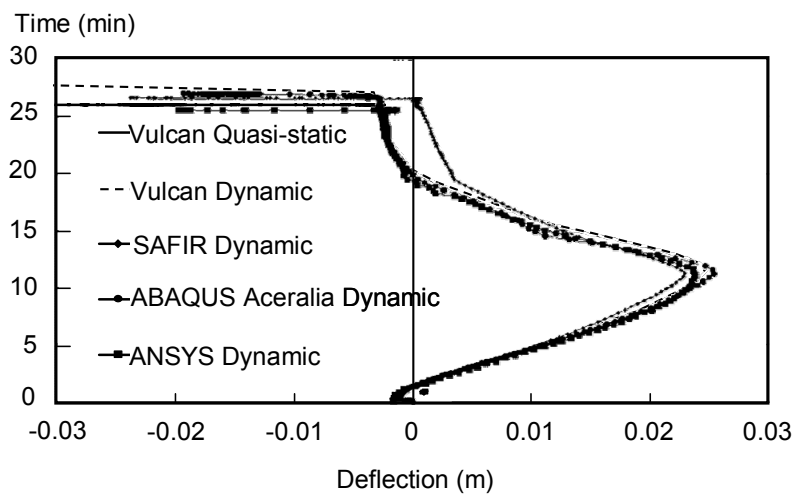
Figure 11. Horizontal Displacement at Node D
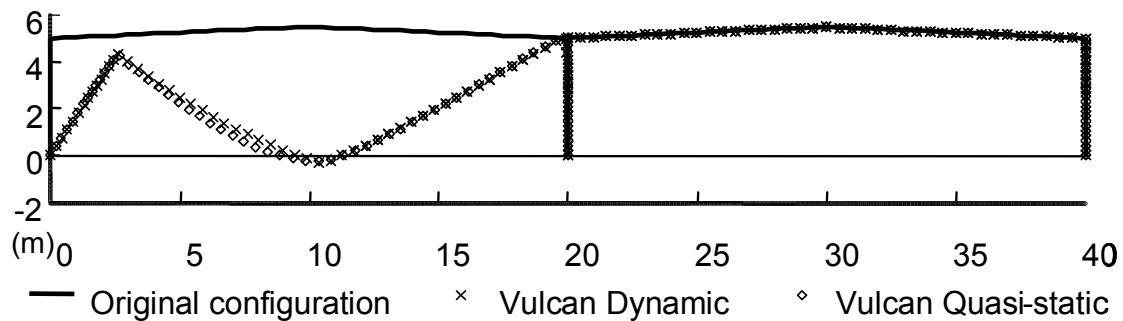
Figure 12. Deflection Shape of the Frame

4.   CASE STUDY

According to previous research conducted at the University of Sheffield [11], the static analysis in Vulcan [1-3] has shown very good accuracy in comparison with experimental fire test results up to the large deflection jump which happens at the limit-load.   This study is designed to trace the post-failure behaviour of the portal frame and to explore the failure mechanism under fire conditions.   A two-dimensional portal frame model was designed as shown in Figure 13 according to plastic theory [17]. For convenience in modelling, the whole frame was assumed to have the same member cross-section size, and was designed using plastic theory for ultimate limit state conditions at ambient temperature. The design loadings and the fire limit state partial safety factors are listed in Table 1, and these loads were applied to the frame before heating.   It was assumed that the whole frame was exposed in fire, and a uniform temperature distribution across the member sections was used.   The distance between centres of adjacent portal frames was 6m, and a horizontal imperfection force of 1.7kN was applied to the left eaves connection. The temperature of the steel used in this test was calculated by the simple Eurocode 3 Part 1.2 method [18].
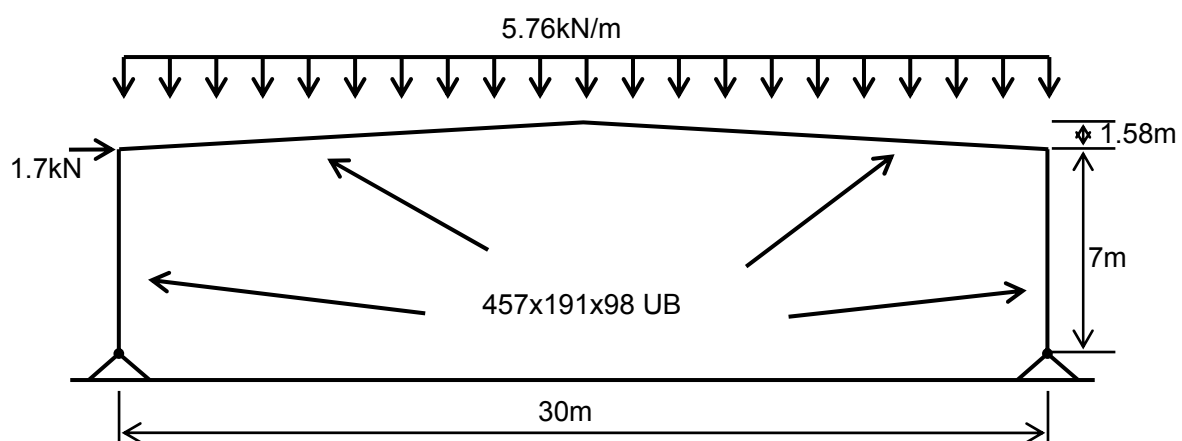
Figure 13. Numerical Model of the Pitched Portal Frame

Semi-rigid column bases were assumed, and modelled by springs with a rotational stiffness which was calculated using the rule recommended in the SCI design guidance document [19].   For a nominally rigid base the rotational stiffness is defined as $4EI_{column}/L_{column}$, and for a nominally pinned base the rotational stiffness is one tenth of this, $0.4EI_{column}/L_{column}$, where E is the Young's

modulus, I_{column} is the second moment of area of the column section and L_{column} is the length of the column. A mean value of rotational stiffness $2EI_{column}/L_{column}$, between the values for the nominally pinned and rigid bases, was defined for a nominally semi-rigid base.

Table 1. Load Combinations

Load Type	Unfactored load kN/m^2	Ambient Load factors	Fire load factors
Dead load	0.66	1.4	1.0
Imposed load	0.60	1.6	0.5

4.1 Frames Without Fire Protection

In this group of numerical tests, the frames are assumed to be uniformly heated. The vertical deflection of the apex and the horizontal deflections of the eaves are presented in Figures 14 to 16. It is clear that the failure modes are very similar, and that the difference in failure temperatures between the defined cases was not more than 2°C. The base rotational stiffness clearly does not show a significant influence on the behaviour of the portal frame for this heating profile.
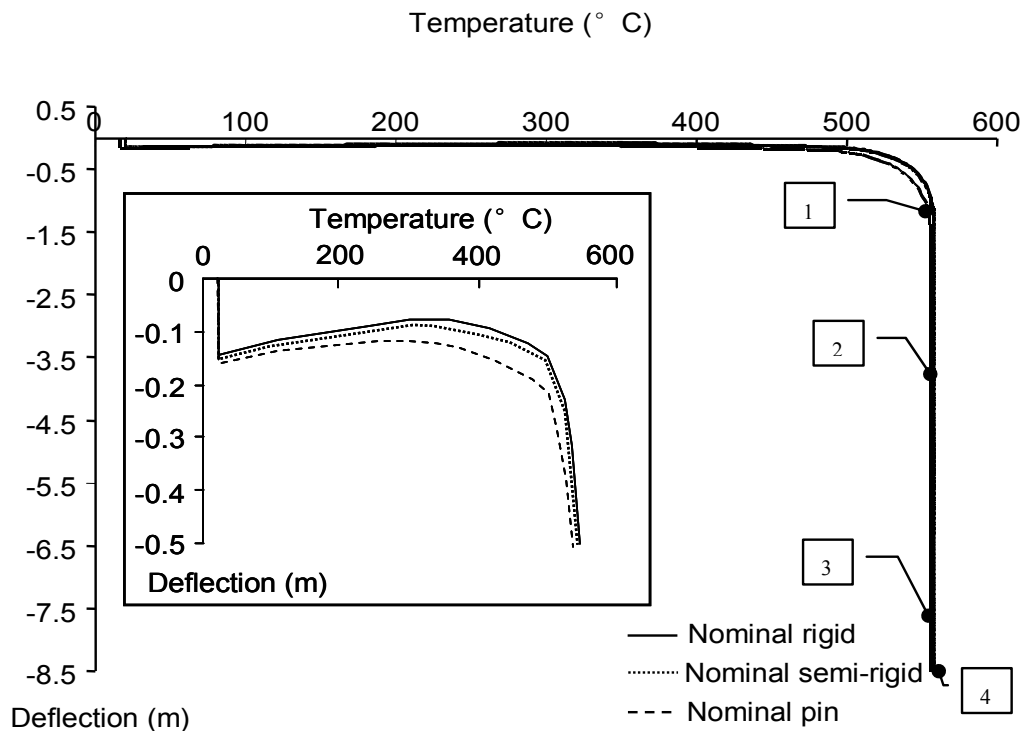
Figure 14. Vertical Displacement of Apex (Numbers are Referred to Figure 17)

Due to the thermal expansion of the steel, the apex initially deflected upward until the steel had reached about 330°C. Under the combined effect of elevated temperature and the external loading, the roof frame then began to lose stiffness and pushed the columns outward. The maximum outward deflection of the eaves was reached when the roof frame had fallen to eaves level at around 560°C (Shape 1 in Figure 17). At this moment, only the two sections adjacent to the eaves had a fully-plastic flange. Beyond this point the apex deflected below the eaves level and the

column tops were pulled inward. After a further temperature increment of about 2°C, one fire hinge had developed at each eaves, which provided considerably more flexibility.   Near to the apex, the strains in the lower part of the rafter cross-section exceeded the plastic limit when the displacement of the apex was greater than half the original height of the frame (Shape 2 in Figure 17).   The plastic region had expanded to about one fifth of the length of the rafters when the apex had deflected to base level, and because of the imperfection force at the left eaves the plastic regions had developed mainly in the left rafter.   It is worth noting that, at this stage, more than half of the cross-section at the Gauss point closest to the left-hand column base had reached its plastic strength (Shape 3 in Figure 17).   Figure 17 presents the sequence of collapse of the frame up to the point at which the apex had descended to column base level.
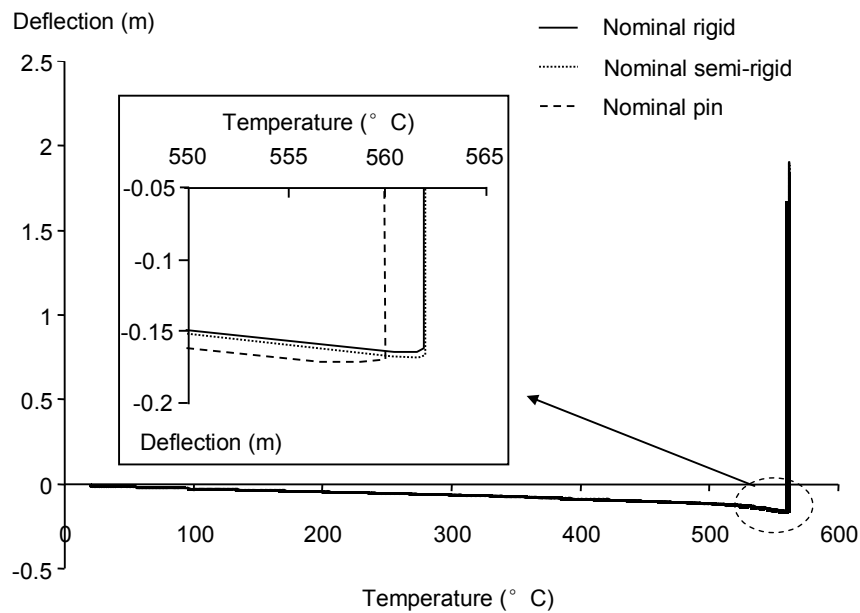
Figure 15. Horizontal Displacement of Left Eave
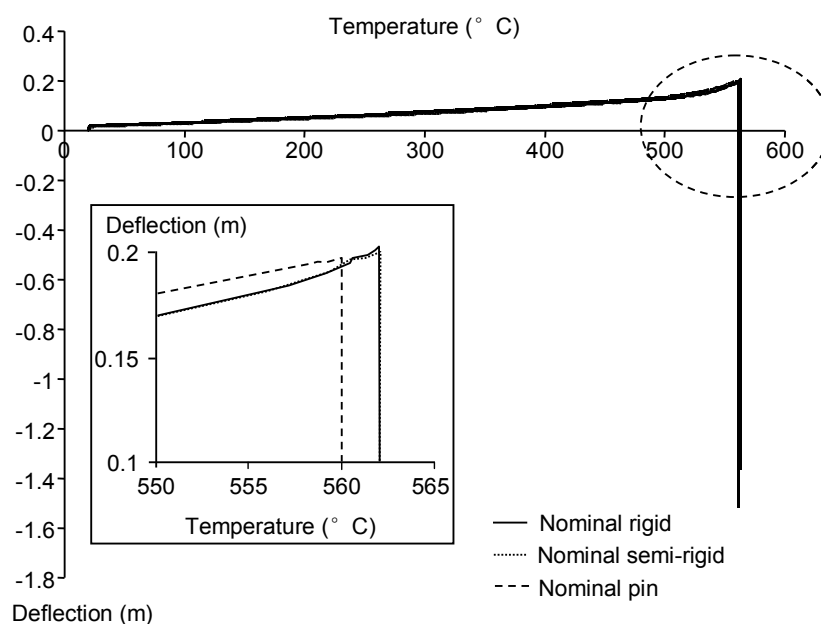
Figure 16. Horizontal Displacement of the Right Eave

The phenomenon of re-stabilisation after snap-through was not detected during these analyses because, beyond the stage at which plastic hinges were generated at the eaves, the columns were too flexible to provide enough restraint to produce any re-stabilisation.
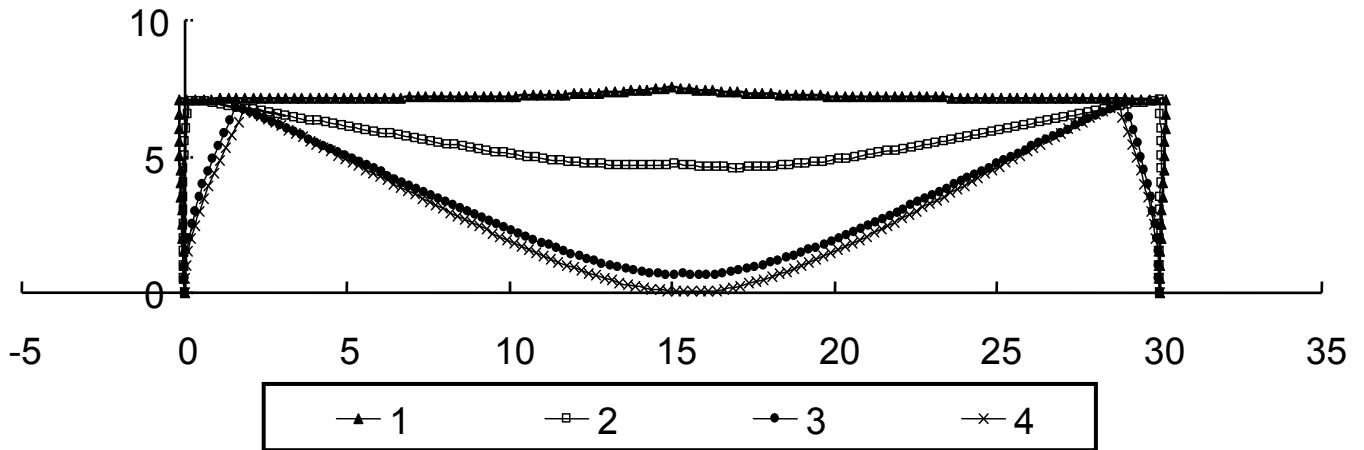
Figure 17. Failure Progress of Portal Frame with Nominally Rigid bases when only Rafters Heated

4.2   Frames with Columns Protected

The re-stabilisation after initial snap-through can be observed clearly for the cases in which the rafters are heated by the Standard Fire and the columns are protected.   According to the load-deflection curves presented in Figures 18 to 20, the rotational stiffness of the column bases shows a significant influence in restraining the frame while the rafters are collapsing.   A secondary stabilised position was found in all three models beyond the phase of rapid deflection.

Due to the expansion of the rafter, the apex initially rose, as the columns were pushed outward symmetrically.   The apex then began to descend as the eaves continued to move outward, because of the degradation of the steel at elevated temperature and the vertical load on the roof.   When one fire hinge had developed near each eaves connection, the peak load at snap-through was initiated, the roof frame lost stability and collapsed downward (Shape 1 in Figure 21), and the columns were pulled inward by the inverted rafters after the apex had fallen below the eaves level (Shape 2 in Figure 21). The frame later achieved stability once more when the rafters had almost completely inverted with the apex deflection being over twice its initial height above the eaves level (Shape 3 in Figure 21).   With increasing temperature, the redistribution of internal forces led to an increase of curvature near to the apex.   This caused the third plastic hinge to form at the apex.   The frame was statically determinate at this stage, causing a plateau to form on the load-deflection curve, which ended as the fourth plastic hinge was generated at the left base to complete the mechanism (Shape 4 in Figure 21).   Thereafter the left column was pulled inward rapidly until the apex reached column base level (Shape 5 in Figure 21).
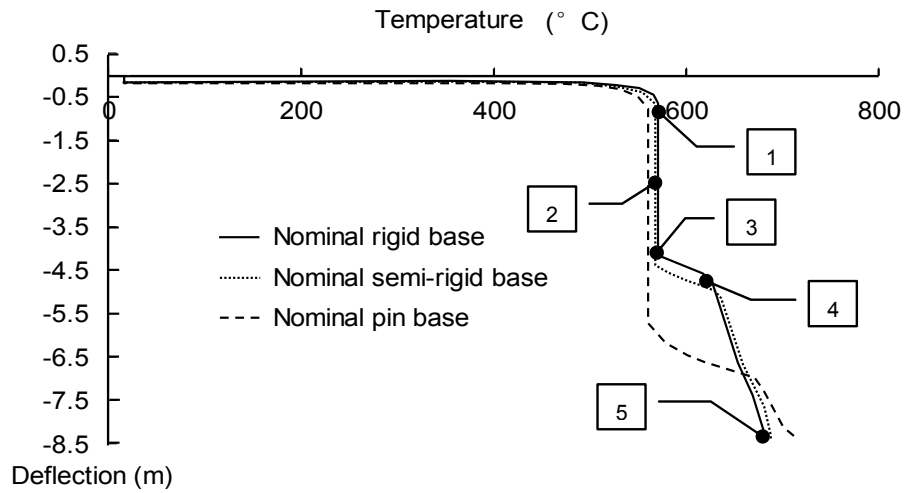
Figure 18. Vertical Deflection of the Apex (Numbers refer to Figure. 21)
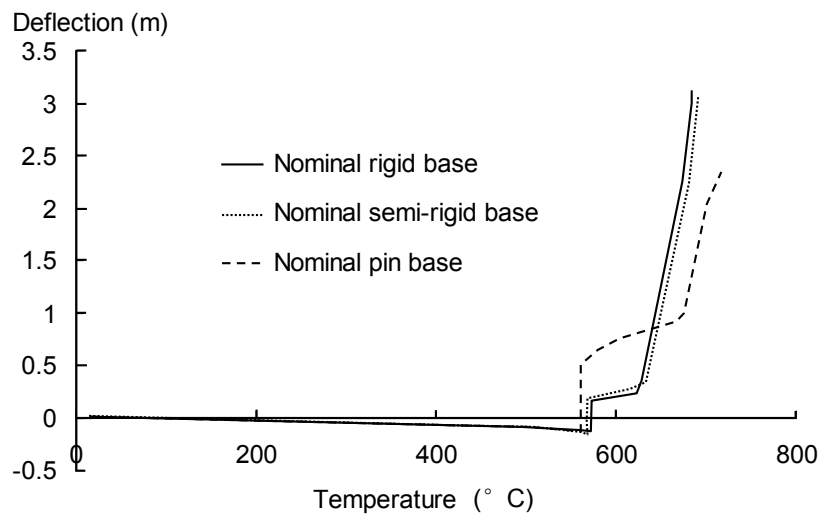
Figure 19. Horizontal Deflection of the Left Eave
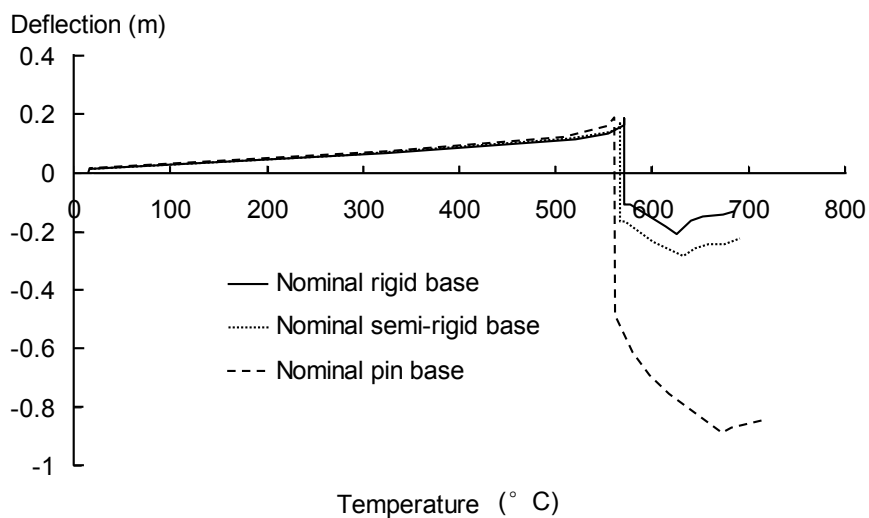
Figure 20. Horizontal Deflection of the Right Eave
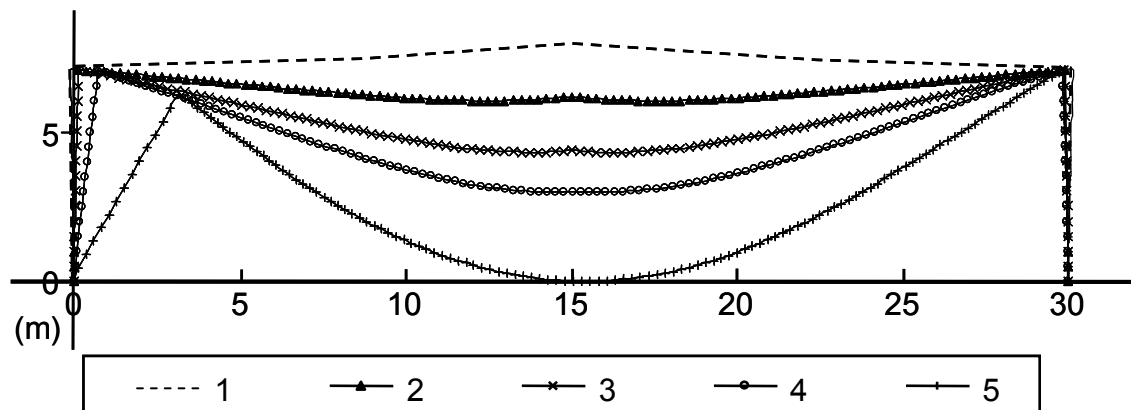
Figure 21. Failure Progress of Portal Frame with Nominally Rigid bases with only Rafters Heated

5.   CONCLUSION

The simplified dynamic model and quasi-static solution procedure developed for this study is suitable to overcome the temporary instabilities encountered in numerical analysis of structures.   It could also be used to accurately predict progressive collapse of portal frames and other steel frames in fire.

For the simplified portal frame case study presented here, the rotational stiffness of column bases had no significant effect on the failure mode of the portal frames in two heating profiles.   For the whole-frame-heated cases, when the two fire hinges formed near the eaves connections, the frames began to lose stability and a full mechanism formed at the same temperature, so that collapse occurred to the base level almost immediately.   However, for the column-protected cases, after the initial mechanism which caused the collapse of the rafters, as for the previous heating profile, a second failure mechanism was created at a higher temperature, which led to the final collapse of the frame to base level.

The different base flexibilities did not show a very significant influence on the structural behaviour in cases where the whole frame was uniformly heated.   However the rotational stiffness of column bases showed a significant influence on the re-stabilised positions after snap-through of the roof frame for the roof heated case (see Fig. 18).   Critical temperatures will be lower for frames with less stiff base connections, if the critical temperature is defined as the temperature at which the structure finally begins to lose stiffness as the final hinge develops, shown as Point 4 on Figure 18. This study reveals that initial instability of the rafters does not always lead to collapse of the frame, because relatively stiff and strong columns may be able to re-stabilise the structure for a while in fire. All frames lose stability in a four-hinge mechanism, and very large deformations of the rafters were experienced.   It seems reasonable to calculate the critical temperature based on plastic theory and the thermal properties of the steel for fire safety design rather than design the moment resistance base connection to prevent inclination of the columns.

REFERENCES

[1]   Huang, Z, Burgess, I.W. and Plank, R.J., "Modeling Membrane Action of Concrete Slabs in Composite Buildings in Fire. I: Theoretical Development", Journal of Structural Engineering, ASCE, 2003, Vol. 129, No. 8, pp. 1093-1102.

[2]   Huang, Z., Burgess, I.W. and Plank, R.J., "Modeling Membrane Action of Concrete Slabs in Composite Buildings in Fire. II: Validations", Journal of Structural Engineering, ASCE, 2003, Vol. 129, No. 8, pp. 1103-1112.

[3]   Huang, Z., Burgess, I.W. and Plank, R.J., "3D Modelling of Beam-columns with General Cross-sections in Fire", Paper S6-5, Third International Workshop – Structures in Fire, Ottawa, Canada, 2004, pp. 323-334.

[4]   ABAQUS, "ABAQUS Analysis User's Manual-Version 6.5", ABAQUS INC., USA, 2004.

[5]   ANSYS, "ANSYS User's Manual for Revision 8.0-Volumn IV-Theory", Swanson Analysis SYSTEM, INC., Houston USA, 1992.

[6]   SAFIR, "A Thermal/Structural Program Modelling Structures under Fire", Jean-Marc Franssen, Proc. NASCC 2003, A.I.S.C.   Inc., Baltimore, 2003.

[7]   Morris, L.J. and Plum, D.R., "Structural Steelwork Design to BS 5950 (2nd edn.)", Addison Wesley Longman, England, 1996.

[8]   The Building Regulations 1991, "Fire Safety, Approved Document B", Department of the Environment and The Welsh Office, HMSO,1991.

[9]   Newman, G.M., "Fire and Steel Construction: The Behaviour of Steel Portal Frames in Boundary Conditions (2nd edn.)", The Steel Construction Institute, UK, 1990.

[10]   Song, Y., Huang, Z., Burgess, I.W. and Plank, R.J., "The Design of Pitched-Roof Steel Portal Frames Against Fire", Proceeding of 5th International Conference on Advances in Steel Structures, Singapore, 2007, Vol. 3, pp. 728-733.

[11]   Wong, S.Y., "The Structural Response of Industrial Portal Frame Structures in Fire", PhD Thesis, University of Sheffield, 2001.

[12]   Song, Y., Huang, Z., Burgess, I.W. and Plank, R.J., "A New Numerical Model for the Industrial Steel Frames in Fire", Research Report F/08/01, University of Sheffield, 2008.

[13]   Bathe, K.J., "Finite Element Procedures", Prentice-Hall, New Jersey, 1996.

[14]   Crisfield, M.A., "Non-linear Finite Element Analysis of Solids and Structures, Volume 2: Advanced Topics", John Wiley & Sons Ltd., Chichester, 1998.

[15]   Franssen, J.M. and Gens, F., "Dynamic Analysis Used to Cope with Partial and Temporary Failures", Paper S6-3, Third International Workshop - Structures in Fire, Ottawa, Canada, 2004, pp. 297-310.

[16]   Vassart, O., Brasseur,M., Cajot, L.G, Obiala, R., Spasov, Y., Griffin, A., Renaud, C., Zhao,B., Arce, C. and De La Quintana, J., "Final Report: Fire Safety of Industrial Halls and Low-rise Buildings", ECSC Steel RTD Program, CEC Agreement 7210-PR-378, 2005.

[17]   Horne, M.R. and Morris, L.J., "Plastic Design of Low-Rise Frames", Granada, UK, 1981.

[18]   CEN, "Eurocode 3: Design of Steel Structures: Part 1.2: General Rules – Structural Fire Design", European Committee for Standardization, 2005.

[19]   Salter, P.R., Malik, A.S. and King, C.M., "Design of Single-Span Steel Portal Frames to BS 5950-1:2000 (2004 Edition)", SCI Publication P252, The Steel Construction Institute, Ascot, United Kingdom, 2004.

SUITABILITY OF TAPERED FLANGE I-SECTIONS IN SEISMIC MOMENT RESISTING FRAMES

R. Goswami [1] and C.V.R. Murty [2,*]

*[1] Ph.D. Scholar, Department of Civil Engineering,
Indian Institute of Technology Kanpur, Kanpur 208016, India
[2] Professor, Department of Civil Engineering,
Indian Institute of Technology Kanpur, Kanpur 208016, India
[*] (Corresponding author: E-mail: cvrm@itk.ac.in)

ABSTRACT: Tapered flange sections offer difficulties of providing connections that are expected to resist overstrength plastic moments of members and associated shear. However, some earthquake prone countries still are using tapered flange sections for constructing buildings to resist severe seismic shaking. Tapered flange sections available in India not only offer low sections properties (moment of inertia *I*, flange width *b*), but also do not meet the internationally accepted stability requirements. This paper highlights deficiencies in tapered flange sections and reiterates some important issues in earthquake-resistant connection design.

Keywords: Tapered flange sections; seismic design; moment frames; stability; compact section; connection design; plastic; overstrength

1.　INTRODUCTION

Satisfactory performance of steel structures in high seismic regions primarily depends on three factors in design namely strength, stability and ductility of individual members. Apart from these, connections play an important role in the overall performance of the structure; inadequate connections can result in failure of the structure even if the structural members are adequately designed. Designed connections, together with a predetermined collapse mechanism under strong seismic shaking can result in good overall performance of the structure. In many Asian countries, including India, hot-rolled tapered flange sections are still commonly used in construction of multi-storey steel frame buildings. This paper reviews international state-of-the-art seismic design specifications for steel I-sections and evaluates the suitability of tapered-flange sections use in high seismic areas.

2.　EARTHQUAKE HAZARD AND STEEL CONSTRUCTION – THE INDIAN SCENARIO

Over the past two decades, India has experienced a spate of earthquakes that caused large damage to residential and industrial structures (i.e., 1984 M5.6 Cachar earthquake, 1988 M6.6 Bihar earthquake, 1991 M6.6 Uttarkashi earthquake, 1993 M6.4 Killari earthquake, 1997 M6.0 Jabalpur earthquake, 1999 M6.5 Chamoli earthquake, 2001 M7.7 Bhuj earthquake, 2002 M6.5 Diglipur earthquake, 2004 M9.3 Sumatra earthquake, and 2005 M7.7 Kashmir earthquake). Besides, during the five decades from 1897 – 1950, India had experienced four great earthquakes (M>8), i.e., 1897 M8.7 Assam earthquake, 1905 M8.6 Kangra earthquake, 1934 M8.4 Bihar-Nepal earthquake and the 1950 M8.6 Assam-Tibet earthquake. Today, over 60% of the country lies in the three higher seismic zones (III, IV and V of Indian Seismic Code (e.g. IS 1893 Part 1 [1]) and only about 3 % of the built environment (of over 250 million houses) is engineered. Even these engineered structures are under suspect owing to poor seismic design practice. Thus, India has potential for strong seismic shaking, and the large stocks of existing buildings are vulnerable. The situation is similar in

many neighbouring countries. In general, reinforced concrete and masonry are still the common choice over steel as a building material. However, recent trends in some of these countries show substantial growth in steel consumption. This is largely attributed to increase in low-to-medium rise residential and office buildings in urban centers. For this, available hot-rolled standard tapered-flange sections are being used.

3.   SECTION GEOMETRY

An important feature of tapered flange sections is the slope in the flange thickness. Due to this slope or taper, bolt-shank bends on tightening thereby increasing the chances of its failure. Also, because of the tapered and thin tip of the flange, only small size welds are possible between the cover plate and the flange tip (Figure 1). Moreover, proper welding between surfaces at such obtuse angle is difficult; also, it increases chance of brittle failure of the weld. Another concern is the small flange width of the sections; the largest is only 250 mm wide. Small flange width allows use of only one bolt on either side of the web and therefore requires unduly large connection length. Poor and unreliable welding in welded connection scheme and large connection length in bolted connection scheme puts the cover-plated connections of tapered flange sections in jeopardy; only hot-rolled sections with uniform thickness flanges should be used in seismic applications as in countries with advanced provisions in seismic design of steel structures, like the USA [2, 3].
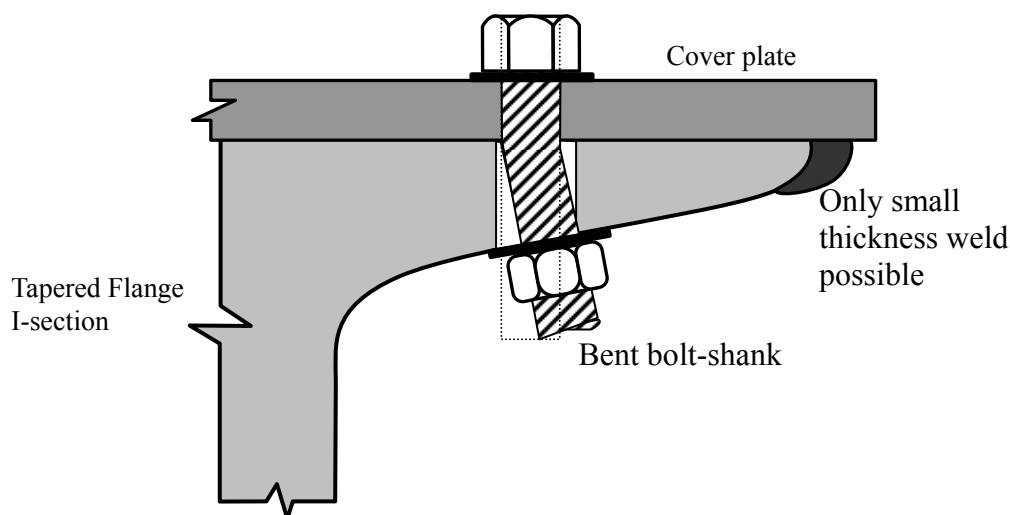
Figure 1. Effects of Tapered Flange: (i) Bolted Connection: Bolt Shank gets Bent on Tightening from the Original Straight Alignment and (ii) Welded Connection: Only Obtuse Angled Small Thickness Weld Possible at the Tapered Tip

4.   STABILITY

Steel as a material has intrinsic ductility. But, the ductility in steel structures is primarily achieved through a design and construction process that ensures stable post-yield behaviour of the material. This entails stringent stability provisions that ensure formation of plastic hinges.

Considering the major instabilities in steel structures (e.g., lateral torsional buckling of beams, flexural buckling of columns, and local buckling of beam-column flanges and webs), and the expected level of inelastic deformation and ultimate strength achieved, sections are grouped as *compact*, *semi-compact* and *slender* sections. Design codes use slenderness or *b/t* ratios to identify stability limits of flange and web plates to demarcate these groups of sections. The AISC Specifications (e.g. Specifications for Structural Steel Buildings [2]) and Provisions (e.g. Seismic Provisions for Structural Steel Buildings [3]) have these limits as: (a) λ_{ps}: slenderness limit for compact elements with a minimum guaranteed ultimate strength M_p (nominal plastic moment capacity) and plastic rotation ductility, (b) λ_p: slenderness limit for compact elements with only minimum guaranteed strength M_p, and (c) λ_r: slenderness limit for non-compact elements with only minimum guaranteed strength M_y (Figure 2). Sections with slenderness ratio λ of flanges and web elements $> \lambda_r$, classified as slender sections buckle locally even before reaching their yield moment capacity M_y. Sections with $\lambda_p < \lambda < \lambda_r$, classified as non-compact sections just reach the yield moment. Sections with $\lambda_{ps} < \lambda < \lambda_p$, classified as compact sections, develop the member plastic capacity M_p with limited ductility, while sections with λ less than λ_{ps} develop full member plastic capacity M_p and sufficient plastic rotation.
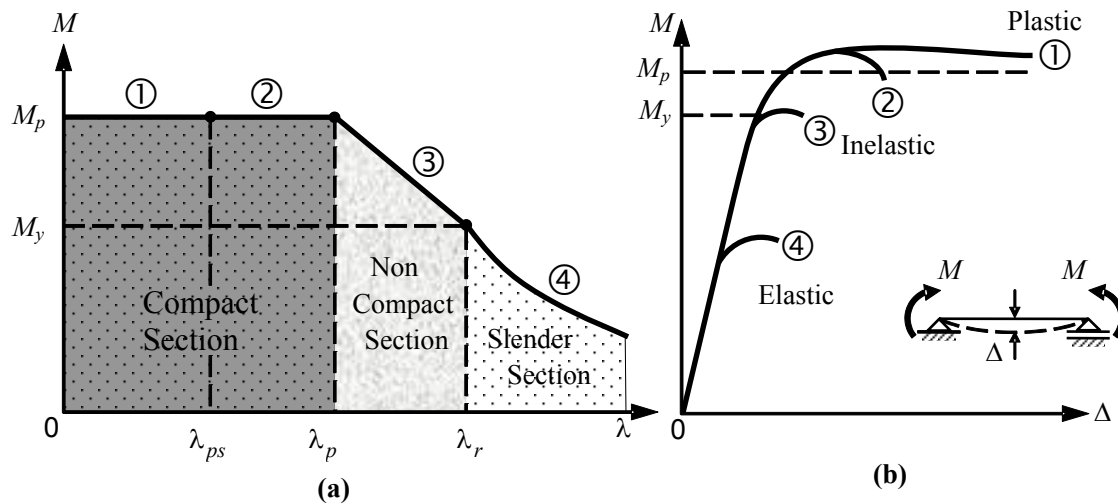
Figure 2. Effect of Slenderness on Developable Member Capacity:
(a) Strength-Slenderness Ratio Relationship; (b) Moment-Deflection Behavior of I-Sections, for Different Levels of Slenderness. Inelastic Buckling Commences much before Yield Moment M_y is Reached because of Residual Stresses

For steel with nominal yield strength F_y = 250 MPa, the above slenderness limits are presented. Plastic design in the Indian Standard (IS-PD) (e.g. IS 800 [4]) limits the maximum unsupported flange width-to-thickness ratio to 8.6, and the maximum web depth-to-thickness ratio to 43.5 for P/P_y exceeding 0.27, 70.8 for zero axial force, and linearly varying for intermediate axial force values. In comparison, the AISC Load and Resistance Factor Design specifications (AISC-LRFD) (e.g. Specifications for Structural Steel Buildings [2]) limits maximum unsupported flange width-to-thickness ratio to 10.7 for compact sections and to 28.2 for non-compact sections. And, the web depth-to-thickness ratio is limited to 106.2 for compact sections and 161.2 for non-compact sections. The AISC Provisions (e.g. Seismic Provisions for Structural Steel Buildings [3]) limits are even more stringent: 8.5 for beam flange and 69.2 for beam web of seismically compact sections, and 42.1 for column webs.

The Indian Standard Handbook (e.g. SP: 6(1) [5]) classifies Indian Standard hot-rolled I-section beams into four categories namely, light (ISLB), medium (ISMB), wide flange (ISWB) and heavy (ISHB). These sections (originally used in British practice) have unique feature of tapered flanges with rounded corners at the flange tips. For the purpose of design, a nominal thickness is used for these tapered flanges. The comparison of width-to-thickness ratios of flange and web plates of the available and commonly used hot-rolled tapered flange I-shaped sections used in India are shown in Figures 3 and 4. The cross-sectional dimensions can be found elsewhere (e.g. SP: 6(1) [5]). The flange and web width-to-thickness ratios of sections with maximum depth of 600 mm or flange width of 250 mm, do not comply with the seismically compact section limits. Hence, structures made with these sections are seismically deficient.

Apart from section compactness, member stability is another important requirement for good seismic performance of the structure. IS-PD limits maximum slenderness ratio to 120 for columns. AISC Specifications limits maximum slenderness ratio to 133 for columns when inelastic analysis and design are performed. For the usual storey height, tapered flange sections fail to comply with required member slenderness for columns under strong seismic action because of their small radius of gyration; additional flange plates are required if these sections are to be used in moment resisting frames (MRFs) intended to resist seismic actions (e.g. Paul, Murty and Jain [6]). As a result, it is expected that these frames built with these sections would exhibit a poor post-yield behaviour, under strong seismic shaking.
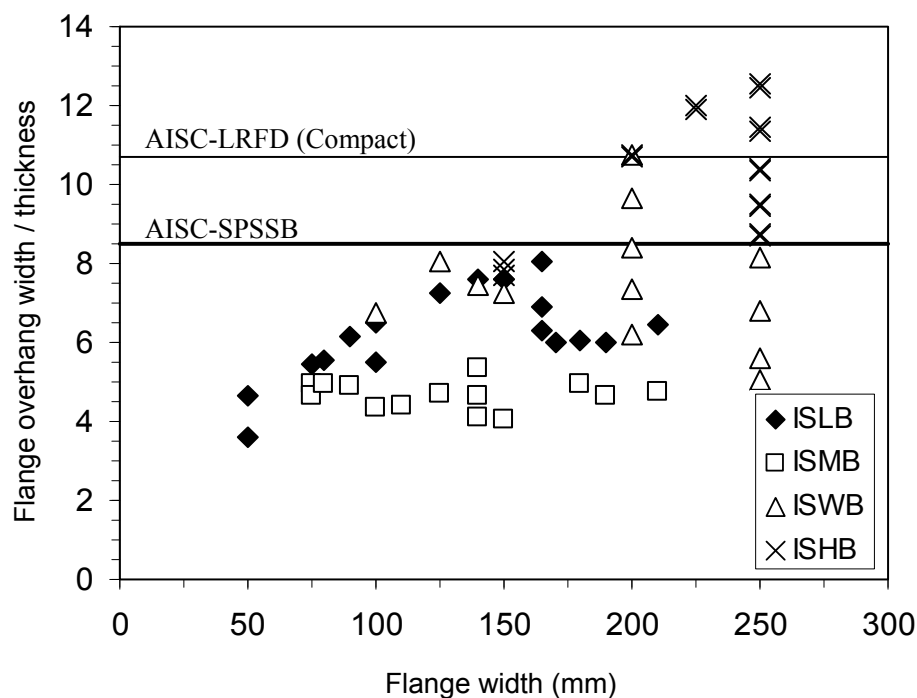
Figure 3. Flange Width-to-Thickness Ratio of Indian Hot-Rolled Tapered Flange I-Sections: Some Sections do not Comply with the Seismically Compact Section Limit Even when the Maximum Available Flange Width is only 250 mm
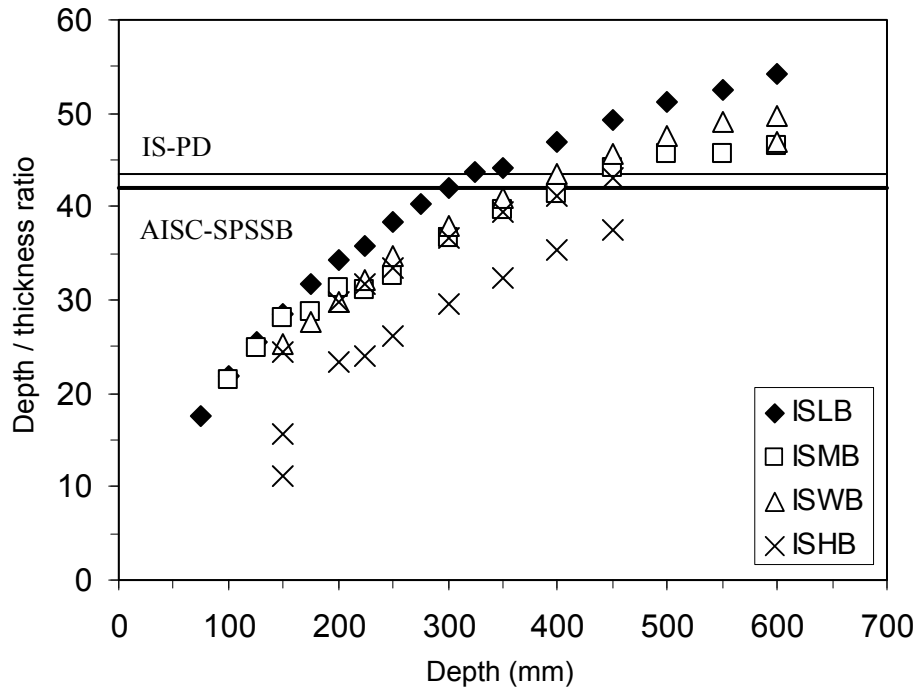
Figure 4. Web Depth-to-Thickness Ratio of Indian Hot-Rolled Tapered Flange I-Sections:
Sections with Higher Depth do not Comply with the Seismically Compact Section Limit even when
the Maximum Available Depth is only 600 mm

5.   STIFFNESS AND STRENGTH

A comparison is made of stiffness and strength of the tapered flange sections with representative parallel wide flange AISC sections commonly used in seismic design (Tables 1 and 2). The maximum depth of Indian tapered flange sections is 600 mm, and the largest moment of inertia I_{xx} (about strong axis of bending) and nominal plastic moment capacity M_p are 1156×10^{-6} m^4 and 987 kNm respectively. However, I_{xx} and M_p of AISC sections of same depth are at least about 3 times higher than those of the tapered flange sections of same depth (Figures 5 and 6). Thus, structures built with even the largest tapered flange sections are too flexible and too weak relative to their international counterparts with parallel flange sections.

6.   CONNECTION DESIGN

Following the large number of connection failures during the 1994 Northridge (USA) and 1995 Kobe (Japan) earthquakes, a fresh approach emerged for the design of beam-to-column and column-to-base connections. Beam-to-column connections are designed now as per the *Capacity Design Concept*. By this design method, premature fracture of welds or fasteners is avoided at the connection; beams and columns undergo ductile yielding and connections remain elastic when designed for the maximum demand arising from the beam or column under plastic condition (Figures 7 and 8). In summary, the capacity design concept enlists a strength hierarchy of the components of a building: (a) the beam-to-column connections joint are to be stronger than the beam, (b) the columns are to be stronger than the beams, and (c) the column base connections are to be stronger than the column (e.g. Penelis and Kappos, 1997 [7]).
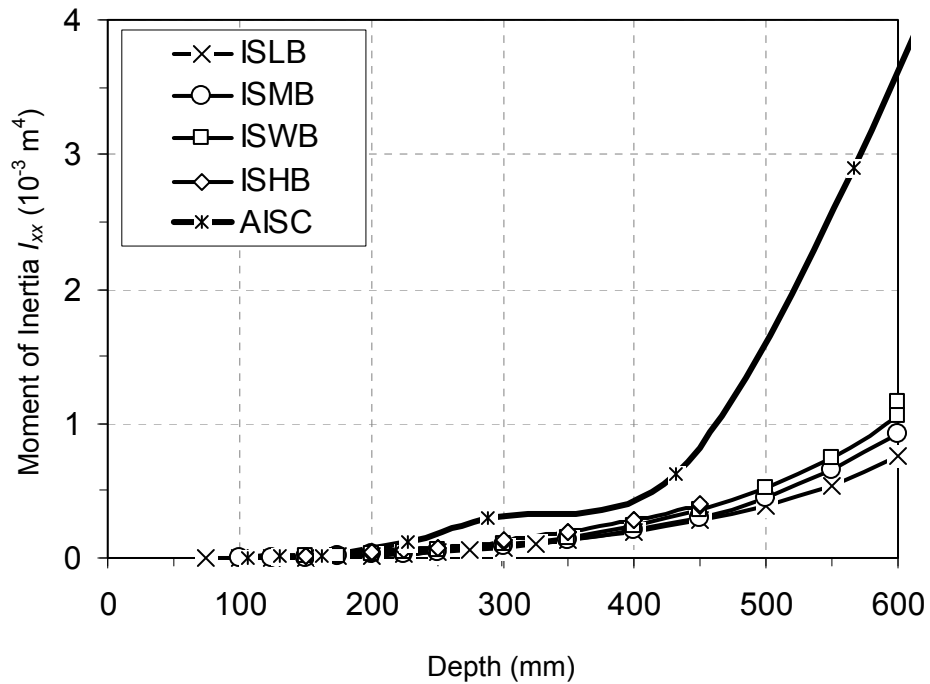
Figure 5. Comparison of Moment of Inertia of Representative AISC and
IS Hot-Rolled Tapered Flange I-Sections: Tapered Flange Sections are much
smaller than the AISC Parallel Wide Flange Sections
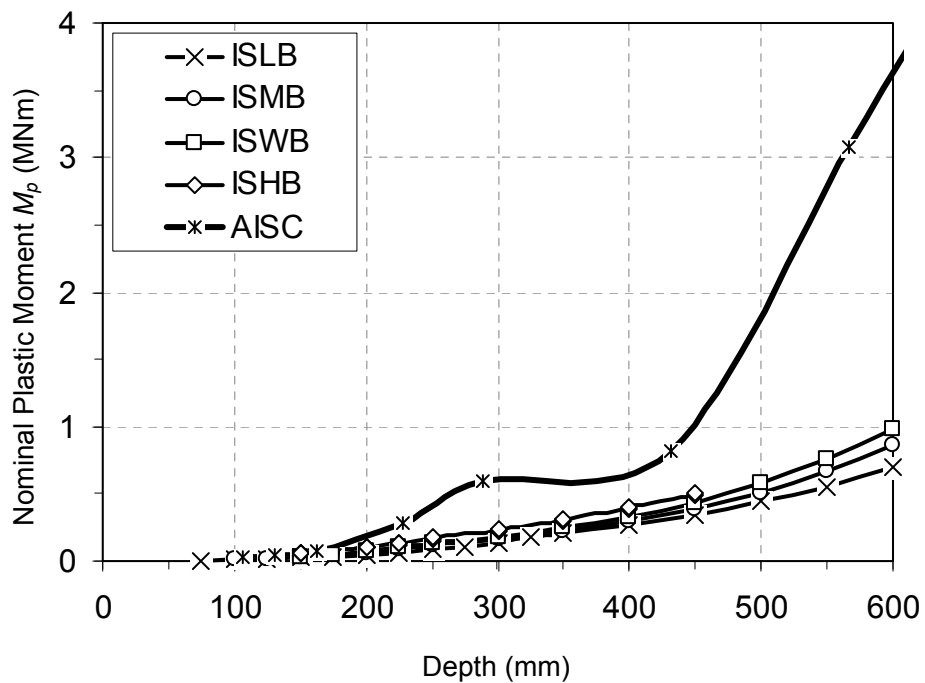
Figure 6. Comparison of Nominal Plastic Moment of Representative AISC and
IS Hot-Rolled Tapered Flange I-Sections: Tapered Flange Sections are much
smaller than the AISC Parallel Wide Flange Sections
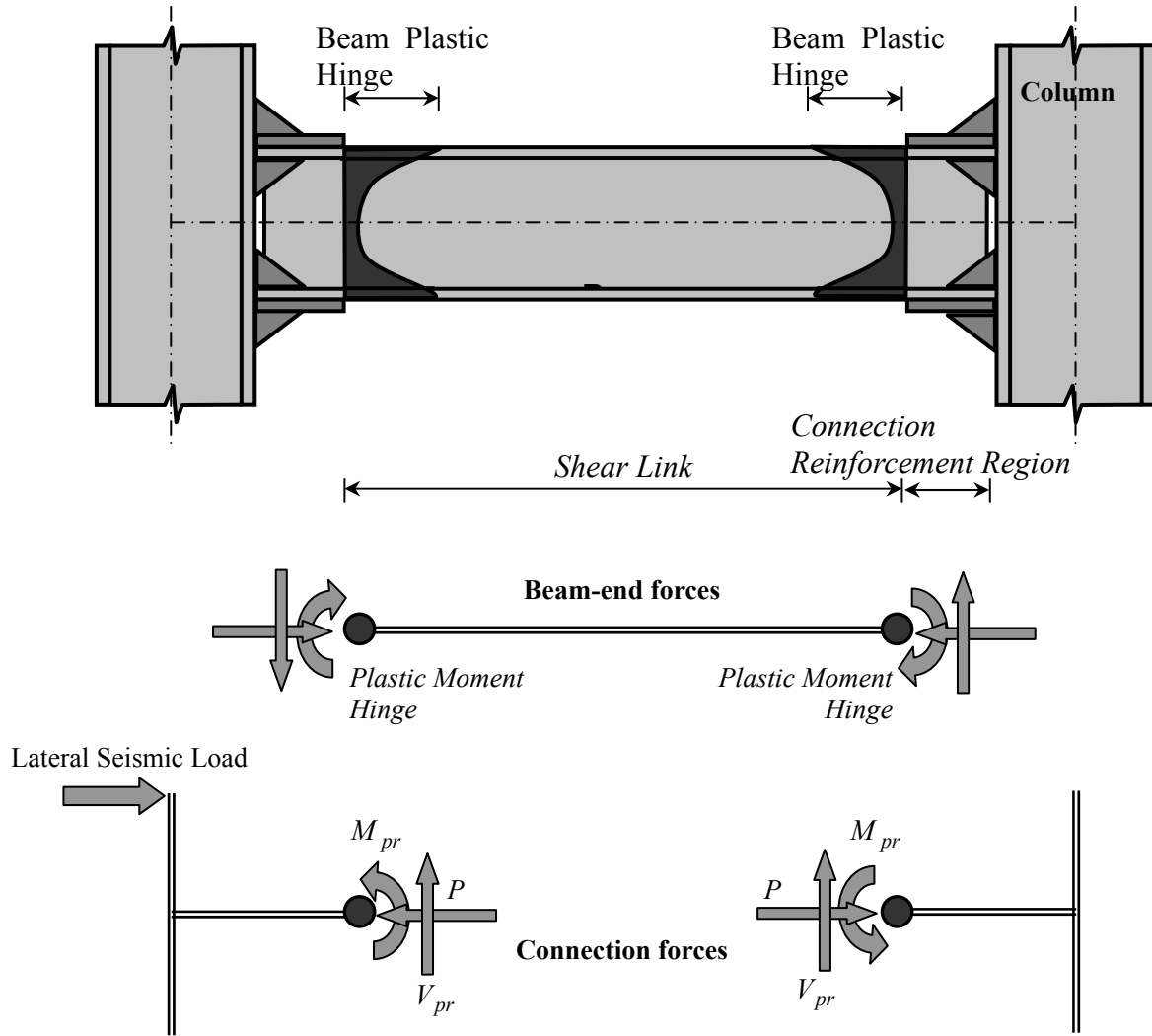
Figure 7. Location of Ductile Plastic Hinges Adjacent to Beam-to-Column Connections: Connection Reinforcement Elements help in Pushing the Inelasticity Away from the Column Face

The connection design forces should be designed for the maximum probable member strength, i.e., moment capacity M_{pr} and the associated equilibrium compatible shear V_{pr}, including effect of gravity load. In using M_{pr} in connection design, three important issues need attention. Following the Northridge and Kobe earthquakes, coupon tests of specimens taken from actual construction and mills have shown that the actual yield strength of steel in rolled-sections can be higher than the minimum specified yield strength F_y (e.g. Engelhardt and Sabol [8]; Malley and Frank [9]). As a result, AISC Provisions recommends the use of higher yield strength for calculating member strength for the determination of connection element design force; the ratio R_y of the expected yield strength to the minimum specified yield strength of the member is to be used. For instance, for ASTM A36 grade steel, R_y is 1.5; at least a 50% increase in connection design force is recommended. However, In India, such data for the available tapered flange sections are not readily available in public literature, and also, the current code provisions do not account for this. Such statistical data from the hot-rolled tapered flange sections obtained through coupon test need to be incorporated in seismic design procedures.
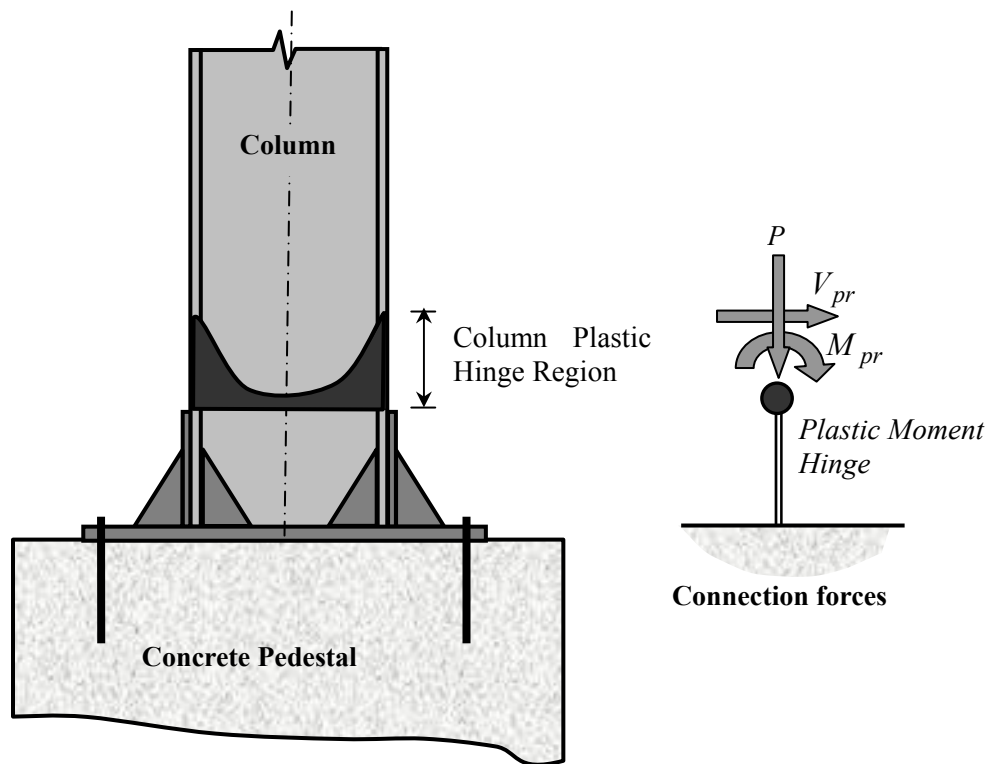
Figure 8. Location of Ductile Plastic Hinges Adjacent to Column-to-Foundation Connections: Connection Reinforcement Elements help in Pushing the Inelasticity away from the Base Plate
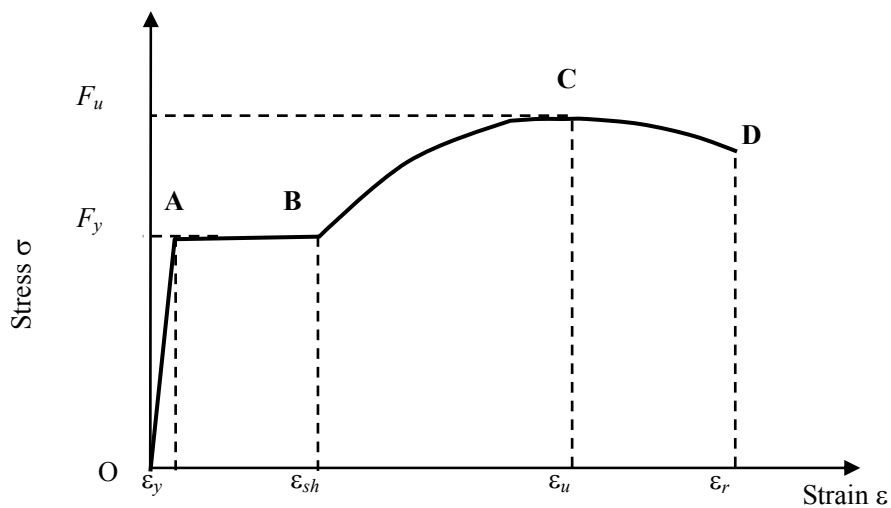
Figure 9. Typical Schematic of Constitutive Curve of Structural Steel: Four Distinct Zones are Evident - A Linear Elastic Zone OA, a Yield Plateau AB, a Strain-Hardening Zone BC and a Strain-Softening Zone CD
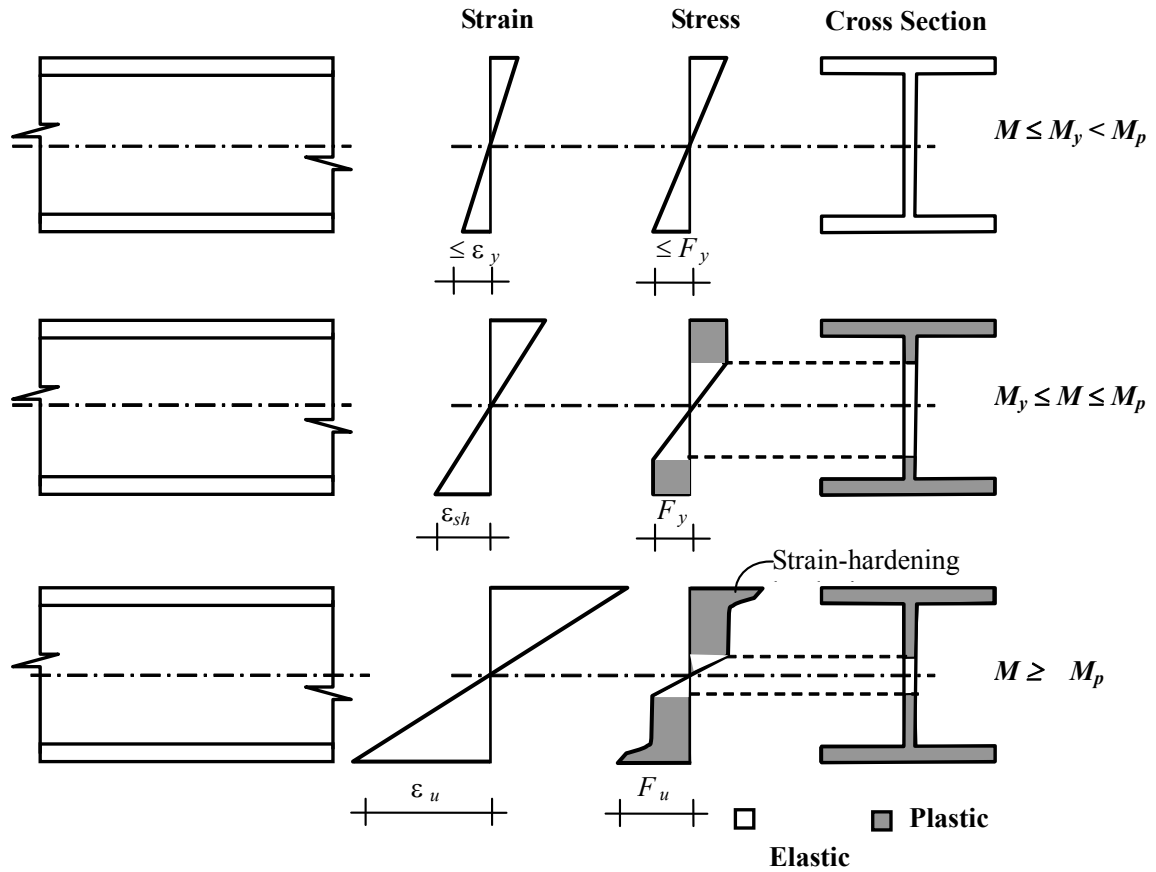
Figure 10. Various Stages of Member Plastification under Pure Flexure: The Fibers at Neutral Axis do not Yield, but the Fibers away from the Neutral Axis Strain-Harden, thus the Cross-Section Develops a Nominal Plastic Moment of M_p and more

Design codes often (e.g., AISC [2], IS:800 [4]) assume an idealized elastic perfectly plastic constitutive law for structural steel with characteristic yield strength as F_y. In reality, structural steel has a distinct constitutive relation (Figure 9) with an initial elastic zone (OA), a yield plateau (AB), a strain hardening zone (BC), and a strain-softening zone (CD) before it fractures. The member nominal flexural capacity M_p for bending about the major axis is computed based on the idealized rectangular stress block with a maximum stress of F_y. Such a stress block is not practically achievable, because to develop a stress of F_y at the fibers at and near the neutral axis, the strains required at the extreme fibers of the section are infinitely large. Secondly, the rectangular stress block can never be achieved without inevitable strain-hardening of the extreme fibers of the beam section. Thus, the representation using rectangular stress blocks deviates from the actual behavior (Figure 10). The beam bending moment equal to the plastic moment value M_p can be realized in a section only when a part of it undergoes strain-hardening while some of it still remains elastic; experimental studies (e.g. Popov et al. [10], Chen and Lui [11], Englehardt and Sabol [8]) showed that beam capacities larger than M_p are achievable with inelastic deformations corresponding to the drift demands expected by some code guidelines (e.g. UBC [12]; FEMA, [13]). Thus, it is the strain hardening of steel that causes an increase in the member capacity, and hence the demand on connections, under strong seismic shaking over the code-prescribed nominal capacity M_p. AISC and FEMA (e.g. AISC [14]; FEMA [15]) recommends strain-hardening factors greater than unity to account for beam overstrength, and increase in connection design strength over M_p; 10-20% increase is recommended. A simple expression, involving the minimum specified yield and ultimate strengths (e.g. FEMA [16]) is given as

$$C_{pr} = \frac{F_y + F_u}{2F_y} = 1 + \frac{1}{2}\left(\frac{F_u - F_y}{F_y}\right),$$

(1)

where F_y and F_u are the specified minimum yield and tensile strengths of the (beam) material, respectively. Later, a more rational approach to estimate R_s was presented (e.g. Arlekar and Murty [17]). For any section, normalized moment M/M_p versus normalized curvature relations can be generated. φ is the curvature of the section, and φ_y, referred to as yield curvature when the farthest material point from the neutral axis reaches yield. Then, the normalized moment M/M_p is the strain hardening factor R_s, and is a measure of strain hardening in the beam. And, φ/φ_y is the curvature ductility μ_φ. Based on a study of 61 hot-rolled tapered-flange I-sections (Table 1), the expression for strain hardening factor R_s was given as (e.g. Goswami, Arlekar and Murty[18]) (Figure 11)

$$\frac{M}{M_p} = R_s = \begin{cases} \mu_\varphi & \text{for } 0 \leq \mu_\varphi \leq \mu_y \\ 1 & \text{for } \mu_y < \mu_\varphi \leq \mu_{sh} , \\ 0.81 + 2\left(\frac{\mu_\varphi}{100}\right) - 2\left(\frac{\mu_\varphi}{100}\right)^2 + \left(\frac{\mu_\varphi}{100}\right)^3 - 0.3\left(\frac{\mu_\varphi}{100}\right)^4 & \text{for } \mu_{sh} < \mu_\varphi \leq \mu_u \end{cases}$$

(2)

where μ_y is the curvature ductility at idealized yield, μ_{sh} is the curvature ductility at the beginning of strain-hardening on the idealized curve, and μ_u is the ultimate curvature ductility. From the data of the 61 sections considered, the values of μ_y, μ_{sh} and μ_u are obtained as 1.0, 11.4 and 150 respectively. Further, curvature ductility μ_φ imposed at a section can be estimated from the amount of plastic rotation θ_p required to be developed at the end of the member, using

$$\mu_\varphi = \frac{2EI\theta_p}{M_p d},$$

(3)

where d and EI are the depth and flexural rigidity of the member. Early experiments have shown that plastic rotation demand of 0.03-0.04 can be achieved without significant loss in strength (e.g., FEMA [13]). Since Indian steel code specifies no such demand, experiments need to be conducted on MRFs made using the available tapered-flange sections to determine desirable plastic rotations and develop associated design guidelines. Still, using Eq. 3, the curvature ductility μ_φ of the sections considered ranges from 7.0 to 29.0 for θ_p varying between 0.01 and 0.04 radians. Then, using Eq. 2, the value of R_s, hereinafter called the strain-hardening factor, is estimated to be in the range 1.0 to 1.24 for the available tapered-flange I-sections. The above expression for R_s was derived for ASTM A36 grade steel with F_y equal to 250 MPa, and F_u/F_y as 1.5.
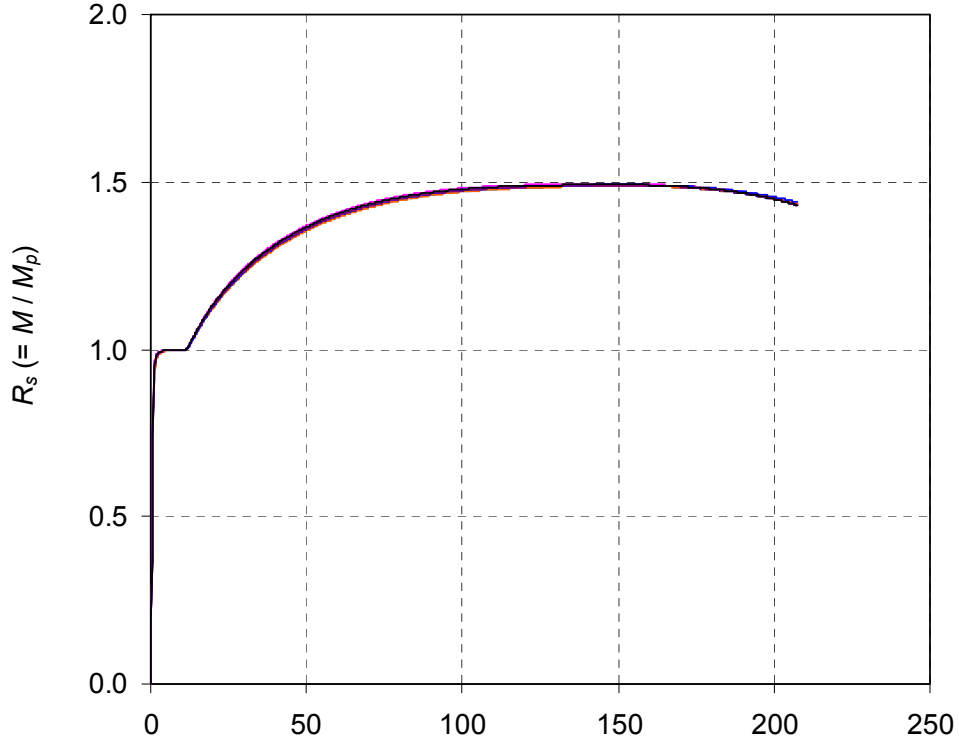
Figure 11. Strain-Hardening of Tapered-Flange I-Sections: Strain-Hardening Factor from Study using 61 Hot-Rolled Tapered-Flange I-Sections with $F_u/F_y = 1.5$

Though member capacity that can be mobilized (and thus, connection design force) is increased due to strain-hardening and uncertainty in material yield strength, section and member instabilities cause reduction of member capacity and connection design force. A compactness factor R_c, is introduced to account for the reduction in the maximum achievable member capacity owing to premature local buckling given by

$$R_c = \begin{cases} 1.0 & \text{for } \dfrac{b}{t} \le \lambda_p \\[2mm] 1.0 - 0.2\left\{ \dfrac{(b/t) - \lambda_p}{\lambda_r - \lambda_p} \right\} & \text{for } \lambda_p < \dfrac{b}{t} \le \lambda_r \\[2mm] 0.8 & \text{for } \dfrac{b}{t} > \lambda_r \end{cases} \qquad (4)$$

Here, the minimum value of R_c is 0.8. The limiting values for λ_r and λ_p are prescribed in the codes. However, the limits prescribed in the codes are originally for the purpose of beam flexural design and thus, will tend to give a conservative underestimate of the member strength. But, in connection design, the upper bound strength is required. Moreover, these values are for prismatic flange and web. For hot-rolled I-sections with tapered flanges, such limits of λ_r and λ_p for connection design purpose and dependence of R_c on these need to be prescribed.

Using R_y, R_s, and R_c, the maximum probable member strength, and hence, the maximum probable demand on the connection elements in beam-to-column connections is given by

$$M_{pr} = R_y R_s R_c M_p .$$

(5)

Column-to-foundation connection (Figure 8) design on the other hand also requires proper account of the axial load on the column, which is often varying, particularly under strong seismic shaking. Further, interactions between axial force, shear force and bending moment capacities of the section need to be looked into in arriving at the connection design forces. In addition, design codes consider the minimum specified yield strength F_y as the limiting strength for capacities and the interactions. This is acceptable for design of the members. However, it is required to properly estimate the maximum possible capacities along with the interactions considering strain-hardening for design of connection elements. Thus, section capacities of tapered-flange I-sections are developed using a fiber model and hysteretic loading and unloading of steel constitutive law (Figure 12). Figure 13 shows typical *P-V-M* interaction surface of a tapered-flange I-section (e.g., ISMB 600, with section properties as given in Table 1). While developing the *P-V-M* interaction curves, the following is considered. For a given normal stress σ_{xx} (due to axial load and bending moment) in a fiber, the von Mises yield criterion for steel represented by

$$\sigma_{xx}^2 + 3\tau_{xz}^2 = Y^2 .$$

(6)

is used to calculate the available shear capacity. Here, Y is taken as the ultimate stress F_u. The curvature is increased from zero to a maximum value corresponding to the maximum rupture strain ε_r at the extreme fiber, and at each level, the shear and normal capacities are estimated. The uniaxial stress-strain curve of steel (Figure 11) has a drop in the stress beyond the strain corresponding to the ultimate stress. The limiting shear stress from Eq. 6 when $\sigma_{xx} = F_u$, is zero. For strains greater than ε_u, Eq. 6 suggests that the shear stress τ_{xz} in fibers is non-zero. However, in this study it is assumed that all fibers having strains beyond ε_u do not have shear capacity. Further, while obtaining the limiting *V-M* boundary, it is assumed that beam flanges and webs do not undergo buckling. The nominal shear strength $\left(V_p = \tau_y t_w d\right)$ and the nominal bending moment capacity $\left(M_p = F_y Z\right)$ of the section are used to normalize the shear and moment capacities, respectively. The first yield shear stress corresponding to a state of pure shear is used and defined as $\tau_y = F_y / \sqrt{3}$.

The most commonly used section capacity interaction in design is the *P-M* interaction. Figure 14 shows *P-M* interactions developed for the tapered-flange section considering strain-hardening using the fiber model. Design codes often assume a linear interaction (for ease in design) and uses yield strength as the limiting strength. Figure 14 also shows the linear interaction recommended by the Indian code (IS 800 [4]) along with the scaled interaction up to the ultimate capacity. The code specified curve depicts an average member capacity for moments up to about M_p. Thus, it underestimates the moment capacity of some members, and hence, connections designed using this interaction would be under-designed. Hence, an upper bound of the *P-M* interaction curves at zero shear is derived as

$$\frac{M}{M_p} = \frac{F_u}{F_y}\left(1 - \frac{F_y}{F_u}\frac{P}{P_y}\right)^{1.54} .$$

(7)
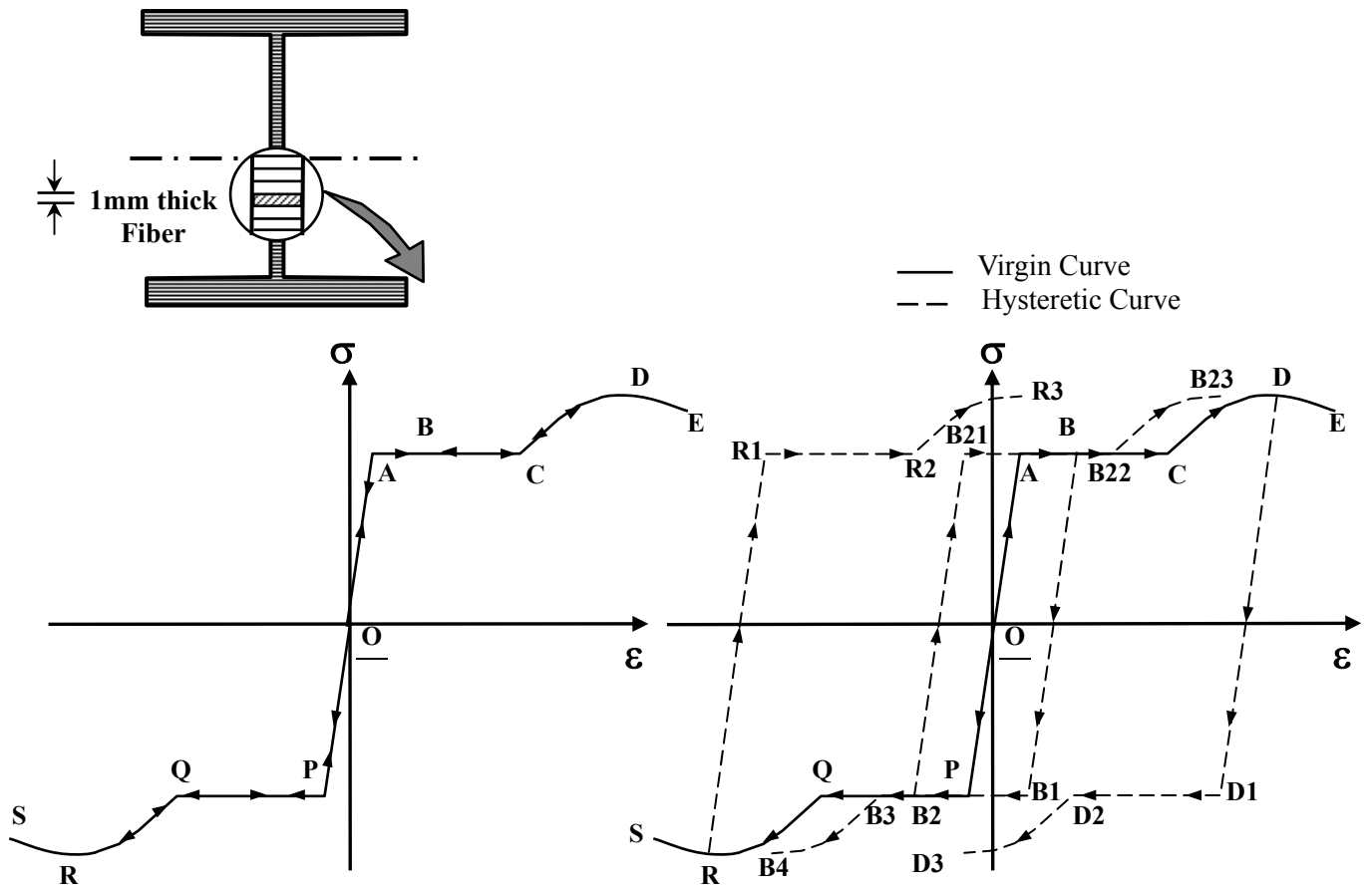
Figure 12. Fiber Model Showing the Discretization of the Beam Section
along with the Explicit form of Stress-Strain Relationship for Steel Along with
Schematic Representation of the Loading and Unloading Paths for Steel
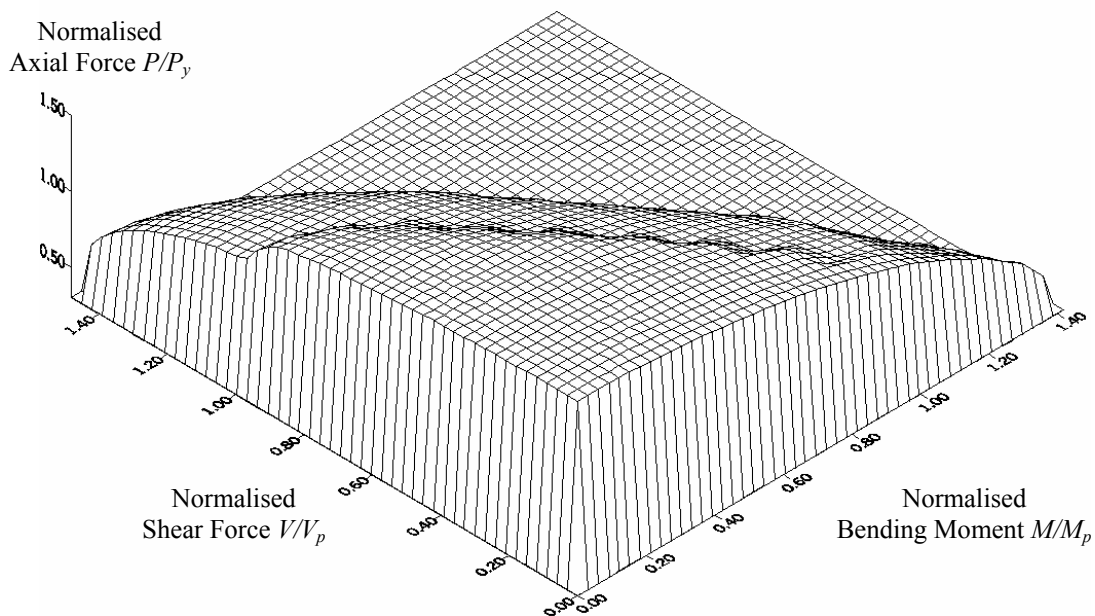
Figure 13. Strength Interaction in ISMB 600: Normalized *P-V-M* Interaction Surface of
ISMB 600 Generated using Hysteretic Stress-Strain Model
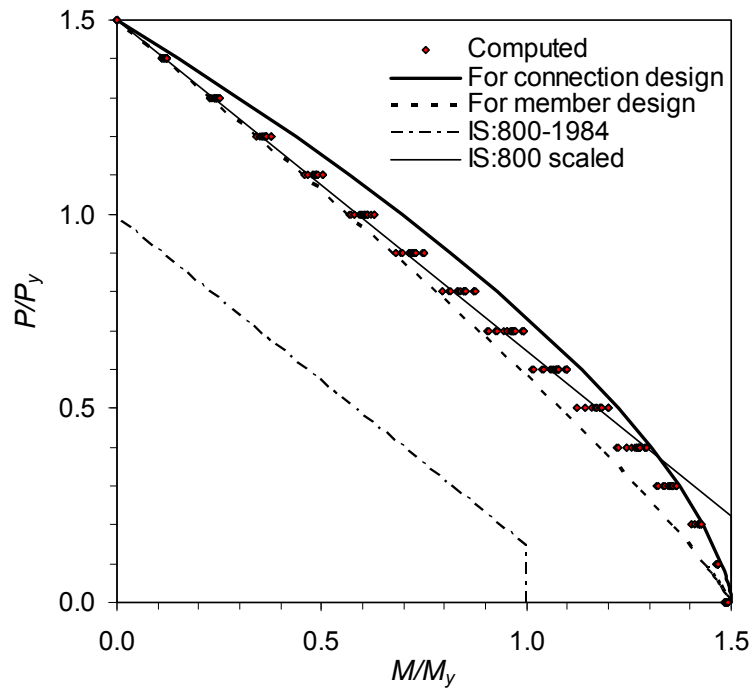
Figure 14. *P-M* Interaction Curve along with the Actual *P-M* Points for
$V = 0$ for Indian Hot Rolled I-Sections
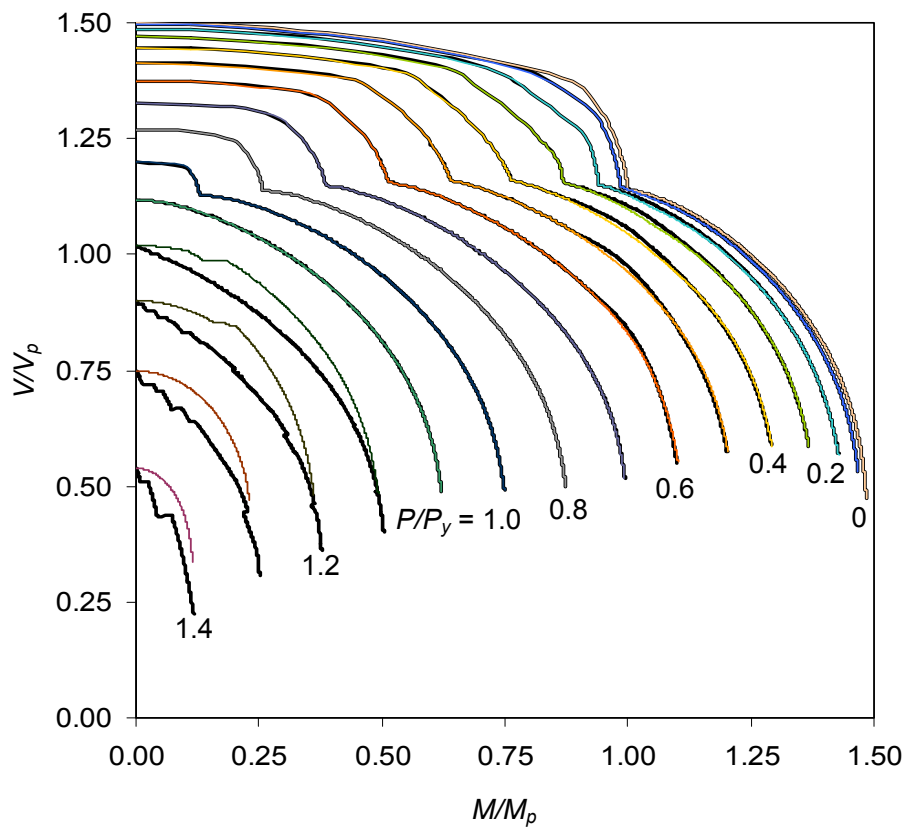
Figure 15. Shear-Moment Interaction showing Normalized *V-M* Curves for a
Typical Tapered-Flange I-Section (ISMB 600) for Different Axial Load Levels with
and Without Hysteretic Stress-Strain Ccurve.

This upper bound limit is conservative for ascertaining the connection demand forces, although, using this for member design would result in an overestimate of the member capacity. Figure 15 shows normalized *V-M* interaction curves for a typical tapered-flange I-section (ISMB 600) for various levels of the compressive axial loads. The moment is normalized with the nominal plastic moment capacity M_p and shear with the nominal shear capacity V_p. The *V-M* interaction curves obtained using strain-hardened virgin stress-strain curve are also shown in Figure 15. The *V-M* curves without hysteretic loading (represented by thinner lines) are higher than the corresponding curves obtained using the hysteretic loading (represented by thicker lines), only when the axial load is higher than the yield load P_y. Thus, the *V-M* curves with non-hysteretic loading, commonly used in codes, are acceptable in static design where the axial load does not change or is below the member yield load. However, under earthquake shaking, the axial load can swing by large amount and the *V-M* curves with hysteretic loading better reflect the actual lower member capacity and should be considered for the member design.

Unlike for beam-to-column connection design, the connection design forces for column-to-foundation design forces needs to account also for the various strength interactions stated above. However, as in beam-to-column connection design, additional strength reductions result due to member instabilities like global flexural buckling in compression and global flexural–torsional buckling. For instance, the reduction due to flexural buckling in compression can be taken into account through a modification factor R_λ as

$$R_\lambda = \begin{cases} 0.658^{\lambda_c^2} & \text{for } \lambda_c \leq 1.5 \\[2mm] \dfrac{0.877}{\lambda_c^2} & \text{for } \lambda_c > 1.5 \end{cases}, \tag{8}$$

where λ_c is the global slenderness parameter given by

$$\lambda_c = \frac{KL}{r\pi}\sqrt{\frac{F_y}{E_s}}, \tag{9}$$

in which, K is the effective column length factor, L the length of the column, and r the governing radius of gyration, and F_y and E_s the yield strength and modulus of elasticity of steel, respectively. Similarly, the reduction due to flexural–torsional buckling can be accounted through a factor R_L given by

$$R_L = \left[\frac{\pi^2 E_s C_w}{(K_z L)^2} + G_s J\right]\frac{1}{(I_x + I_y)F_y}, \tag{10}$$

where C_w is the warping constant, K_z the effective length factor for torsional buckling, G_s the shear modulus of steel, J the torsional constant, and I_x and I_y the moment of inertia about the x and y axes, respectively. Thus, the maximum probable column moment capacity M_{pr}^P under axial load P that can be mobilized (or the design moment for column-to-foundation connection design) is given by

$$M_{pr}^P = R_y \text{Min}[R_c; R_\lambda; R_L]M_p^P. \tag{11}$$

Unlike in Eq. 5, the strain-hardening factor is not explicitly used (in Eq. 11) because with the varying column axial force levels during seismic shaking, the level of strain-hardening also varies. Instead, the capacity curves are developed considering possible strain-hardening.

Using the design forces given by Eqs. 5 or 11, the connections need to be designed. However, in executing the design, various concerns arise in use of tapered-flange sections; it is particularly serious for bolted connections. Typically, the beam flanges are expected to transfer the bending moment, and the beam web the shear forces. However, recent studies have shown that this assumption is not realistic, and a truss analogy model is necessary to represent the realistic flow of forces in the connection (e.g. Lee, Goel and Stojadinovic [19]; Arlekar and Murty [20]). An improved welded cover plated and ribbed moment connection is necessary to transfer the overstrength based design forces (e.g. Arlekar and Murty [20]). Here, the cover plate is designed to transfer part of the bending moment in the form of axial (compressive or tensile) forces, while two outer rib plates are designed to transfer both axial and shear forces (Figure 16).
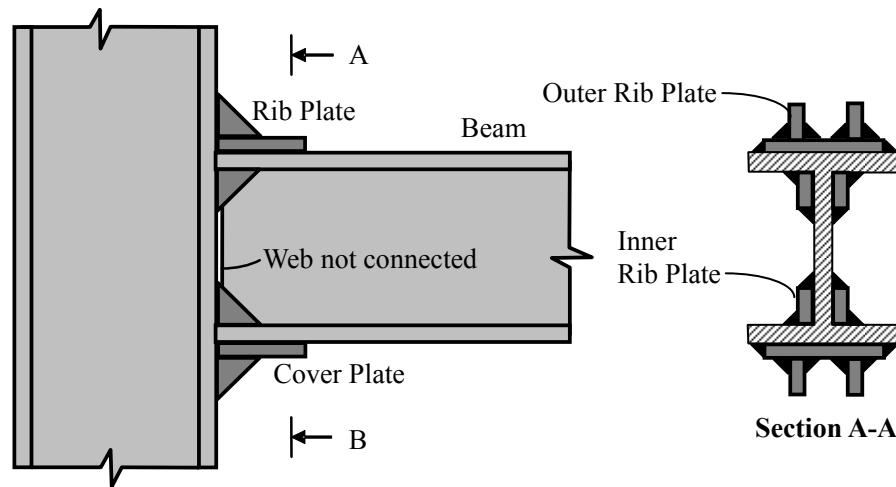
Figure 16. Cover Plated Rib Plated Welded Strong-Axis Moment Connection Configuration in Parallel Flange Sections: Cover Plates Transfer Part of Moment in the Form of Axial (Compressive and Tensile) Forces while (Outer) Rib Plates Transfer Axial and Shear Forces
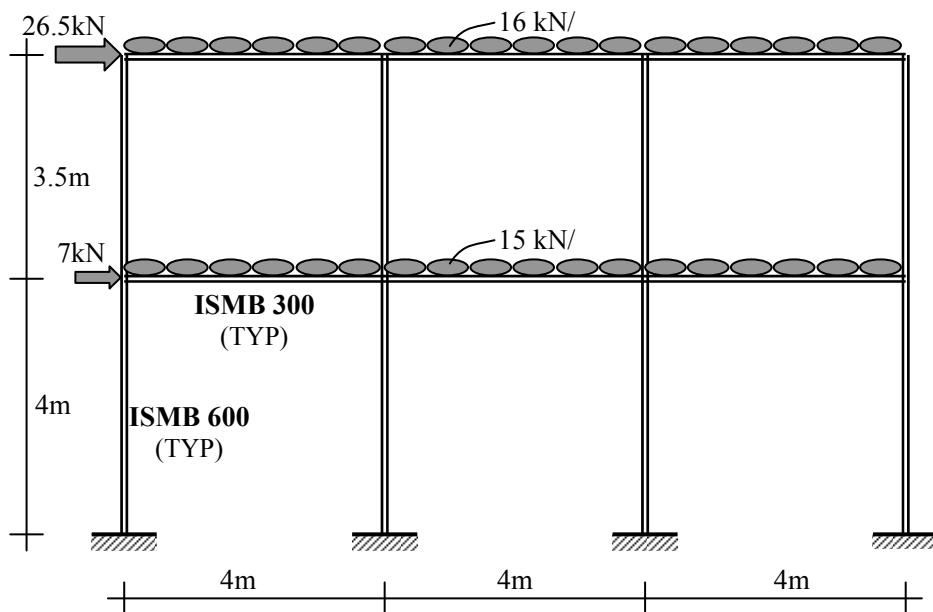
Figure 17. Sample Frame: Member Sizes, Boundary Conditions with Loadings

Tapered flange sections have small flange widths. Hence, in bolted connections, only a single line of weld is possible on either side of the web leading to long connection region. And, in welded connections, often, there is insufficient space between the two outer rib plates to weld them to the cover plates. In addition, due to tapering of these flanges, additional inner rib plates cannot be provided efficiently; these are crucial in minimizing stress concentration near the weld access holes. The following beam-to-column connection design example highlights the concerns in welded connections.

Figure 17 shows a simple 3-bay 2-storey frame made with Indian tapered-flange I-sections. The bay span considered is 4m. The uniformly distributed gravity load (including dead load, fraction of live load on roof and floor, and roof finish load) is 16 kN/m on the roof beam and 15 kN/m on the floor beam. The frame is considered to be in the most severe seismic zone and analysed for code specified load combinations. The maximum joint moment and shear forces for load combination 1.3(DL+LL+EL) are respectively 43 kNm and 48 kN. The beam-to-column connection is designed for this force.

In the common design practice, members and connections are designed based on the linear static analysis results. The web is considered to carry the shear and the two flanges carry the flexure, in the form of tension and compression. Accordingly, from the static analysis results above, 6 mm fillet welds of 100 mm length on both sides of the web are sufficient to carry the shear. The flanges can be connected to the column through a 10 mm full penetration butt weld, or by 10 mm fillet weld along the straight portions of the flanges. As there are no particular recommendations for the type of connection arrangement to be adopted in the existing Indian codes, such simple form of connection can be designed still adhering to the code provisions, if desired.

As an alternative, the beam-to-column connections can be designed using plastic theory wherein the connections can be designed for the nominal plastic moment that is to be transmitted from one member to another. Thus, under the condition of an extreme shaking, assuming that plastic hinges are formed at the beam ends, the design forces for connection design is the nominal plastic moment M_p (161.6 kNm) of the beam and a shear of 120.6 kN, considering the critical sections to lie at the beam-column interface. Thus, now the design shear and moment are increased by 1.5 to 2.8 times over the structural analysis results of the frame discussed earlier, and now, the connection designed earlier becomes inadequate. Further, the code does not specifically say that plastic analysis and design need to be done for seismic conditions. Thus, it remains at the hand of the designer to choose the type of analysis and design one wishes to do, and in the process, the structural safety is put at stake.

As the second alternative, now consider the overstrength based modification factors $R_y = 1.3$, $R_s = 1.24$ and $R_c = 1.0$. The design moment at the column face becomes 261 kNm plus the shear times the length of the connection reinforcement region and plastic hinge length. Thus, there is an increase of more than 62% in the design moment alone. This can cause premature failure of the connection even before the beam reaches its full plastic capacity resulting in collapse of the structure. Further, simple direct connections (directly welding the beam to the column) do not facilitate smooth flow of forces through the connection region; stress concentration at the beam flange-column flange junction severely affects the functioning of the connection. The cover-plated rib-plated connection with connection length of half the beam depth is an improvement (Figure 16). Using this, the associated shear force increases to 186.5 kN, an increase of about 55% compared to a value of 120.6 kN. However, this scheme works best on sections with wide non-tapered flanges. Tapered-flange Indian sections have very small flange width. As such, the available width of cover plate is much less and may be insufficient to transfer the forces in higher structures with higher forces. The example frame is a nominal two-storey lightly loaded structure chosen only with the

intention to discuss the important issues. Also, due to tapering of these flanges, additional inner rib plates cannot be provided efficiently to further reinforce the connection. These are important for minimizing stress concentrations at and near the weld access holes.

7.   TAPERED FLANGE SECTIONS IN OTHER COUNTRIES

Tapered flange sections are still listed in different handbooks and codes across America and Europe (e.g., "Standard Beams" in American (AISC [21]) and Canadian [CISC [22]) handbooks, "Joists" in British Standard (BS 4-1 [23]). However, their use as main structural member in MRFs in seismic applications has become extinct. For instance, such sections are currently not available in the Canadian market, while their availability in the American and European market is questionable. Moreover, the maximum depth of the Standard Beams is 622 mm with flange width of only 204 mm, while that for the Joists, these are 254 mm and 203 mm, respectively. These are comparable to the Indian standard tapered-flange I-sections. For the already stated reasons, countries with advanced seismic provisions for design of steel structures use only wide-flange hot-rolled sections with uniform thickness flanges (e.g., the American W-shapes, British Universal Beams, and European wide flange HEA, HEB, & HEM sections).

On the other hand, in some Asian countries in high seismic regions, tapered-flange sections are still manufactured and are being used for structural applications. Possible reasons for this continued use of inappropriate sections include utilization of the old rolling mills without upgrading, lack of awareness towards seismic hazard of the region, and lack of code provisions.

8.   SUMMARY

Tapered-flange I-sections, of at least a reasonable size, offer low section properties (namely moment of inertia, flange width, and nominal plastic moment capacity), violate stability requirements for stable post-yield behaviour particularly under strong seismic shaking, and offer constructional difficulties. Despite these deficiencies, tapered-flange I-sections are still being used extensively in many Asian countries. Thus, there is an urgent need to stop use of such sections, especially in seismic areas. This can be achieved by disseminating information regarding their deficiencies and challenges in their usage to the industry, architects and design engineers. Also, regional codes and specifications should restrict the use of such sections for seismic applications. Indirectly, this may even open up new opportunities for steel industry to manufacture larger seismically compact sections for the Asian market.

Table 1. Moment of Inertia and Nominal Plastic Moment Capacity of
Indian Tapered-Flange I-Sections.

Section Name	Depth d (mm)	I_{xx} $(10^{-6}\,m^4)$	M_p (kNm)	Section Name	Depth d (mm)	I_{xx} $(10^{-6}\,m^4)$	M_p (kNm)
ISLB 75	75	0.7	5.4	ISMB 100	100	2.6	14.5
ISLB 100	100	1.7	9.4				
ISLB 125	125	4.1	18.0	ISMB 125	125	4.5	20.3
ISLB 150	150	6.9	25.4	ISMB 150	150	7.3	27.3
ISLB 175	175	11.0	34.9	ISMB 175	175	12.7	41.2
ISLB 200	200	17.0	47.1	ISMB 200	200	22.4	62.6
ISLB 225	225	25.0	63.5	ISMB 225	225	34.4	86.0
ISLB 250	250	37.2	84.9	ISMB 250	250	51.3	114.9
ISLB 275	275	53.8	111.3				
ISLB 300	300	73.3	138.9	ISMB 300	300	86.0	161.6
ISLB 325	325	98.8	172.8				
ISLB 350	350	131.6	212.2	ISMB 350	350	136.3	219.6
ISLB 400	400	193.1	273.5	ISMB 400	400	204.6	290.5
ISLB 450	450	375.4	348.1	ISMB 450	450	303.9	383.0
ISLB 500	500	385.8	440.3	ISMB 500	500	452.2	512.8
ISLB 550	550	531.6	553.7	ISMB 550	550	648.9	670.5
ISLB 600	600	758.7	696.6	ISMB 600	600	918.1	867.8
ISWB 150	150	8.4	31.5	ISHB 150	150	14.6	53.4
				ISHB 150	150	15.4	56.8
				ISHB 150_3	150	16.4	60.5
ISWB 175	175	15.1	48.4				
ISWB 200	200	26.3	73.0	ISHB 200	200	36.1	98.9
				ISHB 200	200	37.2	102.4
ISWB 225	225	39.2	96.9	ISHB 225	225	52.8	128.5
				ISHB 225	225	54.8	134.1
ISWB 250	250	59.4	131.8	ISHB 250	250	77.4	169.2
				ISHB 250	250	79.8	175.5
ISWB 300	300	98.2	182.3	ISHB 300	300	125.5	229.3
				ISHB 300	300	129.5	238.1
ISWB 350	350	155.2	247.9	ISHB 350	350	191.6	301.6
				ISHB 350	350	198.0	313.5
ISWB 400	400	234.3	328.0	ISHB 400	400	280.8	388.7
				ISHB 400	400	288.2	402.7
ISWB 450	450	350.6	435.8	ISHB 450	450	392.1	485.5
				ISHB 450	450	403.5	502.2
ISWB 500	500	522.9	585.1				
ISWB 550	550	749.1	760.8				
ISWB 600_1	600	1062.0	987.8				
ISWB 600_2	600	1156.3	---				

Table 2. Moment of Inertia and Nominal Plastic Moment Capacity of
Some Representative AISC I-Sections.

Section Name	Depth d (mm)	I_{xx} (10^{-6} m^4)	M_p (kNm)
W 4 × 13	106	4.7	25.7
W 5 × 19	131	10.9	47.5
W 6 × 25	162	22.2	77.4
W 8 × 67	229	113.2	287.6
W 16 × 100	431	620.2	811.2
W 18 × 311	567	2897.0	3084.9
W 21 × 402	661	5078.0	4629.4
W 24 × 492	753	7950.0	6350.0
W 27 × 539	826	10613.9	7701.9
W 30 × 581	899	13735.6	9053.9
W 33 × 619	977	17398.5	10487.7
W 40 × 655	1108	23517.1	12536.1

LIST OF SYMBOLS

The following symbols are used in this paper:

C_{pr}	Factor to account for possible strain-hardening
C_w	Warping constant
E	Modulus of elasticity
E_s	Modulus of elasticity of steel
F_u	Ultimate (tensile) strength
F_y	Minimum specified yield strength
G_s	Shear modulus of steel
I	Moment of inertia
I_x, I_y	Moment of inertia about x and y axes
I_{xx}	Moment of inertia about strong axis of bending
J	Torsional constant
K	Effective column length factor
L	Length of column
M	Bending moment
M_p	Nominal plastic moment capacity
M_{pr}	Maximum probable overstrength based moment
M_y	Yield moment
P	Axial load
P_y	Axial yield load
R	Strength modification factor
R_c	Strength modification factor to account for compactness of section
R_s	Strength modification factor due to strain-hardening
R_y	Strength modification factor due to uncertainty in material yield strength
R_L	Strength modification factor due to account for flexural-torsional buckling
R_λ	Strength modification factor due to account for flexural buckling in compression

V	Shear force
V_p	Section plastic shear capacity using minimum specified yield
V_{pr}	Connection design shear (equilibrium compatible shear corresponding to overstrength based moment at member ends)
Y	Limiting strength used in von Mises yield criterion
Z	Plastic section modulus
b	Width of plate element; width of flange of section
d	Depth of section
r	Radius of gyration
t	Thickness of plate element
t_w	Thickness of web
Δ	Deformation
ε	Strain
ε_r	Rupture strain
ε_{sh}	Strain at initiation of strain-hardening
ε_u	Strain at maximum stress
ε_y	Yield strain
λ	Slenderness parameter
λ_c	Global slenderness parameter
λ_p	Limiting slenderness parameter for compact section
λ_{ps}	Limiting slenderness parameter for compact section with minimum guaranteed plastic rotation capacity
λ_r	Limiting slenderness parameter for non-compact section
φ	Curvature
φ_y	Yield curvature
μ	Ductility
μ_{sh}	Curvature ductility at initiation of strain-hardening
μ_u	Ultimate curvature ductility
μ_y	Curvature ductility at idealized yield
μ_φ	Curvature ductility
θ_p	Plastic rotation
σ	Stress
σ_{xx}	Normal stress
τ_{xz}	Shear stress
τ_y	Design shear stress

REFERENCES

[1]   IS 1893 Part 1, "Criteria for Earthquake Resistant Design of Structures, Part 1: General Provisions and Buildings", Bureau of Indian Standards, New Delhi, 2002.

[2]   AISC, "Specification for Structural Steel Buildings", American Institute of Steel Construction, Inc., Illinois, USA, 2005.

[3]   AISC, "Seismic Provisions for Structural Steel Buildings", American Institute of Steel Construction, Inc., Illinois, USA, 2005.

[4]   IS 800-1984, "Indian Standard Code of Practice for General Construction in Steel", Bureau of Indian Standards, New Delhi, 1995.

[5]   SP: 6(1), "Indian Standard Handbook for Structural Engineers: Structural Steel Sections", Indian Standards Institution, New Delhi, 1964.

[6] Paul, S., Murty, C.V.R. and Jain, S.K., "Drift-based Re-sizing of Steel Frames Including Joint Deformations," The Bridge and Structural Engineer, The Journal of ING-IABSE, 2000, Vol. 81, pp. 91-100.

[7] Penelis, G.G. and Kappos, A.J., "Earthquake – Resistant Concrete Structures", E & FN Spon, Great Britain, 1997.

[8] Englehardt, M.D. and Sabol, T.A., "Reinforcing of Steel Moment Connections with Cover Plates: Benefits and Limitations," Engineering Structures, 1998, Vol. 20, No. 4-6, pp. 249-260.

[9] Malley, J.O. and Frank, K., "Materials and Fracture Investigations in the FEMA/SAC PHASE 2 Steel Project," Proceedings of the 12th World Conference on Earthquake Engineering, 12WCEE, Paper No. 2544, Auckland, New Zealand, 2000.

[10] Popov, E.P., Amin, N.R., Louie, J.C. and Stephen, R.M., "Performance of Large Beam-to-Column Assemblies," Engineering Journal, AISC, 1986, First Quarter, pp. 9-23.

[11] Chen, W.F., and Lui, E.M., "Static Flange Moment Connections," Journal of Constructional Steel Research, 1988, Vol. 10, pp. 39-88.

[12] UBC, "Uniform Building Code", 1997 Edition, International Conference of Building Officials, Whittier, CA, USA.

[13] FEMA 267, "Interim Guidelines: Evaluation, Repair, Modification and Design of Welded Steel Moment Frame Structures," Report No. SAC-95-02, SAC Joint Venture, CA, USA, 1995.

[14] AISC, "Seismic Provisions for Structural Steel Buildings", American Institute of Steel Construction, Inc., Illinois, USA, 1997.

[15] FEMA 267, "Interim Guidelines Advisory No. 2 – Supplement to FEMA-267 Interim Guidelines: Evaluation, Repair, Modification and Design of Welded Steel Moment Frame Structures," Report No. SAC-99-01, Federal Emergency Management Agency, USA, 1999.

[16] FEMA 350, "Recommended Seismic Design Criteria for New Steel Moment-Frame Buildings," SAC Joint Venture, CA, USA, 2000.

[17] Arlekar, J.N. and Murty, C.V.R., "Capacity Design of Welded Steel MRF Connections," Proceedings of the 4th International Conference on Behaviour of Steel Structures in Seismic Areas (STESSA 2003), 9-12 June 2003, Naples, Italy.

[18] Goswami, R., Arlekar, J.N. and Murty, C.V.R., "Concerns on seismic moment-shear connections using available Indian hot-rolled I-sections," Journal of Structural Engineering, SERC Madras, December 2005 – January 2006, Vol. 32, No. 5, pp. 343-349.

[19] Lee, K.H., Goel, S.C. and Stojadiovic, B., "Boundary Effects in Steel Moment Connections," Paper No. 1098, Proceedings of the 12th World Conference on Earthquake Engineering, Auckland, New Zealand, 2000.

[20] Arlekar, J.N. and Murty, C.V.R., "Improved Truss Model for Design of Welded Steel Moment-Resisting Frame Connections," Journal of Structural Engineering, ASCE, March 2004, Vol. 130, No. 3, pp. 498-510.

[21] AISC, "Manual of Steel Construction", LRFD, 3rd Edition, American Institute of Steel Construction, Inc., Illinois, USA, 2003.

[22] CISC, "Handbook of Steel Construction", 8th Edition, Canadian Institute of Steel Construction, Toronto, Canada, 2004.

[23] BS 4-1, "Structural Steel Sections", Specification for Hot-Rolled Sections, British Standards Institution, London, UK, 2005.

FLUID VISCOUS DAMPER-BASED SEISMIC RETROFIT STRATEGIES OF STEEL STRUCTURES: GENERAL CONCEPTS AND DESIGN APPLICATIONS

Stefano Sorace [1,*] and Gloria Terenzi [2]

[1] Department of Civil Engineering and Architecture, University of Udine
Via delle Scienze 208, 33100 Udine, Italy
[2] Department of Civil and Environmental Engineering, University of Florence
Via S. Marta 3, 50139 Florence, Italy
* (Corresponding author: Phone: +39 432 558050; Fax: +39 432 558052; E-mail: stefano.sorace@uniud.it)

ABSTRACT: Two advanced seismic protection technologies, represented by a dissipative bracing system and a damped cable system, both incorporating fluid viscous dampers as passive control devices, are examined with special reference to their use in retrofitting steel structures. The essential characteristics and performance of the dampers and the two technologies, along with their analytical and computational modelling criteria, are recalled in the first part of this paper. A demonstrative design study concerning the application of both systems to an Italian pre-normative steel school building is then presented, by discussing the mechanical parameters, dimensions, layouts and locations selected for the relevant constituting elements. The advantages of the two rehabilitation hypotheses are assessed in terms of the mutual performance objectives formulated at a preliminary design stage, based on the results of the modal and non-linear dynamic analyses carried out during the final verification phase. Structural implementation and technical installation details are finally provided for both retrofit solutions.

Keywords: Steel structures; advanced seismic protection; seismic retrofit; damping; fluid viscous dampers; dissipative bracing; damped cables

1.   INTRODUCTION

A great number of steel buildings were designed in European earthquake-prone countries throughout the Sixties and early Seventies without any seismic provisions, due to the lack of reference Technical Standards at that time. In the past few years, a new public policy aimed at a seismic evaluation and retrofit of this stock of potentially unsafe structures was started, so as to improve their seismic performance substantially. These retrofit interventions are still generally based on conventional solutions for rehabilitation and strengthening (e.g., addition of reinforced concrete walls and/or traditional steel bracing systems, extensive enlargement of columns and beams, jacketing, etc). As an alternative, supplemental energy dissipation-based seismic protection strategies were recently adopted [1-3], by extending to steel structures the advanced technologies already applied to pre-normative reinforced concrete buildings.

Two special technologies belonging to this class, and namely a dissipative bracing (DB) system and a "damped cable" (DC) system, which incorporate pressurized silicone fluid viscous (FV) spring-dampers as protective devices, have been studied by the authors of this paper for several years. Numerical and analytical modelling; experimental characterization and verification; definition of design procedures; and technical implementation of the two technologies, were particularly developed within these research activities [4-9—dissipative braces; 10, 11, 7—damped cables]. The essential aspects of these studies, which paved the way for a practical use of both systems in the field of seismic retrofit of frame structures, are summarized in the following three sections of this paper. Then, two retrofit hypotheses of an Italian school building—well representative of the above-mentioned stock of pre-normative steel structures—are offered as demonstrative potential applications of the two rehabilitation strategies. A synthesis of the preliminary design structural analyses carried out on both systems, as well as of their best-location

search processes, is provided. Attainment of the mutual seismic performance objectives formulated for the two designs is checked against the results of final verification analyses. Details of the main components of the two design solutions, as well as of their installation and relevant structural interfaces, are finally presented.

2.   PRESSURIZED FLUID VISCOUS DEVICES

The distinguishing mechanical characteristics of the class of silicone FV dissipaters considered herein [12] are represented by: (a) pressurization of the inner casing, produced by a pre-load F_0 applied upon manufacturing, which ensures total self-centering capacity of the devices at the end of their dynamic response; and (b) flow of the silicone fluid through a very narrow annular space between the piston head and the inner casing surface, illustrated in the schematic drawings in Figure 1, which provides a highly non-linear damping capacity [13-15]. Furthermore, the considered FV devices also act as non-linear elastic springs due to the compressibility of the silicone fluid.
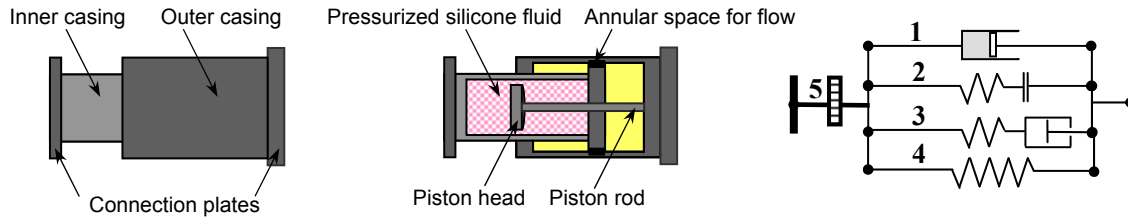
Figure 1. Schematic Front View and Cross Section of a FV Spring-Damper,
and Relevant Computational Model
(1. Non-linear Dashpot; 2. Gap; 3. Hook; 4. Non-linear Spring; 5. Internal Force F_0)

The $F_d(t)$ damping and $F_{ne}(t)$ non-linear elastic reaction forces of the pressurized FV spring-dampers can be expressed analytically as follows [16, 17, 14]:

$$F_d(t) = c\,\text{sgn}(\dot{x}(t))\,|\dot{x}(t)|^\alpha \tag{1}$$

$$F_{ne}(t) = k_2 x(t) + \frac{(k_1 - k_2)\,x(t)}{\left[1 + \left|\dfrac{k_1 x(t)}{F_0}\right|^R\right]^{1/R}} \tag{2}$$

where c = damping coefficient; $\text{sgn}(\cdot)$ = signum function; $|\cdot|$ = absolute value; α = fractional exponent, ranging from 0.1 to 0.2 for the highly non-linear dissipaters considered herein [14]; k_1, k_2 = stiffness of the response branches situated below and beyond F_0; and R = integer exponent, set as equal to 5 for pressurized devices [14]. An effective simulation of the response of FV spring-dampers is obtained by combining Eqs. 1 and 2, which are also incorporated in commercial numerical analysis programs, such as SAP2000NL [18]. In addition to a dashpot and a spring, the reaction forces of which are expressed by Eqs. 1 and 2, the computational model of a FV device is completed by a "gap" and a "hook" assembled in parallel, aimed at disconnecting the device when stressed in tension, and at stopping it when the maximum stroke is reached, respectively [9]. Within this model, also displayed in Figure 1, the static pre-load F_0 is imposed as an internal force to a bar linking the four elements to the interfaced structural elements. Further information on this class of dissipaters, including their rate-dependent behaviour and mechanical qualification procedures, can be found in [14, 19].

3. DISSIPATIVE BRACING SYSTEM

A typical design drawing of a FV spring-dampers–braces–beam connection of the DB system is illustrated in Figure 2, showing that the devices are installed, in parallel with the floor beam, at the tip of each couple of supporting steel braces. A half-stroke initial position is imposed to the pistons of both spring-dampers, so as to obtain symmetrical tension-compression response cycles, starting from a compressive-only response of the single devices. This position is obtained by introducing a pair of threaded steel bars through a central bored plate orthogonal to the interfacing plate of the two devices; the bars are connected at both ends to other two bored plates, threaded into the external casing of the spring-dampers. The axial force required to drive the pistons at their half-strokes is applied to the steel bars by a torque wrench, by acting on the nuts in contact with the two plates threaded on the devices. The terminal section of the external casing of each FV device is encapsulated into a steel "cap" hinged to two vertical trapezoidal plates welded to the upper horizontal plate of the assembly, which is fixed to the lower face of the floor beam. The caps constrain the spring-dampers to move with the same displacement as the floor beam. Thanks to the rigid support offered by the diagonal braces, mounted in an inverse-chevron configuration, this installation helps the devices exploit the entire interstory drift between the upper and lower floor across which they are placed. In order to prevent out-of-plane displacements of the DB system, two small protection plates are mounted in parallel to the vertical plate interfacing the devices, at 1 mm distance from its faces. A Teflon disk is placed on the inner faces of the protection plates, to avoid any frictional effects in case of accidental contact with the interfacing plate during seismic response.
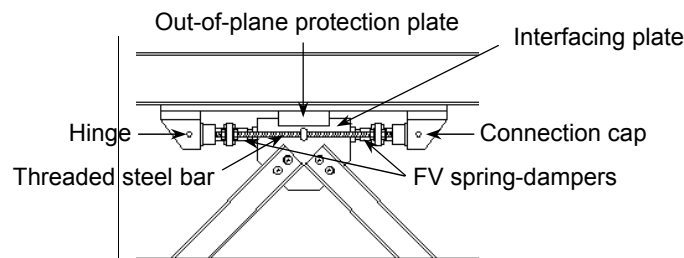
Figure 2. Drawing of a FV Spring-Damper–Braces–Beam Connection in a DB System

It can be observed that the tip installation of the FV devices over the supporting braces neutralizes the stiffening effects of the latter on the frame structure as soon as the static pre-load F_0 is exceeded. Indeed, beyond this threshold, the devices react with their low second-branch spring stiffness k_2. Owing to the in-series connection of FV devices and braces, this produces a limited global stiffness of the DB system, as compared to the one of the original frame structure. This avoids an undesired increase of spectral accelerations—and thus of story forces and shears—associated to the high stiffening effects typically induced by the installation of conventional undamped braces, as well as of dissipative technologies where dampers are installed in parallel with the diagonal braces.

Extensive experimental activities were carried out on the DB technology [5, 6, 8, 9], with a view to studying its practical application to the rehabilitation of steel and reinforced concrete buildings. They evidenced that high seismic performance levels of the tested structures are always attained after retrofit. Moreover, the experiments allowed developing a thorough calibration of the formulated analytical and numerical models, as well as of the proposed design methodology of the DB system [5, 9].

4.   DAMPED CABLE SYSTEM

As opposed to a dissipative bracing technology, the DC system, whose concept was originally formulated and elaborated in [20], considers structural response according to a global approach. As shown in Figure 3, this system includes pre-stressed high-grade steel cables, composed of greased and sheathed unbonded strands in standard production, the lower extremities of which are coupled with FV spring-dampers fixed to the foundation. The unbounded cables have sliding connections (contact being ensured by pre-stress) with the floor slabs, to which they are joined by steel curved deviators specially designed for the purpose. Since the cables extend following the horizontal building deflection, a DC system basically exploits the displacements that occur along the complete height of the building. Based on this operational principle, only one spring-damper for each cable—and thus a small total number of devices—must be incorporated into the building.

Figure 3 also illustrates the finite element model of the cable-floor sliding connection implemented in previous steps of this research. This represents the most critical aspect in the computational modelling of the DC system, where the cable is reproduced by a series of subsequent pre-stressed elastic beam elements, and the spring-dampers by the special assembly shown in Figure 1. The sliding contact is obtained by putting an elastic link between the centre of curvature C of the deviator and the cable joint B that simulates the cable-floor contact in deformed conditions, which constrains B to move along the trajectory determined by the deviator shape. The action of the cable is transmitted to the floor by the truss element AC connecting C to the A joint that represents the contact point in undeformed configuration. A "body constraint" kinematic condition is assigned to the AC truss, so as to impose equal displacements and rotations to A and C. The mechanism illustrated in Figure 3 corresponds to a "pulley" effect, which satisfactorily reproduces the real behaviour of the cable-floor sliding contact in the absence of friction within the deviator. In fact, due to the greasing of the constituting strands, negligible friction effects were actually observed during the dynamic experimental campaigns carried out on prototype cables, as well as on a full-scale mock-up building protected by the DC system [10, 11]. This allowed obtaining remarkable correlations of numerical predictions to test data.

As for the DB technology, high-level performance of the DC system emerged from the experimental programmes above, as well as from simulated designs developed to assess its effectiveness in seismic improvement of frame buildings, including the case study discussed in this paper.
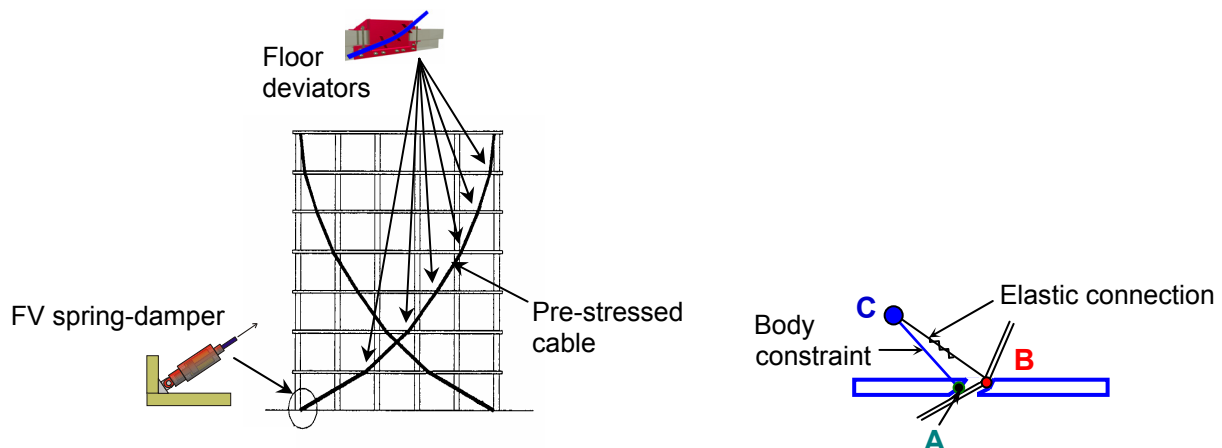
Figure 3. Scheme of a DC System, and Computational Model of a Cable-Floor Contact

5. CASE STUDY BUILDING

5.1 Characteristics and Performance Assessment in Original Conditions

The pre-normative structure examined herein was built in Florence city in the late Sixties. It consists of a two-story central body and two four-story wings, plus an adjacent two-story gym, separated from the main structure by a technical joint measuring 50 cm (wide enough to avoid pounding). Figure 4 shows two photographic views of one four-story wing during the demolition of the infills carried out at an early stage of architectural refurbishment works, and relevant viewpoints on the structural model of the buildings. The load-bearing skeleton of the main building and the gym consists of moment-resisting frames with semi-rigid flanged connections, a detail of which is offered in Figure 5. The beam-to-column connections were designed for yielding and ultimate flexural moments about 10% greater than the corresponding values of connected beams. The frame members and connection plates are made with steel similar to S 275 currently classified by the Italian Technical Standards, characterized by a yielding stress no lower than 275 MPa, and ultimate stress no lower than 430 MPa. The structures were designed for vertical and wind loads, and included no seismic provisions, according to the Italian Technical Standards of the time. No bracing systems or shear walls are included. The foundations are constituted by a mesh of reinforced concrete beams, 80 cm-high, and 100 cm-wide for perimeter frames, and 160 cm-wide for internal frames.
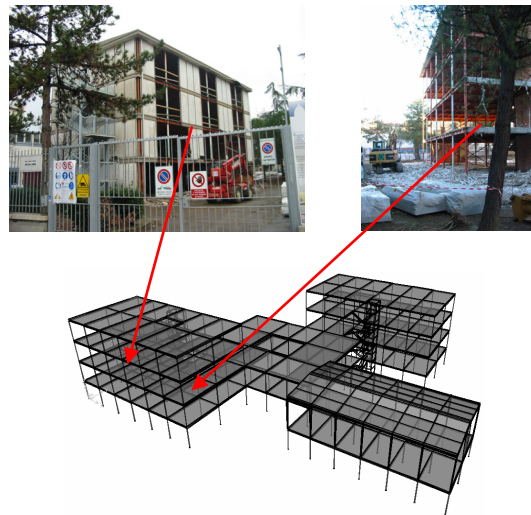
Figure 4. Views of the Building During the Demolition Phases of the Infills,
and Relevant Viewpoints on the Finite Element Model of the Original Structures

Figure 5. Typical Beam-to-Column Connection of the Original Structures

The remarkable asymmetries in plan and elevation of the main building make it very sensitive to torsional components of seismic response. Indeed, the first vibration mode of the main structure is purely rotational around the vertical axis z, as highlighted by the relevant modal shape plotted in Figure 6a, with effective modal mass (EMM) equal to 23.4% of the total seismic mass, and vibration period $T_1 = 1.69$ s. The second and third modes consi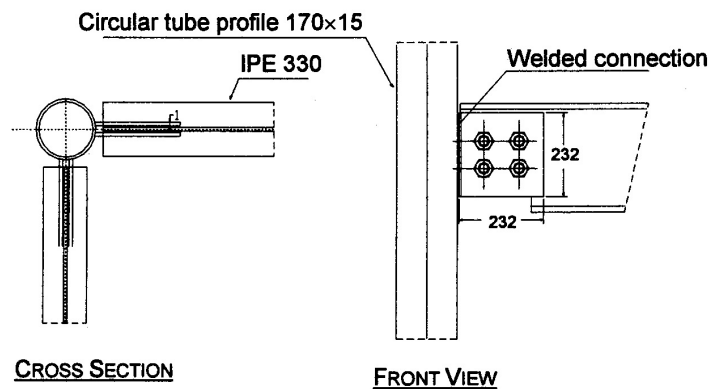st in a translational/torsional mix. EMMs equal to 77.7% along x axis, and 24.8% around z, are found for the second mode, with vibration period $T_2 = 1.62$ s; and equal to 79% along y axis, and 31.1% around z, for the third mode, with vibration period $T_3 = 1.41$ s. The first and second modes of the gym structure are purely translational, with vibration periods $T_{G1} = 0.98$ s, along x (EMM equal to 99.2%), and $T_{G2} = 0.84$ s, along y (EMM equal to 88.8%).

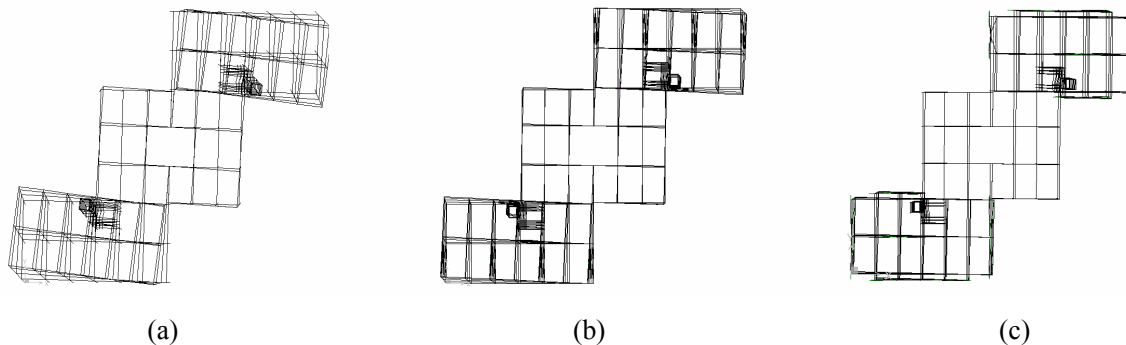(a)   (b)   (c)

Figure 6. First Modal Shapes of the Main Building Structure in
(a) Original, (b) DB-Retrofitted, and (c) DC-Retrofitted Configurations

A performance-based seismic assessment analysis was developed with the finite element model of the structure in its original conditions. Within this model, semi-rigid elastic-plastic connections—schematized by inelastic springs with a bilinear strain hardening moment-rotation constitutive relationship calibrated on the experimental data reported in [21]—were adopted to simulate the response of flanged beam-to-column joints. Furthermore, lumped plastic hinges with bilinear strain hardening moment-curvature response characteristics were introduced at the end sections of beams and columns, so as to reproduce their possible inelastic activity during the most severe seismic response phases. The performance analysis was carried out for the following two reference seismic hazard levels: basic design earthquake—BDE (with a 10% probability of being exceeded over 50 years), and serviceability earthquake—SE (50%/50). According to the Italian territory classification in force at the end of 2007 [22], when this design study was completed, the city of Florence is situated in seismic zone 2. The peak ground acceleration assigned to BDE for this zone is equal to 0.25 g, for rock-soil conditions ("A"-type soil). The foundation soil of the building is of "B" type, for which an amplifying coefficient of 1.25 must be applied to the "A"-soil acceleration. Moreover, an importance factor of 1.2 must be considered to account for the use of the building as a school. In total, a BDE peak ground amplitude of 0.375 g was adopted in the analyses. The SE amplitude was obtained by dividing the BDE amplitude by a factor of 2.5. Five artificial accelerograms generated from the response spectrum of the Italian Seismic Standards [22] (plotted in Figure 7, for seismic zone 2 and B-type soil), and scaled at the above-mentioned peak accelerations, were used as inputs for the non-linear dynamic assessment analyses. Relevant results, elaborated in mean values over the five ground motions, highlighted that: (a) the main structure does not meet the requirement of collapse prevention under BDE, along its weakest direction in plan (parallel to x), and shows the plasticization of a large number of beam-to-column connections and the activation of several plastic hinges in beams and columns, as well as the attainment of maximum transient inter-story drift ratios (i.e., the ratios of interstory drifts to story heights) of 5.59%, and maximum permanent drifts equal to 2.91%, in the second and third stories of the

building wings; (b) for the same direction, only a "limited safety" structural performance level, as defined in [23], is obtained for SE, which descend from maximum transient drift ratios of 2.22% for the same stories. A slightly better but still very poor performance emerged for the y direction, with attainment of near-collapse conditions (with maximum transient and permanent drift ratios of 4.31% and 1.93%, respectively), for the BDE level, and a "life safety" performance level (with maximum transient drift ratios of 1.82%), for SE. Similar results were obtained for the gym structure along both directions (maximum transient and permanent drift ratios of 4.18% and 1.56%—x, and 3.87% and 1.34%—y, for BDE; maximum transient drift ratios of 1.85%—x, and 1.63%—y, for SE). It can be noted that non-structural performance levels were not considered in this analysis, since partitions and infill panels not interacting with the structural skeleton were included in the architectural restoration project.
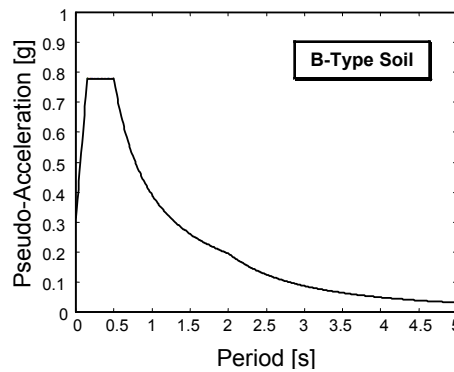

Figure 7. Response Spectrum of Standards [22] for Seismic Zone 2 and B-Type Soil

5.2   DB-Based Retrofit Hypothesis

The plan distribution of the dissipative braces incorporated in this retrofit solution is sketched in Figure 8, where the positions of the sixteen DB systems are outlined with rectangles. A global view of the computational model of the building incorporating the dissipative braces, and a cross section of one of the two wings, are shown in Figure 9. A typical damped brace incorporated in a story of the original structures is drawn in Figure 10. As highlighted in Figure 8, six systems parallel to x (BX1→BX6) and six systems parallel to y (BY1→BY6) were included in the main building, and two (BXG1, BXG2) plus two (BYG1, BYG2) systems in the gym. This distribution was aimed principally at reaching the lowest architectural impact of the rehabilitation intervention inside the two buildings and on their façades. In particular, the need to avoid obstructions to interior spaces (corridors, classrooms, meeting rooms, etc) caused to bring down to six the number of DB alignments in the main building along the weakest direction x. Then, within the limits imposed by this non-structural objective, the existing distances between centre of masses and centre of stiffness were reduced on each story, so as to constrain the torsion effects featuring the response of the original main building structure. This was obtained by placing the six DB alignments in parallel to y, along which lower architectural restraints exist, in the positions displayed in Figure 8.

As a result, the first mode of the main building in protected conditions is still rotational around the vertical axis (Figure 6b), but with EMM decreased to 11% of the total seismic mass. The new first vibration period, denoted by index "DB", is $T_{1DB} = 1.61$ s (5% lower than the T_1 value for the original structure). The second and third modes, again a translational/torsional mix, have EMMs increased to 81.4% along x, and decreased to 18.2% around z; and increased to 81.1% along y, and decreased to 23.6% around z, respectively. Relevant vibration periods are: $T_{2DB} = 1.55$ s (4% lower than T_2), and $T_{3DB} = 1.39$ s (2% lower than T_3). The new first and second mode vibration periods and EMMs of the gym structure are: $T_{G1DB} = 0.93$ s (5% lower than T_{G1}) and EMM equal to 99.9%, along x; and $T_{G2DB} = 0.79$ s (6% lower than T_{G2}) and EMM equal to 99.3%, along y.

The performance objectives of this retrofit hypothesis, as well as of the one based on the use of the DC technology, consisted in reaching, for the main building and the gym: (1) a "damage control" level for BDE, with at most some slight plasticizations in few beams, and 1.5% maximum interstory drift ratios; (2) "immediate occupancy" for SE, with an elastic response of all frame members, and 0.7% maximum drift ratios. The FV spring-dampers were selected by means of the energy-based design method discussed in [5, 9], which is briefly recalled below. The damping coefficient of the devices is selected by assigning them the capability of dissipating a prefixed fraction of the total seismic input energy computed for the structure on each story. This condition is expressed as follows

$$E_{Dj} = \beta_j E_{Ij} \tag{3}$$

where β_j is the imposed energy fraction for the j-*th* story; $E_{Dj} = \int_0^{t_c} c_{tj} |\dot{v}_j|^\alpha sgn(\dot{v}_j) \dot{v}_j dt$ is the energy

dissipated in the j-*th* story by the set of spring-dampers placed on that story, with t_c = instant at which the j-*th* story reaches the maximum interstory drift, c_{tj} = global damping coefficient characterizing the j-*th* story spring-dampers, $\dot{v}_j$ = relative velocity of the j-*th* story; and

$$E_{Ij} = \int_0^{t_c} m_j \ddot{v}_{tj} dv_g$$ is the "absolute" input energy [24] of the j-*th* story, where m_j = mass associated to

the j-*th* story, $\ddot{v}_{tj}$ = absolute j-*th* story acceleration, and v_g = ground displacement. The method starts from an initial choice of the set of β_j values governing (3), to be calibrated on the targeted reduction of interstory drift in protected conditions, for the BDE seismic level. Detailed criteria to perform this selection are presented in [9]. According to these criteria and considering that, based on the retrofit objectives postulated above, the target BDE-related drift reductions are equal to around 4, β_j values of 0.5 were selected for the most stressed stories, represented by the second and third ones of the main building. Moreover, following the suggestions reported in [9] again, β_j values multiplied by factors 0.8 and 0.4 were adopted for the first and fourth story, respectively, to account for the lower drift demands characterizing these levels. To summarize, the following set of β_j values was assumed for the main building: $\beta_1 = 0.4$, $\beta_2 = \beta_3 = 0.5$, and $\beta_4 = 0.2$. A mutual $\beta_j = \beta_1 = \beta_2$ value of 0.5 was fixed for the two-story gym.

Based on these energy fraction coefficients, an iterative search process was developed to locate the relevant set of c_{tj} values satisfying equation (3). This process helped identify the following rounded values of the damping coefficient of each device placed in the main building: $c = 24$ kN(s/m)$^\alpha$ (with $\alpha = 0.15$) at the first story, $c = 30$ kN(s/m)$^\alpha$ at the second and third story, and $c = 16$ kN(s/m)$^\alpha$ at the fourth story—x direction; and $c = 20$ kN(s/m)$^\alpha$ at the first story, $c = 24$ kN(s/m)$^\alpha$ at the second and third story, and $c = 14$ kN(s/m)$^\alpha$ at the fourth story—y direction. The rounded c values found for the gym were, for both axes: $c = 16$ kN(s/m)$^\alpha$ (first story), and $c = 24$ kN(s/m)$^\alpha$ (second story). The currently available FV spring-damper that is capable of supplying these damping demands and, at the same time, has a greater stroke than the maximum BDE-related drifts in protected conditions (as discussed in the next section), is characterized by the following mechanical properties [12]: nominal energy dissipation capacity E_n equal to 7 kJ, $F_0 = 18$ kN, stroke d_{max} equal to 100 mm (± 50 mm in the half-stroke initial position required by the DB system installation), and maximum attainable damping coefficient $c_{max} = 39$ kN(s/m)$^\alpha$. It can be noted that the different c values listed above are obtained, within the c_{max} limit, by imposing upon manufacturing different openings of the annular space between piston head and inner casing surface. The selected type of device represents the final design choice for this retrofit hypothesis. As bracing elements of the system, double UPN

160 European standard channel profiles were adopted for the three lower stories of the main building, and double UPN 120 profiles for the upper story, in both directions; and double UPN 160 profiles in both directions and on both stories of the gym building.
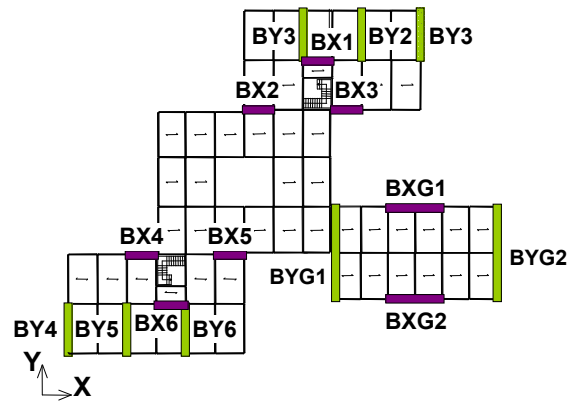

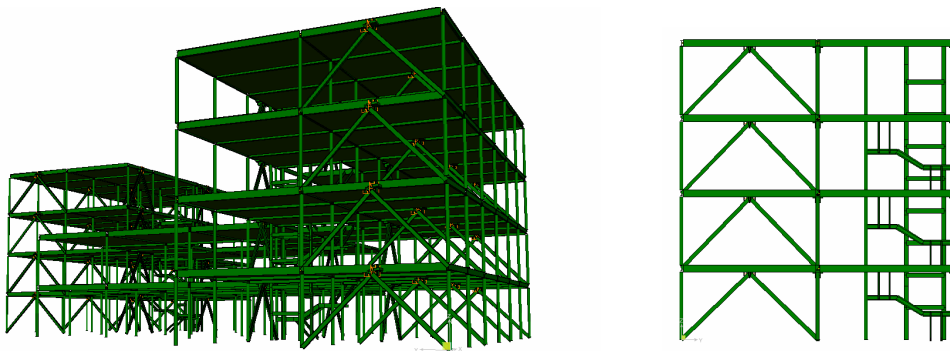Figure 8. Plan Distribution of the DBs included in the Relevant Retrofit Hypothesis

Figure 9. Global View of the Finite Element Model of the DB-Retrofitted Main Building Structure, and Cross Section Over a Four-Story Wing
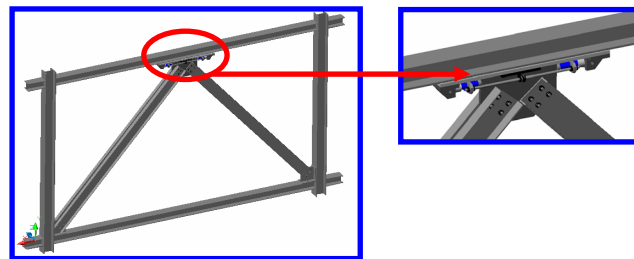

Figure 10. Global and Zoomed Views of a Typical Damped Brace

5.3   DC-Based Retrofit Hypothesis

Similarly to Figure 8, the plan distribution of the damped cables adopted in this retrofit solution is illustrated in Figure 11. In this case too, the location of the protective system was aimed at obtaining the best compatibility with the architectural and operational characteristics of the building, as well as reducing the torsional components of seismic response evaluated for the unprotected structure. Two views of the finite element model of the retrofitted structure zoomed on a four-story wing of the main building are shown in Figure 12. The image on the left shows that the perimeter cables parallel to the x axis (CX1, CX3, CX4 and CX6 alignments) are installed over external steel frames, specially built for the purpose at one meter distance from the perimeter frames, and connected to them by transversal steel beams. This helps avoid all obstructions to the large number of windows included in these fronts, crossed by cables over two (CX3 and CX4) or four spans (CX1 and CX6). The perimeter cables parallel to y, as well as the cables of the gym building, are mounted on the existing frames. Indeed, unlike the x alignments of the main building, obstructions to windows are avoided here by introducing small adjustments to the optimal shape of the cables selected at a preliminary design stage. The shape is represented by the so-called "constant horizontal force" (CHF) layout, which proved to be the most performing cable shape among several possible options examined in [10, 11]. For frame structures with minimum three stories, the CHF layout is characterized by a virtually constant increase in cable-floor angles when passing from one story to the upper one. As a consequence, the CHF configuration allows adopting identical cable-floor deviators on each intermediate story, with a non-negligible cut in costs as compared to the other cable shapes. A front view of the CHF layout designed for the CX1 and CX6 alignments of the main building, which features constant increases in angles by 15° (starting from 27° on the ground floor, to reach 72° on the top floor), is shown in Figure 13. A tridimensional view of the remaining external alignments of the main building (CX3 and CX4), and a front view of the CYG1 and CYG2 alignments of the gym, are illustrated in Figures 14 and 15, respectively.

Once positions and shapes have been fixed, the damping coefficients of the FV devices, and the cross sections and pre-stress forces of the cables were computed to meet the performance objectives mentioned in the previous section. FV spring-dampers were finally selected with the following characteristics: E_n equal to 150 kJ, $F_0 = 240$ kN, $d_{max} = 180$ mm, and $c_{max} = 276$ kN(s/m)$^\alpha$ ($\alpha = 0.15$). Several different damping coefficient values, ranging from 130 to 205 kN(s/m)$^\alpha$, were computed from the preliminary design analysis, and then imposed upon manufacturing to the dissipaters belonging to the various alignments. Cables made of 0.6" (15.2 mm) diameter strands up to a maximum of 23 (with corresponding net areas up to 3450 mm^2) were assumed.

The results of the modal analysis carried out in retrofitted conditions show that the first torsional mode of the main building disappears this time (Figure 6c). The new first and second modes—corresponding to the second and third modes of the original structure—are again mixed translational/torsional, with EMMs equal to 80.3% along x, and 29.8% around z; and equal to 71.2% along y, and 39.6% around z, respectively. The relevant vibration periods, denoted by index "DC", are as follows: $T_{1DC} = 1.20$ s (26% lower than T_2), and $T_{2DC} = 1.02$ s (28% lower than T_3). The new first and second mode vibration periods and EMMs of the gym structure are: $T_{G1DC} = 0.83$ s (15% lower than T_{G1}) and EMM equal to 99.8%; and $T_{G2DC} = 0.70$ s (17% lower than T_{G2}) and EMM equal to 96.3%. These values of the periods highlight that, unlike the DB system, global stiffening effects of the main building and the gym are obtained in the hypothesis of the DC technology installation. The results of the final verification analyses developed for both retrofit solutions are summarized in the following section.
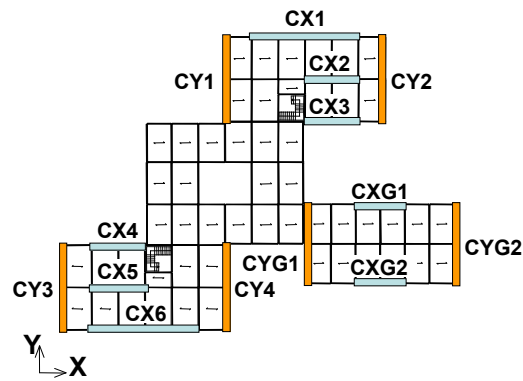
Figure 11. Plan Distribution of the DCs included in the Relevant Retrofit Hypothesis
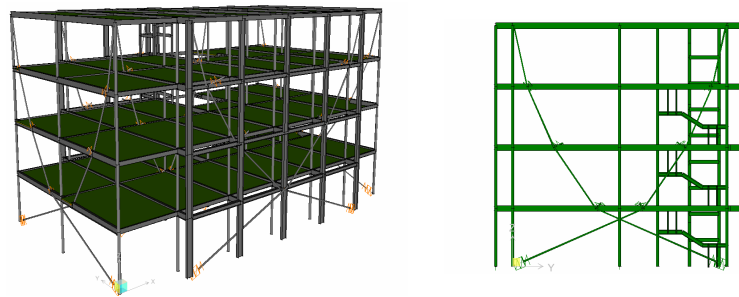

Figure 12. Detailed View and Cross Section of the Finite Element Model of a Four-Story Wing of the DC-Retrofitted Main Building Structure
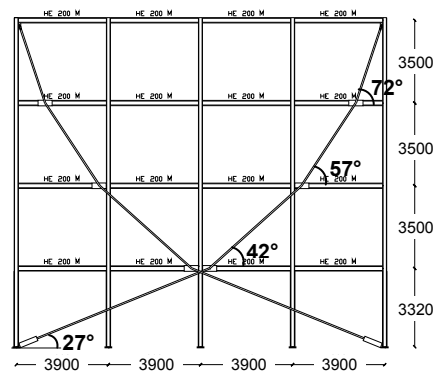

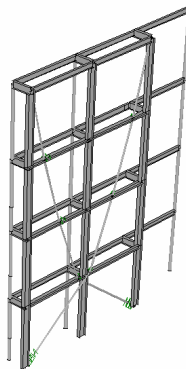Figure 13. Cable Layout for CX1 and CX6 External Alignments in the Main Building

Figure 14. Cable Layout for CX3 and CX4 External Alignments in the Main Building
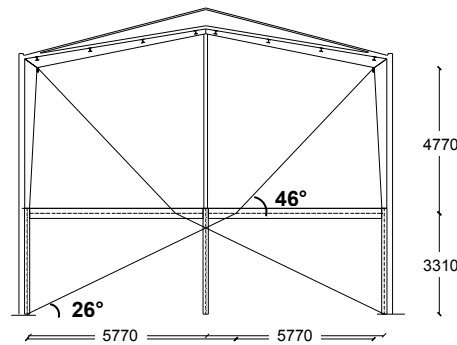
Figure 15. Cable Layout for CYG1 and CYG2 Alignments in the Gym Building

5.4   Final Non-Linear Dynamic Verification Analyses

The seismic analyses were carried out with a non-linear dynamic approach using the finite element models of the main building and gym structures. As way of example of the results obtained, the responses computed before and after retrofit in terms of maximum interstory drift profiles and story shears, for the main building in its weakest direction x and the seismic input applied along the same direction, are compared in Figures 16 and 17. In these graphs, mean values calculated over the assumed set of five input accelerograms are plotted for BDE and SE earthquake levels (Figure 16), and BDE only (Figure 17). Starting from maximum drifts of 76.7 mm for the original structure at SE (corresponding to drift ratios of 2.19%), 12.1 mm (0.35%) and 23.6 mm (0.67%) drifts come out for the DB and DC-based retrofit solutions (indicated as DC-R and DB-R in Figures 16 and 17), respectively. Both values are below the drift ratio limit of 0.7% set for the immediate occupancy level, assumed as a target performance for SE in rehabilitated conditions. Concerning BDE, the 195.6 mm maximum drift (5.59%) obtained in unprotected configuration is limited below 43.6 mm (1.24%, with a 4.49 reduction factor on the original drift)—DB, and 51.7 mm (1.47%, with a 3.78 reduction factor)—DC, none of them exceeding the 1.5% reference threshold for damage control level. Moreover, no plastic activity of beams and columns is noted in the response to BDE, which highlights a very satisfactory performance also in terms of local stress states. Similar drift reductions are observed for the strongest direction y, which also meets the SE and BDE-related drift limits for both retrofit solutions.

The comparative graphs in Figure 16 show very similar responses of the two protective systems for BDE, whereas performance improves further in the DB-based solution under the serviceability earthquake. This is the consequence of earlier activation of the FV spring-dampers incorporated in the dissipative braces, characterized by considerably smaller dimensions and damping capacity as compared to the devices included in the DCS. This effect has virtually no impact on the response to BDE, as it implies complete activation of all the devices incorporated in both retrofit schemes since the early phases of a seismic action. The benefits in terms of story shears range from 19.9% (base) to 27.3% (third story), for the DB system, and from 4.5% (base) to 10.6% (third story), for the DC system, as visualized in Figure 17. The greater advantages provided by the dissipative bracing technology in terms of shears are a consequence of the lower stiffening effects, and corresponding spectral accelerations, produced by it, as discussed in the previous sections.

However, an exhaustive evaluation of the benefits in terms of member stress states deriving from the reductions in story shears is obtained by separating the fractions of the total shears that are absorbed by the protective systems and the existing frame structures, respectively. The fractions absorbed by the two systems are represented, for each direction and story, by the sum of the reaction forces of the FV devices—DB, and the sum of the horizontal components of the reaction

forces exerted by the cables on the floors—DC. The resulting fractions for the two systems along x are as follows: 50.1% (fourth story), 47.4% (third story), 42.6% (second story), and 23.5% (first story)—DB; and 58.2%, 41.6%, 33.7%, and 29.1%—DC. By combining these values with the reductions in total shears reported above, the story shear fractions absorbed by the existing frames along x range from 38.9% (third story) to 62.1% (first story)—DB, and from 41.2% (third story) to 67.3% (first story)—DC of the story shears computed in original unprotected conditions. Similar shear fractions are observed for the y direction. This produces average proportional drops in the stress states of frame members along both directions.

At the same time, the axial forces of the columns involved in the protective system alignments, as well as of other columns, increase in retrofitted condition. Furthermore, some additional stress states in terms of axial force (induced by the horizontal components of the cable-floor contact forces), and flexural moment and shear (induced by the vertical components), are observed in the beams involved in the alignments where the DC system is incorporated. However, on the whole, very favourable variations in the global stress states are obtained when passing from original to retrofitted conditions, in addition to the above-mentioned improvements in terms of drifts, as highlighted by the results of the structural verifications carried out, which are commented at the end of this section.
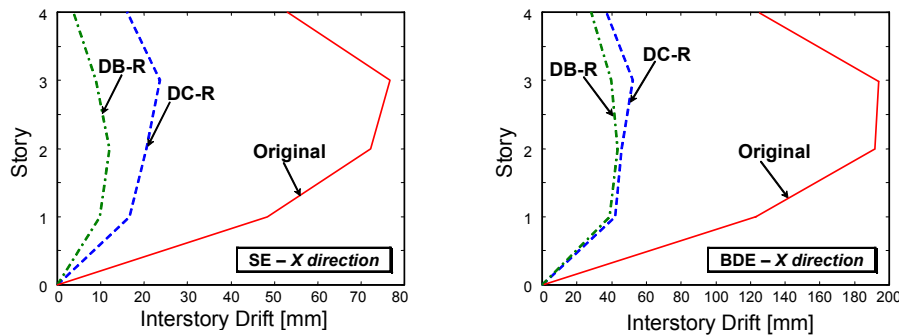
Figure 16. Maximum Interstory Drift Profiles for the Main Building (Mean Values)
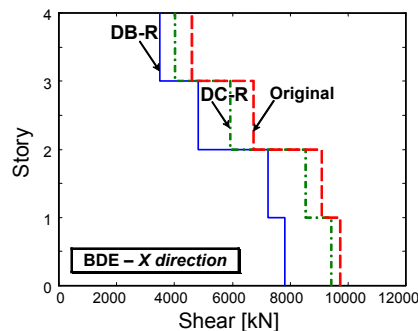
Figure 17. Maximum Story Shear Profiles for the Main Building (Mean Values)

Figure 18 illustrates the base shear time-histories obtained for the main building using the most demanding among the five input accelerograms, when applied along x, for both retrofit hypotheses. In these graphs, the first index of the T base shear force refers to the earthquake input direction, whereas the second refers to the projections of the force on the two axes. It can be drawn from the response time-histories that the T_{xy} orthogonal component of shear is equal to 2%—DB, and 3%—DC, as compared to the parallel one. This underlines a considerable restraint of torsional response effects ensured by both rehabilitation solutions. The maximum transient drift ratios obtained for the gym structure in protected conditions (all relevant to the second story, which is the

most stressed story in this building) are as follows: 0.57%—DB and 0.54%—DC, along x, and 0.48% and 0.59%, along y, for SE; 1.21%—DB and 1.16%—DC, along x, and 1.03% and 1.14%, along y, for BDE. The first story drifts are on average equal to 2/3 of the second story drifts. The maximum reductions of story shears for BDE are equal to 12.3% (first story) and 19.3% (second story)—DB, and 11.5% (first story) and 14.6% (second story)—DC, along x; and 16.8% (first story) and 25.7% (second story)—DB, and 13.8% (first story) and 18.9% (second story)—DC, along y. By considering the story shear fractions relevant to the two protection systems, the fractions absorbed by the existing frames result in the following portions of the total story shears in unprotected conditions: 37.8% (first story) and 57.4% (second story)—DB, and 40.3% (first story) and 62.6% (second story)—DC, along x; and 38.1% (first story) and 48.3% (second story)—DB, and 35.6% (first story) and 51.9% (second story)—DC, along y.
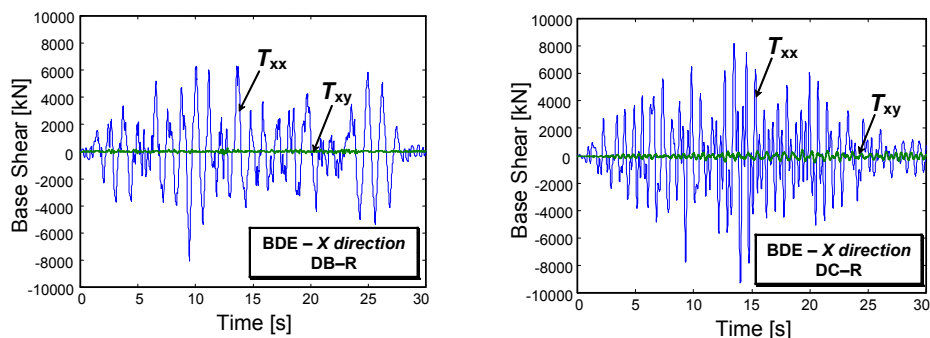
Figure 18. Base Shear Time-Histories for the Main Building
obtained from the Most Demanding Input Accelerogram

Figures 19 and 20 show the energy time-histories of the main building obtained from the most demanding BDE-scaled input accelerogram, for the two retrofit hypotheses and the x direction. The corresponding response cycles of a pair of FV devices mounted on the second story within the DB system, and a device incorporated in the DC system, are also plotted in these figures. The total energy dissipated by the twenty-four pairs of small-sized spring-dampers included in the DB-retrofit solution, and the twelve medium-sized spring-dampers adopted for the DC-retrofit one, is very similar, in both cases equal to around 82% of the total dissipated energy. The residual 18% is determined by the contribution of modal damping, fixed at 1% of critical on the first two vibration modes. A similar correlation between the energies dissipated by the two protective systems is observed also for the y direction, where the fraction absorbed by the FV devices is equal to around 88%—DB and 86%—DC of the total dissipated energy, and the gym structure, for which the following fractions are obtained: 90%—DB and 93%—DC, along x; 87%—DB and 89%—DC, along y.

The verifications carried out on the members of the original structures were met in both retrofitted conditions for all the beams of the main building, and all the elements of the gym. A strengthening intervention was required only for the first and second story columns of the main building involved in the alignments of the two systems, plus all the remaining first story columns and three central second story columns of the four-story wings, in the case of the DB-retrofit solution. Strengthening of columns consists in welding four equal leg angle profiles, linked one to another by horizontal lacings, according to a "box" arrangement in plan. No strengthening intervention was required for the foundations, which resulted within their safety domain after the retrofit interventions on the superstructure, for both rehabilitation hypotheses.
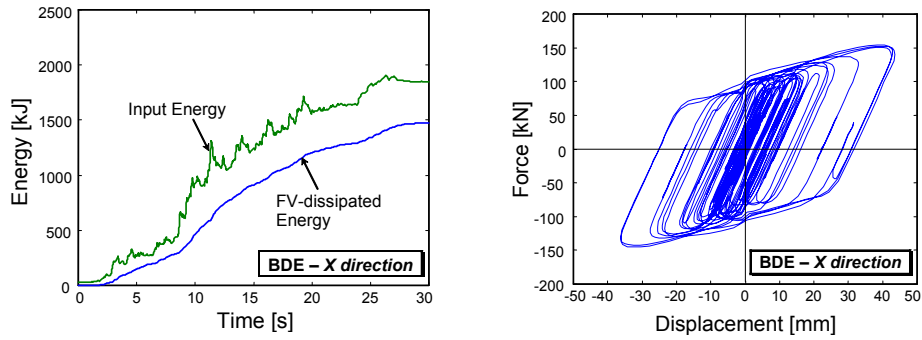
Figure 19. DB-Retrofitted Main Building: Energy Time-Histories and Response Cycles
of a Pair of Second Story FV Devices obtained from the Most Demanding Input Accelerogram
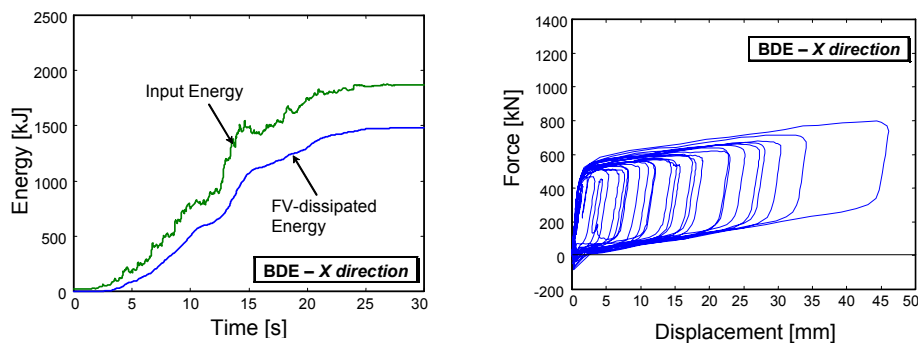
Figure 20. DC-Retrofitted Main Building: Energy Time-Histories and Response Cycles
of a FV Device obtained from the Most Demanding Input Accelerogram

A typical finishing solution for the installation of the DB system in frames that include windows is drawn in Figure 21, showing that no particular technical or cosmetic troubles arise even when braces cross the windows (which can be of a sliding type, in this case). A drawing and the geometrical details of a cable-floor deviator of the DC system are illustrated in Figure 22, in the hypothesis of a welded connection to the floor beams, which is the most suitable type for installation over additional external frames, like the CX1, CX3, CX4 and CX6 alignments in the main building. The shape remains identical for a bolted connection, which is preferably adopted when the cables are mounted on the existing frame structures, like the remaining alignments in this design. The cable diameters, which are at most 130 mm (23-strand element), external covering included, allow easy concealment of the system within infills and partitions, and thus help adopting standard architectural finishes, as in the case of the DB-based, or a conventional rehabilitation intervention.
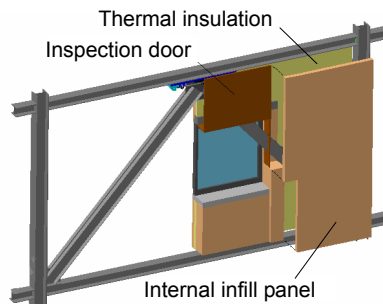
Figure 21. DB-Retrofit: Finishing Solution for the Frames Including Windows
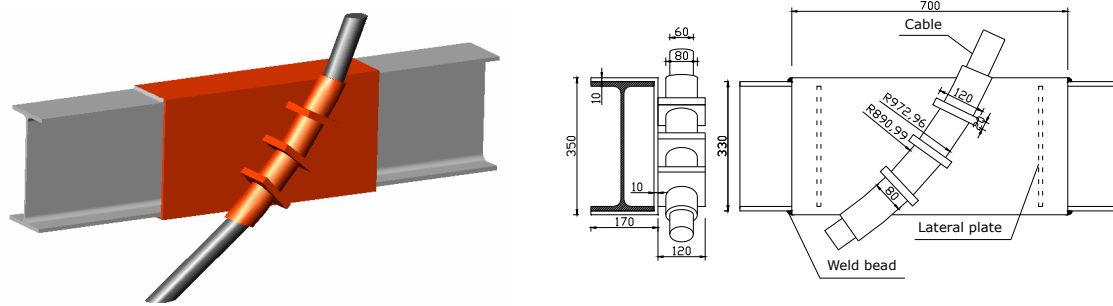
Figure 22. DC-Retrofit: View and Details of a Deviator
in the Hypothesis of a Welded Connection to the Floor Beam

The estimated costs of the structural works on the main building and the gym amount to 515,000 Euros (143 Euros/m^2) and 498,000 Euros (138 Euros/m^2) for the DB and DC-retrofit hypotheses, respectively. These costs are 5.3% and 8.5% lower than the cost (544,000 Euros, 151 Euros/m^2) of a conventional rehabilitation design based on the incorporation of traditional undamped bracings and general strengthening of the existing frame elements (for a total of 80% of columns, and 65% of beams), which was also developed to establish a price comparison with the two advanced protection solutions.

6.   CONCLUSIONS

The two seismic retrofit hypotheses formulated for the steel school building examined in this paper allowed reaching target design performance objectives with reasonably small-sized structural components in both techniques presented. This guarantees acceptable architectural impact and competitive costs as compared to traditional seismic design strategies. The remarks below are prompted by the results of the study.

− Starting from a very poor seismic performance of the original structures in terms of interstory drifts for both design earthquake levels, as well as of safety conditions in the existing frame members for BDE, incorporation of the protective systems helps meeting the strict performance requirements postulated for these retrofit designs, targeted by drift ratios not exceeding 0.7% (SE) and 1.5% (BDE), and a general elastic response for BDE. Furthermore, torsional response effects are substantially constrained in the main building, as highlighted by the modifications in vibration modes and associated masses, as well as by the values of the orthogonal components of base shears in comparison with the components parallel to the seismic input directions.

− As a consequence of the remarkable seismic improvement of the existing structures reached in both retrofit hypotheses, only a portion of first and second story columns of the main building needed strengthening. On the contrary, a general strengthening of beams and columns would be necessary in the case of a conventional rehabilitation design based on the use of undamped bracings.

– The notable correlation between the energies dissipated by the two protective techniques at BDE input level is a consequence of the mutual performance objectives pursued in these designs. Indeed, this led to determine comparable global damping capacities of the two systems, although referred to different passive control approaches (aimed at exploiting interstory drifts—DB, and total drifts—DC, respectively). By considering the noticeable interstory deformability in the original buildings, this difference motivates higher performance of the DB system observed at SE input level. The opposite normally occurs with stiffer pre-normative steel structures (for example, when they include some conventional bracing systems), as well as with reinforced concrete structures, where the DC technology offers the highest benefits at the serviceability earthquake level.

The realistic design simulations developed herein open encouraging perspectives for practical application of DB and DC systems to the stock of pre-normative steel buildings with similar characteristics to the case study.

ACKNOWLEDGEMENTS

REFERENCES

[1]   Constantinou, M.C., Soong, T.T. and Dargush, G.F., "Passive Energy Dissipation Systems for Structural Design and Retrofit", Monograph Series No. 1, MCEER–Multidisciplinary Center for Earthquake Engineering Research, Buffalo, NY, 1998.

[2]   Hanson, R.D. and Soong, T.T., "Seismic Design with Supplemental Energy Dissipation Devices", Publication MNO-8, EERI–Earthquake Engineering Research Institute, Oakland, CA, 2001.

[3]   Soong, T.T. and Spencer, B.F., "Supplemental Energy Dissipation: State-of-the-Art and State-of-the-Practice", Engineering Structures, 2002, Vol. 24, No. 2, pp. 243-259.

[4]   Sorace, S. and Terenzi, G., "Iterative Design Procedure of Fluid Viscous Devices Included in Braced Frames", Proceedings of EURODYN '99 – 4th European Conference on Structural Dynamics, Prague, Czech Republic, 1999, pp. 169-174.

[5]   Sorace, S. and Terenzi, G., "Large-Scale Experimental Validation of a Design Procedure for Damped Braced Steel Structures", Proceedings of STESSA 2003 – 4th International Conference on the Behaviour of Steel Structures in Seismic Areas, Naples, Italy, 2003, pp. 657-662.

[6]   Sorace, S. and Terenzi, G., "Comparative Experimental Investigation on a R/C Structure With/Without Damped Braces", Proceedings of the 13th World Conference on Earthquake Engineering, Vancouver, Canada, 2004, Paper No. 3461, CD-ROM.

[7]   Sorace, S. and Terenzi, G., "Retrofit Hypotheses of a Pre-normative Steel School Building by Fluid Viscous Damper-Based Technologies", Proceedings of ICSAS'07 – 6th International Conference on Steel and Aluminium Structures, Oxford, UK, 2007, pp. 196-203.

[8]   Molina, F.J., Sorace, S., Terenzi, G., Magonette, G. and Viaccoz, B., "Seismic Tests on Reinforced Concrete and Steel Frames Retrofitted with Dissipative Braces", Earthquake Engineering and Structural Dynamics, 2004, Vol. 33, No. 12, pp. 1373-1394.

[9]   Sorace, S., and Terenzi, G., "Seismic Protection of Frame Structures by Fluid Viscous Damped Braces", Journal of Structural Engineering, ASCE, 2008, Vol. 134, No. 1, pp. 45-55.

[10]   Sorace, S. and Terenzi, G., "An Advanced Seismic Protection Technology: The Damped Cable System", Proceedings of ASSCCA'03 – International Conference on Advances in Structures, Sydney, Australia, 2003, pp. 1185-1192.

[11]   Sorace, S. and Terenzi, G., "Verification of Damped Cable System in the Seismic Rehabilitation of Buildings", Proceedings of ERES'03 – 4th Conference on Earthquake Resistant Engineering Structures, Ancona, Italy, 2003, pp. 283-292.

[12]   Jarret SL, "Shock-Control Technologies", URL http://www.introini.info.

[13]   Terenzi, G., "Dynamics of SDOF Systems with Nonlinear Viscous Damping", Journal of Engineering Mechanics, ASCE, 1999, Vol. 125, No. 6, pp. 956–963.

[14]   Sorace, S. and Terenzi, G., "Non-Linear Dynamic Modelling and Design Procedure of FV Spring-Dampers for Base Isolation", Engineering Structures, 2001, Vol. 23, No. 12, pp. 1556-1567.

[15]   Sorace, S. and Terenzi, G., "Non-Linear Dynamic Design Procedure of FV Spring-Dampers for Base Isolation – Frame Building Applications", Engineering Structures, 2001, Vol. 23, No. 12, pp. 1568-1576.

[16]   Reinhorn, A.M., Li, C. and Constantinou, M.C., "Experimental and Analytical Investigation of Seismic Retrofit of Structures with Supplemental Damping: Part 1–Fluid Viscous Damping Devices", Report No. NCEER-95-0001, National Center for Earthquake Engineering Research, Buffalo, NY, 1995.

[17]   Pekcan, G., Mander, J.B. and Chen, S.S., "The Seismic Response of a 1:3 Scale Model R.C. Structure with Elastomeric Spring Dampers", Earthquake Spectra, 1995, Vol. 11, No. 2, pp. 249-267.

[18]   Computers and Structures Inc., "SAP2000NL. Structural Analysis Programs – Theoretical and Users Manual", Version No. 10.10, Berkeley, CA, 2007.

[19]   Sorace, S., Terenzi, G., Magonette, G. and Molina, F.J., "Experimental Investigation on a Base Isolation System Incorporating Steel-Teflon Sliders and Pressurized Fluid Viscous Spring Dampers", Earthquake Engineering and Structural Dynamics, 2008, Vol. 34, No. 2, pp. 225-242.

[20]   Pekcan, G., Mander, J.B. and Chen, S.S., "Balancing Lateral Loads Using Tendon-Based Supplemental Damping System", Journal of Structural Engineering, ASCE, 2000, Vol. 126, No. 8, pp. 896-905.

[21]   Davison, J.B., Kirby, P.A. and Nethercot, D.A., "Rotational Stiffness Characteristics of Steel Beam-to-Column Connections", Journal of Constructional Steel Research, 1987, Vol. 8, No. 1, pp. 17-54.

[22]   Italian Ministry of Public Works, "Norme Tecniche per il Progetto, la Valutazione e l'Adeguamento Sismico Degli Edifici [Technical Standards for the Design, Evaluation and Seismic Retrofit of Buildings]", OPCM 3431, 2005.

[23]   Federal Emergency Management Agency, "Prestandard and Commentary for the Seismic Rehabilitation of Buildings", FEMA 356, 2000.

[24]   Uang, C.M. and Bertero, V.V., "Use of Energy as a Design Criterion in Earthquake-Resistant Design", Report No. UCB–EERC 88/18, University of California at Berkeley, Berkeley, CA, 1988.

PLASTIC DESIGN AND SEISMIC RESPONSE
OF KNEE BRACED FRAMES

Maria Antonietta Conti [1], Luigi Mastrandrea [2] and Vincenzo Piluso [3,*]

[1] *Department of Civil Engineering, University of Salerno, via Ponte Don Melillo, 84084 Fisciano (SA), Italy*
[2] *Department of Civil Engineering, University of Salerno, via Ponte Don Melillo, 84084 Fisciano (SA), Italy*
[3] *Full Professor, Department of Civil Engineering, University of Salerno, via Ponte Don Melillo,*
84084 Fisciano (SA), Italy
*(Corresponding author: E-mail: v.piluso@unisa.it)

ABSTRACT: In this paper a design methodology aiming at the development of a collapse mechanism of global type for seismic resistant knee braced frames is presented. The proposed methodology is based on the assumption that the beam, brace and knee sections are known, while the column sections constitute the unknowns of the design problem. The design requirements are derived by means of the kinematic theorem of plastic collapse. In particular, column sections are obtained by imposing that the mechanism equilibrium curve corresponding to the global mechanism has to lie below those corresponding to all the undesired mechanisms within a displacement range compatible with the local ductility supply of knee elements.

The proposed design procedure has been implemented in a computer program and applied to design some knee braced frames. Successively, static and dynamic non-linear analyses have been carried out aiming at the evaluation of the performance of the designed braced frames in terms of collapse mechanism developed under seismic forces, energy dissipation capacity and global and local ductility demands.

Keywords: Knee braced frames; collapse mechanism; capacity design; limit design; non-linear analyses; equivalent moment; global ductility; local ductility

1.   INTRODUCTION

Knee braced frames (KBFs) constitute an innovative bracing solution. They are obtained by stiffening moment resisting frames by means of diagonal braces which are not connected to beam-to-column joints, but are restrained by means of short elements, namely "knee", which span, at each storey, between the column and the beam (Figure 1). The brace allows to limit interstorey drifts, while the knee element dissipates the earthquake input energy by means of transverse cyclic deformations in shear and/or bending. From this point of view, KBFs combine a lateral stiffness similar to that of concentrically braced frames (CBFs) with a ductile behaviour similar to that of eccentrically braced frames (EBFs). The main advantage with respect to EBFs is that damage is concentrated in a secondary member which can be easily replaced after destructive earthquakes.

The purpose of this study is to illustrate a design methodology able to guarantee a collapse mechanism of global type for KBFs. As universally recognised, the global mechanism is the main goal of the design process of a seismic resistant structure. In fact, among all the possible mechanisms, it allows the maximum global ductility and energy dissipation capacity. Even though modern codes provide the designer with the awareness of the importance of the collapse mechanism typology, the suggested design rules are only able to avoid soft storey mechanisms, without developing the global one. This is the case of member hierarchy criteria, proposed for different structure typologies, which are not able to grasp the distribution of internal actions to be developed to assure a collapse mechanism of global type.

In addition, all code member dimensioning rules are focused on the capacity design principles, while local ductility supplies are assured by means of technological suggestions, such as the use of web stiffeners in the case of members subjected predominantly to shear action (like links in EBFs). Conversely, there are no explicit rules to limit local ductility demands, i.e. to avoid the premature fracture of the dissipative zones.

The proposed design methodology is aimed at satisfying both these design requirements. The targets are represented on one hand by the development of a global mechanism for KBFs, leading to a satisfactory global ductility, and on the other hand by the local ductility control. This is obtained by means of the limit analysis, which allows to define appropriate design conditions and contemporary provides useful tools to account for local ductility demands. This methodology has already been developed in the case of moment resisting frames (Mazzolani and Piluso [1]) and eccentrically braced (Mastrandrea et al. [2]), providing satisfactory results, so that it is proposed as a general design approach for seismic resistant structures.

With reference to KBFs, in Figure 1 the possible collapse mechanisms for KBFs are depicted; among these the global one is to be achieved because it maximizes the energy dissipation capacity and the global ductility supply. These mechanisms, involving the knee elements as dissipative zones, are named type "a" mechanisms. With reference to the portal KB-frame, other mechanism typologies, namely type "b" and type "c", are depicted in Figure 2 (Conti [3]). Their pattern of yielding is characterised by the involvement of undesired non-dissipative zones, such as columns and beams, so that they are responsible of reduced energy dissipation capacity when compared to type "a" mechanisms. The aim of the proposed procedure is to provide a global mechanism of "a" type for multi-storey KB-frames.
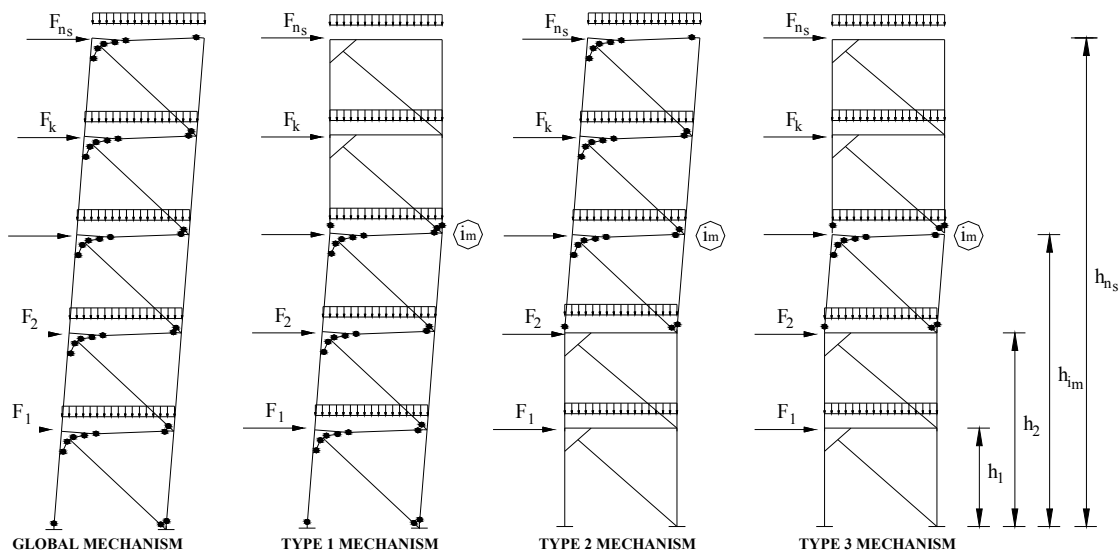

Figure 1. Collapse Mechanisms for a KB-Frame – Type "a" Mechanism
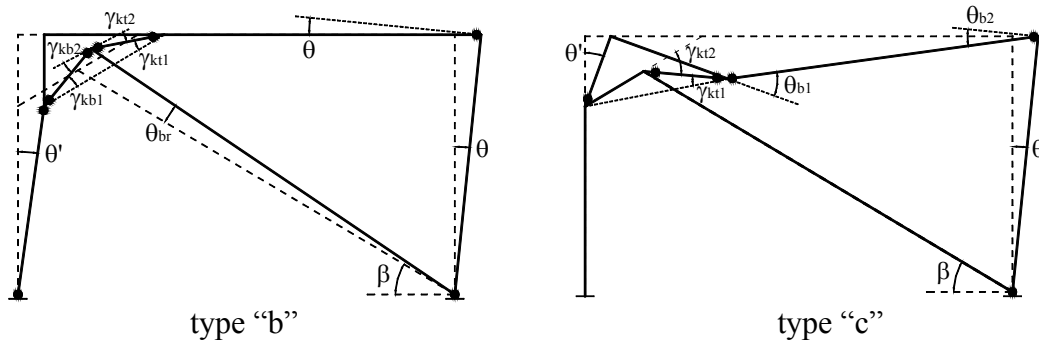
type "b"   type "c"

Figure 2. Collapse Mechanisms for a KB-Frame – Type "b" and Type "c" Mechanisms

In the proposed design methodology, it is assumed that the beam, brace and knee sections are known, while the column sections constitute the unknowns of the design problem. In particular according to *capacity design*, knee elements, which represent dissipative members, are sized considering the internal actions due to the code specified seismic horizontal forces, while the brace sections are designed to prevent buckling under the maximum internal actions which the fully yielded and strain-hardened knee elements are able to transmit. In addition, the beam sections are designed to resist vertical loads. Therefore, the unknowns of the design problem are constituted by the column sections which have to be defined so that the mechanism equilibrium curve corresponding to the global mechanism has to lie below those corresponding to all the undesired mechanisms within a displacement range compatible with the local ductility supply. It means that, according to the upper bound theorem, the global mechanism is the only mechanism which can be developed within a displacement range compatible with the local ductility supplies (Mazzolani and Piluso [4]).

In this paper, the procedure has been developed with reference to one bay KB-frames where the brace connections can be either continuous or pinned. For different KBF layouts the same procedure can be applied by properly accounting for the actual geometrical configuration.

2.   BEHAVIOUR OF KNEE ELEMENTS

The study of the plastic behaviour of knee elements shows several analogies with links in EBFs. In fact, both knee elements and links are subjected to transverse cyclic deformations, so that they are characterised by relevant shear actions (short elements). As a consequence, similarly to the case of links, the ultimate behaviour of knee elements is influenced by their length. In fact, the interaction between shear force and bending moment becomes more and more relevant as the member length increases, up to a value for which shear action becomes almost negligible (long elements). In particular, since the diagonal subdivides the knee element into two different parts, the whole dissipative member can be compared with two links, each one of length equal to $e/2$, being the brace-to-knee joint generally located at midspan. Starting from this consideration, the well known link classification (Kasai and Popov [5]) can be adopted also for knee elements, so that it is possible to recognise three knee typologies: *short knees*, *intermediate knees* and *long knees* (Conti et al. [6]). In particular, the plastic interaction domain provided by Neal [7] is assumed:

$$\left(\frac{|M|-M_f}{M_p-M_f}\right)^2 + \left(\frac{V}{V_p}\right)^2 = 1 \quad \text{for } M_f \leq |M| \leq M_p \tag{1}$$

$$V = V_p \quad \text{for } |M| \le M_f \tag{2}$$

being M_p and V_p the plastic moment resistance and the plastic shear resistance of the cross section, and M_f the contribution of the flanges to the plastic moment of the section. The interpretation of testing results is usually based on the evaluation of the plastic shear resistance as:

$$V_p = 0.6 f_y (d - 2 t_f) t_w \tag{3}$$

where f_y is the yield stress, d the knee section depth, t_f and t_w are the thicknesses of the flange and of the web, respectively, according to the American practice.

In addition, strain-hardening effects are accounted for on the basis of the experimental tests provided by Clement [8], which reveal an increase of the plastic resistance equal to 70% in average. This result is quite similar to the case of links in EBFs, for which, on the basis of several experimental tests performed worldwide (Popov and Engelhardt [9]; Ozaki et al. [10]), a 50% increase of the resistance is recognised, so that an overstrength factor of 1.5 is usually adopted in design practice (CEN [11]). Therefore, within *capacity design* methodologies, this overstrength has to be properly accounted for in predicting the internal actions transferred by the link to the non-dissipative zones of the structure, aiming to their dimensioning so that yielding cannot occur before links develop their ultimate resistance.

Following these issues, on the basis of the similarity between knee elements and links, an overstrength factor has to be adopted also in the case of KBFs. In fact, the dimensioning of non-dissipative zones cannot neglect this contribution, due to the consequent amplification of the internal actions transferred by knee elements. With this aim, an amplification factor of 1.7 can be adopted for KBFs, as suggested by Clement [8]. As a consequence, in this paper the ultimate interaction domain is obtained by means of an homothetic expansion of the plastic one using the amplification factor 1.7 ($V_u = 1.7V_p$, $M_u = 1.7M_p$, $M_{fu} = 1.7M_f$). In order to justify this kind of approach, it is useful to remark that, due to the discussed similarity, the well known ultimate conditions for links (Engelhardt and Popov [12]) can be extended also to knee elements, leading to the following relationships:

$$\begin{cases} V_u = \psi V_p \\ M_u = \dfrac{\psi}{2} e/2 \, V_p \end{cases} \quad \text{for } \; e/2 \le 1.6 \dfrac{M_p}{V_p} \tag{4}$$

$$\begin{cases} M_u = \psi M_p \\ V_u = 2 \dfrac{M_u}{e/2} \end{cases} \qquad \text{for } \; e/2 \ge 3.0 \dfrac{M_p}{V_p} \tag{5}$$

while a linear interpolation, depending on the $e/2$ value, is necessary in the case of intermediate knee elements. The coefficient ψ is the overstrength factor related to the strain-hardening, which assumes the value 1.5 in the case of links of EBFs and the value 1.7 in the case of knee elements as previously discussed. In Figure 3 a comparison with the proposed homothetic formulation is depicted, showing a good agreement. This kind of approach has been already used and validated in the case of links of EBFs (Mastrandrea et al. [13]).

In particular, the KB-frames analysed in this paper are characterised by short knees, i.e. knees for which $e/2 \leq 1.6 M_p/V_p$ (Kasai and Popov [5]). The chosen scheme is characterised by the following properties: the diagonal axis intersects the beam-column joint; diagonal is connected to the knee midspan section, so that the brace and the knee have the same inclination and, generally, they are not perpendicular. With reference to the collapse mechanism of a portal frame (Figure 4), the following relationships between the plastic rotation of each member and the plastic rotation of the column can be obtained:

$$\theta_{br} = \frac{H - e\,\mathrm{sen}\,\beta}{2H - e\,\mathrm{sen}\,\beta}\,\theta \tag{6}$$

$$\gamma_{kb1} = \frac{H}{e\,\mathrm{sen}\,\beta}\,\theta \qquad \gamma_{kb2} = \frac{2H\,(H - e\,\mathrm{sen}\,\beta)}{e\,\mathrm{sen}\,\beta\,(2H - e\,\mathrm{sen}\,\beta)}\,\theta \tag{7}$$

$$\gamma_{kt1} = \frac{H}{e\,\mathrm{sen}\,\beta}\,\theta \qquad \gamma_{kt2} = \frac{2H^2}{e\,\mathrm{sen}\,\beta\,(2H - e\,\mathrm{sen}\,\beta)}\,\theta \tag{8}$$

$$\theta_b = \frac{L}{L - d}\,\theta \tag{9}$$
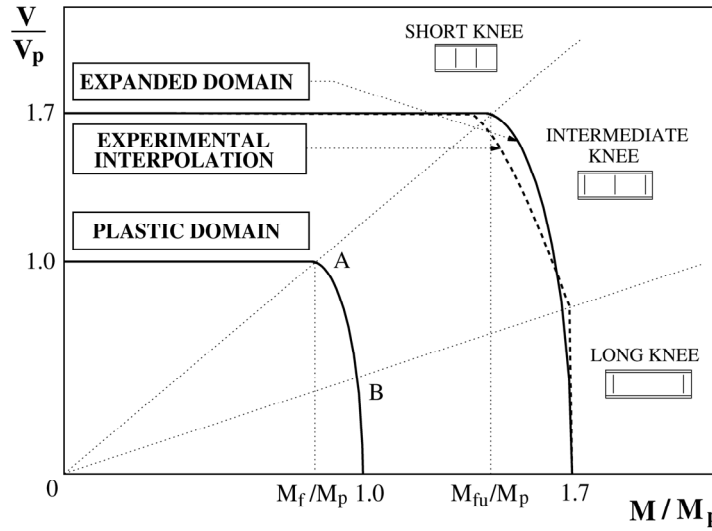
Figure 3. Plastic *V-M* Interaction Diagram and Comparison between Ultimate Interaction Domains.

Regarding the position *d* of the plastic hinge developed within the beam span (Figure 4), due to the superposition of vertical loads and horizontal forces, the maximum bending moment is attained at the abscissa (Mazzolani and Piluso [1]):

$$d = e\cos\beta \qquad \text{for} \quad q \leq q_{\lim} = \frac{4M_b}{(L - e\,\cos\beta)^2} \tag{10}$$

$$d = L - 2\sqrt{\frac{M_b}{q}} \quad \text{for} \quad q > q_{\lim} \tag{11}$$

being M_b the plastic moment of the beam.
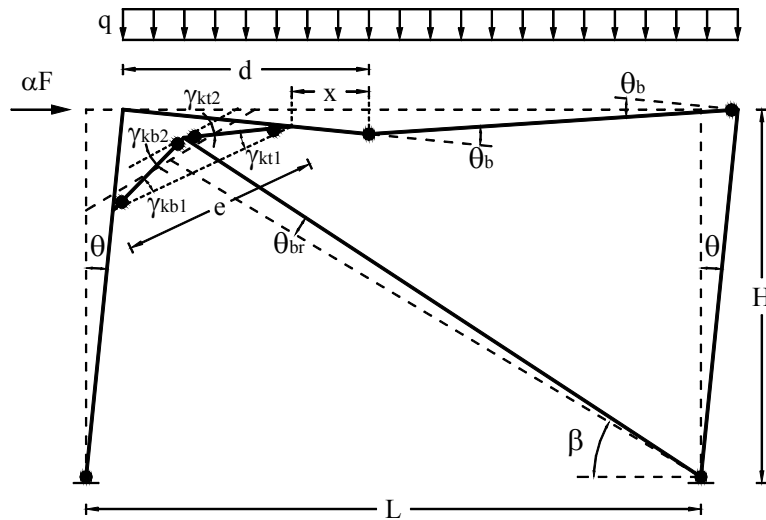
Figure 4. Collapse Mechanisms for a KB-Frame – Type "a" Mechanism

Furthermore, with reference to the collapse mechanism of a multi-storey KB-frame (Figure 5), it is useful to point out that the plastic rotation of braces provided by Eq. 6 is valid only for the first storey ($\theta_{br.1}$). In fact, it is easy to recognize that the plastic rotations of diagonals of second and upper storeys are affected by the rigid rotation θ of the column. The following relationships are obtained:

$$\theta_{br.i} = \frac{h_i}{2h_i - e_i \, \mathrm{sen}\, \beta_i}\, \theta \quad i = 2, 3, \dots, n_s \tag{12}$$

being h_i the interstorey height, e_i the length of the knee and β_i the inclination of the brace of the ith storey, respectively.
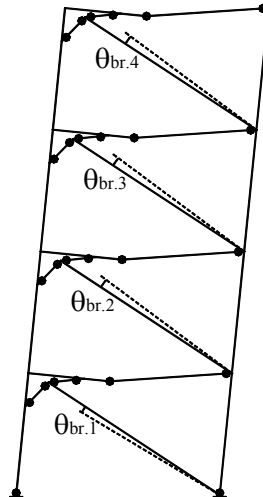
Figure 5. Global Collapse Mechanisms for a KB-Frame

Eqs. 7-8 show that plastic rotations of the two knees (bottom and top) are different. Furthermore, the rotation values are also different at the two ends within a single knee. In the case of dominant shear behaviour (*short knee*, i.e. $e/2 \leq 1.6\, M_p/V_p$ similarly to Kasai and Popov [5]) the previously discussed rotations represent angular distortions under the plastic shear action V_p. Nevertheless, a member subjected to uniform shear action is theoretically characterised by a uniform angular distortion along its length. Therefore, the circumstance for which different values of the rotation arise at the ends of the member leads to the conclusion that the deformation is partially due to the

shear action and partially due to the bending moment. In other words, even a short knee is subjected to moment-shear interaction, which is yet neglected in Eq. 2. For this reason, in the case of short knees an average value of the plastic deformation for each knee portion can be approximately adopted:

$$\overline{\gamma}_{kb} = \frac{\gamma_{kb1} + \gamma_{kb2}}{2} = \frac{H\left(4H - 3\,e\,\mathrm{sen}\,\beta\right)}{e\,\mathrm{sen}\,\beta\left(4H - 2\,e\,\mathrm{sen}\,\beta\right)}\theta \tag{13}$$

$$\overline{\gamma}_{kt} = \frac{\gamma_{kt1} + \gamma_{kt2}}{2} = \frac{H\left(4H - e\,\mathrm{sen}\,\beta\right)}{e\,\mathrm{sen}\,\beta\left(4H - 2\,e\,\mathrm{sen}\,\beta\right)}\theta \tag{14}$$

and it can be assumed that the ultimate behaviour of the member is governed only by the shear force. It is useful to note that, starting from Eqs. 13-14, the following value is obtained for the mean value of the plastic deformation of the entire knee element:

$$\overline{\gamma}_{k} = \frac{\overline{\gamma}_{kb} + \overline{\gamma}_{kt}}{2} = \frac{H}{e\,\mathrm{sen}\,\beta}\theta \tag{15}$$

Eq. 15 is particularly useful, because it provides, at least within the rigid-plastic analysis, a measure of the plastic engagement of the knee element as a function of the lateral displacement, i.e. the column rotation, of the entire structure.

Conversely, in the case of an intermediate knee, moment-shear interaction becomes significant so that plastic deformations provided by Eqs. 7-8 actually represent a combination of plastic shear deformation and plastic moment rotation. An analytical procedure to compute the ultimate resistances and the plastic deformations of intermediate knee elements, accounting for the interaction between bending moment and shear force, has been developed by the Authors within the framework of plastic design (Conti et al. [6]).

However, in this paper reference is made to the case of short knees. As a conclusion, with reference to the proposed KBF layout, Eqs. 6, 9, 12, 13 and 14 constitute useful tools for limit design applications, and they are applied within the design procedure described in the following Sections.

3. THE PROPOSED DESIGN METHODOLOGY

The aim of the proposed design methodology is to allow the dimensioning of KB-frames developing at collapse a mechanism of the global type. Therefore, the design requirements are derived to avoid the partial mechanisms depicted in Figure 1 (type 1, type 2 and type 3 mechanisms) and the less dissipative mechanism typologies depicted in Figure 2.

To this scope, the knee elements are recognised as dissipative zones, so that the design procedure is aimed to assure the engagement of all of them in the collapse mechanism. On the contrary, all other members have to remain in elastic range, except for the first order columns and diagonals (if not pinned at the ground) which participate to the kinematic mechanism.

The procedure is based on the assumption that knee, beam and brace cross sections are known, since they are designed on the basis of the code specified seismic actions as in the following clarified, while sections of the columns constitute the unknowns of the design problem. The design conditions are defined by imposing that the mechanism equilibrium curve corresponding to the

global mechanism has to lay below those corresponding to all the undesired mechanisms within a displacement range compatible with the local ductility supply. According to the upper bound theorem, these conditions guarantee that the true collapse mechanism of the structure is represented by the global failure mode.

3.1   Design of Dissipative Zones, Beams and Braces

According to *capacity design*, knee sections are designed on the basis of internal actions arising from the seismic forces prescribed by the codes. In particular, knee elements are dimensioned with reference to a simplified scheme assuming that the axial internal forces of braces of KBF are approximately equal to those of braces of a concentrically braced frame with the same geometry. Therefore, the axial force of the brace of the generic storey is evaluated as:

$$N_{d.i} = \frac{Q_i}{\cos\beta_i} \tag{16}$$

where Q_i is the seismic shear force of the ith storey and β_i is the brace inclination. The design value of shear force of the knee portion is obtained by means of the approximate translational equilibrium equation of the knee-to-brace joint in the direction orthogonal to the knee:

$$V_{knee.Sd.i} = \frac{N_{d.i}}{2} sen2\beta_i \tag{17}$$

This value underestimates the actual shear forces of the knee elements. Therefore, it is suggested the application to the value provided by Eq. 17 of an amplification factor equal to 1.25.

Similarly, the design axial force of the brace is obtained by maximising Eq. 17. In fact, being non-dissipative zones, braces have to be dimensioned on the basis of the maximum internal actions that dissipative zones are able to transmit, which means that the design axial force of each brace is obtained by assuming that the corresponding knee is yielded and strain-hardened up to its ultimate resistance, so that it is equal to:

$$N_{d.Sd.i} = \frac{2V_{knee.u.i}}{sen2\beta_i} \tag{18}$$

where $V_{knee.u.i} = 1.7\ V_{knee.p.i}$ is the ultimate shear force of the knee portion accounting for strain-hardening (Clement [8]). The brace sections are designed to prevent buckling under the axial force given by Eq. 18.

Finally, the beam sections are designed in order to resist to vertical loads.

3.2   Equilibrium Curves of Analysed Mechanisms

Where not specified, symbols adopted in the following formulas are referred to the notation reported in Appendix.

With reference to Figure 1, it is possible to recognise that, for a virtual rotation value $d\theta$ of columns and diagonals involved by the mechanism, the total internal virtual work is provided by the following relationship:

$$W_i = \left[tr(\mathbf{C}^T\mathbf{R_C}) + \mathbf{B_r^T}\mathbf{R_d} + 2\mathbf{B}^T\mathbf{R_b} + \mathbf{K_{kn}^T}\mathbf{R_{kn}} \right] d\theta \tag{19}$$

where the symbol *tr* denotes the trace of the matrix.

The external work, due to vertical and horizontal loads, is expressed by the following equation:

$$W_e = \left(\alpha\,\mathbf{F^T}\mathbf{s} + \mathbf{q^T}\mathbf{D_v} \right) d\theta \tag{20}$$

where α is the kinematically admissible multiplier.

By means of the virtual work principle, the kinematically admissible multiplier of horizontal forces, for the mechanisms depicted in Figure 1, is given by:

$$\alpha = \frac{tr(\mathbf{C^T}\mathbf{R_C}) + \mathbf{B_r^T}\mathbf{R_d} + 2\mathbf{B^T}\mathbf{R_b} + \mathbf{K_{kn}^T}\mathbf{R_{kn}} - \mathbf{q^T}\mathbf{D_v}}{\mathbf{F^T}\mathbf{s}} \tag{21}$$

The second-order work due to vertical loads is provided by the following relationship (Mazzolani & Piluso, 1997):

$$W_v = \mathbf{V^T}\mathbf{s}\,\frac{\delta}{H_0}\,d\theta \tag{22}$$

therefore, the slope of mechanism equilibrium curve is given by:

$$\gamma = \frac{1}{H_0}\frac{\mathbf{V^T}\mathbf{s}}{\mathbf{F^T}\mathbf{s}} \tag{23}$$

By means of Eqs. 21 and 23, the mechanism equilibrium curve is expressed by:

$$\alpha_c = \alpha - \gamma\,\delta \tag{24}$$

The following notation will be used to denote the parameters of the equilibrium curve of the considered mechanisms:

- $\alpha^{(g)}$ and $\gamma^{(g)}$ are, respectively, the kinematically admissible multiplier of horizontal forces and the slope of the softening branch of the α-δ curve, corresponding to the global type mechanism;
- $\alpha_{im}^{(t)}$ and $\gamma_{im}^{(t)}$ have the same meaning of the previous symbols, but they are referred to the i_mth mechanism of tth type.

In the case of global type mechanism (Figure 1), as all the storeys participate to the collapse mechanism, the shape vector of the horizontal displacements is given by $\mathbf{s}^{(g)} = \mathbf{h}$. In addition, all knee elements are involved so that the kinematically admissible multiplier is given by:

$$\alpha^{(g)} = \frac{\mathbf{M_{c1}^T}\mathbf{I} + \mathbf{B_r^T}\mathbf{R_d^{(g)}} + 2\mathbf{B^T}\mathbf{R_b^{(g)}} + \mathbf{K_n^T}\mathbf{R_{kn}^{(g)}} - \mathbf{q^T}\mathbf{D_v^{(g)}}}{\mathbf{F^T}\mathbf{s^{(g)}}} \tag{25}$$

where $\mathbf{I}$ denotes the unity vector of order n_c.

Furthermore, because all the storeys participate to the global mechanism, H_0 is equal to h_{ns}, and the slope $\gamma^{(g)}$ is obtained from Eq. 23 for $\mathbf{s} = \mathbf{s}^{(g)}$ and $H_0 = h_{ns}$.

With reference to the i_mth mechanism of type 1, the shape vector of the horizontal displacements can be written as:

$$\mathbf{s}_{\mathbf{i_m}}^{(1)} = \left\{ h_1, h_2, h_3, ..., h_{i_m}, h_{i_m}, h_{i_m} \right\}^T \tag{26}$$

where the first element equal to h_{im} corresponds to the i_mth component. The kinematically admissible multiplier corresponding to the i_mth mechanism of type 1 is given by:

$$\alpha_{i_m}^{(1)} = \frac{\mathbf{M}_{\mathbf{c1}}^{\mathbf{T}}\mathbf{I} + \mathbf{B}_{\mathbf{r}}^{\mathbf{T}}\mathbf{R}_{\mathbf{d_{i_m}}}^{(1)} + \mathbf{M}_{\mathbf{ci_m+1}}^{\mathbf{T}}\mathbf{I} + 2\mathbf{B}^{\mathbf{T}}\mathbf{R}_{\mathbf{b_{i_m}}}^{(1)} + \mathbf{K}_{\mathbf{n}}^{\mathbf{T}}\mathbf{R}_{\mathbf{kn\,i_m}}^{(1)} - \mathbf{q}^{\mathbf{T}}\mathbf{D}_{\mathbf{v_{i_m}}}^{(1)}}{\mathbf{F}^{\mathbf{T}}\mathbf{s}_{\mathbf{i_m}}^{(1)}} \tag{27}$$

In addition, only the first i_m storeys participate to the collapse mechanism, so that $H_0 = h_{im}$. As a consequence, the slope of the mechanism equilibrium curve is still computed through Eq. 23, but assuming $\mathbf{s} = \mathbf{s_{im}}^{(1)}$ and $H_0 = h_{im}$.

The expressions of the kinematically admissible multipliers $\alpha_{im}^{(2)}$ and $\alpha_{im}^{(3)}$, and of the slopes $\gamma_{im}^{(2)}$ and $\gamma_{im}^{(3)}$, of the mechanism equilibrium curves corresponding to type 2 and type 3 mechanisms, respectively, can be obtained by means of the same procedure.

3.3   Design Conditions for Failure Mode Control

According to the upper bound theorem of limit design, the cross-sections of columns have to be defined so that the kinematically admissible horizontal force multiplier corresponding to the global type mechanism is the minimum among all the kinematically admissible multipliers.

This condition is sufficient to guarantee the desired mechanism only in the case of rigid-plastic behaviour of the structural material, so that no displacements are developed until the collapse mechanism is reached. Conversely, the actual behaviour is elastoplastic, and it is characterised by significant displacements before the collapse mechanism is completely activated. These displacements are responsible of second order effects which cannot be neglected in the design process. Therefore, to account for second order effects, the design conditions have to be defined by imposing that the mechanism equilibrium curve corresponding to the global type mechanism has to lie below those corresponding to all the other mechanisms within a displacements range compatible with the plastic deformation capacity of members (Figure 6). This represents the extension of the kinematic theorem of plastic collapse to the mechanism equilibrium curve concept. Consequently, the design conditions are provided by the following equations:

$$\alpha^{(g)} - \gamma^{(g)}\delta_u \leq \alpha_{i_m}^{(t)} - \gamma_{i_m}^{(t)}\delta_u \tag{28}$$

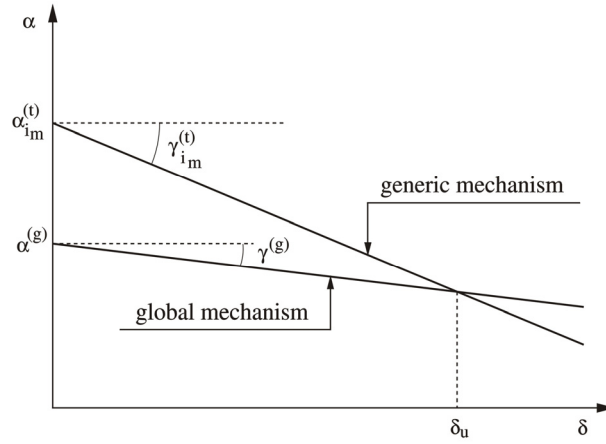for $i_m = 1, 2, ..., n_s$ and $t = 1, 2, 3$.

Figure 6. Mechanism Equilibrium Curves

It is useful to note that the displacement δ_u has to be compatible with the local ductility supply of dissipative zones and it assumes the meaning of design displacement, so that the proposed design methodology leads both to failure mode and local ductility control.

Substituting the values of $\alpha^{(g)}$, $\gamma^{(g)}$, $\alpha_{im}^{(1)}$ and $\gamma_{im}^{(1)}$ in Eq. 28, the conditions to be satisfied to avoid type 1 mechanisms are obtained. In particular, the following design conditions are obtained ($i_m = 1$, 2, …, n_s):

$$\frac{\mathbf{M_{c1}^T I} + \mathbf{B_r^T R_d^{(g)}} + 2\mathbf{B^T R_b^{(g)}} + \mathbf{K_n^T R_{kn}^{(g)}} - \mathbf{q^T D_v^{(g)}}}{\mathbf{F^T s^{(g)}}} - \frac{\mathbf{V^T s^{(g)}}}{\mathbf{F^T s^{(g)}}}\frac{\delta_u}{h_{n_s}} \leq$$

$$\leq \frac{\mathbf{M_{c1}^T I} + \mathbf{B_r^T R_{d_{i_m}}^{(1)}} + \mathbf{M_{ci_m+1}^T I} + 2\mathbf{B^T R_{b_{i_m}}^{(1)}} + \mathbf{K_n^T R_{kn\,i_m}^{(1)}} - \mathbf{q^T D_{v_{i_m}}^{(1)}}}{\mathbf{F^T s_{i_m}^{(1)}}} - \frac{\mathbf{V^T s_{i_m}^{(1)}}}{\mathbf{F^T s_{i_m}^{(1)}}}\frac{\delta_u}{h_{i_m}}$$

(29)

In the same way, the conditions to be satisfied in order to avoid type 2 and type 3 mechanisms can also be obtained. The plastic section moduli of columns, which constitute the unknowns of the design problem, can be determined satisfying simultaneously these $3n_s$ design conditions.

Moreover, it is necessary to guarantee the development of type "a" mechanism, rather than type "b" or type "c". This is made by means of additional design rules, which are still based on the application of the kinematic theorem of plastic collapse. In particular, by comparing the collapse configurations depicted in Figure 2 and Figure 4, it is easy to recognise that the deformed shapes are similar (i.e. the same top-sway displacement is obtained for each structure if the same θ column rotation is considered), so that the external virtual work due to an horizontal force F is given by:

$$W_{e.F} = \alpha\,F\,\delta = \alpha\,F\,H\,\theta$$

(30)

independently of the mechanism typology. Therefore, by applying the virtual works principle, the following relationship is obtained for the horizontal multiplier α ($t = a, b, c$):

$$W_i^{(t)} = W_{e.q}^{(t)} + W_{e.F}^{(t)} = W_{e.q}^{(t)} + \alpha^{(t)} F\,H\,\theta$$

(31)

(32)

$$\alpha^{(t)} = \frac{W_i^{(t)} - W_{e.q}^{(t)}}{F\,H\,\theta}$$

According to the kinematic theorem of plastic collapse, the requirements to be fulfilled to avoid undesired collapse mechanisms are obtained by imposing that the kinematically admissible horizontal force multiplier corresponding to type "a" collapse mechanism is less than those corresponding to type "b" and type "c" collapse mechanisms. Therefore, the following equations have to be satisfied:

$$\alpha^{(a)} \leq \alpha^{(b)} \quad \text{and} \quad \alpha^{(a)} \leq \alpha^{(c)} \tag{33}$$

leading to the required design criteria, respectively:

$$M_c \geq \frac{H - e\,\mathrm{sen}\,\beta}{H + e\,\mathrm{sen}\,\beta}\left[M_b\,\frac{L+d}{L-d} - M_d\,\frac{e\,\mathrm{sen}\,\beta}{2H - e\,\mathrm{sen}\,\beta}\right] \tag{34}$$

$$M_c \geq \frac{e\,\mathrm{sen}\,\beta}{H - e\,\mathrm{sen}\,\beta}\left\{ M_d\,\frac{H - e\,\mathrm{sen}\,\beta}{2H - e\,\mathrm{sen}\,\beta} - \frac{V_u\,H}{2\,\mathrm{sen}\,\beta} - M_b\left[\frac{H(H + e\,\mathrm{sen}\,\beta)}{e\,\mathrm{sen}\,\beta(H - e\,\mathrm{sen}\,\beta)} - \frac{L+d}{L-d}\right] + \frac{qL(L-d)}{2}\right\} \tag{35}$$

which are obtained by means of the plastic rotations depicted in Figure 2 (Conti et al. [6]). With reference to a multi-storey KBF, in order to avoid mechanisms characterised by the alternation of type "a", type "b" and type "c" configurations at different levels, it is sufficient to check that Eqs. 34-35 are satisfied for each storey of the structural system.

Therefore, taking into account all the previously discussed conditions and requirements, handling the previous formulations and pointing out attention on technological conditions, similarly to the case of moment-resisting frames (Mazzolani and Piluso [1]), it is possible to define a design algorithm which allows, by means of an iterative process, to obtain the design solution in terms of column plastic moments (Conti et al. [14]). Due to the presence of the axial forces, these moments represent a reduced value if compared to the resistance provided in simple bending.

Then, the design column sections are obtained by coupling, for each column, the determined plastic moment with the axial force occurring in the collapse state. This axial force can be estimated by means of simplified equilibrium equations. In particular, the column axial force is provided by the vertical translational equilibrium equation of column-to-knee joint and is equal to:

$$N_{c.i} = \sum_{j=i}^{n_s} V_{knee.u.j}\,\cos\beta_j \tag{36}$$

Aiming at the evaluation of its accuracy, the proposed design procedure has been implemented into a computer program and applied to dimension an adequate number of KBFs whose seismic response has been investigated by means of non-linear static and dynamic analyses. In particular, reference is made to the case of short knees, which is the most frequent, due to the length of such members. In next Sections the results of these analyses are presented and discussed.

4.   NON-LINEAR KNEE MODEL: THE EQUIVALENT MOMENT CONCEPT

In order to carry out non-linear analyses for KBFs, the post-elastic behaviour of each element has to be properly modelled. To this scope, due to their shear plastic involvement, the geometrical inclination of the knees introduces some difficulties in their non-linear modelling. In fact, plastic shear deformations for each knee portion are the result of both horizontal and vertical displacements occurring at the member ends. Several computer programs, as for example DRAIN-2DX (which has been used to carry out dynamic non-linear analyses), do not provide the user with an adequate predefined element in their library for modelling a non-linear behaviour in shear, particularly in the case of inclined members.

Therefore, to easily simulate the actual non-linear behaviour of a knee element it is useful to define an equivalent element with plastic hinges in simple bending at its ends. This is obtained by imposing the equivalence between the internal work developed by each actual knee portion and the internal work corresponding to the simplified theoretical model.

The internal virtual work developed, for example, by the bottom knee portion is equal to:

$$L_{i.kb} = \int_0^{e/2} V \, \gamma_{kb} \, dz = V_p \, \bar{\gamma}_{kb} \, \frac{e}{2} \tag{37}$$

where $\bar{\gamma}_{kb}$ is provided by Eq. 13. The internal virtual work developed by the equivalent model in simple bending is given by:

$$L_{i.kb} = 2 \, M_{eq.p} \bar{\gamma}_{kb} \tag{38}$$

being $M_{eq.p}$ the so defined *equivalent moment* in plastic conditions. The equivalence between Eq. 37 and Eq. 38 provides the following expression:

$$M_{eq.p} = V_p \frac{e}{4} \tag{39}$$

which is easily obtained also in the case of the top knee portion. The same procedure can be extended to the ultimate conditions, when the strain-hardening effect influences the behaviour of the member. To this scope, Eqs. 37-38 are applied considering the shear resistance $V_u = 1.7V_p$, so that the ultimate equivalent moment is obtained:

$$M_{eq.u} = V_u \frac{e}{4} = 1.7 M_{eq.p} \tag{40}$$

The Eqs. 39-40 allow to deal with a model in which the shear behaviour of knee elements is taken into account by means of an equivalent element exhibiting flexural behaviour, easier to be handled. However, a validation of the approach has been performed by means of a complete finite element model. In particular, a knee element has been studied by means of STRAUS7 computer program. The cross section is represented by an HEA 200 standard profile. It has been subdivided in several areas, both for the flanges and for the web, while the fillet of the web-to-flange connection has been neglected. An elastic-perfectly plastic law has been assigned to each of them, by assuming a yield stress equal to 275 MPa. The length of the member is equal to 100 cm, and the edge restraints have been modelled as rigid. In order to simulate the interaction with the brace element, a rigid body has been assigned to the middle of the knee element with a length equal to 20 cm representing the

interaction zone due to the brace. Along this part, a monotonically increasing transversal load has been applied, so that the non-linear force-displacement curve has been carried out. In Figure 7 and Figure 8 the FEM model and the distribution of the Von Mises ideal stresses at first yielding are depicted. It is useful to note that at first yielding an ideal stress equal to f_y is almost reached on the whole web panel (Figure 8).
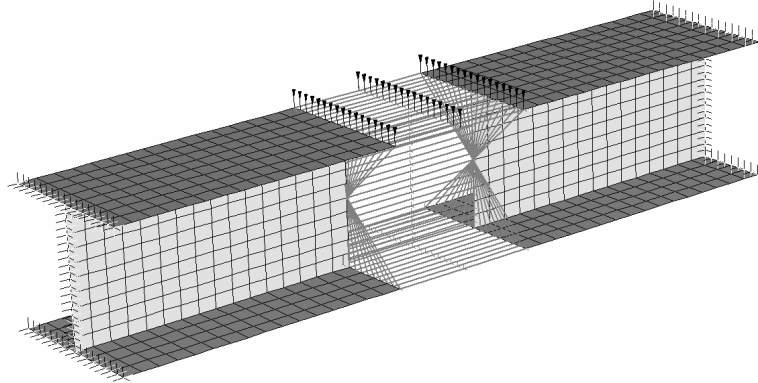

Figure 7. STRAUS7 FEM Model

The described complete FEM model has been compared with the equivalent model in simple bending previously introduced. To this scope, a scheme geometrically equal to the previous one has been analysed by means of SAP2000 computer program. In this case, the knee element has been modelled by means of three beam-column elements, two representing the knee portions and one representing the rigid body in the middle. The post-elastic behaviour has been taken into account by means of plastic hinges in simple bending at the ends. The plastic hinges have been calibrated with an elastic perfectly-plastic moment-rotation curve, by means of the Eq. 39, in which the plastic shear resistance calculated by means of the Eq. 3 is equal to 185.76 kN. In this way, the comparison between the two models is performed under the same constitutive law.

In Figure 9 a comparison between the force-displacement curves of the two models is depicted. It shows a satisfactory agreement, providing the validation of the equivalent model in simple bending. In fact, the scatters between the two curves are very small, both in elastic and plastic ranges. It is useful to note that the difference in the transition zone between elastic and plastic behaviour is due to the fact that the non-linear analysis carried out by means of SAP2000 is based on a lumped plasticity approach, while in the case of STRAUS7 the spreading of plasticity is step-by-step developed as far as the displacement increases.
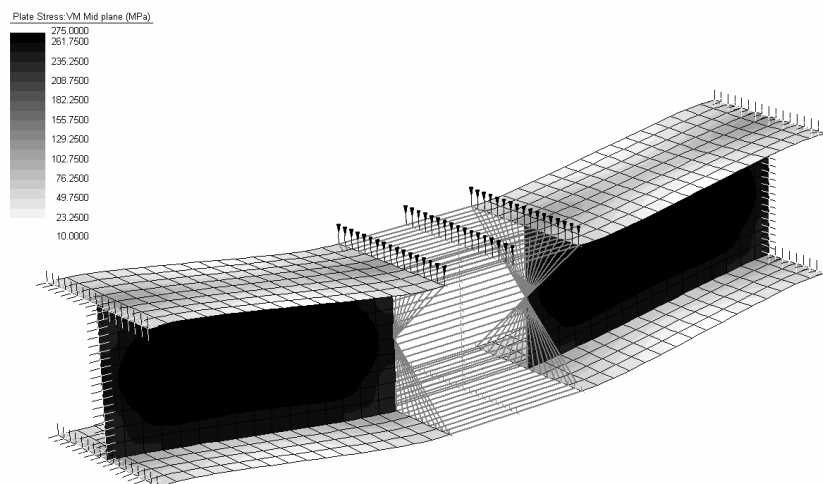

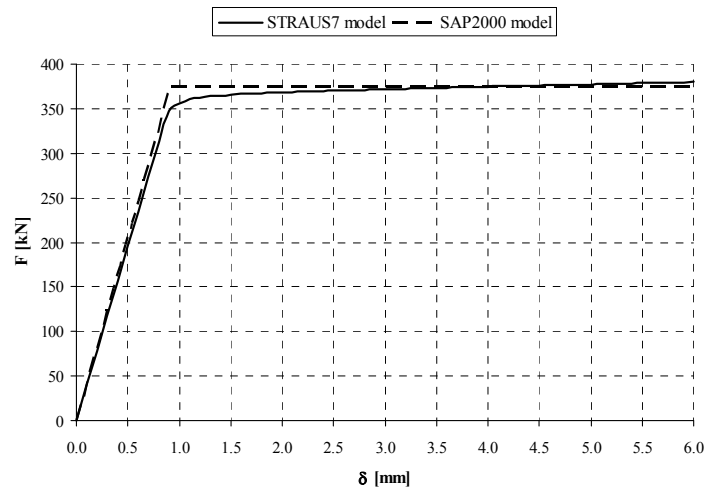Figure 8. STRAUS7stress Map at the First Yielding

Figure 9. Force-Displacement Curves of the Knee Models

Therefore, by means of Eqs. 39-40, the post-elastic behaviour of a knee element can be modelled by introducing two beam-column elements with plastic hinges at their ends. In particular, an elastic-plastic with strain-hardening bi-linear moment-rotation relationship can be assigned to each plastic hinge. The elastic range develops until the condition $(\gamma_y, M_{eq.p})$ is reached, being γ_y the first yielding rotation, which is calculated as the rotation corresponding to the attainment of the moment $M_{eq.p}$ at both ends of the member simultaneously. The second branch, accounting for strain-hardening, terminates at the point $(\gamma_u, M_{eq.u})$, where γ_u is the ultimate monotonic rotation, since the monotonic behaviour represents the envelope of the hysteretic cycles. According to the similarity with links of EBFs, the value of 0.2 radians (Engelhardt and Popov [12]) is chosen for the ultimate monotonic deformation of each knee portion.

5.   STATIC AND DYNAMIC NON-LINEAR ANALYSES

Non-linear analyses have been performed in order to evaluate the seismic response of the designed structures, so that the accuracy of the proposed procedure can be tested. Static and dynamic non-linear analyses have been carried out with different purposes. Static non linear analyses provide useful informations concerning the energy dissipation capacity of each structure and its global ductility. In addition, the pattern of yielding obtained from these analyses can be directly compared with the global failure mode representing the main goal of the proposed design methodology which, even though based on rigid-plastic analysis, operates within the framework of static approaches. As it is well recognised that static approaches do not account for higher mode effects, dynamic non-linear analyses are preferred to predict the actual pattern of yielding for the structure, i.e. the actual collapse mechanism, and the local ductility demands.

Designed KBFs are characterised by the same structural scheme (3 bays, with the KBF in the middle one; bay span $L = 6$ m; knee length $e = 1$ m; interstorey height $h = 3$ m, Figure 10) and different number of storeys (from 4 to 10). In particular, with reference to the considered building layout, it is assumed that only KBFs resist to horizontal forces, while all other beams and columns are only able to carry the vertical loads, since all the beam-to-column connections and the column-bases outside of the KB-frame are pinned.

Nevertheless, the proposed procedure could be extended also to the case of dual systems, in which moment resisting frames are combined with knee braced frames. To this scope, it is sufficient to combine the design procedures developed for each structural typology (Mazzolani and Piluso [1]); this means that the design equations described in the previous Sections have to be updated in order to account for the internal works due to all the beams and the columns, external to the KBF, involved in each mechanism typology. In addition, the axial forces in the columns have to take into account for the contribution of the framed bays, which is significant due to the shear forces transmitted by the beams when plastic hinges are developed at their ends.

However, since both moment resisting frames and knee braced frames are involved in seismic forces absorption, particular care has to be taken in the determination of the respective rates. In fact, as far as the rate of seismic shear acting on the KB-frame increases the dimensioning of knee elements becomes more and more severe, leading to a stronger braced structure. Consequently, the design of a dual system should be obtained by means of a calibration of the seismic shear distribution, in order to obtain an effective seismic response with the minimum structural weight. Researches in this field are currently in progress by the Authors with reference to dual systems constituted by the combination of moment resisting frames and different brace typologies.

With reference to Figure 10, the characteristic values of the vertical loads acting on the floors of the analysed scheme are equal to $3kN/m^2$ and $2kN/m^2$ for dead and live loads, respectively. The structural material adopted for all the members is S 275 steel grade ($f_y = 275MPa$).

The design horizontal forces have been determined according to Eurocode 8, assuming a peak ground acceleration equal to $0.35g$, a seismic response factor equal to 2.5, a behaviour factor q equal to 6, and an importance factor γ_I equal to 1.0 (CEN [11]). Therefore, an horizontal force distribution according to the first vibration mode is assumed for the design process. Nevertheless, this assumption does not constitute a restriction of the method. In fact, the design approach could be carried out by means of an iterative process, in which the triangular distribution of horizontal forces represents only the first tentative distribution for dimensioning the structure. Successively, by means of a modal analysis, the vector **F** can be updated by means of a combination of the most relevant vibration modes, and the design process can be applied again. However, since dynamic non-linear analyses directly account for the influence of all the vibration modes, the corresponding results provide the actual response of the structure, and they constitute a measure of the accuracy of the proposed procedure even when it is led according to the first eigenmode like in this work.
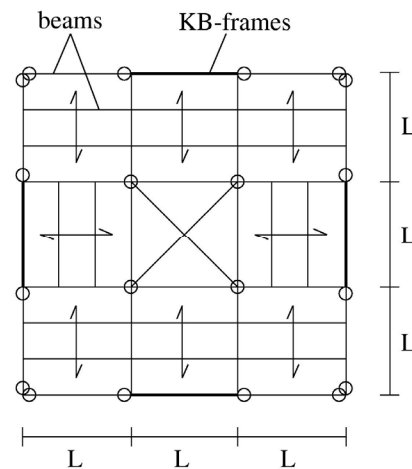

Figure 10. Building Layout

The design displacement δ_d ($\delta_u = \delta_d$) has been determined as the value corresponding to the maximum allowable engagement of the more involved knee element, i.e. its ultimate rotation γ_u. With reference to Eq. 15, this leads to the following relationship:

$$\delta_d = \theta\, h_{n_s} = \left\{ \frac{e_k\, sen\beta_k}{h_k - h_{k-1}} \right\}_{min} \gamma_u\, h_{n_s} \tag{41}$$

where γ_u is assumed equal to ± 0.08 rad for short knee in cyclic loading like the case of short links of eccentrically braced frames (Engelhardt and Popov [12]).

For each examined KBF both the scheme with pinned column-to-brace joints and the scheme with continuous column-to-brace joints have been considered (Conti [3]). In this paper, for sake of shortness, only the results concerning 8-storey KBF with pinned brace-to-column joint are presented. In particular, the application of the design procedure described in the previous Sections (with $\delta_u = 32$ cm) leads to the standard HEB profiles reported in Table 1 for each member.

Static non-linear analyses have been performed by means of SAP2000. The structure has been modelled by means of non-linear elements with possible plastic hinges located at the ends of each member. In particular columns, diagonals and beams have been modelled using hinges accounting for axial force-bending moment interaction while the shear deformations of each knee portion are accounted for by means of shear hinges. In fact, SAP2000 computer program is supplied with a plastic hinge in pure shear, referred to the local axes of the member, so that the inclination of the knee element with respect to the global reference system is not relevant, and the use of the previously discussed non-linear model in equivalent bending is not necessary. The shear versus plastic displacement diagram has been modelled through a rigid-hardening behaviour. The hardening branch is developed between the values V_p and $V_u = 1.7 V_p$, whose corresponding ultimate displacement is given by $\gamma_u\, e/4$, as obtained by assuming that each plastic hinge is related to an half knee element portion (2 plastic hinges both for bottom and top knee portions, 4 plastic hinges for all the member), so that it is related to the half part of the internal work provided by Eq. 37.

Table 1. 8-Storey KBF – Designed Sections

storey	Knee	Brace	Beam	Column
1	HEB 300	HEB 300	HEB 160	HEB 450
2	HEB 280	HEB 300	HEB 160	HEB 450
3	HEB 280	HEB 300	HEB 160	HEB 400
4	HEB 260	HEB 280	HEB 160	HEB 340
5	HEB 240	HEB 280	HEB 160	HEB 340
6	HEB 220	HEB 260	HEB 140	HEB 300
7	HEB 180	HEB 240	HEB 140	HEB 240
8	HEB 120	HEB 180	HEB 120	HEB 140

The push-over analyses have been led under displacement control accounting for both mechanical and geometrical non-linearities. Moreover, for each step of the analysis, out-of-plane stability checks for compressed elements have been executed. In Figure 11 the push-over curve and the distributions of plastic hinges for a top-sway lateral displacement both equal and exceeding the design value are reported. These figures underline that according to the goal of the proposed design procedure, yielding occurs for all the knee elements at the design displacement, so that satisfactory energy dissipation capacity and adequate inelastic performances are achieved. Furthermore, the distribution of plastic hinges for displacement values exceeding the design one shows the development of a collapse mechanism of global type. Similar results have been obtained for all the examined KBFs.

In addition, incremental dynamic non-linear analyses (IDA) have been carried out for the designed KBFs. Dynamic non-linear analyses allow to predict the actual seismic response of the examined structures in terms of actually developed collapse mechanism, energy dissipation capacity and local ductility demands. These analyses have been carried out by means of DRAIN-2DX computer program considering three different seismic motions: two simulated records matching Eurocode 8 inelastic design response spectrum, with A and C subsoil class respectively (CEN [11]), and an historical one (Tolmezzo 1976, PGA = 0.313g). The results coming from these analyses have been post-processed to perform out of plane stability check of the members.

The structure has been modelled as an assembly of non-linear elements characterised through specific hysteretic constitutive laws. In particular columns, braces and beams have been modelled using beam-column elements. For these members the bending moment versus plastic rotation diagram has been modelled through an elastic-perfectly plastic behaviour. The axial force-bending moment interaction domain has been defined according to the plastic domain provided by Eurocode 3 (CEN, 2005). The modelling of knee elements has been carried out, as previously discussed, by means of equivalent plastic hinges in simple bending.

Aiming at the evaluation of the seismic response of the designed KBFs, for each ground motion, the plastic hinge distribution, the maximum absolute and relative displacements and the maximum plastic deformation demands for each structural element have been evaluated. In particular, in order to validate the results provided by the static non-linear analysis, the results concerning 8-storeys KBF with pinned column-to-brace joint are herein presented. In particular, reference to the Eurocode 8 simulated ground motion for subsoil class A (EC8-A) is made.
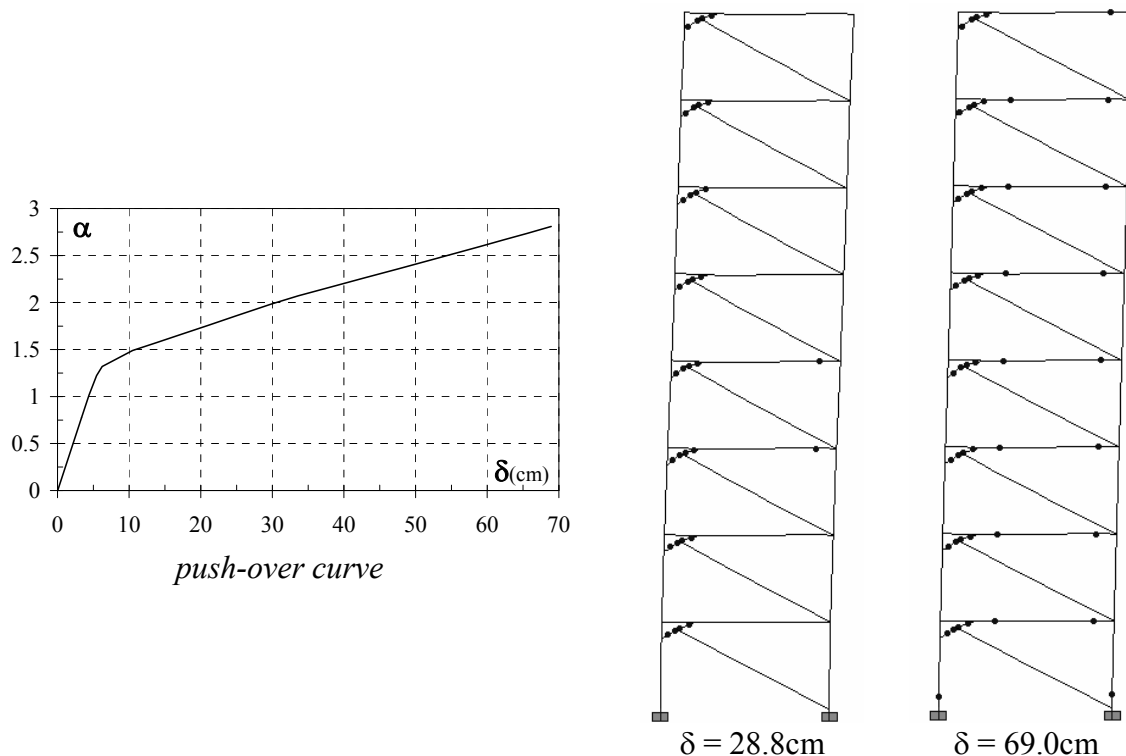

Figure 11. 8-Storeys KBF Push-Over Results

In Figure 12 the maximum required plastic deformations are reported for increasing values of the peak ground acceleration (PGA). In addition, Figure 13 provides the values of the plastic deformations for all the members (in the figure plastic rotations have to be scaled for the factor 10^{-2}). In Figure 14 the maximum absolute displacements for different values of PGA are depicted in non-dimensional form by means of the roof displacement angle (in symbols $RDA = \Delta/H$). In addition, in the same Figure 14 the maximum inter-storey drift ratios are shown (in symbols $MIDR = \delta_{max}/h$). Similar results have been obtained for all the analysed structures and for all the examined ground motions (showing that the most evident differences in terms of seismic response occur for EC8-C ground motion) and lead to the following observations (Conti [3]).

First of all, the designed structures are characterised by the fulfilment of the design goal, i.e. the development of a collapse mechanism of global type. In fact, the distribution of plastic hinges shows that all the dissipative zones, i.e. all the knee elements, are involved in the collapse mechanism (Figure 13), so that large dissipation capacity and global ductility are achieved. Furthermore, for increasing values of PGA, yielding occurs in the other members (beams and base columns) according to the prediction of the design methodology, and a global collapse mechanism develops.

In addition, regarding local ductility demands, the maximum values of plastic rotations have to be compared with the cyclic local ductility supply provided by short knees (i.e. ±0.08rad). With reference to Figure 12, knee elements reach the limit value of 0.08 rad for a PGA value equal to about 1.0g. Similar results have been obtained for the other analysed structures, where the ultimate knee rotation is reached for high values of PGA (generally between 0.7g and 1.0g). This result points out that the KBFs designed according to the proposed design procedure are able to withstand severe earthquake exploiting their large global ductility without the fracture of the dissipative zones, unless very high values of PGA are reached. This is a relevant result, since local ductility demands for short members, such as knee elements or short links in EBFs, are adversely affected by the influence of the geometrical configuration.
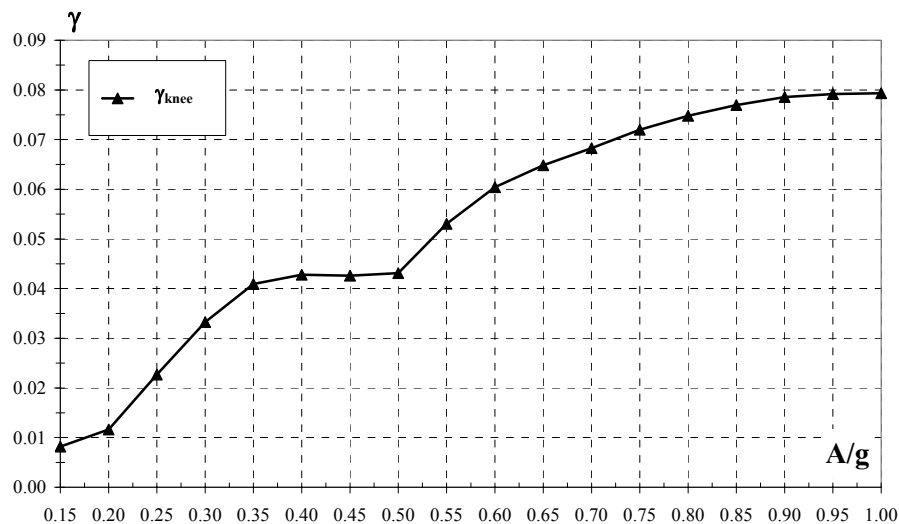

Figure 12. 8-Storeys KBF IDA – Maximum Plastic Knee Deformations (EC8-A)

Finally, it is useful to point out some considerations about the irregular behaviour of the curves depicted both in Figure 12 and in Figure 14. In fact, it is possible to recognize a significant variation of the curve slopes within the PGA range [0.35g, 0.55g]. First of all it is necessary to underline that not all the analysed structures show the same kind of response, even if several of them are characterised by non-monotonic behaviours.

It is well known that IDA curves often provide counter-intuitive results, as thoroughly discussed by Vamvatsikos and Cornell [16]. In fact, segments of softening or hardening can be provided after the initial stiffness of the structure, i.e. regions in which the slope of the curve decreases with higher intensity measures or other regions where such slope increases. This means that the structure can experience an acceleration responsible of damage accumulation, but at the following time it is subjected to a deceleration that can be powerful enough to momentarily stop the damage accumulation or even reverse it. So the IDA curve is characterised by lower damage measures and it becomes a non-monotonic function of the PGA. In particular, the examined case is analogous to the case of *severe hardening* (Vamvatsikos and Cornell [16]). In fact, the system shows an high response for a given intensity level, but exhibits the same or lower response for higher seismic intensities due to excessive hardening. Within this issue, it is the pattern and timing of the accelerogram rather than just the intensity that make the difference. As the earthquake is scaled up, weak response cycles in the early part of the response time-history become amplified enough to generate yielding, so that the structure properties result modified when the stronger cycles are reached. The extreme case of hardening leads to the case in which a structure reaches the global collapse for an intensity measure but not for an higher one, reappearing with high response but still in an equilibrium state. This issue is known as *structural resurrection*.

6.   CONCLUSIONS

This paper has been focused on several issues concerning the design of knee braced frames aiming at the attainment of satisfactory seismic performances with the primary goal of developing a collapse mechanism of the global type.

First, the behaviour of knee dissipative zones located in knee elements has been briefly discussed, pointing out the relevant aspects concerning their plastic involvement. These results are particularly useful in the development of a design procedure which is the natural extension to KB-structures of a design methodology already suggested for seismic-resistant frames (Mazzolani and Piluso [1]) and for eccentrically braced frames (Mastrandrea et al. [2]). Therefore, this methodology constitutes a general design approach which allows the control of the failure mode for any type of seismic-resistant structure.

In particular, the procedure starts from the knowledge of the dissipative zones (i.e. knee elements), which are dimensioned in order to resist the internal actions due to the design horizontal loads. Then, according to capacity design, by means of simplified equilibrium equations, the brace cross sections are dimensioned on the basis of the maximum internal actions that the knee elements, at the ultimate limit state, are able to transmit. In addition, the beam cross sections are dimensioned on the basis of the vertical loads acting on the floor. Finally, the column cross sections are obtained by applying the kinematic theorem of plastic collapse (taking into account second order effects due to vertical loads), which allows to derive the design conditions to be satisfied to guarantee a global collapse mechanism for the structure. In addition, in this procedure, a target design displacement of the structure is selected according to the maximum allowable plastic rotation for the dissipative zones, so that also the local ductility demands are under control.

Push-over analyses carried out for an adequate number of designed KBFs have pointed out the goodness of the proposed design procedure. In fact, for all the designed KBFs all the dissipative zones are involved in the collapse mechanism, leading to large global ductility.

Furthermore, the actual seismic response of the designed KBFs has been studied by means of IDA. The results still show the accuracy of the design procedure, in fact all the designed structures actually exhibit a global mechanism and are characterised by high global ductility and energy dissipation capacity. In addition, the local ductility demands are compatible with the corresponding supplies, even for high PGA values ranging between 0.7g and 1.0g. This means that the proposed procedure is able to control both the collapse mechanism typology and the local ductility demands.
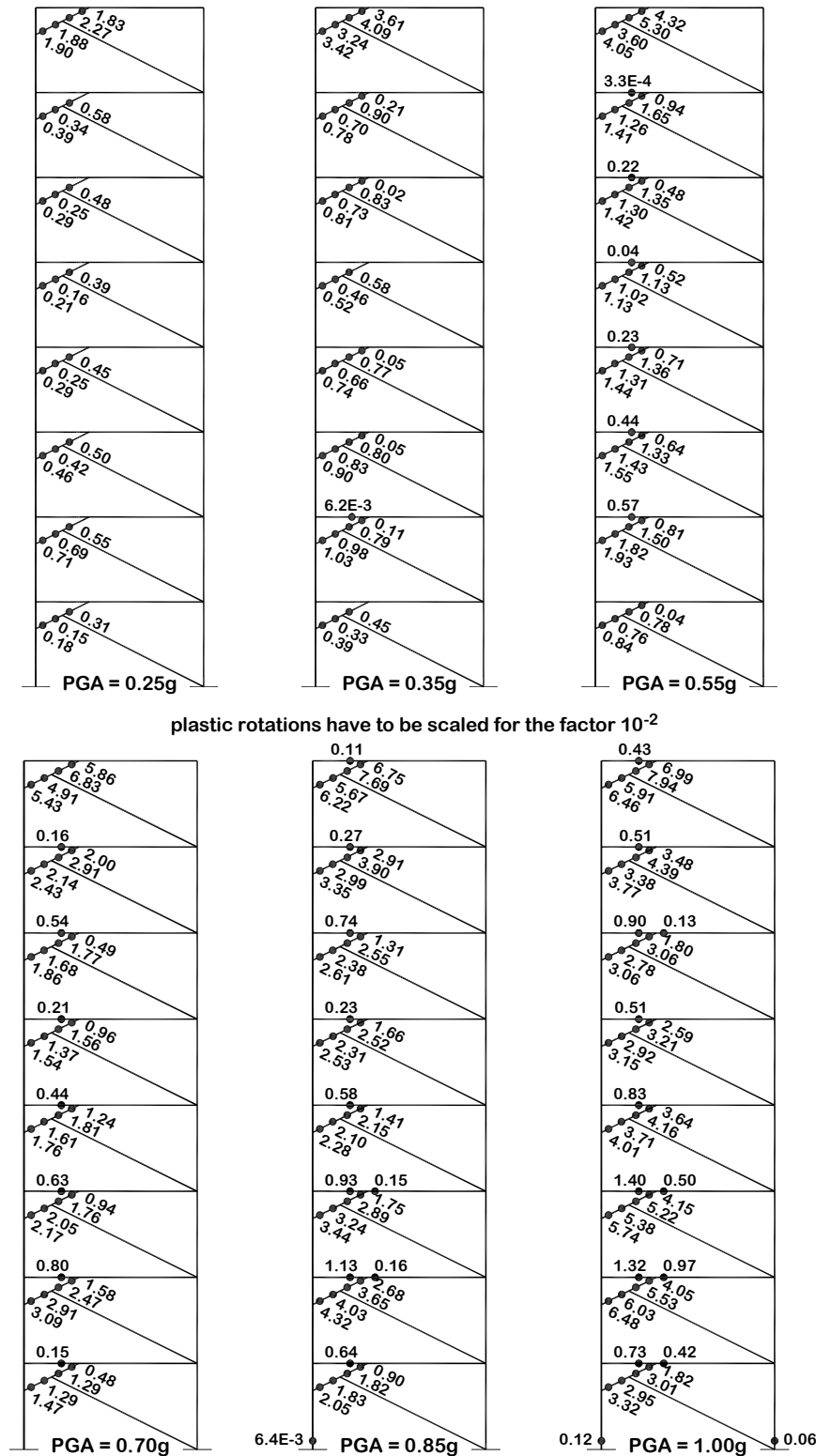

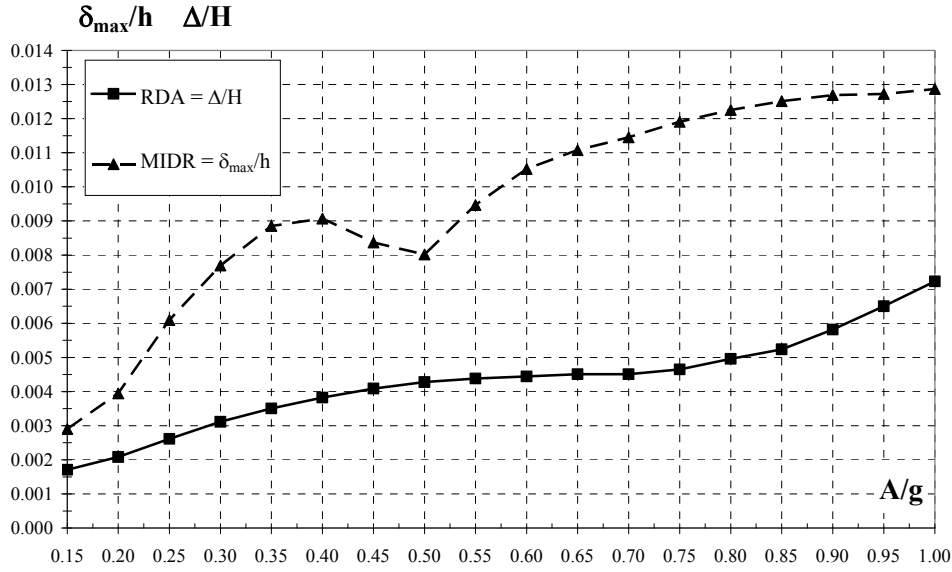Figure 13. 8-Storeys KBF IDA – Plastic Hinges Envelope (EC8-A)

Figure 14. 8-Storeys KBF IDA – Maximum Absolute and
Relative Non-Dimensional Displacements (EC8-A)

APPENDIX

Notation:

- **B**   vector of order n_s whose elements B_k are equal to the beam plastic moments, reduced for the contemporary presence of the axial force (elements $B_k = M_{b,k}$);
- **B$_r$**   vector of order n_s whose elements B_{rk} are equal to the diagonal plastic moments, reduced for the contemporary presence of the axial force (elements $B_{r,k} = M_{d,k}$);
- **C**   matrix of order $n_c \times n_s$ whose elements C_{ik} are equal to the column plastic moments, reduced for the contemporary presence of the axial force (elements $C_{ik} = M_{c,ik}$);
- d_k distance between the plastic hinge located in the beam (close to the knee) and the first column axis;
- **D$_v$**   vector of order n_s of the coefficients $D_{v,k}$;
- $D_{v,k}$ coefficient related to the external work of the uniform load acting on the beam of the kth storey (equal to $Ld_k/2$ for the examined scheme) (Conti et al. [6]);
- e_k length of knee of the kth storey;
- **F**   vector of the design horizontal forces;
- **h**   vector of the storey heights;
- H_0 sum of the interstorey heights of the storeys involved by the generic mechanism;
- h_k storey height of the kth storey;
- i column index;
- i_m mechanism index;
- k storey index;
- **K$_n$**   vector of order n_s whose elements K_{nk} are equal to the knee ultimate shear forces (i.e. $K_{nk} = V_{u,k}$);
- L bay span;
- $M_{c,ik}$ plastic moment, reduced for the presence of the axial internal force, of the ith column of the kth storey;
- **M$_{ck}$**   vector of the plastic moments of the columns of the kth storey, reduced due to the influence of the axial force (elements $M_{c,ik}$);

- M_k plastic moment, reduced for the presence of the axial internal force, of the diagonal ($M_{d,k}$) or of the beam ($M_{b,k}$) of the kth storey;
- n_c number of columns for each storey ($n_c = 2$ for one bay KB-frames);
- n_s number of storeys;
- **q**   vector of order n_s of the uniform loads acting on the beams;
- q_k uniform vertical load acting on the beam of the kth storey;
- **R_b**   vector of order n_s of the coefficients $R_{b,k}$;
- **R_c**   matrix of order $n_c \times n_s$ of the coefficients $R_{c,ik}$;
- $R_{c,ik}$ coefficient related to the participation of the ith column of the kth storey to the collapse mechanism: $R_{c,ik} = 1$ when the element is involved in the mechanism, $R_{c,ik} = 0$ in the opposite case;
- **R_d**   vector of order n_s of the coefficients $R_{d,k}$;
- R_k coefficient related to the participation of the beam ($R_{b,ik}$), knee ($R_{kn,ik}$) or diagonal ($R_{d,ik}$) of the kth storey to the collapse mechanism: it is equal to plastic deformation of the beam, the knee or the diagonal of the kth storey for a unitary rotation of the KBF columns (Eq. 6-9) when the element is involved in the mechanism, $R_k = 0$ in the opposite case;
- **R_{kn}**   vector of order n_s of the coefficients $R_{kn,k}$;
- **s**   shape vector of the storey horizontal virtual displacements;
- **V**   vector of the storey vertical loads, whose kth element V_k is the total load acting at the kth storey ($V_k = q_k L$);
- $V_{u,k}$ ultimate shear force of the knee of the kth storey;
- β_k angle between the direction of the diagonal of the kth storey and the horizontal direction.

REFERENCES

[1]   Mazzolani, F.M. and Piluso, V., "Plastic Design of Seismic Resistant Steel Frames", Earthquake Engineering And Structural Dynamics, 1997, Vol. 26, pp. 167-191.

[2]   Mastrandrea, L. and Piluso, V., "Plastic design of eccentrically braced frames: II. Failure mode control", Journal of Constructional Steel Research, Elsevier, ISSN: 0143-974X, doi: 10.1016/j.jcsr.2008.10.001, May 2009, Vol. 65, No. 5, pp. 1015-1028.

[3]   Conti, M.A., "Progettazione a Collasso Controllato di Controventi del tipo *knee*", PhD Thesis (in Italian), University of Salerno, Italy, 2007.

[4]   Mazzolani, F.M. and Piluso, V., "Theory and Design of Seismic Resistant Steel Frames", An Imprint of Chapman & Hall, 1996.

[5]   Kasai, K. and Popov, E.P., "General Behavior of WF Steel Shear Link Beams", Journal of Structural Engineering, 1986.

[6]   Conti, M.A., Mastrandrea, L. and Piluso, V., "Theoretical Analysis of Moment-Shear Interaction in Knee Braced Frames", Proceedings of Stessa 2006, 5th International Conference on Behavior of Steel Structures in Seismic Areas, Yokohama, Japan, 2006a.

[7]   Neal, B.G., "Effect of Shear Force on the Fully Plastic Moment of an I-Beam", Journal of Mechanics and Engineering Science, 1961, Vol. 3, pp. 258-266.

[8]   Clement, D.E., "Seismic Analysis of Knee Elements for Steel Frames", PhD Thesis. University of Oxford, England, 2002.

[9]   Popov, E.P., Engelhardt, M.D., "Seismic Eccentrically Braced Frames", Journal of Constructional Steel Research, 1988, Vol. 10, pp. 321-354.

[10]   Okazaki, T., Arce, G., Ryn, H., Engelhardt, M.D., "Recent Research on Link Performance in Steel Eccentrically Braced Frames", Proceedings of 13th WCEE, Vancouver, Canada, 2004, Paper No. 302.

[11]   CEN, "EN 1998-1:2004 – Eurocode 8: Design of Structures for Earthquake Resistance – Part 1: General Rules, Seismic Actions and Rules for Buildings", Comité Europeén de Normalisation, 2004.

[12]   Engelhardt M.D. and Popov E.P., "Behavior of Long Links in Eccentrically Braced Frames", Earthquake Engineering Research Center, University of California, 1989, Report No. UCB/EERC – 89/01.

[13]   Mastrandrea, L. and Piluso, V., "Plastic design of eccentrically braced frames: I. Moment-shear interaction", Journal of Constructional Steel Research, Elsevier, ISSN: 0143-974X, doi: 10.1016/j.jcsr.2008.10.002, May 2009, Vol. 65, No. 5, pp. 1007-1014.

[14]   Conti, M.A., Mastrandrea, L. and Piluso, V., "Plastic Design of Seismic Resistant Knee Braced Frames", Proceedings of Stessa 2006, 5th International Conference on Behavior of Steel Structures in Seismic Areas, Yokohama, Japan, 2006b.

[15]   CEN, "EN 1993-1-1:2005 – Eurocode 3: Design of Steel Structures – Part 1-1: General Rules and Rules for Buildings", Comité Europeén de Normalisation, 2005.

[16]   Vamvatsikos, D. and Cornell, C.A., "Incremental Dynamic Analysis", Earthquake Engineering And Structural Dynamics, 2002, Vol. 31, pp. 491-514.